The Nonlinear Mechanics and Rheology of Oriented Polymers

by

Thomas C. O'Connor

A dissertation submitted to The Johns Hopkins University in conformity with the requirements for the degree of Doctor of Philosophy.

Baltimore, Maryland

May, 2018

Abstract

This thesis applies nonequilibrium molecular dynamics simulations to study the mechanics, failure, and formation of highly oriented polymers. The first portion focuses on the mechanics of ultrahigh molecular weight (UHMW) polyethylene (PE) fibers. PE fiber strength is dominated by the properties of the crystal phase, but a complex, composite-like structure makes predicting fiber properties challenging. We simulate perfect PE crystals as a model fiber in order to predict upper bounds on fiber strength, creep, and shock propagation. In all cases, we identify the molecular-scale mechanisms mediating plasticity and relate them to macroscopic response. In the second part, we explore the nonlinear rheology of extensional flows of highly entangled polymers. We apply recently developed algorithms to simulate steady-state uniaxial extensional flows of entangled polymers for the first time. The steady-state chain conformations are characterized and related to trends in macroscopic properties like the nonlinear viscosity. Next, we study relaxation from the far-from-equilibrium states produced by extensional flows. Unexpectedly, relaxations reveal that many equilibrium properties, like the entanglement length N_e and the disentanglement time

ABSTRACT

τ_d, remain constant for even the most extreme deformations.

Primary Reader: Mark O. Robbins, Professor of Physics

Secondary Reader: Robert Leheny, Professor of Physics

Acknowledgments

I am deeply grateful to my mentor of my adviser, Prof. Mark O. Robbins. His inexhaustible investment of care and patience have helped me to become a better researcher, professional, and mentor. He has taught me much about the importance of careful attention and deliberate action, and how to channel my often undirected enthusiasm into focused and meaningful research.

My work at JHU has been made much easier by the friendship and camaraderie of my officemates. I'm thankful to Mike, Ting, Tristan, Lin, Joel, Joe, and Marco for many fun memories and conference trips. I look forward to many more to come. I'd also like to thank my undergraduate mentees, Hayley and Austin, for their work, patience, and the valuable lessons they have taught me about being a mentor.

The Village Church has been a second home and family while I have lived in Baltimore. I am grateful for their love and faithfulness to me, my marriage, and to the Hampden community. I am especially grateful to Pastor Dan Hyun and Judie Hyun for the sacrafice of time and prayer made for me. They have taught me how to be a better man and husband. Lastly, I am grateful to the Village community for

introducing me to my wife, Virginia.

Virginia, thank you for your love, understanding, and belief in me in the face of an uncertain future. Thank you for reassuring me when I lose confidence in myself and for listening to me talk about "boring" physics things because you know it makes me happy. I am happy you are on this adventure with me, and I am excited to build our future together.

This thesis would not exist if not for the love and support of my family and especially my mother, Noelle. Her understanding my interest in physics and encouraging me to pursue it at a young age was essential for everything that I have accomplished. Thank you for raising me in the way in which I was bent.

Finally, I owe thanks to the many scientists and administrators who have provided and managed the funding for my research. My early graduate studies and training were financially supported by the Modeling Complex Systems IGERT Fellowship through Grant No. DGE0801471. My thesis work was performed within the Center for Materials in Extreme Dynamic Environments at the Hopkins Extreme Materials Institute. Financial support was provided by the U.S. Army Research Laboratory through Grant No. W911NF-12-2-0022 and NSF DMREF No. 90079795. I'd like to thank Prof. Lori Graham-Brady, Dr. Jan W. Andzelm, Prof. K.T. Ramesh, and Prof. Thao D. Nyugen for their time, mentoring, and support through these programs.

Dedication

To Virginia, for choosing me and the years to come.

Contents

List of Tables

List of Figures

Chapter 1

Introduction

Materials are often used to mark stages of development in modern history. The use of stone, bronze, iron, and steel has transformed human civilization and how we interact with the world. Of all the materials developed in the twentieth century, polymer materials (plastics) have arguably had the greatest impact on everyday life. Polymers are used everywhere from bullet proof glass to prosthetic limbs. They have revolutionized how we preserve food, practice medicine, and design armors for soldiers. Polymers are also some of the cheapest materials to produce and process, requiring much less energy than metal or ceramic materials. This ensures that polymers will remain a relevant and important class of materials as constraints on energy consumption rise in the twenty-first century.

The diverse applications of polymer materials originate from their molecular scale structure. Polymers are made of long molecular chains that extend throughout a

plastic material. The volume a single chain pervades can be thousands of times larger than the total volume of its monomers. Like macroscopic wool fibers, polymer chains are flexible and can adopt a wide variety of tortuous conformations as they intertwine with each other, and these conformations determine how plastic materials behave. In amorphous polymers, chain conformations are isotropic random walks. These random coils entangle with each other and form a dense mesh, similar to wool felt. Amorphous polymers can be quite durable and are often used for water bottles and trash bags. If, instead, the chains are extended along a single direction then they can form fibers that are the molecular equivalent to wool yarn. Like yarn, polymer fibers are exceptionally strong along the direction of alignment but are soft in the transverse directions. This makes them easy to weave into cables and textiles or embed within other materials to form fiber-reinforced composites.

The ability to change a polymer's mechanical behavior by changing only its molecular organization helps make polymers versatile and cost-efficient materials. Nonlinear flows are a common way of deforming polymers to change both the macroscopic shape and the local orientation and alignment of polymer chains. Flow induced changes in molecular order can be used to continuously tune the stiffness and failure stress of polymers by orders of magnitude [1, 2], producing materials as stiff as steel but with only 1/8th the density. Such oriented polymer fibers are often found in ship sails, vehicular chassis, prosthetic joints, and body armors.

While applications of oriented polymers have grown rapidly, many important ques-

tions about their structure and nonlinear deformation remain unaddressed. Polymer deformation is a challenging problem because chains extend across many length scales [3, 4]. Established theories for conventional crystalline solids, like metals, do not work well for oriented polymers. Metals often have one molecular length scale and one type of interatomic bond. Polymers may be a million times longer than their width and are joined together by covalent backbone bonds that are a hundred times stronger than the van der Waals (vdW) interactions between monomers. The competing length, time, and energy scales make polymers difficult to model analytically and hard to fully characterize with experiments.

In this thesis we apply molecular simulations to study the nonlinear deformation of oriented polymers. Our work is separated into two parts. In part one, we develop models for, and study the nonlinear mechanics of, oriented polyethylene (PE) fibers. In part two, we study the rheology and flow of entangled polymer liquids as they are oriented by extensional flows. These two problems are related. The first addresses the mechanical behavior of a widely used material, while the second considers the question of how such oriented polymers are formed. Our simulations provide detailed microscopic data that allow us to identify the molecular- scale plastic mechanisms that mediate macroscopic mechanical behavior. We then use these data to inform simple, analytic theories which we apply to interpret and predict experimental results.

1.1 A New Potential for High Pressure and Mechanical Failure - AIREBO-M

The unique mechanical properties of polymers arise because of anisotropic bonding at the molecular scale. Chain backbones are held together by strong covalent bonds with binding energies of order several eV. Meanwhile, interchain interactions are mediated by weak van der Waals bonds with meV scale binding energies. Polymer crystal deformation and plasticity arise from the competition between these two types of interaction, and molecular models must capture the physics at both energy scales. Incorrectly modeling the physics of covalent bonding can substantially alter predictions for the chain stiffness and fracture strength, and inaccurate van der Waals forces can change the density, elastic moduli and even the stable crystal structure.

Covalent interactions are the highest energy interactions that occur in molecular simulations and are also the easiest to optimize. Covalent bond lengths, stiffnesses, and binding energies can be characterized with many experimental techniques or with quantum chemistry calculations [5]. Van der Waals interactions are much harder to measure and characterize and they are highly sensitive to molecular architecture. The van der Waals interactions between two carbon atoms in PE are completely different than those for two carbons in diamond or in graphite [6]. Because of this structural sensitivity, van der Waals interactions are usually fit to reproduce the structure and properties of liquid phases of molecular materials [7]. This approach produces van

der Waals interactions that average over many different configurations rather than accurately modeling specific ordered phases. Unsurprisingly then, many interatomic potentials for polymers have accurate covalent interactions and liquid properties but make poor predictions for crystal phases [8, 9].

In Chapter 2 we develop a reactive interatomic potential for hydrocarbons called AIREBO-M that accurately captures the physics of both covalent and van der Waals interactions in polymer crystals [10]. Our model is a refinement of the Adaptive Intermolecular Reactive Empirical Bond Order (AIREBO) potential for hydrocarbon chemistry [11]. AIREBO is a reactive interatomic potential, which is a potential that uses classical many-body interactions to mimic the quantum mechanics of chemical bonding. Most potentials used in MD model covalent bonding by connecting atoms with permanent springs. This is computationally efficient but does not permit covalent bonds to break. Reactive potentials like AIREBO do not explicitly define chemical bonds. Instead, they form bonds dynamically based on the atoms in the local neighborhood. AIREBO models CH chemistry, and attempts to find the most energetically favorable bonding configuration for each atom based on its environment. This allows AIREBO to model fracture processes in a wide variety of CH chemistries, including polyethylene, graphite, and diamond, without resorting to expensive quantum mechanical calculations [11].

While AIREBO's treatment of covalent bonding is desirable, its intermolecular interactions are modeled by a Lennard-Jones (LJ) potential whose unphysically di-

vergent power-law repulsion causes AIREBO to fail when applied to systems at high pressure [9]. We present a modified potential, AIREBO-M, where we have replaced the singular Lennard-Jones potential with a Morse potential [10]. We optimize the new functional form to improve intermolecular steric repulsions, while preserving the ambient thermodynamics of the original potentials as much as possible. The potential is fit to experimental measurements of the layer spacing of graphite up to 14 GPa and first principles calculations of steric interactions between small alkanes. To validate AIREBO-M's accuracy and transferability, we apply it to a graphite bilayer and orthorhombic polyethylene. AIREBO-M gives bilayer compressions consistent with quantum calculations, and it accurately reproduces the quasistatic and shock compression of orthorhombic polyethylene up to at least 40 GPa.

In Chapters 3, 4, and 5, we apply the AIREBO-M potential to study several problems in the nonlinear mechanics of oriented polyethylene crystals. Extended-chain PE crystals are the most ordered arrangement of chains possible and they can be thought of as a "perfect" polymer fiber. Real polymer fibers never achieve complete order, but modern fibers come close. By studying the perfect crystal, we can understand the limiting properties of PE fibers and the dynamic processes that occur within most of a fiber's structure.

The polyethylene crystal is composed of fully-extended chains that are uniformly oriented along a single axis. The chains pack laterally into an orthorhombic unit-cell with chain backbones alternating to form a "herring-bone" texture, as shown

in Figure 1.1. The PE crystal has highly anisotropic mechanical properties due to different bonding mechanisms along different directions. The stiff covalent bonds along the chain backbones generate a large Young's modulus $E \approx 260$ GPa along the chain axis. In the transverse directions, chains are held in cohesion by much weaker van der Waals bonds, producing an approximately isotropic stiffness $E \approx 10$ GPa. The large mechanical anisotropy makes fibers susceptible to elastic instabilities as well as a variety of complex plastic mechanisms. This makes revealing the molecular processes controlling fiber failure and plastic deformation a challenging problem.

1.2 Strength of PE Fibers

A fiber's ultimate strength is the largest load it can hold before catastrophically failing. The origins of polymer fiber strength have been a topic of active debate for nearly 40 years. This is because the strongest PE fibers fail under tensile loads of around 5-7 GPa which is much weaker than the theoretical strength of the chains themselves. The C-C backbone bonds of PE chains should be able to hold ~ 20 GPa in tension before breaking. However, after several decades of research and development, the strength of PE fibers has not substantially improved [2, 3]. Many have suggested that fibers may never be as strong as their constituent chains because defects within the crystal allow the crystal to fail before chain scission [2, 3, 12].

The most popular alternative explanation of failure is chain slip where chains lose

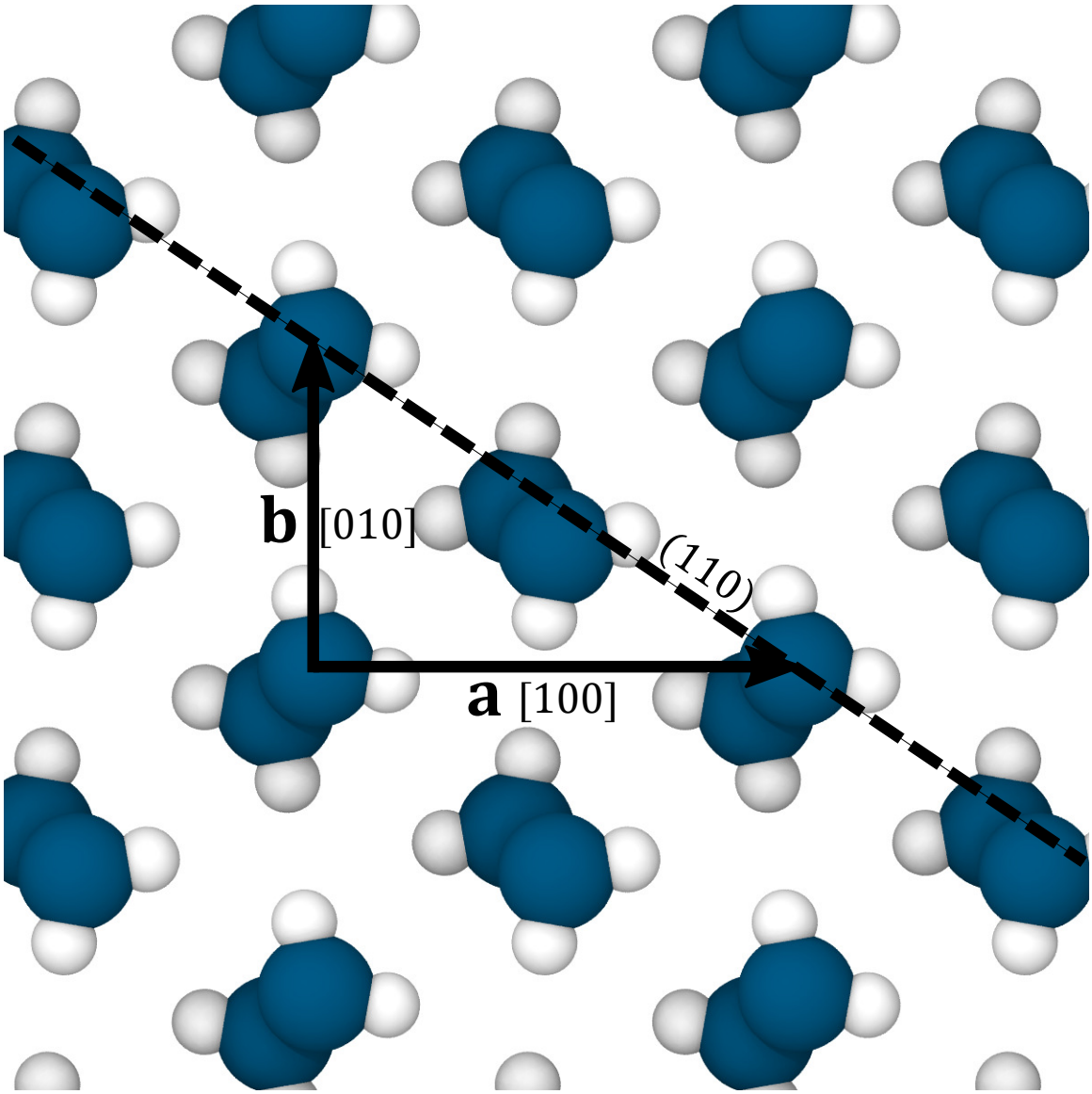

Figure 1.1: Molecular structure of orthorhombic PE. Chains are fully extended in an all-trans conformation out of the plane along the **c**-axis ([001] direction). Chains pack laterally with alternating backbone orientation, forming a herringbone pattern with orthogonal lattice vectors **a** and **b**. The Young's moduli along **a** and **b** are ~ 8 GPa, while the modulus along **c** is ~ 260 GPa. Slip on the (110) plane (dashed line) dominates transverse plasticity during quasistatic shock compression.

their cohesive grip on each other and slide past each other along the fiber axis by breaking and reforming van der Waals bonds [3]. Breaking van der Waals bonds is much easier than breaking covalent bonds, but many van der Waals bonds must be broken for a long chain to slip. Chains in Ultra-High Molecular Weight PE fibers typically have at least $\sim 10^5$ monomers, making the energy cost for an entire chain to slip much larger than the cost for chain scission. It is easier for chain slip to occur at a localized defect that disrupts only a few bonds within the crystal.

The simplest type of defect that must be present in real materials is a chain end. A chain-end defect is shown in Figure 1.2(a) and can be thought of as missing covalent bonds where one chain terminates, and another begins. The backbone cannot carry tension near the chain end because of the missing C-C bonds. This causes strains to localize near chain ends and can facilitate chain slip [13].

In Chapter 3, we use molecular simulations of crystalline PE to determine how chain ends limit the ultimate strength of PE fibers. We control the density of chain-end defects by varying the chain length between 10^2–10^4 carbons. We find the yield stress σ_y saturates for long chains at 6.3 GPa, agreeing well with experiments. We show that crystals always yield by chain slip, and that slip is mediated by the nucleation of 1D dislocations at the chain ends. Our simulations provide the first theoretical prediction of such dislocations, and, by analyzing their properties, we can explain many aspects of the deformation and failure of fibers observed in experiments.

A 1D dislocation, shown in Figure 1.2(b), is a lower dimensional version of the

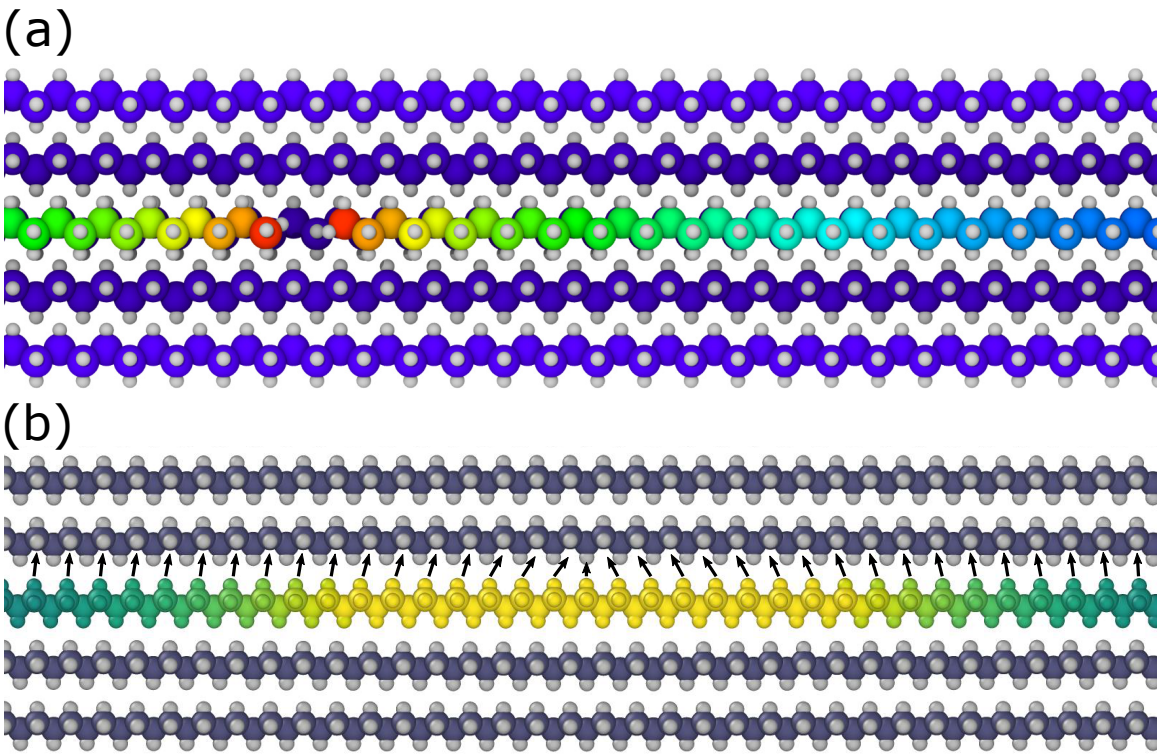

Figure 1.2: (a) Removing the monomer between the two red carbons leads to two chain-end defects in an orthorhombic polyethylene crystal under tensile strain. Carbons are qualitatively colored by bond length to show how strain localizes near the missing backbone bonds. (b) A 1D dislocation that carries one excess monomer. As it passes, it translates the chain by one lattice spacing.

dislocations that determine the mechanical response of metals. While metallic dislocations are lines or loops moving within the planes of a 3D crystal, 1D dislocations are point-like defects localized to a single chain. Moving them along the chain translates the chain by one monomer. The size and structure of the dislocation core emerges from the competition of chain tension, mediated by C-C bonds, and intermolecular friction that resists disruption of the registry of neighboring chains. The localization of the dislocation to a single backbone is a remarkable result of the large mechanical anisotropy resulting from the very different strength of these two interactions.

1D dislocations are an example of "dimensional reduction," where the excitations that emerge from the interactions of a complex system exhibit simpler dynamics than the system itself. As shown in Chapter 3, the results of large, fully atomistic molecular dynamics simulations can be reproduced with a simple 1D Frenkel-Konotorova (FK) model of dislocations [13]. The FK model captures the competition between chain tension and friction by considering the dynamics of a single chain of monomers resting within a periodic crystal potential. The potential represents the collective intermolecular friction created by the van der Waals interactions of all neighboring chains. The FK model gives analytic predictions for the structure, stability, and energetics of 1D dislocations in terms of three parameters which we measure with MD simulations of very small crystals [13–15]. The FK model with these parameters reproduces full MD results for the strain and stress to failure of PE crystals and even the size and geometry of individual dislocations.

Chapter 4 uses the FK model to study the slow process of creep, which is difficult to treat direcly with MD simulations. A fiber that is loaded below its yield stress will deform slowly through rare, thermally activated plastic rearrangements. Creep is common in fibers of many polymers and leads to strength degradation and premature failure below the yield stress [1, 3]. Identifying and modeling fiber creep mechanisms will improve understanding of fiber aging and aid development of safe standards for their use and replacement.

Experiments usually characterize creep in fibers by fitting data to a stress-activated Eyring model [1]:

$$\dot{\epsilon}_c \propto \omega_0 e^{-E_a^0/k_bT} \sinh(\sigma V^*/k_bT) \tag{1.1}$$

which relates the rate of creep $\dot{\epsilon}_c$ to a thermally activated process with an attempt frequency ω_0, energy barrier E_a^0 and an activation volume V^*. The activation barrier determines how rare creep events are, and V^* determines how rapidly the barrier decreases with external load. Their functional form depends upon the dynamics of the specific defects mediating plasticity.

Chapter 4 applies the FK model to fiber creep by studying the energetics of 1D dislocation nucleation at chain ends. We use it to calculate the load dependent energy barrier for chain slip at chain ends, and derive effective Eyring activation barriers and volumes to compare to experimental measurements. Our analytic predictions for chain-slip mediated creep give values for E_a and V^* that agree well with experimental data.

1.3 Shock of PE Crystals

Chapter 5 applies AIREBO-M to investigate the impact and shock mechanics of crystalline and amorphous phases of polyethylene (PE). Shock loading is an important form of nonlinear mechanical response that occurs when the thermodynamic state of a material is suddenly changed through impact or rapid heating. PE fibers are often incorporated into load bearing mooring lines or composite armors which typically fail through sudden loading. Understanding how this failure occurs is important for designing safer cables and armors.

Shock impact occurs when loading occurs faster than sound waves can distribute the resulting deformation uniformly throughout the material. Instead, a shock-wave travels through the solid and mediates a sudden jump in the thermodynamic and hydrodynamic state of the material [16, 17]. The speed at which a shock propagates is called the shock speed U_s and it depends upon both the properties of the quiescent material and the strength of the impact. Impact strength is usually characterized by either a jump in the material stress σ or a jump in the particle velocity U_p of the material that is imposed by the shock front [17]. A common experimental method for characterizing shock response is to plot U_s versus U_p [18]. The functional form of these curves is constrained by the Rankine-Hugoniot jump conditions that ensure the change in thermodynamic and hydrodynamic properties across the shock front conserve mass, energy, and momentum [16, 19].

The Rankine-Hugoniot jump conditions limit the states that can be accessed by

shock loading and determine the shape of the U_s versus U_p curves measured in experiments. Such curves are called Hugoniot curves and the locus of all possible curves that satisfy the Rankine-Hugoniot conditions is called the Hugoniot equation of state. Given the initial thermodynamic state of a material and the strength of a shock, either as a jump in particle velocity or jump in stress, the Hugoniot equation of state gives the thermodynamic state the material will be driven to behind the shock front [17,19]. Hugoniots for solid materials are usually complex and lack closed form solutions. This is because the constitutive response of solids changes significantly as they undergo plastic deformation [16]. The lowest impact velocity U_p that activates plastic deformation determines the Hugoniot elastic limit (HEL), which is an important engineering parameter for materials. All solid materials flow like fluids when shocks are much larger than the HEL, but most polymer applications involve shock impacts near the HEL where the detailed nature of the plasticity is important [18, 20]. Previous work has made theoretical predictions for the "fluidized" limit of strong shocks but not for the plasticity dominated regime [21, 22].

Molecular simulations are well suited to studying weak shocks. AIREBO-M's accuracy at high-pressure has allowed us to study shock-induced plasticity in amorphous and crystalline PE and our simulations reveal a complex hierarchy of mechanisms that is unique to polymers. The amorphous PE phase is isotropic and has a low yield stress, producing a shock-Hugoniot that agrees well with previous theoretical predictions [22]. Crystal simulations follow these earlier predictions at high impact

velocities, above 1000 m/s. At low velocities, the shock mechanics of the crystal is highly anisotropic and is controlled by molecular scale yield mechanisms that depend on the crystal plane of impact. For shock along the polymer backbone, an elastic front is followed by a plastic front where chains buckle with a characteristic wavelength. Shock perpendicular to the chain backbone can produce plastic deformation or transitions to different orthorhombic or monoclinic crystal structures, depending on the impact speed and direction. Tensile loading does not produce stable shocks: Amorphous systems craze and fracture, while for crystals, the front broadens linearly with time. This diverse and anisotropic plasticity is unique to polymers and innovative constitutive models will be required to capture it at macroscopic scales.

PE fibers contain a mix of crystalline and amorphous regimes. Each interface can scatter shock waves and lower the transmission of energy. Although it is not included in this thesis, I also studied shock of multi-domain systems in collaboration with a group at the Army Research Laboratory [23]. We found that the sudden change in density and mechanical stiffness at a crystal/amorphous interface leads to partial reflection of passing shock fronts and substantial absorption of the shock energy. The amount of energy absorbed by nanoscale amorphous domains depends upon their size when it is comparable to the width of the shock front. We characterized this size-dependent absorption and related it to the nanoscale kinetics of amorphous chains. These results suggest that shock attenuation in PE may be controlled by tuning amorphous domains.

Another related project that is not included in the thesis examined the low speed response of multidomain PE fibers [24]. I used AIREBO-M to determine the full elastic and plastic response of crystalline and amorphous domains for quasistatic loading. With collaborators at JHU we then considered the elastic response and yield of a range of representative geometries for PE fibers. For tensile loading, we found that crystalline regions carry most of the load, and the elastic and plastic properties of the crystal dominate tensile strength. In contrast, transverse loading showed much more sensitivity to the spatial organization of amorphous and crystalline domains.

1.4 Extensional Rheology

The second part of this thesis applies molecular simulations to explore the structure and dynamics of oriented polymers in the liquid phase. Oriented fibers are formed by stretching molten polymers with nonlinear elongational flows. Chains in the disordered melt state are extended and aligned by the flow, precipitating the formation of the resulting fiber's coherent crystalline structure. Understanding this process is difficult because chains interact strongly with each other as they respond to flow. Additionally, the flowing fluid's hydrodynamic properties are highly sensitive to the rapidly changing chain conformations [4]. Macroscopic quantities like the fluid viscosity couple to changes in chain elongation and alignment. Predicting how chain conformations adapt to flow and how these changes alter liquid proper-

ties is essential for polymer manufacturing; however, little is understood about the far-from-equilibrium dynamics of polymer melts at large extension [25, 26].

Experiments cannot easily measure the microscopic properties of polymers during extensional flow. Instead, they typically measure changes in flow properties like the viscosity and can only suggest how they relate to rearrangements occurring at the molecular scale [27, 28]. In a typical experiment, a constant uniaxial extension flow rate is applied. The liquid is stretched along one direction (the fiber axis) while it contracts in the two transverse directions to preserve volume. The flow rate is given by the Hencky strain rate $\dot{\epsilon} \equiv \partial \log L(t)/\partial t$, where $L(t)$ is the sample length along the fiber axis. Whether the flow deforms chain conformations depends upon the characteristic timescales on which chains relax. A dimensionless Weissenberg number $Wi = \dot{\epsilon}\tau$, where τ is a characteristic relaxation time for the polymer, is usually used to measure a flow's strength.

Experiments measure the time dependence of the extensional viscosity $\eta_{ex}(t) = \sigma_{ex}/\dot{\epsilon}$, Here $\sigma_{ex} = \sigma_{zz} - \sigma_{rr}$ is the extensional component of the stress, with σ_{zz} the stress component along the extension direction and σ_{rr} the transverse component. The evolution of η_{ex} depends upon the polymer architecture and flow rate. For a polymer in constant extensional flow, the dynamic viscosity grows over many decades in time until it plateaus to a steady-state viscosity as shown in Figure 1.3. In the limit of weak linear flows, $\eta_{ex}(t)$ is determined by the linear viscoelastic response of the polymer. The linear evolution, $\eta_0(t)$, is independent of flow rate and plateaus to

the Newtonian viscosity $\eta_0(t \to \infty) = \eta_N$ (black curve). For strong, nonlinear flows, $\eta(t)$ deviates above the linear response and plateaus to a steady nonlinear viscosity η_{ex} (red curve). The value of the steady viscosity typically depends on the flow rate and can increase (thicken) or decrease (thin) with increasing rate [27].

The complex behavior of the dynamic viscosity is due to the dynamics of chain conformations as they adapt to flow. Molten chains are disordered in their equilibrium state [4, 27]. Thermal fluctuations allow chain backbones to bend and lose orientational order for segments longer than a thermal persistence length of n_k bonds called a Kuhn segment. At larger scales, chains explore their configurational entropy and adopt random coil conformations. Chain conformations can be described by the internal distance function $R(n)$ which measures the rms magnitude of the vector connecting monomers separated by n bonds. $R(n)$ grows linearly with n for straight segments shorter than ℓ_k. At larger scales, chains behave like random-walks and $R \sim \ell_k n^{1/2}$. Scattering experiments have shown the scaling form of $R(n/n_k)$ is independent of chemistry and applies for many linear polymer melts above their chemically specific Kuhn length [4, 30].

Individual chains cannot move independently because they cannot pass through neighboring chains. These constraints are called entanglements and force chains to undergo undergo complex, collective motions as they move around each other. Entanglements introduce an important length scale called the entanglement length N_e. Chain segments that are longer than N_e bonds will form entanglements and their dy-

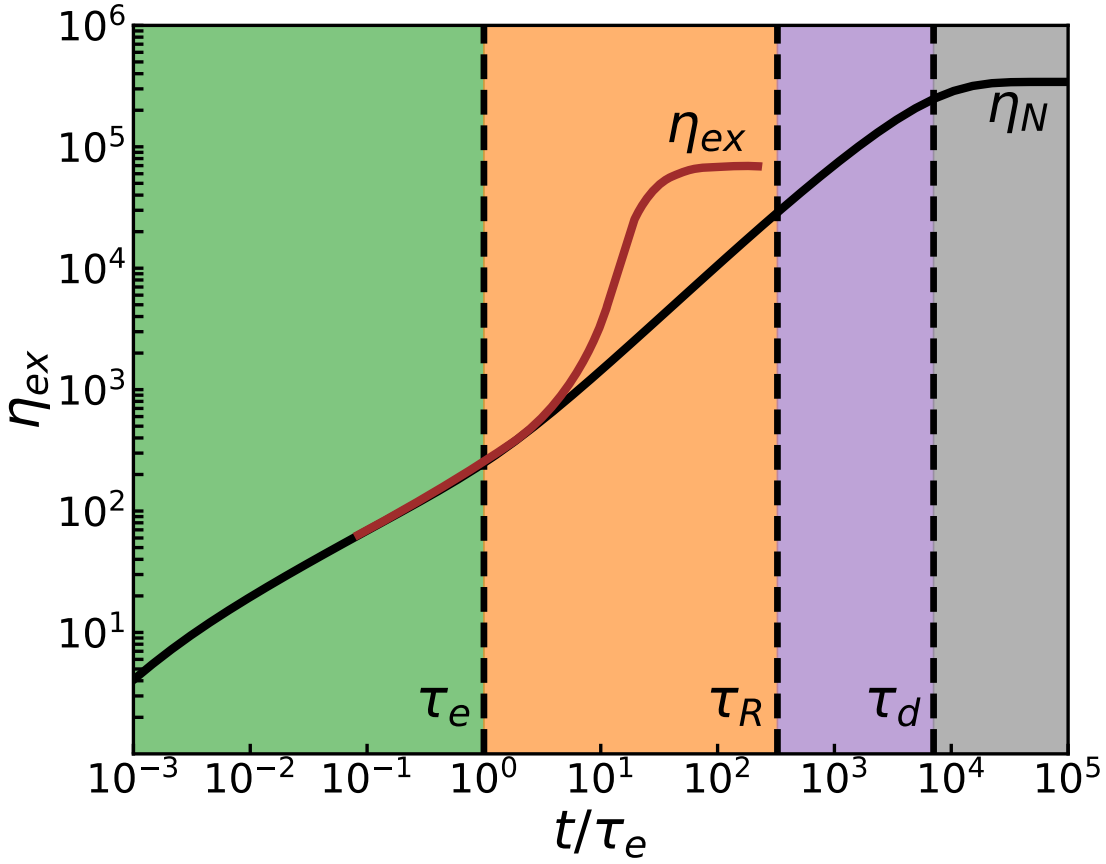

Figure 1.3: Dynamic viscosity for entangled polymers during uniaxial extensional flow. The viscosity increases over several decades in time as viscoelastic relaxation modes contribute. The mode spectrum is complex and governed by the entanglement (τ_e), Rouse (τ_R), and reptation (τ_d) times, which are labeled with dashed lines. τ_d is defined relative to τ_e as in Reference [29]. For weak flows, the viscosity follows a limiting linear viscoelastic envelope (black line) and plateaus to the Newtonian viscosity η_N. For nonlinear flows, $\eta_{ex}(t)$ deviates above the linear response and plateaus to a different, nonlinear viscosity.

namics will be constrained by the entanglement network. A chain of N bonds forms $Z = N/N_e$ entanglements with other chains. Z is called the degree of entanglement.

The highly-correlated diffusion of entangled chains has been likened to the wriggling of a pile of snakes in a pit and has been given the name "reptation." A phenomenological framework for reptation is the "tube model," based on the Nobel prize winning work of P.G. de Gennes [4, 31]. The tube model includes the effect of entanglements by imagining each chain is trapped inside a confining tube created by entanglements with neighboring chains as shown in Figure 1.4(a). A chain can only move freely along the length of its tube and is hindered from moving perpendicular to the tube because it cannot cross other chains. In order for a chain's conformation to relax, the chain must escape its current tube by diffusing out one of the ends (Figure 1.4(b)). The tube diameter, a, sets the scale of confinement and is related to the entanglement segment length through random-walk statistics $a \approx \ell_K N_e^{1/2}$. ℓ_K is called the Kuhn length and is the effective random-walk step size for a given polymer chemistry. Remarkably, the tube model correctly predicts the linear viscoelastic flow of many entangled liquids to be universal and insensitive to the specific polymer's chemical details. Specifically, tube theory predicts that the functional form of $\eta_0(t)$ only depends upon the degree of entanglement Z.

Although simple, the tube model has been incredibly successful at predicting the linear flow $\eta_0(t)$ of entangled polymers. Its limitations only become apparent when it is applied to the nonlinear extensional flows relevant for fiber formation [25, 26, 32].

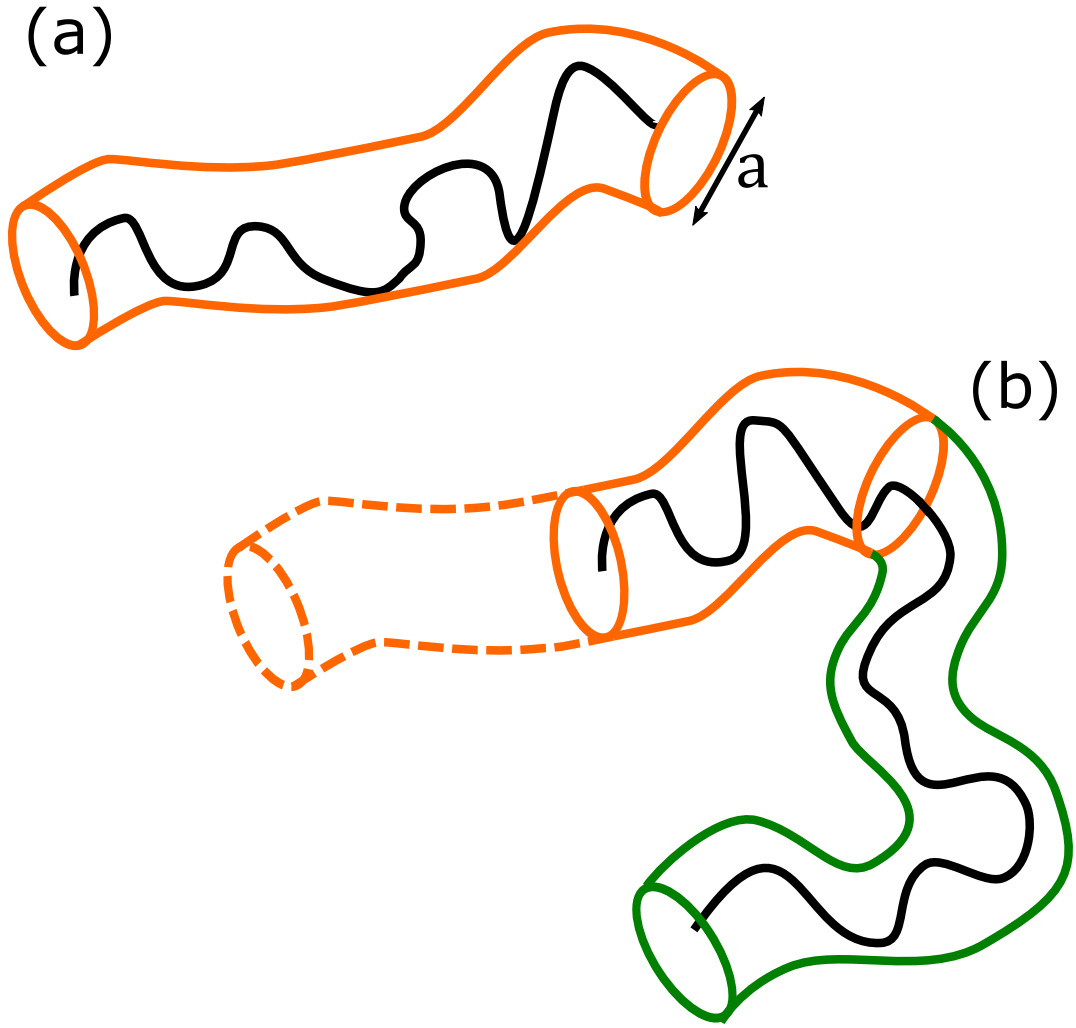

Figure 1.4: A schematic of the tube model for entangled polymer dynamics. (a) Because chains cannot cross each other, entanglements confine each chain (black line) to a confining tube (orange) with a diameter $a \sim b^{1/2} N_e$. (b) The chain can only diffuse along its tube. It relaxes by escaping out one end, forgetting the evacuated section (dashed lines) while generating a new section of tube (green).

Large extensions deform the entanglement network far from equilibrium, changing how neighboring chains interact with each other and how macroscopic deformation is transmitted to molecules. In this regime, the tube model's simple treatment of entanglement breaks down. Recent experiments show that different melts with identical tube model predictions for linear response exhibit different rate dependent viscosities during nonlinear flow [26, 28, 32]. These experiments suggest the tube model's description of chain dynamics is incomplete and must be enriched with new physics, but identifying the appropriate physics is difficult without microscopic data.

In Chapter 6, we use coarse-grained MD simulations to generate uniaxial extensional flows of polymer melts and directly relate nonlinear trends in the extensional viscosity to the microscopic polymer structure. Since the qualitative dynamics of molten polymers is insensitive to chemical detail, we forego the complexity of the AIREBO-M potential and simulate polymers with a much cheaper bead-spring model. The bead-spring model simulates chains of chemically-generic, featureless particles that are connected by finitely-extensible springs. This simple model captures the large-scale dynamics of chain conformations and entanglements which dominate polymer rheology.

We apply a recently developed technique to simulate extensional flows called Generalized Kraynik-Reinelt (GKR) boundary conditions [33,34]. Traditional extensional flow simulations are limited in the maximum strain they can reach because the simulation cell stretches exponentially with time along one axis while contracting along the

other two directions. Eventually the contracting dimensions become too small and the simulation crashes. This limitation has prevented traditional simulations from reaching the large strains needed to produce steady-state flows of entangled polymers. The GKR method was derived in 2014 by Dobson [33] and prevents the contracting directions from becoming too small by carefully selecting the initial simulation box and systematically remapping it to a physically equivalent box of less skewed geometry during flow. Nicholson and Rutledge recently implemented the GKR algorithm in the LAMMPS MD simulation code and used it to study flow induced crystallization during extensional flow [34, 35]. We apply this technique to study large extensional deformations of entangled polymers.

Through application of the GKR algorithm, we have simulated extensional flows of entangled polymers out to maximum strains $\epsilon \geq 6$, larger than any reported experiment. Simulations resolve the molecular structure of steady-state flows and reproduce experimental trends in the extensional viscosity with time, rate and molecular weight. Analysis of chain conformations reveals an elongation and thinning of the confining tube with increasing flow strength. The rising stress is quantitatively consistent with the decreasing entropy of chain segments at the equilibrium entanglement length, and we can develop a scaling law that explains the nonlinear trends in the extensional viscosity that are observed in experiments.

Finally, in Chapter 7, we study the stress relaxation after extensional deformation of aligned systems is ceased. Stress relaxations are a common experimental protocol

for characterizing the viscoelastic response of complex fluids [27], and provide useful data for developing accurate hydrodynamic models. By detailing the dynamic relaxation of a fluid after a well-defined flow history, stress relaxations provide valuable data that continuum modelers can use to test and calibrate their hydrodynamic theories. Relaxations from steady-state flows are particularly useful because they allow modelers to assume an infinite and constant flow history prior to relaxation, which greatly simplifies analysis.

The relaxation of polymer conformations is difficult to characterize experimentally because entanglements hinder chain motion and create a hierarchy of relaxations spanning many decades in time [30]. Individual monomers can diffuse freely only before a characteristic time τ_0, called the monomer relaxation time. At longer times, monomer diffusion is slowed due to the connectivity of the chain backbone. Monomers must diffuse collectively as bonded segments, slowing their diffusion. For a chain of N monomers, the Rouse time $\tau_R = \tau_0 N^2$ is the longest relaxation time associated with the connectivity of the chain. Relaxation in entangled polymers is further slowed by entanglements between chains. For an entangled chain to relax, it must diffuse away from its current neighbors and form new entanglements with other chains. In the tube model, this corresponds to the chain escaping its current tube by diffusing out one of the ends. This process occurs over the disentanglement time $\tau_d \approx \tau_R Z^{1.4}$, which is the longest relaxation time for an entangled polymer. τ_d depends nonlinearly on Z and can be $\sim 1 - 100$ seconds even when $T \gg T_g$ for industrial molecular weights [4, 30].

We measure the dynamic evolution of chain conformations for times longer than several τ_d. Our simulations offer insights into how entangled chains confine each other as the entanglement network becomes highly aligned by extensional flow. Several recent theories suggest that chains should confine each other less when they become highly aligned [28,36,37], leading to an increase in the tube diameter a. However, our data directly contradicts this view and shows chains rapidly recover their equilibrium tube diameter during relaxation, even when they have been completely aligned by an extensional flow. This suggests the physics employed by recent hydrodynamic models is incorrect and must be modified. The detailed dynamics of our stress relaxations should provide a useful benchmark for the development and testing of new rheological models.

Chapter 2

Reactive Models for Hydrocarbons at Extreme Pressures

2.1 Introduction

Extreme pressures can activate many mechanical and chemical processes in solids that are usually dormant at ambient conditions. A wide array of complex phenomena are common at 10 to 100 GPa including: defect nucleation in metals, structural phase transitions in molecular crystals, and bond rehybridization and wear in covalent solids [38–40]. Such dynamic complexity makes high pressure material behavior a rich avenue for research. However, the extreme conditions necessary are difficult to maintain experimentally, making robust numerical tools desirable.

Quantum mechanics (QM) based numerical methods, such as Density Functional

Theory (DFT), have been successfully applied to explore the dynamic chemistry and energetics of many materials at high pressure and temperatures [9, 41, 42]. However, the computational expense and purely covalent form of such methods prevents them from describing the structural and mechanical properties of many extended molecular materials, such as graphitic and hydrocarbon solids, which are a rapidly growing focus of industrial applications. Dispersion interactions can be included in DFT calculations [43–46], for example by adding semi-emperical potentials [46–49], but this increases the computational expense. More efficient methods are needed to study dynamic problems in large systems.

An attractive alternative to QM calculations is the family of reactive bond order potentials (BOP's). Traditional interaction potentials define and maintain a fixed topology of chemical bonds. The development of BOP's, such as the Adaptive Intermolecular Reactive Empirical Bond Order potential (AIREBO) [11] and the Reactive Force Field (REAXFF) [50], have allowed modelers to explore dynamic bonding processes. The complexity of the many-particle interactions in BOP's makes parameterization difficult. As a result, current BOP's quickly lose fidelity outside a limited range of ambient pressures and temperatures, corresponding to near equilibrium states of their molecular and chemical bonds. In order to accurately describe far from equilibrium dynamics at high pressure, existing BOP's must be modified to improve their description of highly compressed molecular configurations. For AIREBO and REAXFF, these limitations are well illustrated by the recent work of Mattsson et

al. on polyethylene (PE) [9], which concluded that both models greatly over-predict the stiffness of PE compared to experimental data at pressures above a few GPa. For AIREBO, the excess stiffness results from the use of Lennard-Jones (LJ) interactions between molecules that diverge rapidly at small separations.

In this chapter and Ref. [10], the Lennard-Jones interactions in AIREBO are replaced by a nondivergent Morse potential. The Morse potential has an additional parameter that allows the repulsive region to be softened with little change to the potential minimum and attractive regions. This allows us to extend the validity of the potential to pressures of about 40 GPa without affecting the behavior at ambient pressure that has been successfully captured by the original AIREBO [11]. The Morse potential for carbon-carbon interactions is fit to x-ray experiments on graphite and tested against theoretical calculations for bilayers. Similar x-ray data for hydrocarbons does not separately constrain the form of C-H and H-H interactions. This is accomplished by fitting to post-Hartree Fock quantum calculations for a range of configurations. The resulting parameters are then validated against x-ray and shock Hugoniot data for crystalline polyethylene (PE).

In what follows, we discuss the underlying theory and the parameterization and validation of the new model. Section 2.2 discusses the theoretical underpinning and algorithmic details of the simulations performed. Section 2.3 explains the rationale for our parameterization protocol and reports the resulting Morse parameters. Section 2.4 presents results from the new model for the graphene bilayer and the isothermal

compression and shock properties of orthorhombic PE.

2.2 Potentials and Simulation Methods

2.2.1 Potentials

The Second Generation Reactive Empirical Bond Order Potential (REBO2) of Brenner et al. [51], is a reactive potential that dynamically describes covalent hydrocarbon chemistry with classical many-body potential energy functions. Brenner's potential, originally intended to study network carbon solids like diamond, does not contain any energy terms for intermolecular interactions. Thus, REBO2 cannot describe the structure of liquids or molecular solids with any accuracy.

The AIREBO potential of Stuart et al. [11] adds nonbonded/intermolecular interactions for hydrocarbons to the purely covalent REBO2 via a set of Lennard-Jones potentials for the three interaction types: C-C, C-H, and H-H. The literature contains many applications of AIREBO to a wide variety of carbon and hydrocarbon allotropes - ranging from gas phase hydrocarbon combustion to phase separation in organic fluids to exotic carbon-nanotubes [52–54]. AIREBO is openly available in Sandia's LAMMPS software, which is used for all MD calculations presented in this thesis. A thorough and concise description of the model can be found in the appendix of Stuart's original article [11].

AIREBO's nonbonded interactions are modeled by a smoothly truncated 12-6

Lennard-Jones (LJ) potential:

$$U_{ij}(r) = 4\ \epsilon_{ij}\left[\left(\frac{\sigma_{ij}}{r}\right)^{12} - \left(\frac{\sigma_{ij}}{r}\right)^{6}\right] \tag{2.1}$$

where the ij indices indicate the chemical species (C or H) of the two interacting atoms, ϵ defines a depth for the interaction potential well, and $2^{1/6}\sigma$ defines the location of the minimum energy. The potential is smoothly set to zero by a third-order spline at a long-range cutoff value of 3σ. For separations less than $2^{1/6}\sigma$, similar splines reduce the strength of intermolecular repulsions if it is favorable for a pair of atoms to bond chemically [11]. When covalent bonding is unfavorable, the two atoms interact with the full LJ.

The use of a repulsive r^{-12} power law in the LJ potential was motivated more by computational convenience than physical reasoning. It causes the potential to rise to rapidly as molecular separation decreases past the minimum [9]. The anomalously high repulsive forces cause AIREBO to fail to describe the details of many high pressure systems, even while accurately describing the same systems in ambient conditions. To improve the model's accuracy at high pressures, we have replaced its Lennard-Jones potentials with a Morse potential:

$$U_{ij}(r) = -\epsilon_{ij}\left[1 - \left(1 - e^{-\alpha_{ij}\left(r - r_{ij}^{eq}\right)}\right)^{2}\right] \tag{2.2}$$

where ϵ and r^{eq} define the depth and location of the minimum energy, and the new parameter α modifies the curvature of the potential energy at its minimum separation. The Morse potential is truncated with a third-order spline at the same cutoffs used

in AIREBO, and the splines for adaptive repulsion are implemented by the same technique as AIREBO. Specifically, the outer and inner cut-offs for these splines are set respectively to the location of the energy minimum and the location where the energy crosses zero [11].

The Morse potential's parameters can be adjusted to match the equilibrium properties of hydrocarbons that are captured by the LJ potentials in AIREBO. One approach is to fit the location, depth and second derivative of the potential energy minimum for each interaction type. This gives a mapping from (ϵ, σ) to (ϵ, r^{eq}, α):

$$\begin{aligned} \epsilon &\rightarrow \epsilon \\ r^{eq} &\rightarrow 2^{1/6}\sigma \\ \alpha &\rightarrow 3 * 2^{5/6}\frac{1}{\sigma} \end{aligned} \tag{2.3}$$

The resulting unoptimized parameters are listed in Table 2.1. However the presence of a third parameter in the Morse potential allows more freedom in fitting a wide range of separations than in the LJ potential. We use Eq. 2.3 and AIREBO's LJ parameters to obtain initial values of Morse parameters and then adjust α to fit repulsive interactions without affecting the equilibrium spacing and energy. In this way, we improve the high pressure response while retaining agreement with the region of the AIREBO potential that determines equilibrium thermodynamic properties at ambient pressures.

Interaction	ϵ (eV)	α (Å^{-1})	r^{eq} (Å)
C-C	0.0028437	1.5722	3.8164
C-H	0.0020649	1.7671	3.3955
H-H	0.0014994	2.0171	2.9745

Table 2.1: Morse parameters obtained from mapping the Lennard-Jones parameters of Stuart et al. [11] to Morse potentials with the same equilibrium properties using Eq. 2.3.

2.2.2 Simulation Methods

In the model parameterization and validation that follows, we perform two types of simulation protocol. When making comparisons to experimental measurements for the PV curves of graphite and PE or the shock Hugoniot equation of state for PE, we utilize NPT and NVT ensemble molecular dynamics (MD) with periodic systems of the corresponding bulk material. When making comparison to first principle calculations of the microscopic interactions between ethane and pentane dimers or a graphene bilayer, we simply perform static energy calculations on pre-generated rigid configurations of the molecules. we next briefly describe the generation of these structures and the numerical details of the simulation protocols. Snapshots of simulation cells are shown in the figures presenting the associated properties.

2.2.2.1 Structure Generation

The bulk graphite configuration consists of ten graphene layers, each layer containing 416 carbons as shown in Fig. 2.1. The layers are approximately square and arranged in an alternating AB stacking. we create the rigid graphene bilayer by taking two layers of the bulk graphite system and making the simulation box periodic for the in-plane directions only. The trajectory is generated by varying the layer separation.

The polyethylene configuration consists of 5 by 7 by 12 unit cells of the orthorhombic (Pnam) PE crystal [55]. Thus the simulation cell has 70 PE chains with 12 monomers along the chain per period of the simulation box. Configurations undergo geometry optimization with the FIRE minimizer [56], before undergoing further MD treatment.

I use ethane and pentane molecules to generate dimer configurations exploring coordination registries relevant to bulk PE, while still being small enough molecules for use with accurate quantum mechanical techniques. we create six dimer trajectories, four for pentane-pentane dimers and two for ethane-ethane, illustrated in Fig. 2.2. Each trajectory is generated by rigidly rotating and translating a second ethane or pentane molecule with respect to the first, varying their separation along a fixed axis. we generate initial geometries for the alkane molecules with geometry optimization at the DFT level (M06/aug-cc-pvTZ) [57].

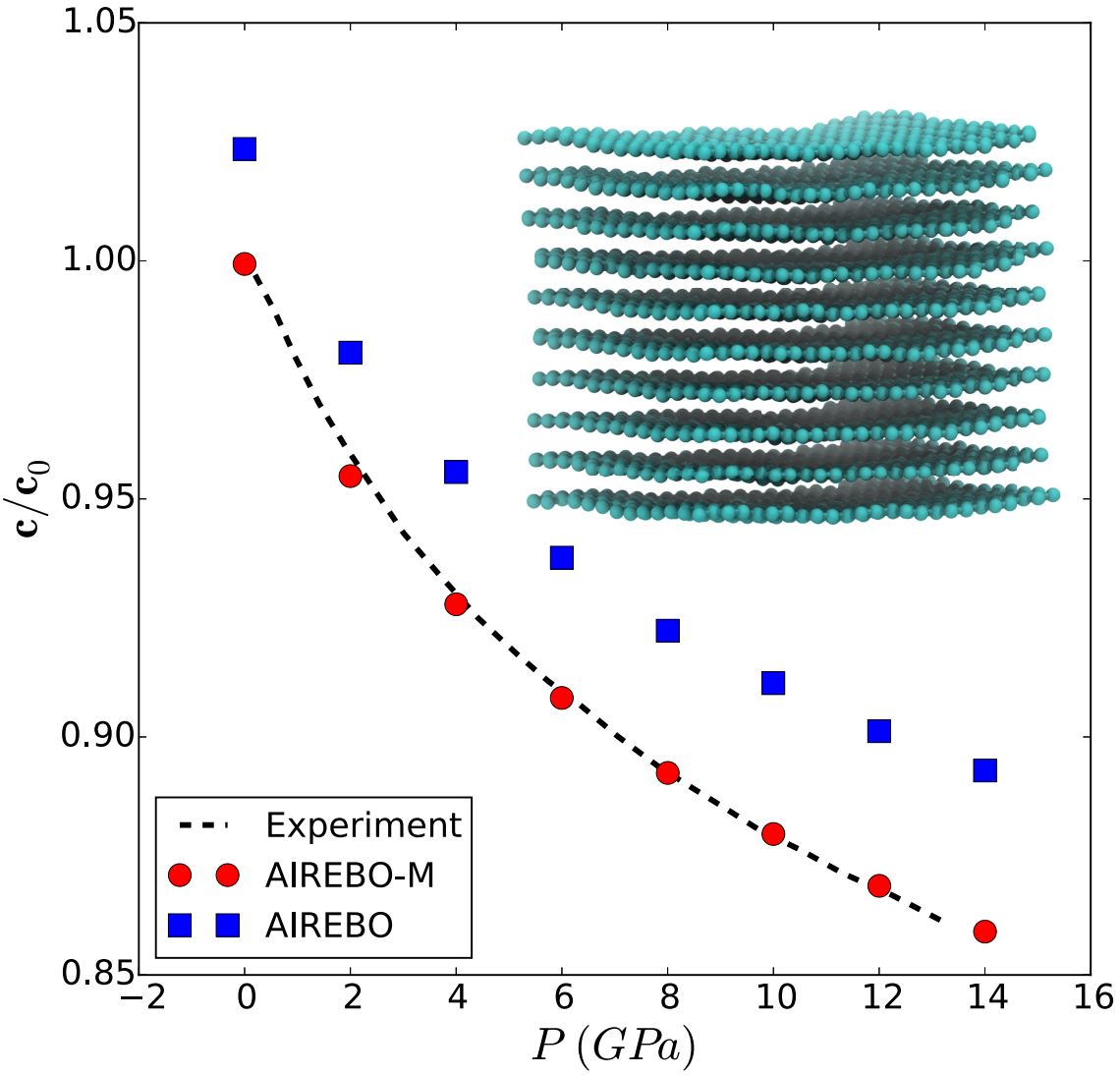

Figure 2.1: Pressure dependence of the interlayer spacing of bulk graphite, c/2, normalized by the zero pressure value, $c_0/2 = 0.335$ nm, from x-ray experiments (dashed line), AIREBO (blue squares) and AIREBO-M (red circles). AIREBO over-predicts the spacing by 3% at ambient pressure and gives a stiffer response than observed in experiment.

2.2.2.2 Molecular Dynamics Methods

Aside from the specific atomic configurations used, the protocols for computing the equation of state for both graphite and PE systems are identical. All MD simulations use the LAMMPS simulation package [35]. The velocity-Verlet integrator with a time-step of 1 fs is used to solve the equations of motion within a periodic simulation box. A Nose-Hoover thermostat with time constant 0.25 ps is used for constant temperature simulations. To maintain a specified hydrostatic pressure, the three periods of the simulation cell are adjusted independently by a Nose-Hoover barostat with time constant 1.0 ps [58].

For pressure-volume curve generation, systems equilibrate to their initial isotherm temperature (300 or 553 K) and pressure (0 GPa) during 20-30 ps of simulation in the NPT ensemble. Next, the system pressure is increased by 2 GPa over 2 ps, followed by equilibration at fixed pressure for 4 ps. Such 6 ps pressure steps continue up to a pressure of 40 GPa, with PV points generated from the average of the last 2 ps of equilibration. Tests with longer equilibration times gave equivalent results. The Hugoniot equation of state for PE is produced from such MD generated isotherms via the quasi-static method of Erpenbeck. The method is described in detail in Ref. [59] and has been shown to be insensitive to the system size and simulation parameters [8, 60].

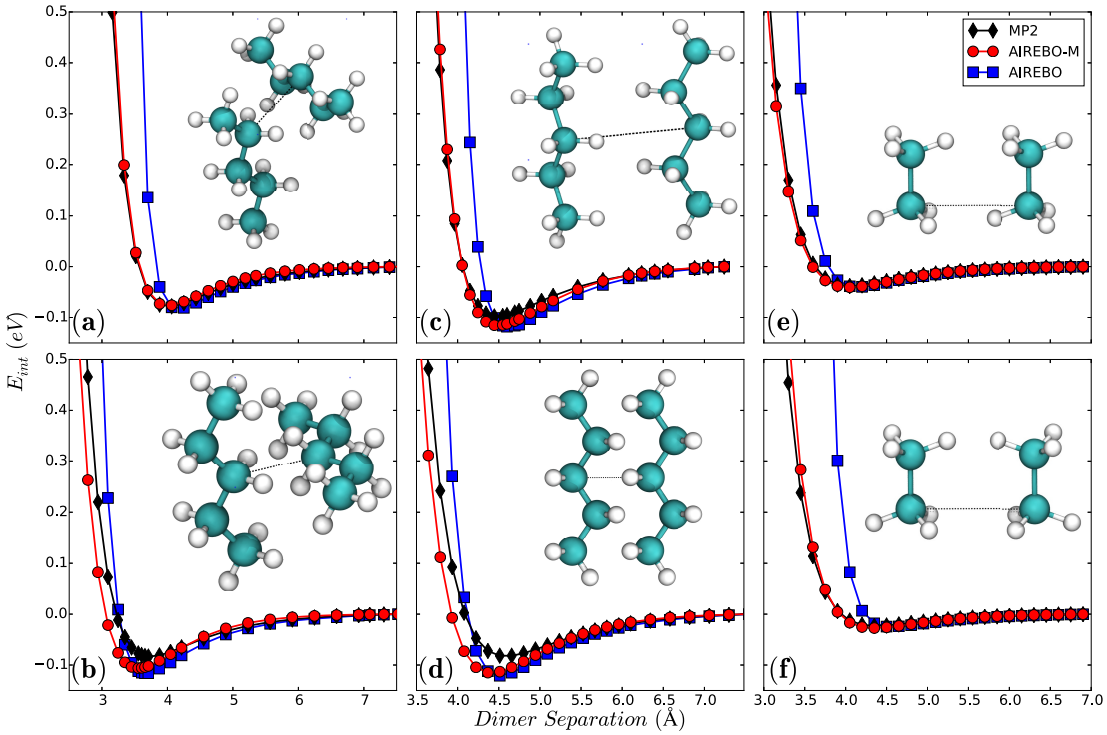

Figure 2.2: Interaction energy scans calculated with MP2 (black diamonds), AIREBO (blue squares), and AIREBO-M (red circles) for ethane and pentane dimers. Dimer orientations are illustrated by the inset images. Separations are measured along the dashed lines. The strong divergence of AIREBO compared to the quantum calculations is immediately apparent. The AIREBO-M is fit to MP2 in the repulsive region while retaining the binding energy and separation of AIREBO.

2.2.2.3 Quantum Calculation Methods

Dispersion corrected density functional theory (DFT) methods are the most commonly used quantum mechanical techniques for studying molecular crystals and large clusters [61]. However, despite their successes in predicting equilibrium structures for models of crystalline PE, the same methods predict bulk moduli that are significantly too large [61, 62]. DFT methods without dispersion corrections predict crystal structures more accurately as pressure increases [55, 62], but at pressures of 2-3 GPa the error in unit cell vectors may be as large as 0.2 Å [55]. These findings suggest that more accurate ab initio methods may be necessary to study the steric interactions of hydrocarbon solids at extreme pressures.

Ab initio calculations on small models of n-alkane dimers [63] have revealed that the second-order Moller-Plesset (MP2) values of equilibrium interaction energies obtained by using the correlation consistent basis set of triple zeta quality (aug-cc-pvTZ) [64] are within 0.01 eV, or better, of the MP2 energies at the basis set limit. Such MP2 energies are also very close to results obtained from the more accurate CCSD(T) calculation method [63, 65]. The CCSD(T) method is prohibitively expensive for some of our non-symmetrical pentane dimmers and therefore, in this work we use the MP2/aug-cc-pvTZ approach. Interaction energies are further corrected for basis set superposition errors (BSSE) [66] by using the counterpoise (CP) method [67].

Using the MP2/aug-cc-pvTZ/CP model, we compute dimer interaction energy curves from each frame of the ethane and pentane dimer trajectories, which range

in separation from the limit of molecular dissociation to large steric repulsions at short distances. As expected, we find the BSSE corrections to be critically important and they account for up to 50% of the total binding energy at equilibrium distances. While accurate dispersion forces play a diminishing role at high pressure, where steric interactions dominate, they are essential for accurately defining the equilibrium separations which distinguish between repulsion and attraction dominated regions. Our fitting strategy is based on the fact that the unmodified AIREBO captures the ambient thermodynamic and structural energetics of many alkanes. Thus we use our MP2 calculations to improve the steric rise in energy with small separation, while defering to the unmodified AIREBO for the details of interaction energy wells.

2.3 Parameterization

In the original AIREBO paper, Lennard-Jones potentials were fit in two stages. C-C interactions were first fit to the properties of graphite, then C-H and H-H interactions were fit simultaneously to the x-ray structure and thermodynamics of small alkane liquids. To fit our Morse parameters we follow a similar process. First Morse C-C interactions are tuned to accurate high pressure experiments on graphite by Hanfland et al. [68]. This approach is difficult to apply for hydrocarbons because structural measurements do not isolate the separate contributions of C-H and H-H intermolecular bonds. Thus we use MP2 calculations for a range of ethane and

pentane dimer geometries to determine the C-H and H-H Morse potentials.

2.3.1 Fitting C-C Interactions

For typical hydrocarbon systems, carbon atoms rarely come within steric interaction distances of one another due to the steric repulsion of surrounding hydrogens. This makes it difficult to use hydrocarbon data to determine C-C interactions. Using pure carbon allotropes, such as graphene, carbon nanotubes, or graphite, isolates the effect of C-C interactions. These interactions directly determine the interlayer spacing of graphite which has been measured with high pressure x-ray scattering by Hanfland et al. [27]. Over the studied range of pressures, the in-plane lattice constant is nearly constant. Since it is mostly determined by covalent interactions, AIREBO and AIREBO-M give consistent in-plane results.

Hanfland et al. [68] used x-ray scattering to track the equilibrium layer separation $c/2$ of a graphite sample at room temperature from 0-14 GPa. To reproduce this experiment, we perform finite temperature MD in the NPT ensemble at pressures across this range, for a periodic bulk graphite system. We measure the layer spacing of the system as a function of pressure and modify the C-C Morse parameters until our system reproduces the equilibrium spacing and compression profile seen by Hanfland et al. [68].

We found that the parameters in Table 2.1 did not give the measured lattice constants of graphite at ambient pressure. Thus in addition to optimizing the new

Interaction	ϵ (eV)	α (Å^{-1})	r^{eq} (Å)
C-C	0.0028437	1.8168	3.6891
C-H	0.0020649	1.5317	3.3955
H-H	0.0014994	1.7484	2.9745

Table 2.2: Optimized Morse potential parameters for the van der Waals interactions of all three hydrocarbon interaction types. The energy scales, ϵ, are unchanged from their LJ values. Length scales, r^{eq}, are mapped directly from the Lennard-Jones σ, with only minor modification to r_{CC}^{eq}. Protocols for fitting r_{CC}^{eq} as well as the interaction moduli, α_{ij}, are detailed in section 2.3 of this work.

degree of freedom, α, we also slightly reduced the length scale of the interaction, r^{eq}. This is necessary because AIREBO's LJ parameters for C-C were originally fit to graphite using an analytic expression that excluded the effects of AIREBO's splines for adaptive repulsion. Plotting the resulting curves in Fig. 2.1, we see the original AIREBO overestimates both graphite's equilibrium layer spacing at 0 GPa as well as its mechanical response under compression for T = 300 K. Note that this difference will have little effect on simulations of hydrocarbons.

The new Morse potential parameters for C-C may be found in the first row of Table 2.2. The model with the new parameters, which we call AIREBO-M, produces equilibrium and response properties for graphite layer compression in excellent agreement with Hanfland et al's experiment (Fig. 2.1).

2.3.2 Fitting C-H & H-H Interactions

Compared to pure carbon, we find hydrogen's dispersion forces are substantially weaker, and steric repulsion dominates its intermolecular interactions. Such steric repulsions are due to Pauli exclusion effects, which quantum mechanical methods tend to capture very well. Additionally, C-H and H-H interactions tend to be sensitive to the geometry and relative orientations of participating hydrocarbon molecules. Such details are beyond the scope of most experimental techniques, which typically only provide average lattice constants. In contrast, first principle calculations provide independent information about the energies of different geometries. To this end, we have used Moller-Plesset second-order perturbation theory (MP2) [64], a post Hartree-Fock quantum chemistry method, to construct a training set of interaction energies for rigidly translated ethane and pentane dimers, illustrated in Fig. 2.2.

The MP2 calculations compute the total energy as a function of separation for each dimer, and since the individual molecules are held fixed, changes in the energy correspond to intermolecular interactions only. Analogous energy vs. separation curves are calculated with the AIREBO-M for different parameters to determine the best fit. Since we are primarily concerned with improving the interaction's high pressure response, and we wish to preserve the accuracy of AIREBO in ambient conditions, we limit the range of separations used for calculating the fit to those where steric repulsions dominate. We define the steric region of each trajectory as any separation where the MP2 energy is greater than 0.1 eV (with 0 eV at infinite

separation). Fig. 2.2 shows data to 0.5 eV, but fits extended up to energies where covalent bonding changed, typically 1.5 eV.

To minimize changes from AIREBO, we optimize by scaling the α's by the same factor for C-H and H-H - i.e. $\alpha_{ij} = \kappa\, \alpha_{ij}^0$ where the α_{ij}^0 are defined in Table 2.1. The least mean squared fit gives $\kappa = 0.877$. The results are in excellent agreement with MP2 in four of the panels in Fig. 2.2 but give a higher binding energy and shorter distance in panels b and d. Fits with other α and r^{eq} do not improve the agreement in these panels without producing comparable deviations in the other panels. we expect that the difficulty in simultaneously fitting all configurations may reflect directional bonding that is not captured in the LJ or Morse potential. Given that varying r^{eq} and ϵ does not improve the global fit and that the AIREBO values have been validated in ambient conditions, we leave them unchanged. The Morse potential parameters for C-H and H-H may be found in the second and third rows of Table 2.2.

Figure 2.3 illustrates the effect of rescaling α in the manner just described. It compares the LJ potential to the Morse potential with α chosen to match the second derivative at the minimum, via Eq. 2.3, as well as with α reduced by the factor $\kappa = 0.877$ used in Fig. 2.2. Note that reducing κ from 1.0 to 0.877 produces a much better fit of the entire attractive portion of the LJ potential. Although κ was chosen to match the repulsive region where the LJ potential rises too rapidly, it produces a Morse potential that is very close to providing the best fit to the attractive region of the LJ potential from $r/\sigma = 2^{1/6}$ to 3. Over this range the rms deviation from the

LJ potential is only 0.0004ϵ. Thus this choice of κ satisfies both of our objectives for the revised potential.

2.4 Validation

In the parameterization protocol, we applied a mixed training set of experimental data and theoretical quantum chemistry calculations chosen to distinguish most cleanly and accurately the interactions for different atoms. To validate the fits we use information from complementary techniques. Our fits of C-C interactions to finite temperature x-ray experiments are compared to theoretical DFT calculations of the energy of graphene bilayers. Similarly, to validate our fits of C-H and H-H interactions to quantum chemistry calculations of the energy of small alkanes, we compare to finite temperature experiments on cyrstalline PE at high pressure and during shocks.

2.4.1 Compressing a Graphene Bilayer

Understanding the planar interactions of two graphene sheets is important for the development of exfoliation-based processing and nanoscale fabrication in general. The literature contains many high quality studies on the layer interactions of graphene, including a recent dispersion-corrected DFT-based analysis by Reguzzoni et al. [69]. Their work calculates the interaction energy as a function of the separation of two flat graphene sheets, using the DFT-D method of Grimme [46]. Grimme's method

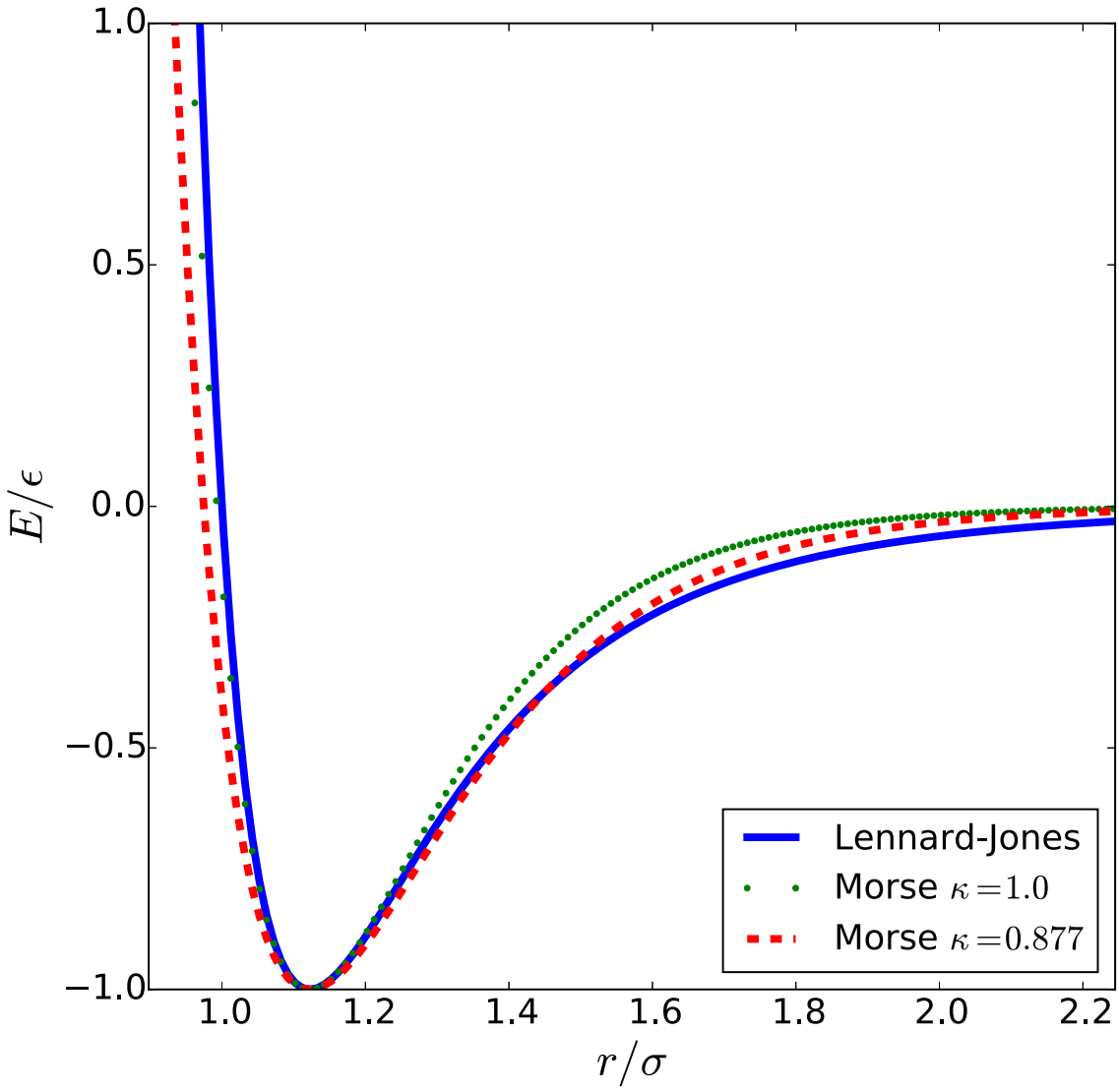

Figure 2.3: Comparison of a Lennard-Jones potential and Morse potentials with α scaled to fit the second derivative at the minimum ($\kappa = 1$), and obtained from fitting MP2 calculations ($\kappa = 0.877$).

for dispersion corrected DFT is widely used [46–49] and we consider the DFT-D calculations of Reguzzoni et al. to be a well-characterized theoretical reference for testing the compression mode our C-C interaction potential is fit to.

In Reguzzoni et al.'s analysis, they compute an energy versus separation curve for two rigid and periodic graphene sheets. To compare to their data, we generate an analogous configuration and repeat their calculation with our potential. Fig. 2.4 compares the interaction energy of the bilayer planes for AIREBO-M (red circles), AIREBO (blue squares), and DFT-D (black diamonds). we see that AIREBO-M produces a rise in steric energy under compression in very good agreement with the quantum calculation. AIREBO-M also reproduces the location and curvature of the DFT-D minimum energy, even though we did not intentionally seek to reproduce these features. While this agreement may be due to similar training systems for AIREBO-M and the DFT-D dispersion corrections, we consider AIREBO-M's excellent reproduction of the bilayer mechanics calculated with the more theoretically sophisticated and expensive DFT-D to be a strong validation of our experimental fits for C-C interactions. Note that the repulsive interactions at the smallest separations correspond to significantly larger pressures ($\sim$ 18 GPa) than achieved in Hanfland et al.'s experiments.

The three methods show different behavior at large distances and thus have different binding energies. Both theoretical and experimental values of the cohesion of a graphene bilayer show variations that are comparable to the difference between the

three values [70]. For this reason, we are satisfied that our model produces a cohesive energy comfortably within the range of current experimental values.

2.4.2 PV and Shock Compression of Crystalline Polyethylene

Highly aligned polyethylene has become a focus of research for wide-scale industrial application due to its high tensile strength and relatively low mass density [71,72]. Ultra-High Molecular Weight Polyethylene (UHMWPE), in the form of fibers and composite fabrics, is already used to create cables, helmets, body armor, and other products where a high strength to weight ratio is critical. Building an understanding of PE's structural behavior at high pressures is critical to improving its application; however, there are relatively few detailed experiments available in the literature.

One such experiment is Fontana et al.'s thorough x-ray analysis of PE brought to high pressures in a diamond anvil cell [55]. Their work explores the anisotropic deformation of the orthorhombic PE crystal from 2-40 GPa at 553 K, as well as its eventual structural transition to higher-pressure monoclinic phases around 16 GPa. It is an ideal experiment to validate the AIREBO-M's theoretically fit C-H and H-H interactions, which dominate the mechanical response of the molecular crystal. To compare to Fontana et al.'s experiments, we again perform finite temperature MD in the NPT ensemble, analogous to that used for bulk graphite, to generate a series

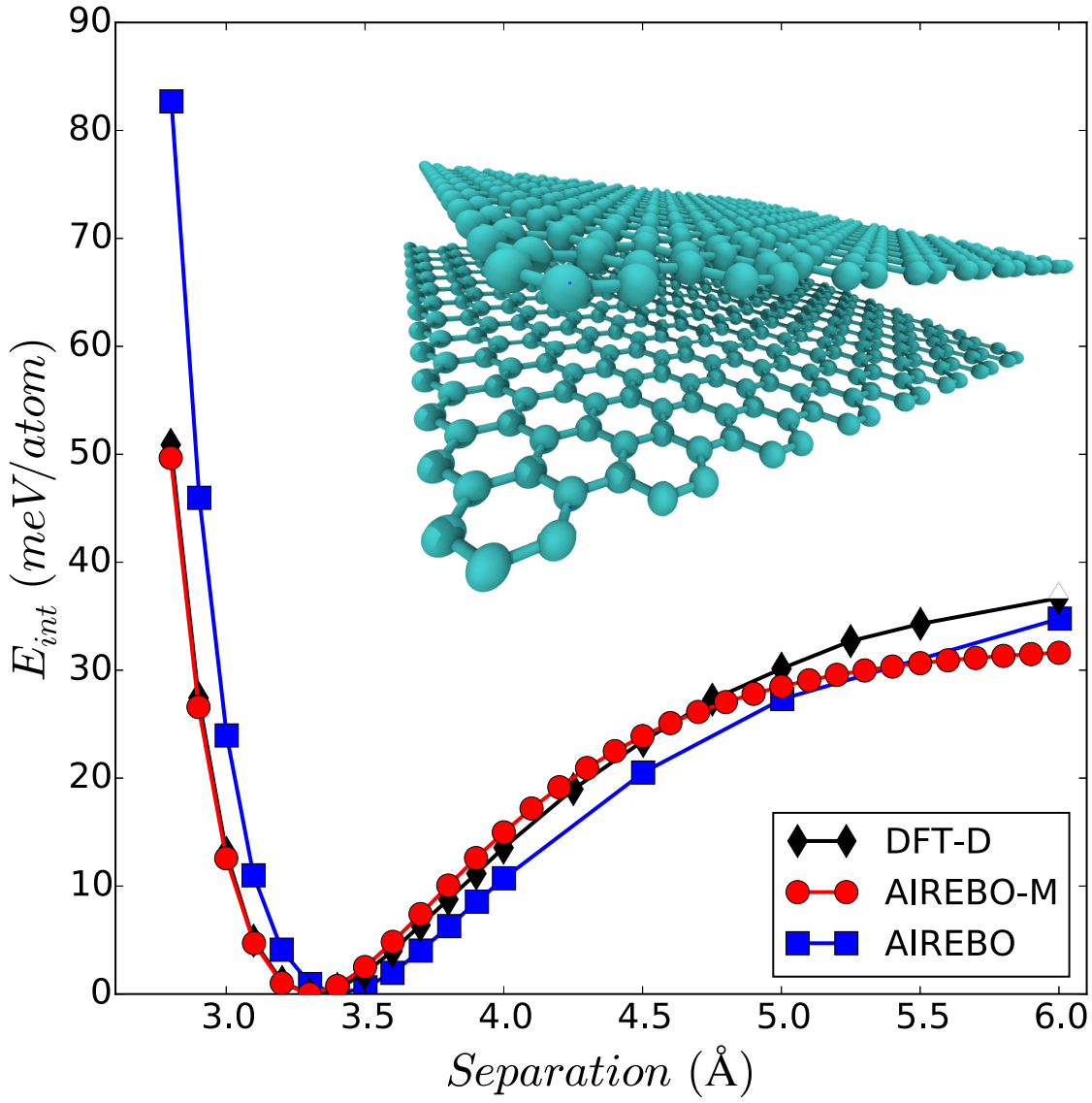

Figure 2.4: Interaction energy versus separation for a rigid graphite bilayer. Results for AIREBO-M (red circles) track DFT-D results (black diamonds) at small separations while the AIREBO energy (blue squares) rises too rapidly.

of states along the T = 553 K PV isotherm. From these states we determine the deformation of the PE unit cell for all three lattice directions.

In Fig. 2.5(a) we plot the change in the lattice vectors of orthorhombic PE with increasing pressure. The experimental data shows that deformation primarily occurs in the lateral (**a** and **b**) lattice directions, where the crystal is stabilized by weaker intermolecular interactions. The axial (**c**) direction, dominated by covalent carbon-carbon bonds, responds negligibly to the pressures explored. Based on their data, Fontana et al predict that the orthorhombic PE phase becomes metastable at pressures higher than 16 GPa, in favor of a high-pressure monoclinic phase. Beyond 25 GPa, the x-ray experiments were no longer able to distinguish the orthorhombic signature. After losing the orthorhombic signature, Fontana et al. continued tracking higher pressure crystal phases, and used them to generate PV data up to 40 GPa, as reproduced in Fig. 2.5(b).

The AIREBO-M (red circles) shows excellent agreement with the Fontana experiment (black diamonds) for deformation in all three lattice directions. It accurately distinguishes between the structural differences in the lateral lattice directions and reproduces the shape of their mechanical response. AIREBO-M also predicts a structural phase transition to a new orthorhombic phase, seen as a jump in the lattice parameters, between 18-20 GPa. This new phase corresponds to a flattening of the herringbone pattern of the orthorhombic crystal as the constituent chains come in closer contact. This transition is also observed during shock loading and is described

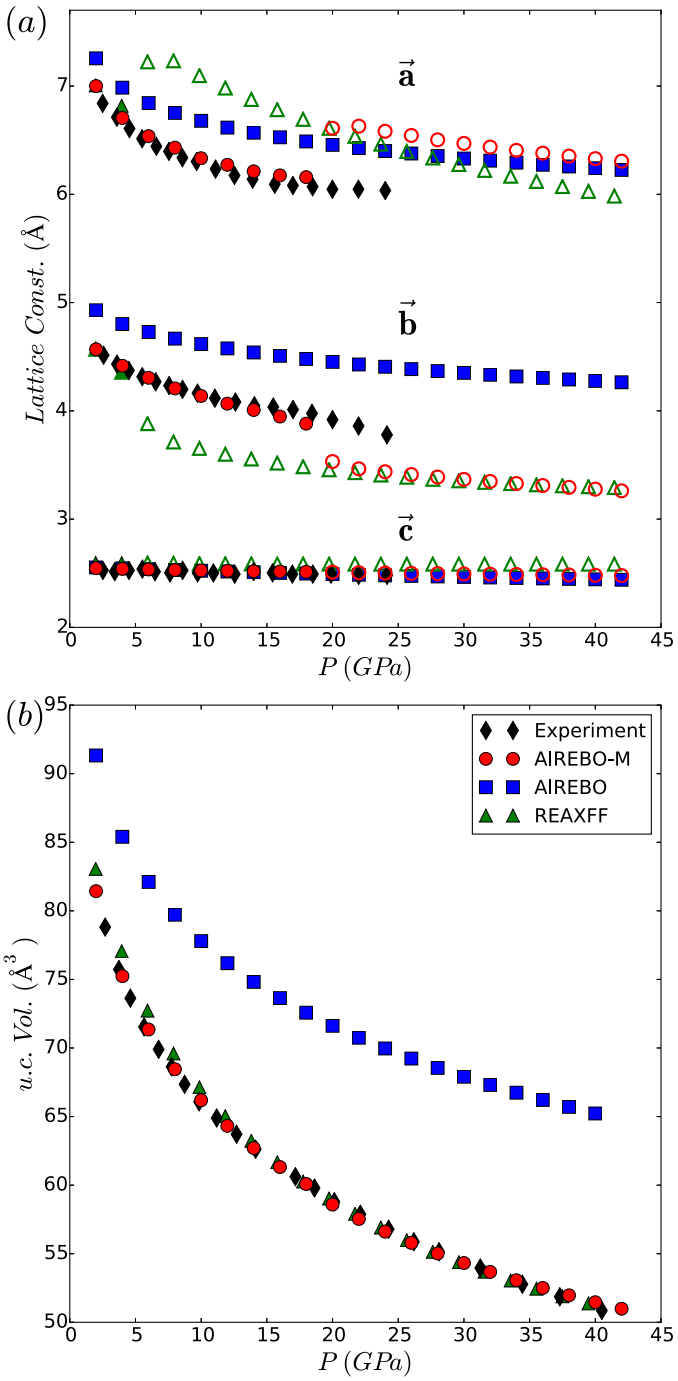

Figure 2.5: Variation of **a**, **b** and **c** lattice parameters of an orthorhombic PE unit-cell along the T = 533 K PV isotherm from experiment [55], AIREBO (blue squares), AIREBO-M (red circles) and REAXFF [50] (green triangles). Closed symbols are for the low temperature orthorhombic phase and open symbols for a new high pressure phase. (b) PV curves for the same systems.

in detail in Chp. 5. AIREBO-M predicts this structural transition soon after the 16 GPa point where Fontana et al. report that the low pressure orthorhombic phase becomes metastable and begins to coexist with a high pressure monocolinic phase. Whether this new phase is compatible with the x-ray data of Fontana et al. or is another metastable phase is still an open question. In contrast, AIREBO (blue squares) over-predicts the stiffness for deformations in both lateral directions. This is caused by the diverging repulsive interactions of the LJ potentials. Consequently, it washes out much of the underlying molecular structure and does not show any structural transitions.

We have performed similar calculations with the REAXFF parameterization of Chenoweth et al. [50] (green triangles). we use this parameterization because of its recent use in studies of similar systems by Mattsson et al. [9], and because it is the version that is distributed in current and previous versions of LAMMPS. Our REAXFF results agree with the experimental data at the lowest pressures (2 GPa), but quickly lose fidelity as pressure increases. REAXFF also shows a structural transition to a new orthorhombic phase, similar to that of the AIREBO-M, but it occurs far before the proposed metastability point at 16 GPa. Additionally the REAXFF shows extension in the axial, **c**, direction with increasing compressive load. This counterintuitive expansion under compression is not seen in experiments and calls into question the applicability of this parameterization for PE solids.

In Fig. 2.5(b), we see that the AIREBO-M reproduces the entire experimental

PV curve of Fontana et al. very well. Note that both curves evolve smoothly through the transition between crystalline phases. As before, the AIREBO potential is too stiff and dramatically under-predicts the compression. The REAXFF results agree well with experiments at higher pressure even though they give unphysical expansion along the axial direction. They gradually rise above experiments as P decreases below 15 GPa.

As a final validation of the AIREBO-M, we compute the Hugoniot equation of state for orthorhombic PE [55]. This state function, given an initial state, encodes the accessible pressure states a material can be driven to by density shock-waves of various speeds. As PE becomes more widely used for protective armors and other impact-oriented material applications, models that accurately describe its shock properties will grow in utility. To generate the T = 300 K Hugoniot curve, we perform a series of NVT and NPT simulations, utilizing the quasistatic methodology of Erpenbeck [59], as performed by Chantawansri et al. [8].

For our standard of comparison we follow other recent studies of shock in PE [8,9] and use the accepted shock Hugoniot curve for crystalline PE derived by Pastine [21]. Work by Carter and Marsh has shown Pastine's crystalline Hugoniot curve to be an accurate ordered limit of the available experimental data on semicrystalline samples [18].

Fig. 2.6 compares our computed Hugoniot curve for AIREBO-M to Pastine's curve. For comparison, we plot several other Hugoniots computed by Mattsson et

al. [9] with various models, including AIREBO, the all-atom optimized potential for liquid simulations (OPLS-AA) [73], and the exponential-6 model (EXP-6) of Borodin and Smith [74]. AIREBO-M (red circles) produces a Hugoniot curve for the orthorhombic system that closely follows the accepted crystalline curve, which we interpret to mean our model effectively captures the shock properties of the crystal system. In constrast, AIREBO (blue squares) and OPLS (magenta triangles) greatly over-predict the stiffness of the shock response, while REAXFF (green triangles) gives a Hugoniot that is slightly softer than Pastine's curve. The EXP-6 (cyan pentagons) shows similar performance to AIREBO-M. This is unsurprising since both AIREBO-M and EXP-6 utilize exponential repulsive forces.

2.5 Summary and Conclusions

We have developed a new potential, AIREBO-M, that describes the high pressure response of hydrocarbons. In the original AIREBO [11], intermolecular interactions were modeled with Lennard-Jones potentials that rise too steeply at small separations [9]. These are replaced by Morse potentials in AIREBO-M. The extra degree of freedom in the Morse potential is used to fit high pressure data while retaining most equilibrium properties of AIREBO.

The C-C interaction was fit to experimental data for the layer spacing of graphite from 0 to 14 GPa [68]. To match the experimental results for zero pressure, the

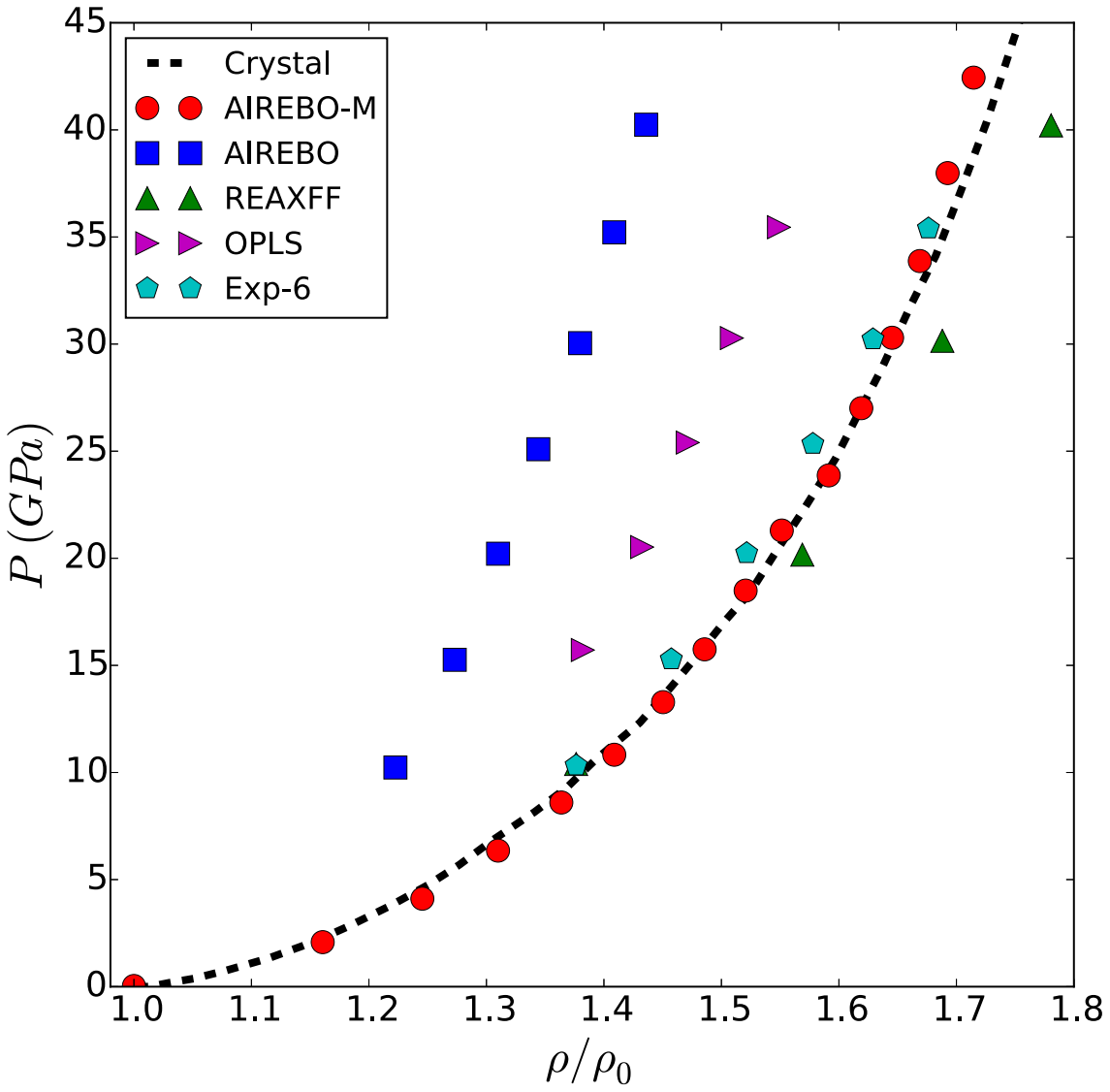

Figure 2.6: Hugoniot equation of state points relative to an initial state with T = 300 K and $\rho = \rho_0$, the zero pressure density for each model. The dashed line represents the theoretical curve for pure crystal PE of Pastine [21], extrapolated from Ref. [18]. Symbols show results for orthorhombic crystals from AIREBO-M (red circles) and calculations [9] with AIREBO (blue squares), REAXFF (green triangles), OPLS (magenta triangles) and EXP-6 (cyan pentagons).

equilibrium C-C spacing must be reduced by about 3% from that in AIREBO. This change has little effect on hydrocarbons where C-C interactions are normally screened by hydrogen. The fit was then tested against DFT-D calculations for graphite bilayers [69]. Excellent agreement was obtained down to separations corresponding to significantly larger pressures ($\sim$ 18 GPa) than were achieved in experiments.

The repulsive region of C-H and H-H interactions was fit to dimer interaction energies calculated with Moller-Plesset second-order perturbation theory while retaining the interaction energy and equilibrium spacing of AIREBO. The resulting potential closely matches the entire attractive range of AIREBO while softening the hard core repulsion. Thus the high pressure response is corrected without sacrificing the quality of AIREBO's fits to ambient pressure data. AIREBO-M reproduces the equilibrium pressure-volume isotherm and Hugoniot equation of state for crystalline polyethylene up to 40 GPa.

The Morse potentials for intermolecular interactions developed here can be paired with different versions of the REBO2 for covalent interactions. The calculations shown above were performed with the REBO2 potential of Ref. [51] as implemented in LAMMPS. This has been shown to overestimate the forces needed to break carbon bonds under tension [5]. Better agreement can be obtained by screening covalent interactions and extending their range [5, 75].

There are active efforts to extend REBO2 to other elements, including sulphur, oxygen and nitrogen. we expect that Morse potentials will also be useful in describ-

ing their intermolecular interactions. Fig. 2.3 suggests that an approximate translation between Lennard-Jones and Morse potentials should use Eq. 2.3, and then multiply α by 0.877. Another useful extension would be to consider configuration dependent intermolecular interactions. For example, allowing carbons and hydrogens to have coordination dependent dispersion forces substantially improves AIREBO's fluid properties [76].

Chapter 3

Chain Ends and the Ultimate Strength of Polyethylene Fibers

Ultra-high-molecular-weight polyethylene (UHMWPE) fibers are highly ordered materials with up to 95% crystallinity and near perfect chain alignment. Measurements of elastic moduli range between 150-300GPa, approaching metallic stiffnesses but at a fraction of the weight and cost [3, 77–79]. Applications have rapidly grown to include cables, fabrics, and composite armors [80].

The ordered fiber state is usually obtained by plastically straining (drawing) a UHMWPE gel. The drawing process aligns chains and facilitates the formation of large ordered crystalline domains with a uniform orientation, leading to a high strength in the direction of alignment [81]. Advances in processing have led to commercial PE fibers that yield at strains $\epsilon_y \sim 0.02 - 0.04$ with tensile strengths of about

$\sigma_y \sim 3-4$GPa [82,83]. Strengths of 6-7GPa [84–86] have been obtained in the laboratory by increasing chain alignment and crystallinity (black diamonds in Figure 3.1). While impressive, first-principal calculations predict that carbon bonds along the backbone would allow strengths four times higher ($\epsilon_y \sim 0.10$ and $\sigma_y \sim 20-40$GPa) before breaking [87, 88]. Classifying the defects and yield mechanisms that cause the reduction in strength remains a topic of active interest.

Real PE fibers are made of finite-length chains and thus have chain-end defects (see Figure 1.2). Chain ends allow the fiber to yield by chains slipping past each other. Such chain slip is mediated by intermolecular van der Waals bonds ($\sim$ 10 meV), which are much weaker than the intramolecular C-C bonds ($\sim$ 4eV). Mesoscale investigations have shown that atomic scale studies are needed to accurately quantify these weak van der Waals forces and determine if fibers yield primarily by chain slip, bond breaking, or some combination of the two [89–92].

In this chapter we use large scale MD simulations to determine the tensile strength of crystalline PE, which is believed to provide an upper bound for PE fibers. We find that infinite chains fail through chain scission at $\sim$ 20GPa, which is consistent with previous estimates. In contrast, introducing chain ends leads to failure by chain slip. Simulated crystals with finite chain lengths ranging from $10^2 - 10^4$ carbon atoms yield by slip at chain ends and give a limiting tensile yield stress of 6.3GPa that is consistent with the best laboratory fibers. The yield stress, its dependence on chain length, and its high and low rate limits can be understood using a simple Frenkel-

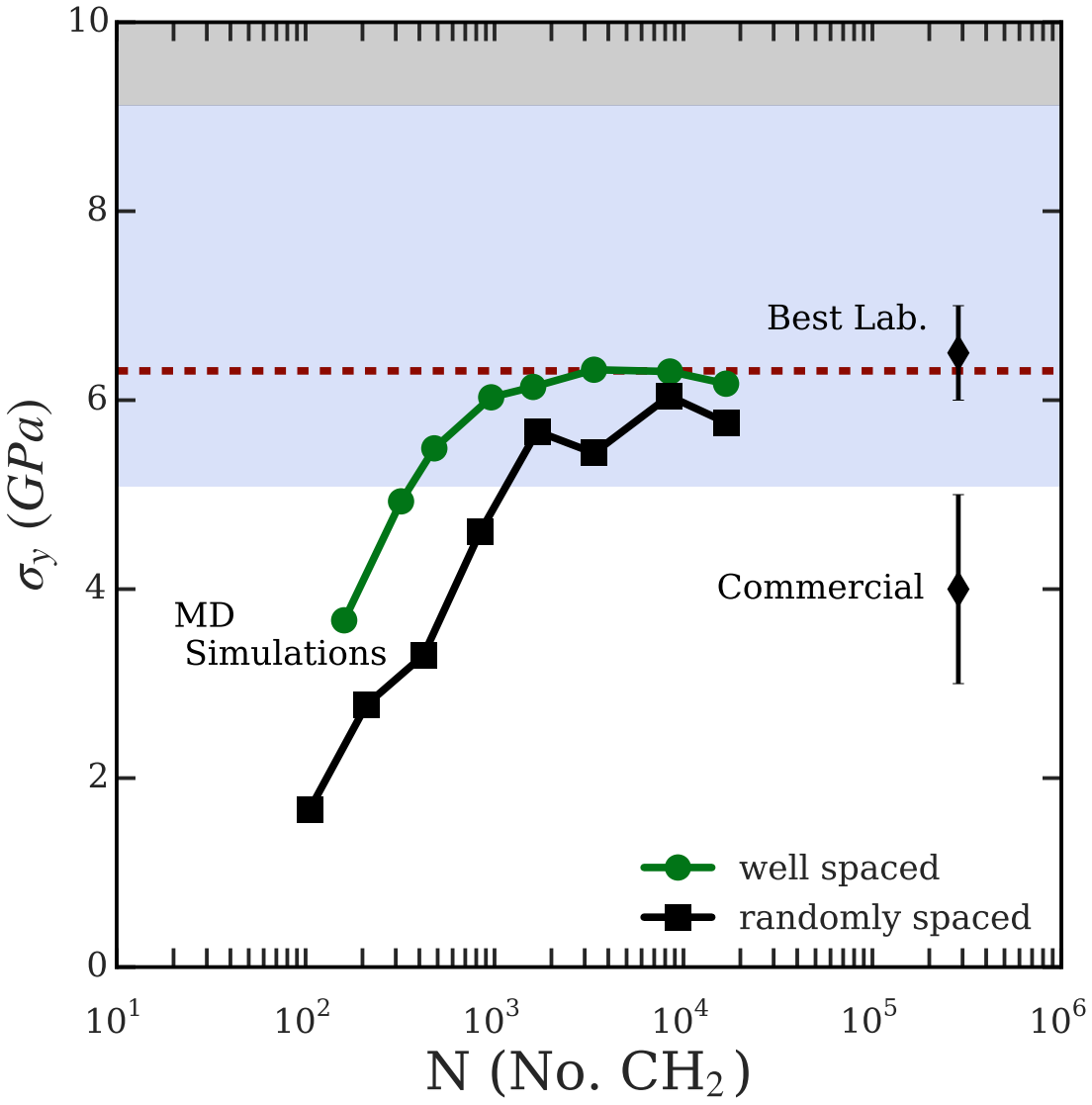

Figure 3.1: Yield stress σ_y vs. number of carbons per chain N at 300K for simulations with well-spaced (green circles) and random (black squares) chain-end distributions are compared to experimental strengths for commercial [82, 83] and lab [84–86] fibers (black diamonds). The yield stress corresponding to the onset of plastic flow in simulations is shown while the reported experimental points are from the peak yield stress. Experimental chain lengths range from $N = 10^5 - 10^7$. Variations between simulation runs are indicated by symbol size. The dashed red line indicates the stress where an isolated chain end defect slips by thermal activation of a dislocation at 300K. Shaded regions show FK model predictions for chain end metastability (blue) and instability (gray) against slip by dislocation nucleation.

Kontorova model with parameters extracted from simulations of the ideal crystal.

We model PE with AIREBO-M, the reactive bond-order potential for hydrocarbons described in the last chapter and Ref. [10]. Its van der Waals interactions have been optimized for alkanes and give accurate PE crystal phase behavior [10]. Covalent interactions use the bond screening method of Pastewka et al. [5]. The stable phase of PE at T=300K is orthorhombic, described by the three lattice constants (a, b, c). The constant $c = 2.54$Å is the C_2H_4 monomer spacing which points along the chain axis. We align the three lattice directions with the (x, y, z) axes of our periodic simulation cell. There are 80 chains in the xy-plane of the cell. The period along the z-axis is N/2 monomer spacings, corresponding to $N = 105 - 16800$ C atoms. The box dimensions are $(L_x, L_y, L_z) = (36.77, 39.53, 2.54 \times N/2)$ Å.

We make finite-length chains by deleting one monomer (C_2H_4) from each chain's backbone, breaking the chain and creating two chain ends as shown in Figure 1.2(a). Newly exposed chain ends are sp2 hybridized so we add an extra hydrogen atom to each to saturate the missing bond. This yields periodic crystals with an axial length of N carbons, composed of finite chains that are N-2 carbons in length. The spatial distribution of chain end defects can significantly impact crystal strength [12]. We address this by distributing defects in two ways. In the first set of systems, locations are selected so that defects on nearest and next-nearest neighbor chains have large axial separation ($> \frac{1}{20}Nc$). In the second set, defects have a random axial distribution.

We equilibrate all systems to T=300K and zero pressure using the LAMMPS

software package with a Nosé-Hoover NPT ensemble and a time-step between 0.5-1.0 fs [35]. Once equilibrated, we load each crystal in uniaxial tension by applying a constant engineering strain rate along the z-axis up to 5% strain, while allowing the stress in x and y to relax to 0GPa. Strain rates $\dot{\gamma}$ range from $\sim 9 \times 10^6$ – 10^9 s^{-1}. Rates are selected to fix $\dot{\gamma}N$ so that strains can be accommodated by chain ends moving at a velocity that is independent of the chain length N.

Stress-strain curves for the uniaxial tension tests are plotted in Figure 3.2. All systems show an initial linear response. For $N > 1000$ the modulus E saturates at $\sim$ 258GPa, which is comparable to experiments and theory for ideal crystals [79, 88]. As strain increases, the tangent modulus, $d\sigma/d\epsilon$, shows a sudden drop indicating the initiation of failure. We take this as the yield stress (σ_y) since each crystal fails if the stress is maintained at this value. Peak stresses are sometimes slightly higher ($\sim$ 0.3GPa), but are sensitive to the high strain rates in our simulations, implying post yield effects.

For infinite chains, chain scission is observed at yield, and the yield stress of $\sim$ 20GPa is consistent with estimates based on carbon-carbon bond strength [77, 87]. For all finite chains the yield stress is much lower, no bond scission is observed, and yield is associated with chain slip. Figure 3.1 shows σ_y as a function of N for crystals with different arrangements of chain ends. Maximizing the separation between defects on nearby chains leads to $\sigma_y = 6.3$GPa with a saturation in strength at about $N = 1000$. Breaking bonds at random gives a slightly lower σ_y and slower

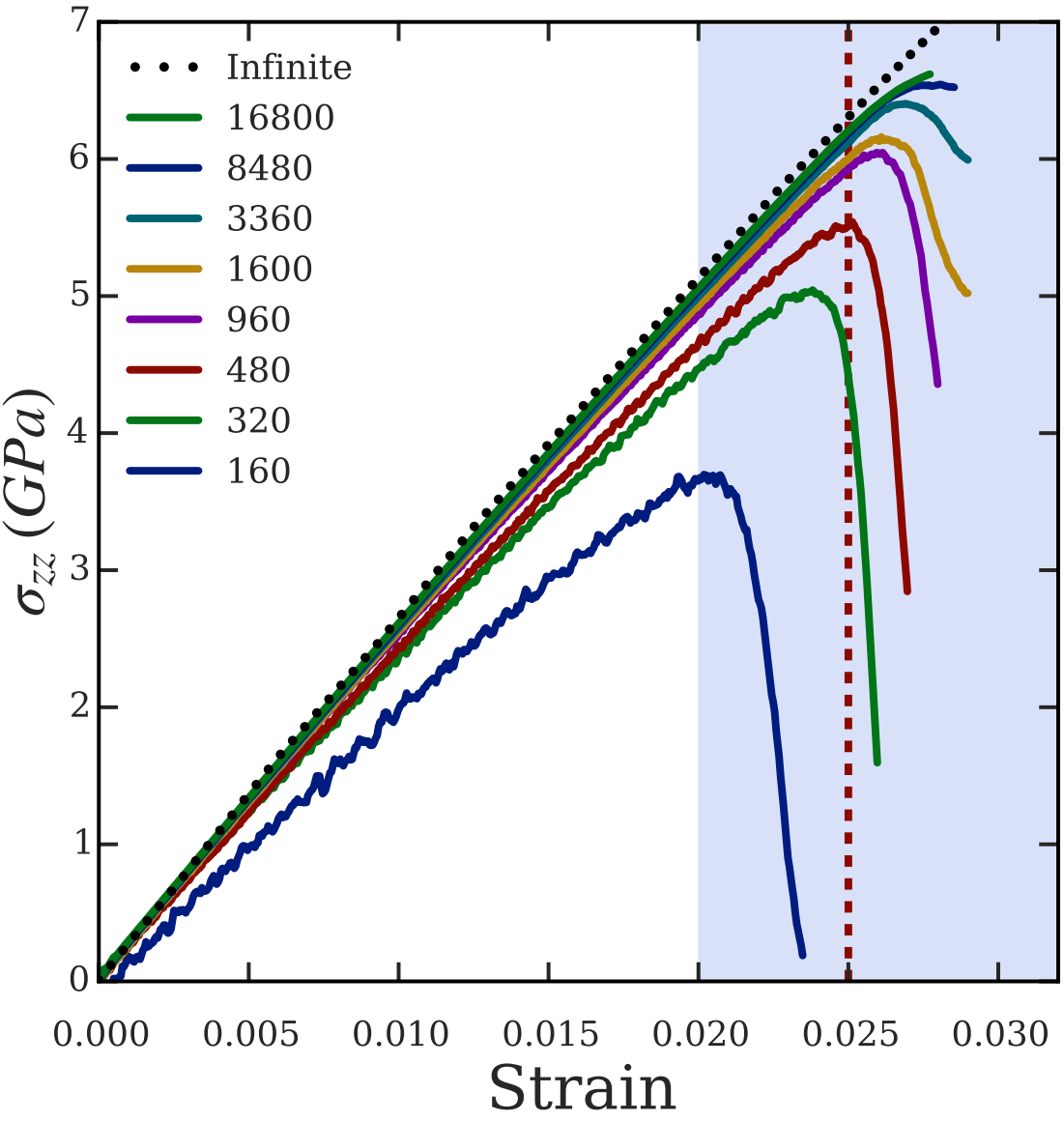

Figure 3.2: σ vs. ϵ curves for uniaxial tension tests of crystals with well-spaced defects at T=300K (solid lines) and a defect-free periodic crystal (black dotted line). The mechanical response saturates as N increases with $E \to 258$GPa, $\sigma_y \to 6.3$GPa, and $\epsilon_y \to 0.025$ (vertical dashed line). The defect free crystal yields by scission at much higher stress ~ 20 GPa.

saturation. This reduction in strength can be associated with the minimum separation between chain-end defects. In general we find saturation at a stress comparable to the best laboratory fibers, at chain lengths much less than the $N \sim 10^5 - 10^7$ in experiments [84, 85, 93]. Detailed analysis of a range of configurations shows that the key limitation is the minimum separation of chain-end defects. Lab fibers have much longer chains than our systems and are expected to be in this saturated limit [3].

We analyze the detailed changes in the molecular configurations at yield and find the yield mechanism to be slip at chain ends. A simple way of quantifying this is to measure the mean separation between chain end pairs $\langle \Delta z \rangle$ (Figure 1.2(a)). In Figure 3.3 we plot $\langle \Delta z \rangle$ normalized by the monomer spacing c as a function of strain for systems with well-spaced defects (solid lines). At small strains, all systems show the same gradual rise in $\langle \Delta z \rangle$, which represents the elastic response in the confining potential of surrounding chains. There is then a rapid rise, indicating yield by chain slip. Here we define the yield strain (ϵ_y) for chain slip as the strain when $\langle \Delta z \rangle > c = 2.54\,\text{Å}$ - i.e., when the majority of chain ends have slipped by 1 monomer spacing. Once $N \geq 320$, ϵ_y reaches a limiting value of ~ 0.025, which is consistent with our analysis of the stress-strain curves (Figure 3.2).

Figure 3.3 suggests ϵ_y becomes independent of N when chain end defects are far apart and their interactions are weak. Since we have kept $\dot{\gamma}N$ constant, our well-spaced simulations with $N > 320$ are at strain rates between $9 \times 10^6 - 2 \times 10^8\, s^{-1}$, but yield at nearly the same ϵ_y. Additional simulations for the longest ($N = 16800$)

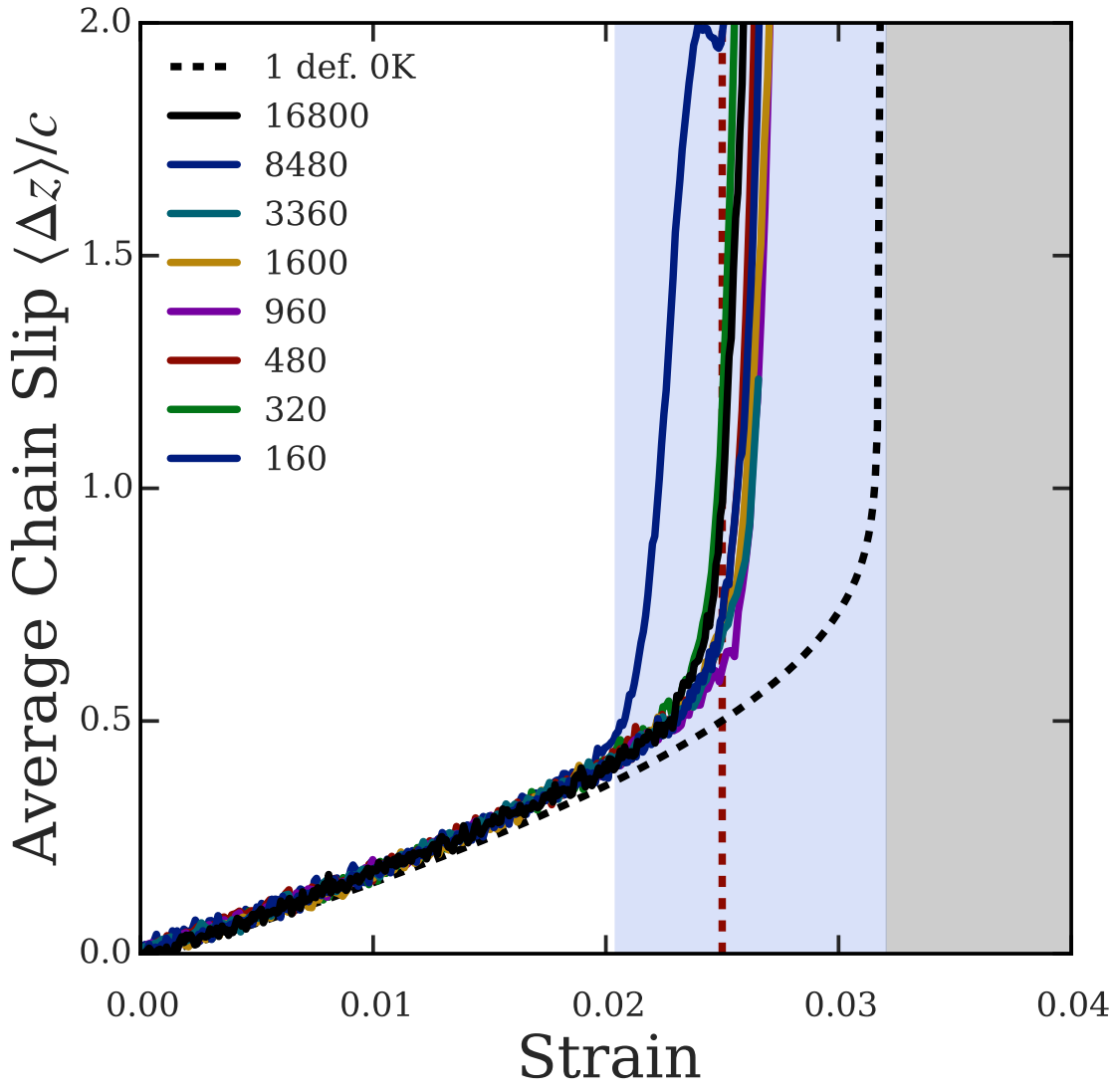

Figure 3.3: Average chain end seperation $\langle \Delta z \rangle$ vs. strain at T=300K for systems with well-spaced defects (solid lines). The dashed black line is Δz for an isolated defect in a perfect crystal at T=0K. The dashed red line indicates $\epsilon = 0.025$, where an isolated defect at T=300K slips by thermal activation of dislocations. At small strains, all systems follow the T=0K curve of the isolated defect before slipping thermally. For large N, all systems slip near $\epsilon = 0.025$.

chains show that increasing $\dot{\gamma}$ from $9 \times 10^6 s^{-1}$ to $5 \times 10^9 s^{-1}$ only increases ϵ_y to 0.028, corresponding to $\sigma_y \sim 7$GPa. We expect that experiments will not exceed these rates or the associated stresses.

We next investigate what sets the limiting value of ϵ_y. In order to probe this limit, we seek a system that eliminates the interaction of chain ends on different chains. By repeating our previous analysis for a crystal with sufficient axial length (N = 480), but with only one of the 80 chains broken, we measure the slip and yield properties of a single finite chain in an otherwise perfect crystal. This system lets us study the stability and slip of a single chain-end defect in the limit of "infinite" defect separation that is appropriate for laboratory chain lengths.

We first investigate the stability of the single defect in the absence of thermal fluctuations (T=0K), by performing a series of energy minimizations on the single defect crystal with the FIRE minimizer [56] for $\epsilon \leq 0.05$. The resulting curve of Δz vs ϵ for the single defect is plotted in Figure 3.3 as a black dashed line. We see that Δz grows gradually with ϵ until the isolated defect becomes unstable to slip around $\epsilon \sim 0.032\%$ and $\sigma \sim 9.3$GPa. This stress and strain sets the upper limit of stability of the chain end defect. Past this strain, chain ends slip spontaneously, even in the absence of thermal fluctuations.

A finite chain can also be metastable and slip by thermal activation at finite temperature. To study thermal activation at 300K we held the system at a fixed strain and monitored Δz to see if chains slipped in 1.0ns. Increasing strain in steps of

0.001 mimics strain rates of $10^6\ s^{-1}$, compared to $\dot{\gamma}$ up to $10^9 s^{-1}$ in direct simulations. All configurations of the single defect with strain $\epsilon \geq 0.025$ slip by thermal activation within 1.0 ns. This gives an upper bound on the stress and strain for thermally activated slip of $\sigma = 6.3$ GPa and $\epsilon = 0.025$ respectively. Plotting these values as red dashed lines in Figures 3.2, 3.1, and 3.3, we see the slip of a single defect at 300K effectively predicts ϵ_y and σ_y in the limit of large chain length.

In order to understand the nature of chain slip, we must examine how stress is transferred between chains in the PE crystal. While an infinite chain can be loaded in tension directly along its backbone bonds, a finite chain can not. Instead the periodic potential produced by adjacent chains favors stretching to remain in registry, but at the expense of elastic energy. This competition between the elastic stiffness of a chain and shear stresses imposed by a periodic potential is the essence of the well-studied Frenkel-Kontorova (FK) model [15, 94].

The FK model describes the dynamics of a chain of masses connected by springs of stiffness k resting on a periodic potential "substrate" with a period λ that can be different from the equilibrium length of the springs, c. In our case, c equals the equilibrium monomer spacing $c = 2.54$Å, but the period of the potential created by neighboring chains grows with strain as $\lambda = c\,(1 + \epsilon)$. As strain increases, the peak force τ from the periodic potential is insufficient to balance the elastic tension of the stretching bonds, and the chain ends depin by nucleating 1D dislocations.

Frank and van der Merwe were the first to consider 1D dislocations for fixed k

and mismatch λ/c [14]. A large group of researchers has extended their ideas to describe a multitude of condensed matter systems [15]. This includes many who have invoked the ideas of Frank and van der Merwe to describe the dynamics of PE and other polymer crystals [95–102]. None have considered the actual geometry of chain ends in the orthorhombic PE crystal under tension. Instead, they typically apply FK theory to simple bead-spring or united-atom potentials [95–99, 102]. We find that explicit hydrogens are essential to the shear modulus and interchain forces within the PE crystal. Shear forces are underestimated by a factor of $2-3$ in united-atom models. More detailed applications of FK theory to all-atom PE crystals consider short chains ($N < 1000$) in unstressed crystals, and do not address yield [100, 101].

We find that an FK model, parametrized from all-atom simulations of the orthorhombic PE crystal, describes the tensile yield in our detailed finite-chain simulations as due to chain slip by dislocation nucleation at chain ends. The properties of the dislocations allow us to understand trends in yield with N and place bounds on σ_y that agree well with our simulations and experiments.

Only two parameters are needed to parameterize the FK model, k and τ. We determine a per monomer (C_2H_4) stiffness $k = 11.4\,eV/\text{Å}^2$ from a uniaxial tension simulation of a defect free crystal. This is consistent with the experimental Young's modulus. We calculate the peak force per monomer of the periodic potential $\tau = 46.72$ meV/Å by displacing a single chain along the chain axis while measuring the force exerted on it by the surrounding crystal. The chain can relax in the transverse

directions, but the surrounding crystal is held rigid by stiff harmonic constraints. This corresponds to a T=0K measurement of τ. We find that k and τ change little as T increases to room temperature. The next chapter discusses parameterization of the FK model in more detail.

FK theory [14,15] predicts a characteristic length over which the chain and periodic potential remain in registry called the dislocation core size

$$\xi = \left(\frac{kc^3}{2\pi\tau}\right)^{1/2} = 25.24\,\text{Å} \approx 10\,c.$$

Tensile stress builds from 0 at the chain ends to the bulk value over a length $\sim \xi$. Over this scale, bond lengths must change from the relaxed length c to the uniformly stretched length $c\,(1+\epsilon)$ in the chain center. Figure 3.4 compares numerical results and anlytical predictions for the change in bond length near chain ends. For small strains, $\epsilon \leq 0.0206$, changes in bond length follow the predicted exponential decay, $\sim \exp(-x/\xi)$, with x the distance from the chain end. At strains just before slip, the analytic prediction takes the form of a dislocation with bond length $\sim \exp(-x/\xi)/\left[1+\exp(-2x/\xi)\right]$. This captures our numerical result for $\epsilon = 0.0315$ in Figure 3.4. For larger strains, the chain end slips by a period or more, creating a dislocation that moves away from the end and leads to yield.

The core size also sets the axial length-scale over which chain end defects on neighboring chains interact [15]. As shown above in Figure 3.1, σ_y saturates at the strength of the isolated defect when $N \geq 1600$, corresponding to a minimum separation of 80 monomers ($\sim 8\xi$) between defects on neighboring chains. When the separation is

less than ξ, as for $N = 160$ in Figure 3.2, even the linear modulus is substantially reduced.

In the presence of chain ends, we can also derive the strains at which an end becomes metastable (ϵ_m) and unstable (ϵ_u) to dislocation formation (i.e. chain slip). The result, originally calculated by Frank and van der Merwe [14], gives: $\epsilon_m = \frac{2}{\pi^2}\left(\frac{c}{\xi}\right) = 0.020, \quad \epsilon_u = \frac{1}{\pi}\left(\frac{c}{\xi}\right) = 0.032$. Using these values we have shaded regions in all figures corresponding to the metastability (blue) and instability (gray) of an isolated chain end to dislocation nucleation. The boundary between blue and gray regions represents an upper bound for yield: $\sigma_y \leq E\frac{c}{\pi\xi} = 9.3\,\mathrm{GPa}$, that can only be reached in the limit of zero temperature or extremely high strain rate. It shows excellent agreement with our T=0K analysis plotted in Figures 3.3 & 3.4. The lower boundary of the blue region corresponds to the low rate limit of ϵ_y and a lower bound for yield: $\sigma_y \geq E\frac{2c}{\pi^2\xi} = 5.26\,\mathrm{GPa}$, where dislocations become energetically favorable, and creep-like yield can occur by thermally activated dislocation nucleation. Experimental values for PE crystals should fall somewhere between these bounds determined by rate and temperature effects. As noted above, we found increasing $\dot{\gamma}$ from 9×10^6 to $5 \times 10^9 s^{-1}$ changes σ_y less than 1GPa at room temperature. Thus experimental strengths are unlikely to exceed 7GPa.

In summary, all atom simulations of tensile failure show that the limiting strength of polyethylene fibers is determined by slip of chains near free ends. The yield stress grows with increasing chain length and saturates at values comparable to the best

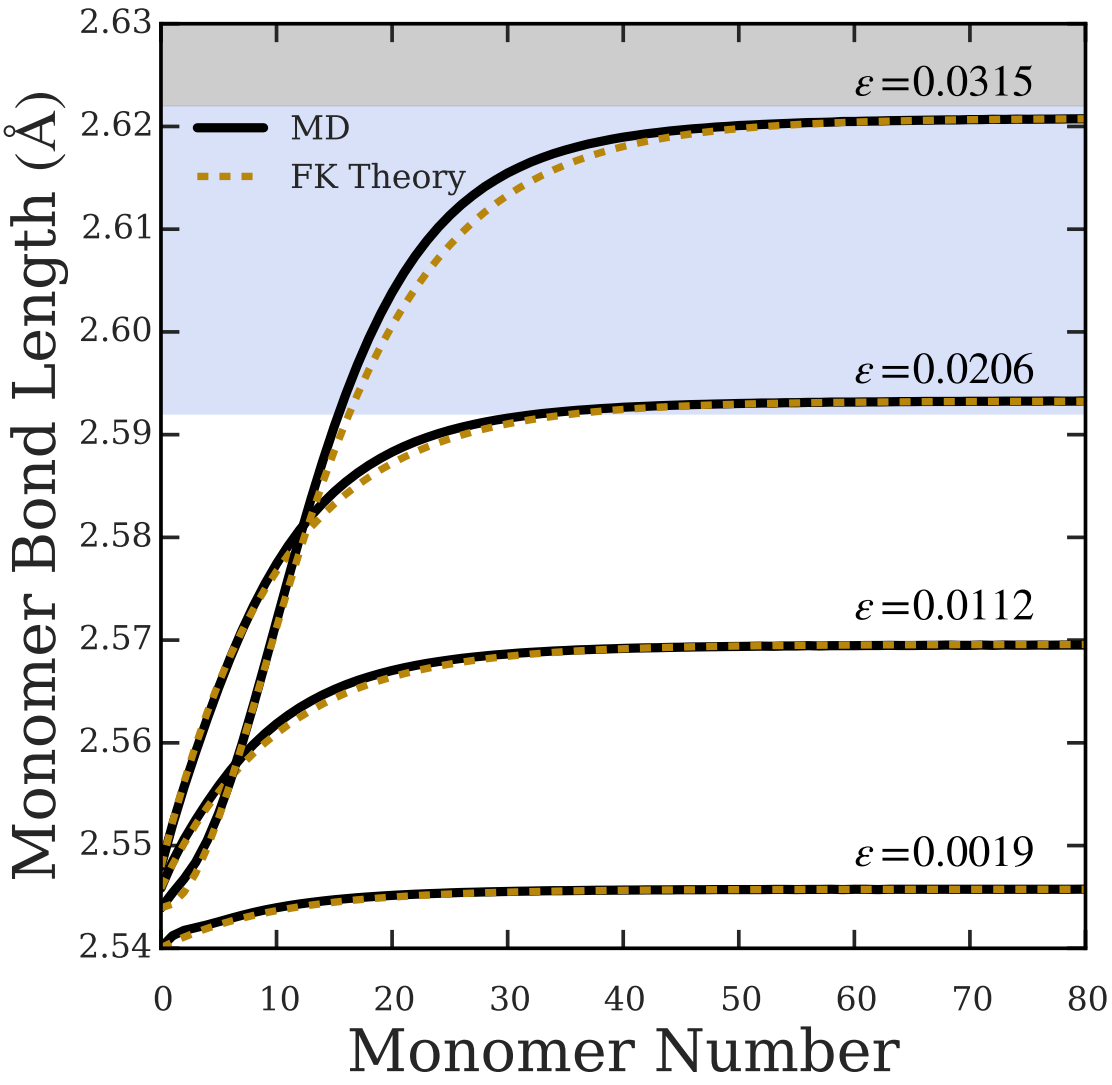

Figure 3.4: Bond lengths as a function of distance from chain end from simulations (solid black) and theory (dashed lines) for the indicated strains. Interior bonds stretch uniformly with the crystal, while bonds near the end relax to the unstressed length.

experimental fibers, 6.3GPa, and far below the stress required for chain scission. Little rate sensitivity ($<$ 1GPa) is seen for rates from 10^6 to $10^9 s^{-1}$. The strength saturates when the separation between nearby chain ends is much larger than the dislocation size ξ characterizing the length for transfer of tensile stress between adjacent chains. A simple Frenkel-Kontorova model parameterized by studies of small crystals captures the essential features of full simulations. The model provides analytic predictions for ξ, bond lengths, and the strains and stresses where the system is metastable and instable against chain slip. These can be related to bounds on the yield stress at low temperature and high and low rates. The approach is readily extended to other polymer fibers and can be used to study creep as shown in the next chapter.

Chapter 4

A Microscopic Model for Creep in PE Fibers

4.1 Introduction

High performance polyethylene fibers are highly oriented polymer materials with stiffness comparable to steel while having one eighth the density. Polyethylene's simple chemical structure and controllable semi-crystalline morphology make it an affordable and versatile material for applications including: ship sails, mooring lines, vehicular chassis, prosthetic implants, composite armors, and fabrics. Fibers are typically formed by plastically drawing a melt or solution of entangled linear chains. Drawing orients and extends chains along the fiber axis, creating extended chain crystals that compose $> 90\%$ of the final fiber. The crystal domains uniformly orient

chain backbones along the fiber axis, and interpenetrate with each other to form a mesoscale network spanning the fiber.

Chains in fibers are not permanently cross-linked like rubbers or elastomers. Thus, most fibers creep during sustained loading [3]. Creep causes fibers to fail at stresses well below their ultimate strength, severely limiting their potential applications. Understanding the microscopic mechanisms mediating fiber creep is important for developing new processing protocols to make better fibers. However, creep processes usually occur at the nanoscale where direct observation is difficult. Instead, experiments characterize creep mechanisms indirectly by observing how changes in fiber length depend upon temperature and tensile load.

In a typical creep experiment, fibers are subjected to a constant tensile load σ at a constant temperature T while the time dependent engineering creep rate $\dot{\epsilon}_c(t) = (L(t) - L_0)/L_0$ is measured. L is the fiber length and L_0 is its value prior to loading. Creep is assumed to result from activated hops over a barrier $E_a = E_a^0 - V^*\sigma$ that decreases linearly with the applied tensile stress σ. The propotionality constant V^* is called the activation volume and represents the sensitivity of the barrier to stress rather than a literal volume size. If the attempt frequency for activation is ω_0, Eyring theory gives a creep rate [103]

$$\dot{\epsilon}_c \propto \omega_0 e^{-E_a^0/k_bT} \sinh(\sigma V^*/k_bT) \tag{4.1}$$

PE's hierarchical structure produces multiple relaxation mechanisms during tensile loading. Wilding and Ward showed creep data for a wide variety of PE fibers

could be fit by two Eyring processes in parallel [104,105]. One process in their model accounts for the rapid creep that occurs as the mesoscale crystal network initially responds to the load. This "network relaxation" dominates the first 2-4% strain and is highly sensitive to the composition and processing history of a fiber. At larger strains, $\dot{\epsilon}(t)$ plateaus to a steady creep rate that is controlled by the second Eyring process. Experiments suggest that the steady creep process is localized in the crystalline phase [104]. Unlike the first process, its contribution and activation volume are largely insensitive to processing history and only depend upon the percent crystallinity of a fiber. Of the two processes, the steady creep rate dominates the lifetime and rupture of loaded fibers because it is largest at long times.

Many experiments have measured E_a and V^* for the steady, crystal creep process. Regel et al. [106] and Dijkstra et al. [92] studied how fiber fiber rupture times vary with load and temperature. Later Ward et al. and Govaert et al. tracked and analyzed the time-dependent total strain $\epsilon(t)$ [104,105,107,108]. Most recently, Jenket systematically studied how temperature and rate affected the failure of hundreds of high-performance PE fibers [109]. All these studies suggest a range $V^* = 10 - 100$ Å^3 [92,104] and $E_a \approx 1 - 1.7$ eV [104,107–110] for steady creep.

The value of V^* is consistent with the volume of a single monomer in the crystal phase, which is about 47 Å^3 [55,111]. Originally, this barrier was associated with the scission of chain backbones within the PE crystal [104,106]; however, it has been pointed out that failure by scission alone is inconsistent with experimental measure-

ments of fiber strength [3, 89, 110, 112].

The strongest fibers reported in experiments fail at loads $\sigma \leq 6 - 7$ GPa [86, 113, 114]. This is much lower than the theoretical strength of $\sim 20 - 40$ GPa calculated for C-C bonds near room temperature [87, 88]. If fibers deform plastically by chain scission then their ultimate strengths should be substantially larger than 7 GPa. However, the past 40 years of process development have not produced substantial increases in fiber strengths. The energy barrier for C-C bond scission (~ 4 eV) is also significantly larger then the ~ 1.5 eV measured in creep experiments, which would significantly slow the rate of creep.

Some have suggested the low fiber strengths may be due to the motion of defects within the crystal that mediate failure prior to chain scission [3]. PE hosts a variety of crystal defects and many have been considered, including: braids, hair-pins, crank-shafts, and twistons [100, 115–119]. Twistons in particular have received a great deal of study and some have suggested creep is mediated by their motion. They are soliton defects that smoothly rotate a single chain backbone by 180 degrees, while also stretching or compressing the chain backbone by half a monomer spacing [100, 116, 117]. These are called twist-extension (TE) and twist-compression (TC) twistons, respectively. Twistons have been observed in equilibrium crystals with NMR and are known to play an important role in the disordering of the crystal phase during melting [100, 120]. However, theoretical studies of twiston properties seem to suggest they are likely not responsible for steady creep in fibers.

Zhang found both TC and TE twistons to be stable near 0K with similar formation energies ~ 0.7 eV. However, at finite temperature, Zhang observed that TC twistons are highly unstable to thermal fluctuations and collapse into a localized sequence of highly rotated dihedral angles. Mowry and Rutledge showed that these collapsed TC defects are relatively immobile with large energy barriers (0.14-0.65 eV) for translation [118]. Subsequent studies by Zubova et al. [119], and most recently by Milner and Wentzel [100] have expanded upon these findings. Notably, Milner and Wentzel studied twistons near room temperature and found a TE twiston formation energy ~ 0.43 eV at $T = 350$ K.

The twiston formation energy of Milner and Wentzel is significantly lower than $E_a^0 \sim 1.1 - 1.7$ eV reported for steady creep at room temperature. At these experimental temperatures, only the TE twistons should be stable, but they do not relax tension and become *less* energetically favorable with increasing tensile strain. The collapsed TC defects can relax tension but their high barrier for translation limits their ability to mediate slip effectively. Thus, it seems unlikely that twistons could produce the stress-activated Eyring process observed in experiments.

Given these results, it is worth considering whether fiber creep can be explained by the motion of another type of defect within the crystal. The most popular alternative explanation of failure is chain slip where chains lose their cohesive grip on their neighbors and slide past each other along the fiber axis [13,115,121]. Breaking bonds between neighboring chains is much easier than breaking covalent bonds, but many

neighbor bonds must be broken for a long chain to slip. Chains in PE fibers typically have $\sim 10^5$ monomers, making the energy cost for an entire chain to slip much larger than the cost for chain scission. It is easier for chain slip to occur at a localized defect that disrupts only a few bonds within the crystal. The simplest type of defect that must be present in real materials is a chain end. A chain end defect is shown in Figure 4.1(a) and can be thought of as a missing covalent bond where one chain ends and another chain begins. The backbone cannot carry tension near the chain end because of the missing C-C bond. This causes strains to localize near chain ends and can facilitate chain slip.

In the last chapter we applied MD simulations to study the effect of chain end defects on the strength of otherwise perfect, crystalline fibers. Our simulations found the presence of chain end defects (Figure 4.1(a)) lowered the ultimate strength of a perfect fiber to a value consistent with the 6-7 GPa measured in experiments. At larger loads, we observed chain ends embedded within the crystal became unstable and caused chains to slip past each other in registry. These results suggest chain slip at chain ends should prevent crystals from developing the large stresses necessary for chain scission to contribute substantially to creep.

In this chapter, we consider whether the barrier for steady creep can be explained by thermal activation of the chain slip mechanism we previously identified when studying fiber failure. Specifically, we compute the stress dependent activation barrier $E_a(\sigma)$ for a chain to slip at a chain end that is embedded within the PE crystal.

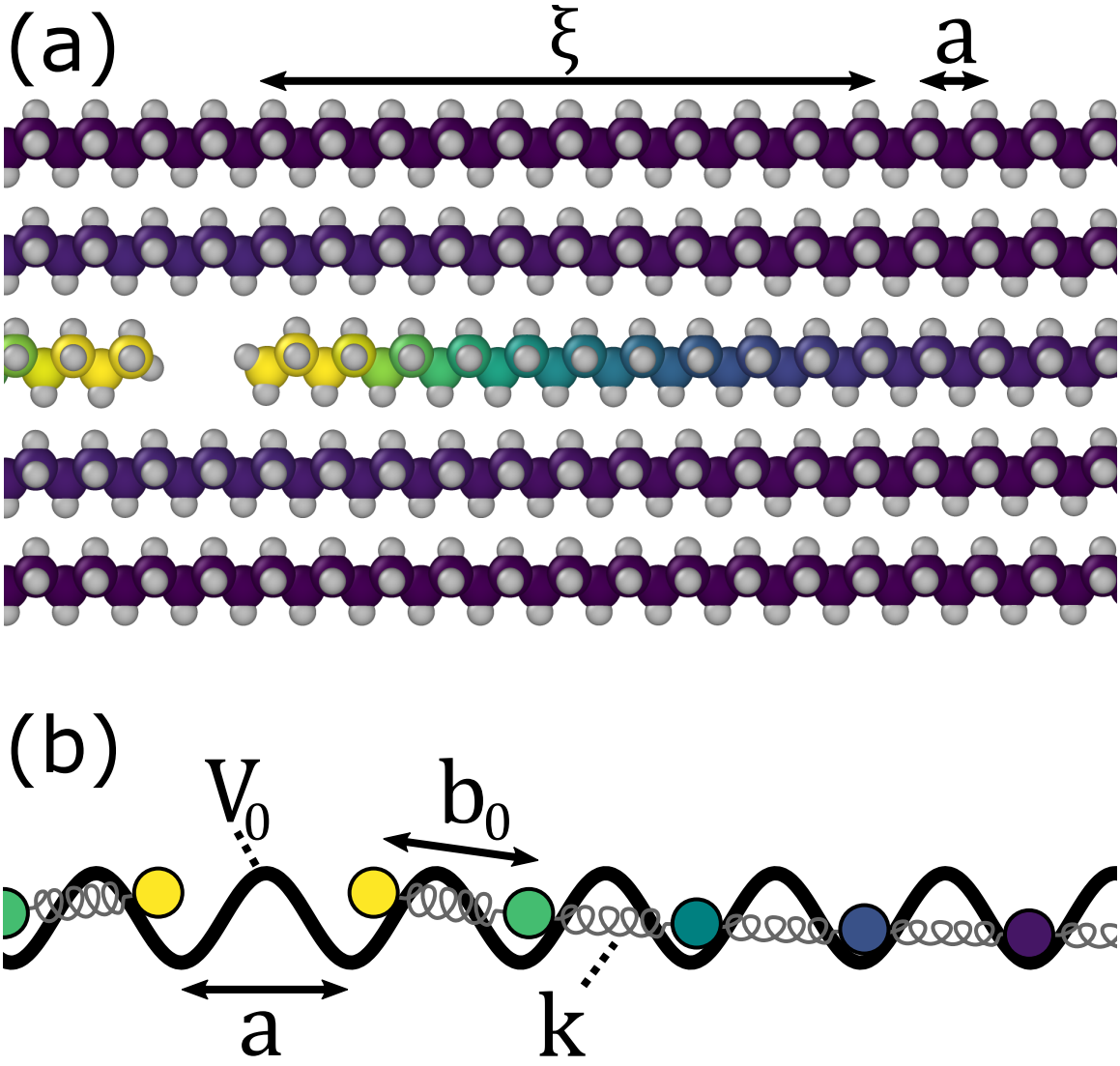

Figure 4.1: (a) A chain end defect within an orthorhombic PE crystal at a fixed tensile strain. Monomers are colored by the non-affine displacement. Most monomer bonds stretch affinely with the strain to $a = b_0(1+\epsilon)$ (purple), where b_0 is the equilibrium bond length. Monomers near the chain end relax in the potential over a length-scale $\sim \xi$ so bonds approach their equilibrium length (yellow) at the chain end. (b) Schematic of the FK model that describes (a). A chain of N atoms connected by springs of stiffness k and equilibrium bond length b_0 rests in a crystal potential with wavelength a and amplitude V_0. The ratio kb_0^2/V_0 sets the length-scale ξ while the ratio a/b_0 controls the stability of the ends against slip.

Chain end slip is mediated by the nucleation of 1D dislocations at the chain end. A dislocation that has nucleated at a chain end and moved along a chain in a simulated PE crystal is shown in Figure 4.2(a). The dislocation carries one excess monomer and distributes the associated bond distortions over $\sim 2\xi$ lattice spacings. ξ is a dimensionless length called the dislocation core size. Each dislocation nucleated at an end can travel along the chain backbone, resulting in translation of the chain by one lattice spacing as shown in Figure 4.2(a). This process is a promising candidate for creep because dislocation nucleation couples directly to tensile loading through the stability of the chain ends. It is possible for dislocations to form away from a chain end; however, this requires forming both a compresssional and a tensile dislocation, which has twice the energy cost and does not couple to tensile loading.

The crystal distortions created by dislocations are localized to a single chain, and the properties of these 1D dislocations can be accurately captured by a simple Frenkel-Kontorova model. The FK model reduces the many chain problem of chain slip to a problem for the stability of a single chain in a mean crystal field (Fig. 4.1(b)). Here, we apply the FK model to consider how tensile loading of crystallites lowers the barrier for chain ends to slip and nucleate dislocations. The theory gives an analytic prediction for the stress dependent activation barrier for slip $E_a(\sigma)$ that should set an upper bound for creep in actual fibers. By linearizing $E_a(\sigma)$, we derive an effective Eyring activation energy E_a^0 and activation volume V^* for chain slip. Our calculated Eyring parameters agree well with the experimental measurements.

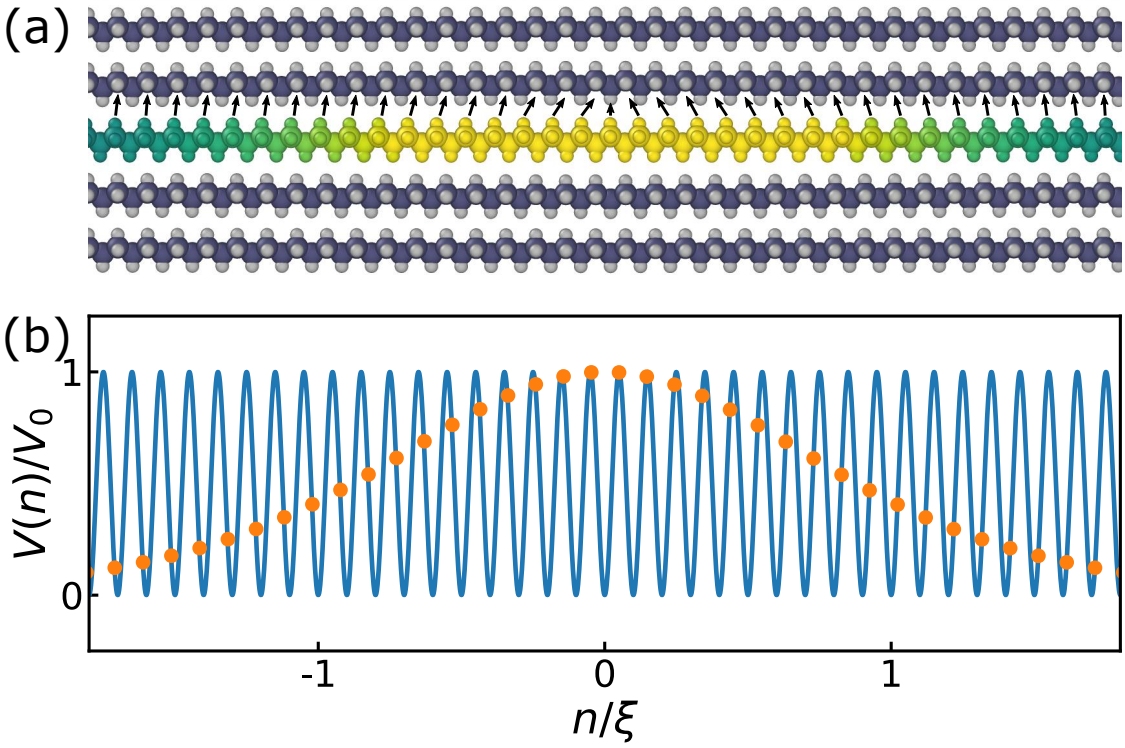

Figure 4.2: (a) A positive 1D dislocation within an orthorhombic PE crystal modeled by AIREBO-M. The dislocated chain is colored as in Figure 4.1. The dislocation has a core-size $\xi \approx 10$ monomers and carries one excess monomer. It translates the chain by one lattice site as shown by the arrows indicating the chain registry. (b) A 1D dislocation of the FK model with the same ξ and horizontal scale as (a). Monomers (orange circles) are shown transitioning by one lattice spacing of the crystal potential (blue).

The FK model has three free parameters that characterize the covalent bond length b_0, covalent bond stiffness k, and van der Waals (vdW) traction τ between chains. We calculate these parameters from simple MD simulations of perfect PE crystals. As in our the previous chapter and Ref. [13], we report results for PE crystals with the AIREBO-M potential [122]. AIREBO-M is a reactive model for hydrocarbons with intermolecular interactions that have been carefully optimized to accurately model the mechanics of solid hydrocarbons, including crystalline PE at high pressures. It has been shown to accurately reproduce experimental data for the structure, elasticity, yield, and shock mechanics of crystalline PE [10, 24, 112].

In any simulation, the choice of interaction potential may introduce uncertainty in the conclusions. Given its thorough validation for solid PE, we believe AIREBO-M should be accurate. However, in order to characterize the uncertainty of our model predictions, we have calculated three additional sets of FK parameters using three other popular interatomic potentials for hydrocarbons: AIREBO [11], L-OPLS [123], and PCFF [124]. We provide FK parameters for all four potentials and compare them to experimental data when available.

In section 4.2 we summarize the finite FK model and use it to derive Eyring parameters for thermally activated chain slip. Section 4.2 details our MD methods and compares FK parameterizations for different interatomic potentials. In section 4.4, we compare our FK theory predictions to experimental data for PE fibers.

4.2 Microscopic Theory for Chain Slip

4.2.1 FK Theory for Chain End Stability

We consider the stability of the chain ends of a chain embedded within a PE crystal (Figure 4.1). For simplicity, we will assume all chains have N backbone bonds. Chains in real fibers are polydisperse, but we find that this does not influence our predictions for fiber strength or creep when chains are much longer than the characteristic core size of a dislocation ξ. For PE, we will find $\xi \approx 10$ monomers, which is much smaller than the typical molecular lengths $N > 10^5$ for PE fibers.

End stability is determined by the competition between the tension in the chain backbone and the corrugated potential produced by the collective van der Waals interactions from neighboring chains. The FK model captures both of these effects with the minimal model illustrated in Figure 4.1(b). The backbone bonds have an equilibrium monomer spacing $b_0 \approx 2.54$ Å^3 [111] and a harmonic spring constant k describes the energy cost of distortions from this value. The crystal potential generated by neigbhors is also periodic with a wavelength a. The chain is held in crystal registry along the fiber axis by the periodic potential. The wavelength a is determined by the average monomer bond length and is equal to b_0 in equilibirum. When subjected to a local elastic tensile strain ϵ_e, the period of the potential will increase, producing a misfit $a - b_0 = \epsilon_e b_0$. The macroscopic strain of the fiber will reflect both the local elastic strain from tensile forces and the plastic strain ϵ_p from

chain-end slip or other effects: $\epsilon = \epsilon_e + \epsilon_p$.

The FK chain configuration can be expressed with a per monomer displacement $u_n = r_n - na$ of the position r_n of the nth monomer relative to the minimum of the nth potential well. Stable solutions minimize the Hamiltonian [14, 125]

$$U = \sum_{n=1}^{N} \left[\frac{1}{2} k(u_{n+1} - u_n + \epsilon b_0)^2 + \frac{1}{2} V \left(1 - \cos\left(2\pi u_n / a\right)\right) \right] \tag{4.2}$$

The first term is the covalent energy representing deviations from the equilibrium length b_0 and the second gives the energy of monomers in the corrugated potential from the surrounding crystal. The core-size emerges from the competition of the two terms and is given by

$$\xi = \sqrt{\frac{ka^2}{2\pi^2 V}} = \sqrt{\frac{ka}{2\pi\tau}} \tag{4.3}$$

where we have defined the peak traction force $\tau = \pi V/a$ for the periodic potential, which is $\pi V/b_0$ in equilibrium. We note, the FK model assumes a sinusoidal potential, which is rarely true. However, the core-size is most sensitive to the amplitude τ and the $\xi \sim \tau^{-1/2}$ scaling relationship of 4.3 should hold for more complicated potentials.

Frank and van der Merwe showed the behavior of the discrete chain is well approximated by its continuum limit when ξ is larger than several lattice spacings, as is the case for PE [14]. We applied the continuum approximation in the previous chapter and found good agreement with atomistic simulations of PE [13]. As detailed in Reference [14], stable solutions of the continuous FK chain satisfy the differential

equation

$$\frac{\partial^2 u}{\partial n^2} = \frac{a}{2\pi}\frac{1}{\xi^2}\sin\left(\frac{2\pi}{a}u\right) \tag{4.4}$$

where $u(n)$ is the continuum limit of the monomer displacement. Chain stability requires the tension in the chain backbone go to zero at the chain ends. The backbone tension is given by $t(n) = k(\partial u/\partial n + \epsilon b_0)$, so the boundary condition at either end is

$$\frac{\partial u}{\partial n} + \epsilon b_0 = 0 \tag{4.5}$$

Note, only the potential wavelength $a = (1+\epsilon)b_0$ enters the equation of motion, and the equilibrium bond length only explicitly affects the boundary condition for the chain ends.

The equation of motion supports a commensurate solution $u(n) = 0$ that corresponds to all bonds stretching uniformly with the crystal potential $\delta b(n) = b(n) - b_0 = \epsilon b_0$. It also supports dislocation solutions which translate the registry of the chain by one site in the crystal potential. Dislocations can be either compressional, creating an interstitial monomer, or tensile (an "anti-dislocation"), creating a monomer vacancy. Since the chain is already stretched, anti-dislocations have a much higher energy. If defects are to nucleate in the center of the chain, both types of defect must be formed as a pair. The total energy is ~ 2 times higher than for the nucleation of a single compressional defect at a chain end. The FK solution for an isolated dislocation centered at the origin is given by [125]:

$$u_d(n) = \frac{2a}{\pi}\tan^{-1}\left[e^{-n/\xi}\right] \tag{4.6}$$

and is plotted in Figure 4.3(a). As the dislocation travels rightward, it translates monomers by one lattice spacing to the right. Dislocations and anti-dislocations compress or stretch bonds relative to the uniformly stretched state $b(n) = a$. The local compression $\delta b_d(n)$ produced by a dislocation is given by:

$$\delta b_d(n) = -\frac{2a}{\pi\xi}\frac{e^{-n/\xi}}{1+e^{-2n/\xi}} \tag{4.7}$$

and is plotted in Figure 4.3(b).

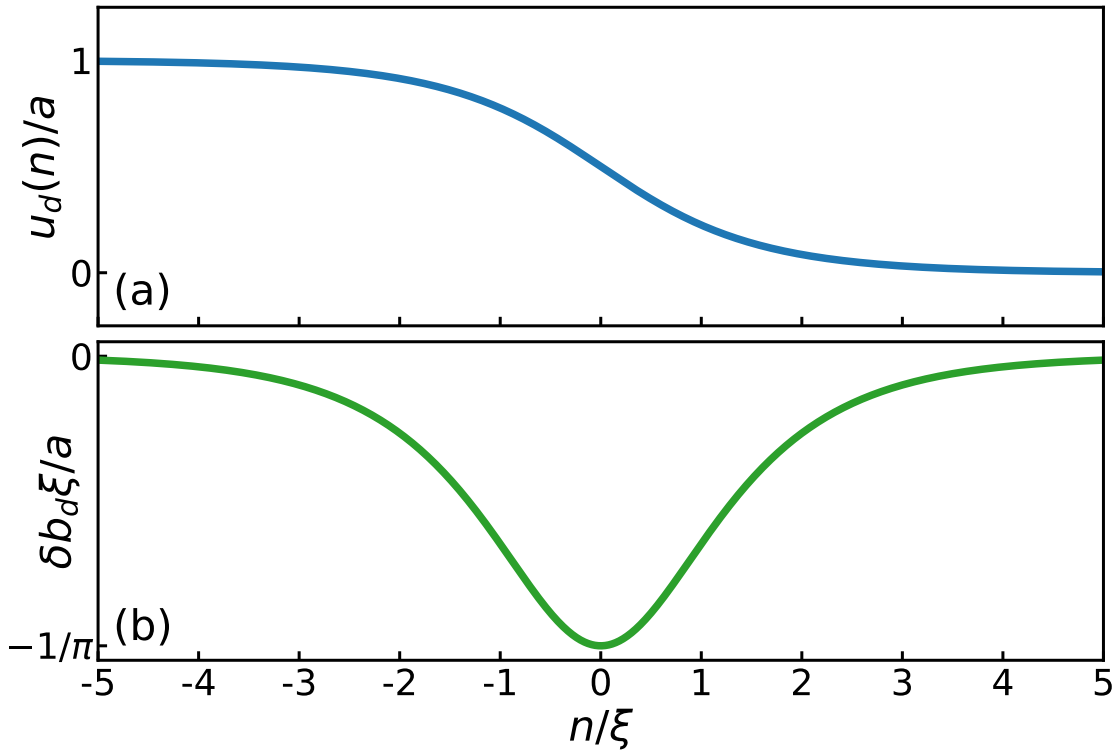

Figure 4.3: (a) Normalized displacement $u_d(n)/a$ for a compressional 1D dislocation solution of the FK model. The dislocation contains one excess monomer within its core as for Figure 4.2(a) and translates monomers by $+a$ as it moves rightward. (b) Normalized bond distortions $\delta b\xi/a$ produced by the dislocation in (a). Accommodating the interstitial monomer requires compressing bonds relative to a, which can relax tension when $a > b_0$.

When a fiber is loaded in tension, most chains are not loaded directly but by interacting with the crystal potential produced by their neighbors. Bonds far away from chain end defects stretch affinely with the periodic potential so $\delta b(n) = b(n) - b_0 = \epsilon b_0$ and the backbone tension is constant. $b(n)$ is not constant near the chain ends since there is a missing covalent bond that cannot maintain the backbone tension. Thus the backbone tension must decrease to zero at the chain end in any stable configuration. Bonds near the end relax so $b(n) \to b_0$ and transfer the tension that would be balanced by the missing bond to the corrugated crystal potential.

In the limit where $N \gg \xi$, the behavior at the two ends can be decoupled. Each end looks like part of a dislocation superimposed on a uniformly stretched chain. Figure 4.4(a) plots $\delta b(n) = b(n) - \epsilon b_0$ for a chain with $\epsilon > 0$. The chain is indicated by the solid line and is centered at the origin with its ends at $\pm N/2$. Bonds far away from the chain ends stretch uniformly with the strain to remain commensurate with the periodic potential. This creates a background tension in the chain equal to $k\epsilon b_0$. However, the boundary condition requires that this tension decrease to zero at the chain ends so that they are stable. The chain accomplishes this by forming a partial dislocation at each chain end. In Figure 4.4(a), only part of these dislocations penetrate the finite chain, so we show the full dislocation profile with dashed lines that extend beyond the chain ends at $\pm N/2$.

Chains will slip if the partial dislocations can nucleate by fully penetrating the chain. The energy barrier E_a for nucleation can be measured by calculating the work

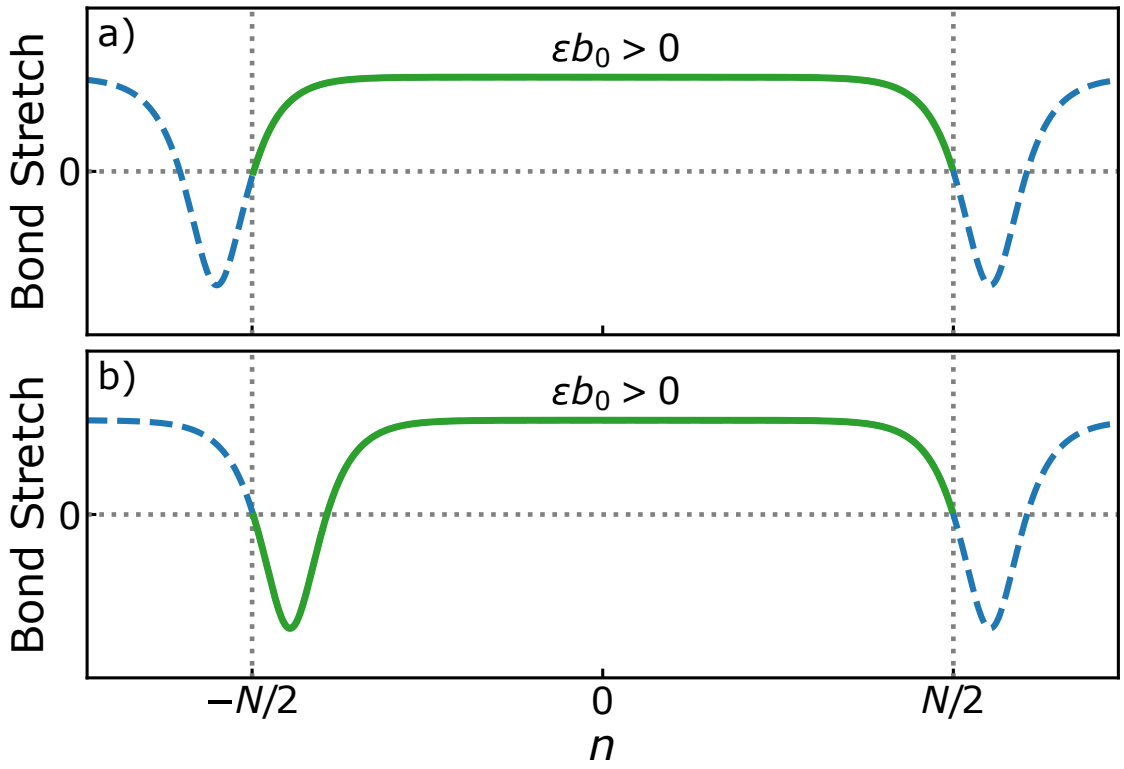

Figure 4.4: Bond stretch profiles $\delta b(n)$ for a finite FK chain of $N+1$ monomers centered at the origin. (a) A stable solution for a chain with $\epsilon > 0$. The bulk of the chain stretches affinely with the strain so $\delta b(n) = \epsilon b_0$. The stretch $\delta b \to 0$ near the ends as two dislocations partially penetrate the chain to satisfy the boundary condition (blue dashed lines). The barrier E_a is the work required to move the left dislocation from its stable configuration in (a) to its unstable configuration in (b).

needed to move a partial dislocation from the stable configuration shown in Figure 4.4(a) to the unstable equilibrium shown for the left dislocation in Figure 4.4(b). This configuration is unstable to the dislocation moving further into the chain. For $N \gg \xi$, the two ends slip independently and E_a can be calculated analytically as [14, 125]

$$E_a(\epsilon) = \frac{4}{\pi}\xi\tau a\left(\epsilon_* \cos^{-1}(\sqrt{1-\epsilon_*^2}) - \frac{\pi}{2}\epsilon_* + \sqrt{1-\epsilon_*^2}\right) \tag{4.8}$$

where $\epsilon_* = \epsilon_e/\epsilon_u$ and $\epsilon_u = 1/(\pi\xi)$. The barrier decreases with increasing ϵ because partial dislocations must penetrate further into the chain to maintain stability. E_a vanishes once ϵ increases to ϵ_u. This defines the strain where the background tension is equal to the maximum compression produced by the dislocation and is $\approx 1/(\pi\xi_0)$, where ξ_0 is the core size at $\epsilon = 0$. Chain ends cannot be stable at larger strains and will spontaneously nucleate dislocations to release tension until stability is reestablished.

Once nucleated, dislocations increase the system energy by an amount E_d which depends upon ϵ. Dislocations are energetically unfavorable in an unstrained crystal, but applying a tensile strain decreases E_d for compressional dislocations because they relax tension in the backbone. An expression for E_d can be calculated by substituting the dislocation solution Equation, 4.6, into the Hamiltonian and integrating. The energy of an isolated dislocation relative to the uniformly stretched state is given by [14]:

$$E_d(\epsilon) = \frac{4}{\pi}\xi\tau a\left(1 - \frac{\epsilon}{\epsilon_m}\right) \tag{4.9}$$

where $\epsilon_m = 2/(\pi^2\xi) \approx 2/(\pi^2\xi_0)$ implicitly defines the strain at which dislocations become energetically favorable at $T = 0K$. Once ϵ exceeds this value, the commen-

surate state is no longer the zero temperature ground state and the chain can lower its energy by nucleating a dislocation.

An important subtlety of Equations 4.8 and 4.9, is that ξ, τ depend upon a and implicitly upon the strain ϵ since $a = (1+\epsilon)b_0$. Relative to their equilibrium values: $\xi = \xi_0(1+\epsilon)^2$ and $\tau = \tau_0(1+\epsilon)^{-1}$. This dependence introduces additional terms that add small corrections to the energies predicted by Equations 4.8 and 4.9. These corrections are small and can be neglected provided the maximum supported strain $\epsilon_u \ll 1$. We know that $\epsilon_u \leq b_0/\pi\xi$, which we will find to be < 0.032. Thus, we can can greatly simplify our analysis by approximating ξ and τ with their equilibrium values ξ_0 and τ_0, and this will only contribute errors of a few percent. In the following section, we report values for ξ, τ, ϵ_m, and ϵ_u using this approximation.

In the unstressed state, the energy to nucleate an anti-dislocation is the same as that for a compressional dislocation. Nucleating a compressional/tensile pair in the middle of a chain would raise the energy by $2E_d(0)$ and the activation barrier would be even larger. To first order, this total energy for creation of a pair is independent of ϵ and the associated σ. Thus nucleation of a pair of dislocations would not follow the Eyring relation but instead give a stress independent of strain rate. We shall see that $2E_d(0) \sim 120\ k_bT$ so that this double defect nucleation is extremely unlikely in experimental conditions.

4.2.2 Creep Through Thermal Activation of Dislocations

To describe elongational creep we divide the macroscopic strain into elastic and plastic components: $\epsilon = \epsilon_e + \epsilon_p$. The elastic component will be given by the applied stress in the fiber creep experiment: $\epsilon_e = \sigma/Y$, where Y is Young's modulus. This elastic strain determines the change in bond lengths and enters the above equations for the energy barriers for forming dislocations. The plastic stress reflects relative slip of adjacent chains that allow extension of the fiber. The symmetry of the problem means that chains are equally likely to slide in either direction along the tensile axis. Those with center of masses above a chain end tend to move up relative to it, and those below tend to move down. The key idea is that once a dislocation is nucleated at a chain end, it can allow translation of the chain and thus enable plastic deformation.

Creep experiments on PE fibers have typically been performed at stresses below 1 GPa and thus at strains much less than 1% [2,104,115]. In this limit E_a and E_d are nearly the same. Using the Young's modulus to calculate the elastic strain yields:

$$E_a \approx E_d = \frac{4}{\pi}\xi\tau a\left(1 - \frac{\sigma}{\epsilon_m Y}\right) \tag{4.10}$$

Thus the barrier has the linear dependence on stress assumed in the Eyring model with $E_a^0 = \frac{4}{\pi}\tau\xi b_0$ and $V^* = \frac{4\tau\xi b_0}{\pi\epsilon_m Y}$.

One can estimate V^* using the fact that covalent bonds along the chain backbone are much stronger than the van der Waals bonds between molecules. In this limit

the elastic coupling between tensile and perpendicular directions is small and Y is approximately given by the modulus at constant cross-sectional area. The latter is simply related to the spring stiffness k and number of chains per unit area: $Y = knb_0/A$ where A is the area per unit cell perpendicular to the tensile axis and n the number of chains per unit cell. This happens to give a V^* equal to the volume of a monomer within the crystal, but this need not be the case for the Eyring theory.

The rate at which dislocations are nucleated and enter the chain scales as $\omega_0 \exp(-\frac{E_a}{k_b T})$ where ω_0 is an attempt frequency. Typically $\omega_0 \sim 1$ ps^{-1}, a typical vibration frequency of a monomer. Once a dislocation has nucleated, it can move quite freely along the chain. There is a periodic potential associated with the location of the dislocation with respect to the discrete atoms of the chain, called the Peierls barrier. However, this barrier is small for PE because $\xi \gg b$ and this is also why the continuum expressions for the energy given above are accurate. The barrier for leaving either end of the chain is small because $E_d \sim E_a$ for small strains.

In the ideal symmetric case of the FK model, the dislocation is equally likely to move in either direction. In a real fiber, the symmetry will be broken and energy will be lowered by motion of the dislocation to translate the chain relative to some or all of its neighbors. This will cause the dislocation to move along the chain rapidly. About half the time it will move back out the end where it nucleated, but the rest of the time it will move away from that end until it reaches another chain end or leaves the local crystalline domain. This translation will contribute to the plastic strain,

giving:

$$\dot{\epsilon}_p \propto \omega_0 \exp(-(E_a - V^*\sigma)/k_bT) \tag{4.11}$$

In principal the opposite process could also be activated, leading to a reduction in the plastic strain. In Eyring theory, stress has the opposite effect on this backward process and the rate rises as a hyperbolic sine of the stress (Eq. 4.1). In practice the backward process is only important near equilibrium, where the material is flowing like a Newtonian fluid. Experiments on PE fibers are typically in the limit where Eq. 4.11 and Eyring theory (4.1) are indistinguishable.

4.3 Molecular Dynamics Parameterization

Application of the FK model to specific polymers requires measuring values for b_0, k, and τ. Here, we follow our previous work and compute these parameters with small molecular dynamics simulations of perfect polymer crystals. FK parameterizations of PE are computed for four popular interatomic potentials for hydrocarbons: AIREBO-M, AIREBO, L-OPLS, and PCFF. AIREBO-M and AIREBO are reactive potentials for hydrocarbons and AIREBO-M has been shown to accurately reproduce the static and dynamic behaviour of crystalline PE [13, 112, 122]. L-OPLS and PCFF are popular all-atom potentials for modeling polymer melt mechanics and thermodynamics [123, 124]. As we will show, the high energy covalent interactions of the four potentials are relatively similar, but the low energy van der Waals interactions, which

are much harder to parameterize, produce large variability in the crystal structure. This leads to a significant variability in k and τ for different potentials. We compare the four FK parameterizations to experimental data to determine which models give the most accurate predictions and estimate uncertainties due to the choice of potential.

For all potentials, we simulate 5x8x12 unit cells of a perfect and periodic PE crystal with the **a**, **b**, and **c** lattice vectors aligned along the x, y, and z Cartesian axes, respectively. We use the LAMMPS software package [35] to numerically solve the equations of motion with a velocity-Verlet integrator and a 0.5 fs time-step. Crystals are equilibrated to $T = 300$ K or $T \approx 0$ K and $P = 1$ bar with a Nose-Hoover thermostat and barostat. The thermostat and barostat relaxation times are 0.25 ps and 1.0 ps respectively. We measure b_0 by taking the average monomer spacing along the chain backbone at $T = 300$K.

Chain stiffnesses k are calculated from uniaxial tension tests on crystals at $T = 300$ K. Crystals are loaded in tension along the fiber axis with a constant engineering strain rate $\dot{\epsilon} = 10^8\ s^{-1}$, while a Nose-Hoover barostat maintains a constant 1 atm pressure in the lateral directions. A Young's modulus Y is measured by linearly fitting the axial stress σ_{zz} as a function of strain for the first 1% of tensile strain. Values for Y are recorded in column 3 of Table 4.1. While values of Y are most commonly measured, the spring constant k of the FK model is most cleanly related to C_{zz}, the elastic modulus at constant cross-sectional area. In Ref. [24] we found the elastic

moduli for PE with the AIREBO-M potential. The value of $C_{zz} = 270$ GPa is only slightly larger than Y because the off diagonal terms from van der Waals interactions, C_{xz} and C_{yz} are only 4-5 GPa. We thus take

$$k = C_{zz}A/nb_0 \approx YA/nb_0 \tag{4.12}$$

with the understanding that this may introduce errors of order 3% that are smaller than variations between potentials.

We measure the amplitude of the intermolecular friction τ by translating one chain along the fiber axis and measuring the periodic force exerted on the chain by the surrounding crystal. Due to our small simulation sizes, collecting accurate statistics for the periodic potential at $T = 300$K can be challenging. The van der Waals energies between chains are of similar order to the thermal energy scale and this leads to significant fluctuations of the intermolecular forces about their average values. In order to make accurate measurements, we follow our previous work [13] and measure the periodic potential at $T \approx 0$K where thermal fluctuations are absent. In previous work, we found that both k and τ show only a weak temperature dependence for $T < 300$K, and using low temperature measurements of τ produced FK model predictions that agreed well with simulations at $T = 300$K.

The z-component of the translating chain's center of mass is coupled to the center of mass of the surrounding crystal by a stiff spring with a stiffness of 4.34 eV/Å^2. The equilibrium length of the spring is repeatedly increased to shift the axial registry of translating chain in 0.1 Å increments relative to the surrounding crystal. At each

increment, the average intermolecular force exerted on the chain is measured over 3 ps of simulation time which is much longer than the time required for the crystal to accommodate to the displacement.

4.3.1 FK Parameters for PE Models

Simulation measurements of FK parameters for the four PE models are given in the first four rows of Table 4.1. Values for b_0 are shown in column 2 of Table 4.1 and are 2.54 Å for all four potentials, which is consistent with WAXS experiments [111]. The four models show good agreement since b_0 is set by the length and angle of the C-C covalent bonds in the chain backbone, which is well understood chemistry. The backbone bond stiffness k is also dominated by covalent chemistry and values for the four models (column 5 of Table 4.1) show relatively good agreement, varying from from 8.7 to 12 eV/Å^2 for PCFF and AIREBO, respectively.

Values for the Young's modulus can also be compared to past experimental and theoretical predictions. WAXS measurements give values of 235 to 260 GPa [126–128] for crystalline regions and lattice dynamics theories give 257 GPa [129]. The latter value is very close to results from AIREBO and AIREBO-M. In contrast, L-OPLS and PCFF give moduli that are substantially below the experimental range.

The spring constant k depends on both Y and the monomeric volume $V_{mon} = Ab_0/2$. The 4th column in Table 4.1 shows that the models give a range of volumes from 45 to 50 Å^3. AIREBO-M was parameterized for crystal systems and gives a

Potential	b_0 (Å)	Y (GPa)	V_{mon} (Å^3)	k $(eV/$Å$^2)$	τ $(meV/$Å$)$	ξ/b_0
AIREBO-M	2.54	260	46.4	11.60	46.5	10.0
AIREBO	2.54	254	49.2	12.03	64.5	8.7
L-OPLS	2.54	211	45.4	9.23	92.7	6.3
PCFF	2.54	181	50.0	8.70	39.0	9.5
WAXS	2.54	235-260	47	10.6-11.75		
Latt. Dyn.	2.54	257	47	11.6		

Table 4.1: FK model parameters for crystalline PE from four MD potentials. The last two rows give data from WAXS experiments [126–128] and lattice dynamics models [129] for comparison.

volume only about 1% lower than experiments. AIREBO and PCFF give volumes that are too large and L-OPLS gives too small a volume. Note that a modified version of AIREBO that gives more accurate densisites has been developed, but is not part of the LAMMPS distribution [76].

The 5th column of Table 4.1 gives values for k for each model and experiment using Eq. 4.12. Once again, AIREBO-M is closest to experiment. AIREBO gives too large a value because of the low density and the other models give values that are too soft by more than 10%.

Periodic force traces for the four PE models are shown in Figure 4.5. The intermolecular force per monomer is plotted against the translating chain's registry relative to equilibrium for one complete lattice period. The four PE models produce

periodic potentials that are qualitatively similar to each other and to the sine potential of the FK model. All periodic potentials exhibit a small inflection at the unstable displacement $0.5a$. This corresponds to a small rotation of the chain backbone (10%) that allows hydrogen atoms on adjacent chains to reduce their overlap during translation. This feature is due to the internal geometry of the monomer, which does not appear to manifest until after the peak force is achieved. The value of the peak force and changes near the peak play the most important role in FK theory, and the non-sinusoidal form in the unstable region near $0.5a$ has little affect on the activation energies.

All four curves show an increasing restoring force for small shifts in registry that reaches a maximum amplitude τ at about $\pm b_0/4$. However, the values of τ vary significantly for the four models. PCFF and AIREBO-M have similar values of $\tau = 39$ and 46.5 meV/Å respectively, whereas L-OPLS and AIREBO give values that are more than 50% larger. This variability is typical of different atomistic potentials since measurements of vdW forces with either experiments or with ab initio methods are both subject to larger uncertainties [130].

The specific functional form used for vdW interactions may also contribute to the variability in τ. L-OPLS and AIREBO give the largest values of τ and both model vdW forces with a Lennard-Jones potential while PCFF and AIREBO-M both use a softer exponential repulsion and give similar values for τ [11, 123]. As mentioned previously, the LJ potential is known to overestimate the intermolecular interactions

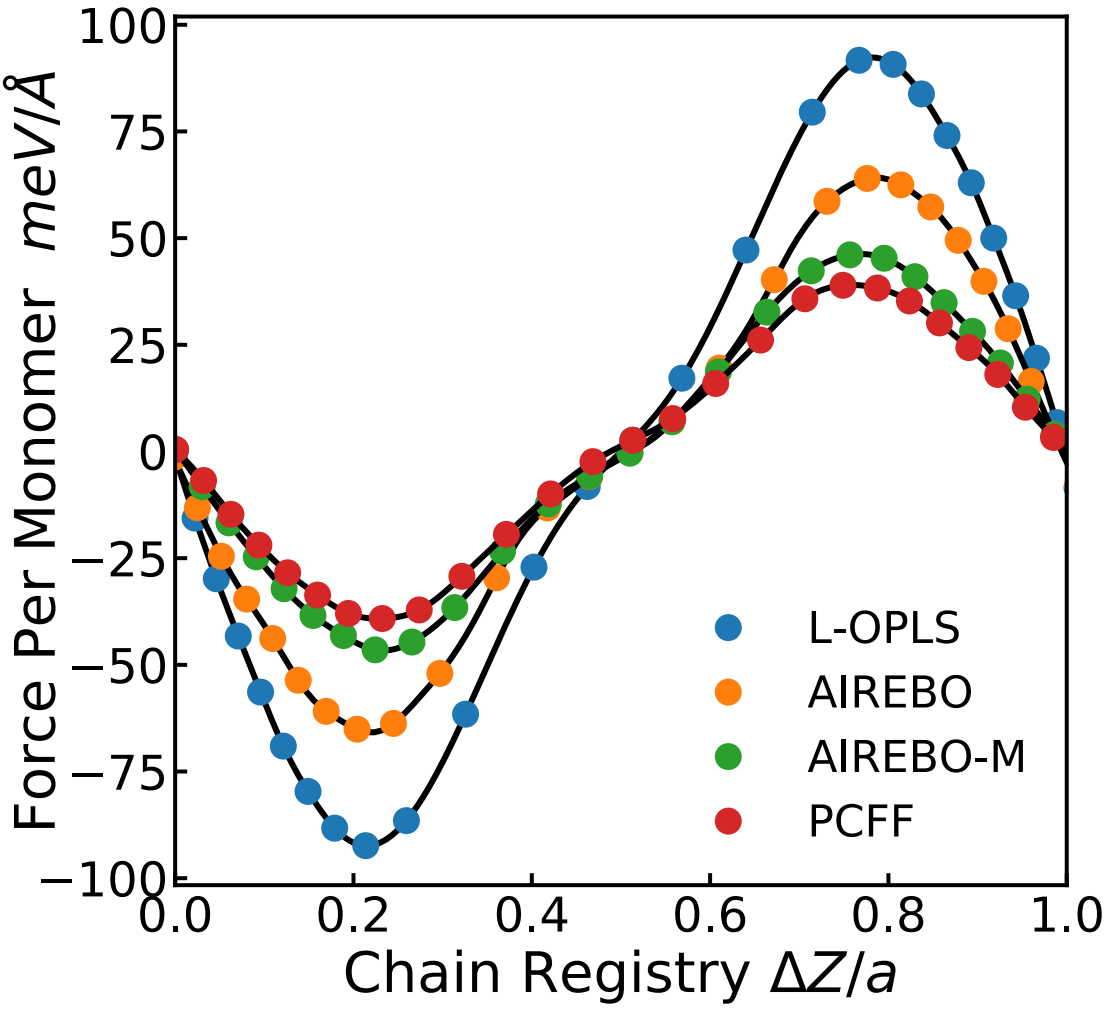

Figure 4.5: Periodic crystal force for a chain translated along the chain axis in a perfect PE crystal at $T \approx 0$. Forces are computed by translating a single chain while holding the centers of mass of all other chains fixed. MD results for four common polyethylene potentials are shown. Both L-OPLS and AIREBO model intermolecular interactions with a stiff Lennard-Jones potential and give the largest intermolecular forces. AIREBO-M and PCFF use softer intermolecular repulsion and produce similar results. All give potentials qualitatively consistent with the sine potential of the FK model.

between chains in PE crystals and thus may overpredict the value of τ [9, 122]. By again comparing AIREBO and AIREBO-M, which only differ in the functional form of the vdW potential, we see AIREBO gives $\tau = 64.5$ meV/Å which is 40% larger than the 46.5 meV/Å of AIREBO-M. Thus, the larger values of τ given by AIREBO and L-OPLS may be from overestimating steric repulsion from the LJ potential. We expect PCFF and AIREBO-M provide more accurate measures for τ than AIREBO and L-OPLS. Note however that PCFF gives too a value for k.

The measured values for b_0, k, and τ completely parameterize the FK model for each of the four potentials. Calculated predictions for the core size ξ are given in column 7 of Table 4.1. AIREBO-M and PCFF have similar dislocation core sizes $\xi \approx 10$. Even though k and τ are smaller for PCFF than for AIREBO-M, the core size and critical strains are sensitive to the ratio kb_0/τ which is similar for the two models. Due to their much larger interchain friction, AIREBO and L-OPLS give smaller core sizes equal to 8.7 and 6.3 monomers, respectively.

4.4 Comparing Model Predictions to Experiments

4.4.1 Predictions for Fiber Failure

When comparing to experiments, it is important to remember that our model considers an ideal and perfectly crystalline fiber which cannot be achieved in the laboratory. Real fibers have additional plastic relaxation processes associated with disorder and other types of defects. These mechanisms can produce additional creep that our model does not account for. We have also assumed that slip events are independent of each other, while the plasticity of real fibers may be correlated. For instance, when a chain slips it transfers the tensile load it was carrying to neighboring chains, which may increase their tendency to slip. In addition, disorder in real fibers leads to variations in the local stress that activates creep, reducing the effective activation energy. Thus, we expect our theoretical predictions to set an upper bound on fiber strength and a lower bound on creep observed in experiments.

The FK theory predicts $\epsilon_u \approx b_0/(\pi\xi_0)$ is the maximum strain a crystal can support before yielding. Above this strain, the crystal is unstable and chains can spontaneously slip at their chain ends. This sets an upper bound on the high-rate/low-temperature strength of a PE fiber. Assumming the Young's moduli do not change

FK Models	ϵ_u	σ_u (GPa)	E_a^0 (eV)	V^* (Å^3)
AIREBO-M	0.032	8.2	1.4	46
AIREBO	0.037	9.3	1.6	49
L-OPLS	0.050	10.6	1.9	45
PCFF	0.033	6.1	1.2	50
Exp.	0.03-0.034	6-7.5	1.1-1.7	10-100

Table 4.2: FK model predictions of the ultimate tensile strength and creep behavior of crystalline PE. FK predictions for all four potentials are shown. Experimental ranges for ϵ_u [109, 110], σ_u [86, 110, 113, 114], E_a^0 [92, 104, 107–110], and V^* [92, 104] are also provided.

much over this strain interval, the maximum load a fiber can sustain is

$$\sigma_u = \frac{Yb_0}{\pi\xi_0} \tag{4.13}$$

Predicted ϵ_u and σ_u for the four FK models are recorded in column 2 of Table 4.2. Literature values for ϵ_u [109, 110] and σ_u [86, 113, 114] are also provided.

The four models predict ultimate strengths ranging from 6.02 GPa for PCFF to 10.60 GPa for L-OPLS with an average value $\sigma_u = 8.5$ GPa. Note that all values are much lower than the failure stress of 20-40 GPa that is predicted to be necessary for C-C scission [87, 88]. The highest published strengths are between 6-7 GPa and tend to be found for fibers with the highest crystal concentration. This is consistent with the average value of σ_u from the four models. Only the PCFF model gives σ_u in the experimental range, suggesting that it underpredicts τ and k.

FK model predictions for the maximum strain ϵ_u also agree well with recent exper-

imental analyses by Jenket and by Wang et al. [109, 110]. Jenket studied the tensile failure of hundreds of UHMWPE fibers while systematically varying temperature and strain rate. For all rates, he observed a limiting strain at failure of $\epsilon \approx 0.03$ as fiber temperatures were decreased [109]. Through extrapolation of their own data, Wang and Smith predicted a maximum strain at failure of 0.034 for a perfectly crystalline fiber [109]. The value of ϵ_u from L-OPLS is about 50% higher than this value, but all other models give values with 10% of this extrapolated value.

Note that the strength of a fiber can exceed σ_u if chain ends are removed from the fiber interior. This may be impractical for conventional processing of high performance fibers, but it was recently demonstrated at the nanoscale by Shrestha et al. [131]. They used thermal annealing to create a highly ordered, nanoscale PE filament that is much smaller in length and diameter than the extended length of the chains. This nanofiber is expected to contain few chain ends, and Srestha et al. report failure strengths approaching 12 GPa, which are the largest ever reported for PE fibers.

4.4.2 Predictions for Fiber Creep

Figure 4.6 plots $E_a(\epsilon_e)$ (solid line) using Equation 4.8 and the FK parameters for AIREBO-M. The shaded regions indicate strains where the ground state is metastable (blue) and unstable (gray) to chain slip. Creep typically occurs at stresses much lower than σ_u. The largest loads applied in the creep experiments by Ward et al. were only

about 0.5 GPa [104, 105], corresponding to $\epsilon_e \sim .001$. Creep at these loads should be controlled by the small strain behavior of $E_a(\epsilon_e)$ given in Equation 4.8. In this regime, dislocations should remain dilute. In addition, the activation barrier is nearly linear in the elastic strain and thus can be modeled by the stress activated Eyring parameters of Equation 4.10. Note that high rate experiments see failure at *total* strains that may be outside this linear regime ($\epsilon > 0.02$) [132].

In Figure 4.7 we directly compare model predictions for the stress dependence of E_a to experimental data. We plot Equation 4.10 using values for E_a^0 and V^* averaged over all four models (solid line). The blue region gives a rough measure of the uncertainty in E_a^0 derived from the standard deviation of the four models. Experimental data of Jenket [109], Govaert [107] and Regel [106] are shown as points. For Jenket and Govaert, only an activation energy at 0 load is given. Broken lines show Eyring fits to experimental data as reported by Ward and Wilding (dashes) [104] and Dijkstra (dash-dots) [92]. Ward and Wilding fit many fiber types by first finding an optimal $E_a^0 \approx 1.3$ eV and then varying V^* for each fiber. The span of their fits is indicated by the gray shaded region. Except for the data of Dijkstra et al. [92], the average model prediction sits above experimental values for all tested loads. We expect this to be the case since our perfect fibers at zero temperature should set an upper bound on E_a^0 for creep in actual fibers. Indeed, even in crystals there are variations in the distance between chain ends and other defects that will produce lower barriers for some chain ends, and fibers have non-uniform local stresses that

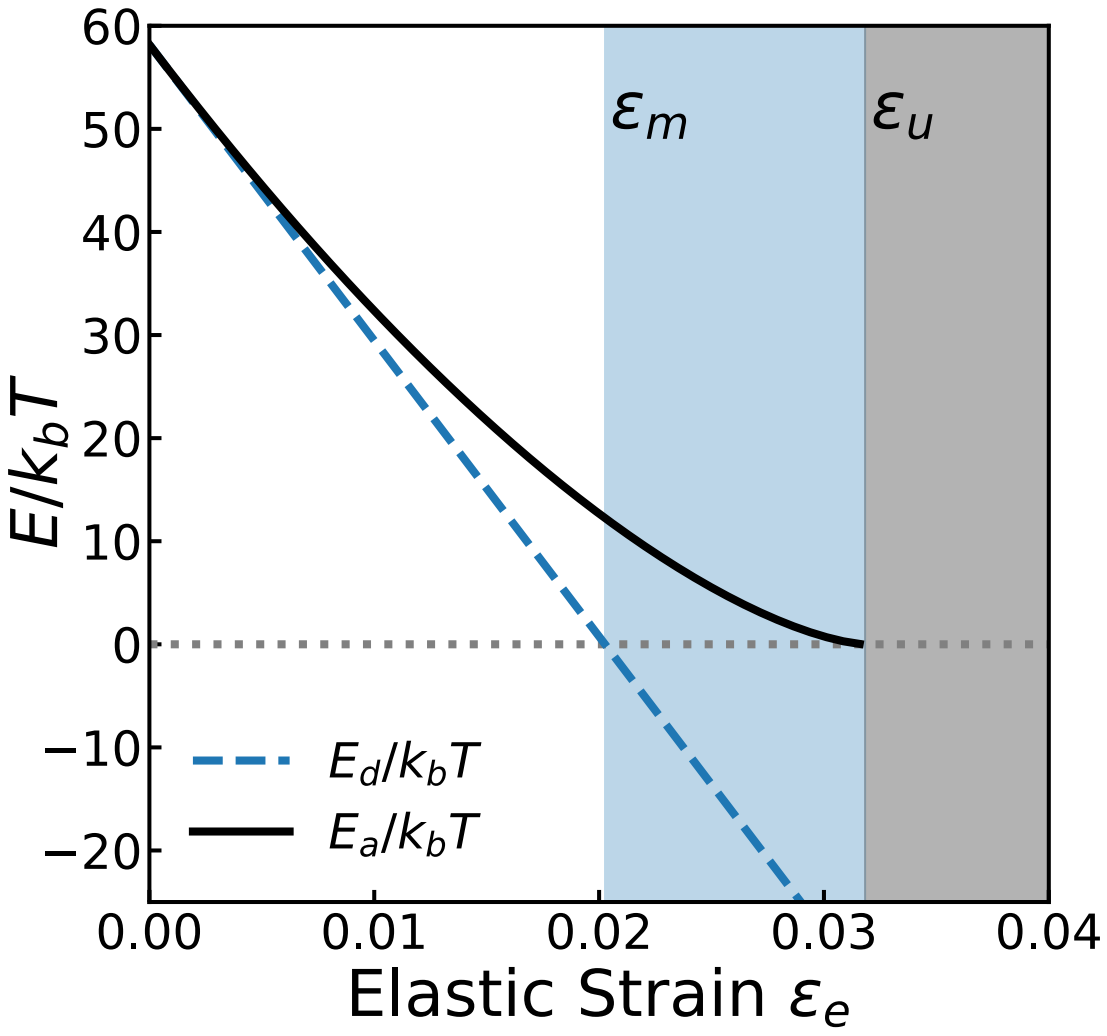

Figure 4.6: Formation energy E_d and activation energy barrier E_a for a dislocation nucleated from a chain end as a function of the local elastic strain $\epsilon_e = (a - b_0)/b_0$. Energies are reduced by the thermal energy $k_bT = 25.852$ meV at $T = 300K$. Curves shown are for the FK parameters of AIREBO-M. Two critical strains ϵ_m and ϵ_u correspond to E_d and $E_a \to 0$, respectively. For $\epsilon_m < \epsilon_e < \epsilon_u$ (blue region), the commensurate ground state is meta-stable to dislocation nucleation. When $\epsilon_e > \epsilon_u$, $E_a = 0$, and dislocations form spontaneously.

will facilitate local nucleation [13].

Experimental values for E_a^0 range from 1.1–1.7 eV. This is about double the value reported for the twiston formation energy ~ 0.6 eV [100] and less than half the binding energy of C-C bonds ~ 4 eV. FK model predictions for E_a^0 are recorded in column 4 of Table II. Models give values ranging from 1.2–1.9 eV with an average ≈ 1.5 eV. Model predictions are consistent with the experimental range 1.1–1.7 eV and are intermediate between the energies associated with twistons and chain scission. AIREBO-M gives $E_a^0 = 1.4$ eV $\approx 60\ k_bT$ which is closest to the average for both models and experiments.

Model predictions for V^* are also consistent with the range of experimental values. The four FK models give similar values for V^* between 45–50 Å^3 that are recorded in column 5 of Table II. As discussed previously, FK theory predicts V^* for chain slip is equal to the monomer volume within the crystal, which X-ray scattering experiments find to be about 45 Å^3 [111]. Few experiments have measured V^* during creep but available data suggest it lies between $10--100$ Å^3 [104,106]. While the experimental variation in V^* is high, the range is compatible with the FK model values for chain slip.

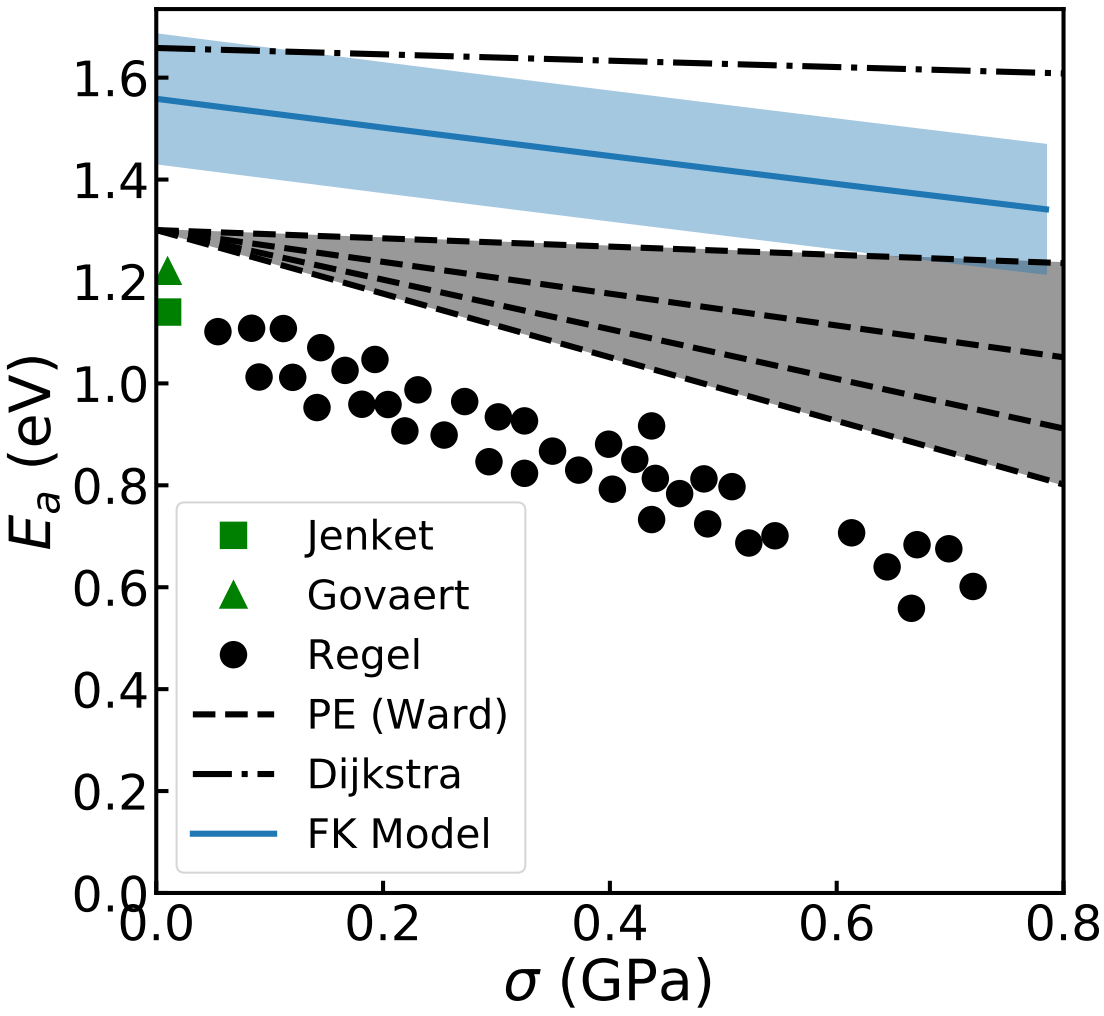

Figure 4.7: Comparison of E_a vs load predicted by FK theory (solid line) and measured by creep experiments of Regel et al (circles) [106] and Wilding et al. (dashed lines) [104, 105]. The blue shaded region indicates the standard error of the four molecular potentials. The FK theory gives $E_a \approx 1.5$ eV and $V_0 \approx 47$ Å^3 for an ideal fiber, which should set an upper bound on creep in experimental fibers.

4.5 Conclusions

We have developed a simple analytic model of thermally activated chain slip to predict the steady creep behavior of PE fibers. Our theory is informed by prior work where MD simulations identified chain slip as the strength limiting failure mechanism of PE fibers. Chain slip is mediated by the nucleation of 1D dislocations at chain ends which can be modeled with a simple Frenkel-Konotrova model. The FK model has three independent parameters that are parameterized by MD simulations of perfect PE crystals.

We parameterized FK models for four popular atomic potentials: L-OPLS, PCFF, AIREBO, and AIREBO-M. Of the four, AIREBO-M best represented the average response and produced an equilibrium crystal structure and elastic moduli in best agreement with available literature [24, 55, 126–128]. Averaged over the four models, the FK theory predicts an average activation barrier $E_a^0 \approx 1.5$ eV and activation volume $V^* \approx 47$ Å^3 for chain slip in a perfect crystal. These effective Eyring parameters should set an upper bound on the energy barrier for creep in real fibers. Additional defects and disorder within a real fiber should tend to decrease E_a^0 and increase V^*. The effective Eyring model for chain slip gives a stress-dependent activation barrier $E_a(\sigma)$ that remains above all considered experimental data except Dijkstra et al. [92]. The average E_a^0 from FK theory lies above all considered experimental data except for that of Dijkstra et al. [92].

The FK theory for chain slip is relatively simple, but it produces an activation

energy barrier that is consistent with steady creep experiments and is unambiguously distinct from the barriers for twiston formation or C-C bond scission [100]. The chain slip mechanism also sets upper bounds on the ultimate strain and strength of fibers that is consistent with experiments [86, 109, 113, 114]. We believe these results make a strong case for 1D dislocations being the microscopic mechanism mediating steady creep within PE crystals. At present, we know of no other microscopic model that gives comparable predictions for fiber creep.

Our theory only considers the nucleation of dislocations at chain ends in an otherwise undefected fiber. Real fibers contain amorphous domains and crystal-amorphous interfaces. These disordered interfaces may serve as additional locations for chain slip to occur and could lead to lower experimental values of E_a and V^*. Thus, our Eyring parameters should be seen as setting an upper bound on thermally activated creep in PE fibers.

Even as an upper bound, the E_a^0 predicted for chain slip is significantly lower than the 4 eV binding energy needed for C-C bond scission. This suggests chain slip will be active and dominate crystal creep well before chain scission. While we do not expect chain scission to control the creep rate, EPR experiments have shown that scission does occur during tensile loading. In order to be consistent with our predictions, these chains should not be breaking within the bulk crystal phase. Instead, we expect chain scission to be occuring primarily on "tie-chains" bridging separate crystallites within the fiber, which may be highly stretched due the low stiffness amorphous regions.

Recent AFM experiments characterized the internal structure of high performance PE fibers and observed numerous tie-chains between adjacent crystal domains [81]. These can be pulled taut and break as adjacent crystallites shear past each-other during deformation [133, 134].

Chapter 5

Anisotropic Shock Propagation in PE

5.1 Introduction

In the last forty years, we have seen great advances in our ability to draw and align long, linear polymers like polyethylene (PE) into highly oriented fibers and films. These highly anisotropic materials have stiffnesses comparable to steel but are much cheaper to process and incorporate into cables, fabrics, and composites [3,80,128,135]. Drawn polymer materials are found in a growing number of mechanically demanding applications — ship sails, vehicular chassis, prosthetic joints, and body armors — which often fail when mechanical shock waves are generated by sudden impacts. Improving applications requires a better understanding of how shocks propagate through

aligned PE and how mechanical energy is dissipated by plastic mechanisms.

While the phenomenology of shock propagation in hydrostatic fluids and isotropic solids is well-developed, these theories are not easily adapted to highly anisotropic solids like polymer crystals, where direction-dependent mechanics and plastic yield are important. The heterogeneous structure of drawn PE makes experimental measurements of shock propagation in specific phases challenging. Micromechanical models often aid interpretation of experiments but they require accurate constitutive laws for PE's crystalline and amorphous phases [3, 18]. Given the analytic challenges, few constitutive laws have been developed, and the most widely used theory for shock in crystalline and amorphous PE, derived by D. J. Pastine nearly 50 years ago, only considers hydrostatic loading (no shear stress) [21, 22]. Such hydrostatic laws neglect the shear strength of materials. They work well for high velocity impact when shock stresses exceed the yield stress and plastically "fluidize" material, but they ignore the detailed effects of anisotropy, material strength, and plasticity [19].

Molecular dynamics (MD) simulations have proven a useful tool for studying the effect of material strength on shock [8, 136–146], but few MD potentials accurately describe PE at the large pressures produced in shocks. The AIREBO-M reactive potential for hydrocarbons described in Chapter 2 was developed to meet these challenges [10]. It produces PE crystal structures that agree with X-ray measurements up to $\sim$ 40 GPa and gives an equation of state that is consistent with Pastine's hydrostatic theory for shock of crystalline PE [10].

In this chapter, AIREBO-M is used in dynamic impact simulations to generate and characterize shock wave propagation in amorphous PE and crystalline PE along its 3 principal axes. The complexity of the response is illustrated by the plot of shock velocity U_s against impact velocity U_p in Fig. 5.1. The results for strong shocks are consistent with Pastine's hydrostatic calculations. Shocks travel faster through the crystal because of its higher density and ordered structure. As the impact velocity decreases, the yield stress becomes important, leading to deviations from Pastine's curve and strong anisotropy in the crystal response. We identify the Hugoniot elastic limit in each direction – the maximum shock pressure that produces completely recoverable deformation. We then follow molecular trajectories to characterize the direction-dependent modes of plasticity above the elastic limit and the approach to hydrostatic behavior. Shock along the chain backbone direction [001] produces an elastic front followed by a plastic shock front that buckles chains. Shock along the perpendicular axes leads to plastic deformation at low impact velocities and phase transitions to different crystal structures at higher U_p. For shock along the b-axis [010], the phase transition suppresses plastic deformation, leading to separate transition and plastic shock fronts at intermediate U_p.

In the next section, we briefly review the formalism of solid shock and previous efforts to model shock in PE. Section 5.3 details our simulation and analysis methods, and Section 5.4 contains detailed analysis for impacts in each phase and crystal orientation. We highlight our results and comment on their implications in Sec. 5.5.

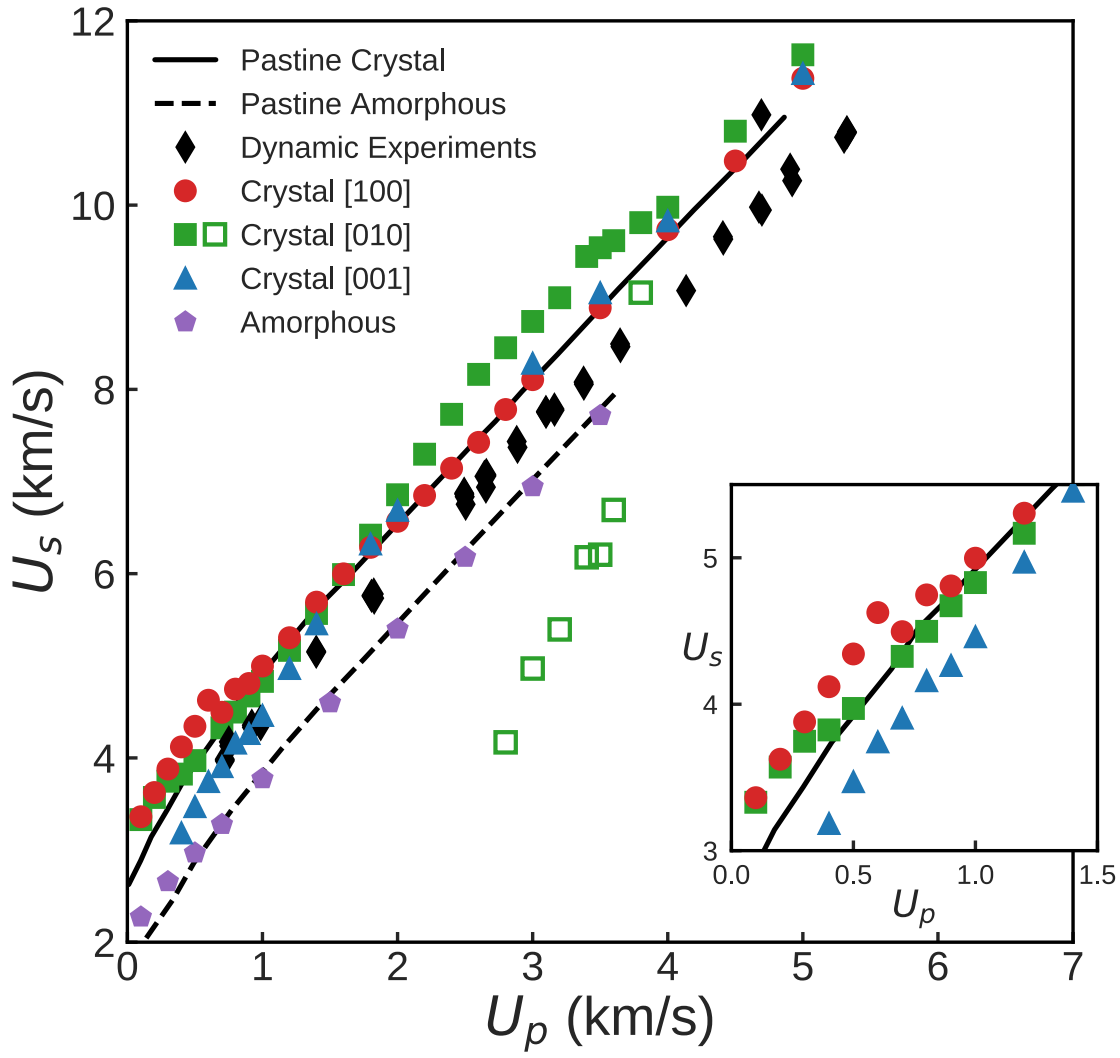

Figure 5.1: Shock velocity U_s versus impact velocity U_p in different polyethylene phases. Experimental data (black diamonds) for semicrystalline PE was used by Carter and Marsh to validate Pastine's hydrostatic models for pure crystal (black solid line) and pure amorphous (black dashed line) PE [18, 21, 22]. Colored symbols (legend) show our dynamic simulation results for amorphous PE and crystalline PE shocked along the three principle lattice directions. For strong shock, plasticity relaxes the shear stress and our simulations follow Pastine's hydrostatic models. For weak shocks (inset) simulations show deviations from hydrostatic models due to material strength. A pair of shock fronts are observed in the [010] direction at intermediate velocities. They merge into a single front when $U_p \geq 4.0$ km/s. A phase transition occurs at the first front (filled symbols) and plastic yield at the second (open symbols).

5.2 Theory and Modeling of Shock in PE

We consider the simple case of one-dimensional loading where a rigid body moving at impact speed U_p along the z direction contacts a stationary sample along a planar interface normal to the z direction (Fig. 5.3). Impact generates a planar shock front traveling into the sample at speed U_s along the z-axis. The shock front separates regions near the impactor moving at mean particle velocity U_p from quiescent regions with mean velocity zero. In the more general case of a non-rigid impactor, deformation of the impactor leads to reduced momentum transfer and the material is accelerated to a particle velocity U_p that is lower than the initial velocity of the impactor. The specific U_p depends upon the relative shock impedances of the impactor and sample [16, 17].

As the shock front propagates into the sample, conservation of hydrodynamic variables, mass, momentum and energy, imposes three "jump conditions" on the change in mass density ρ, internal energy density e and normal stress σ_{zz} across the shock front. These Rankine-Hugoniot conditions can be written as:

$$\rho_1 U_s = \rho_2 (U_s - U_p) \tag{5.1}$$

$$\rho_1 U_s U_p = \sigma_{2,zz} - \sigma_{1,zz} \tag{5.2}$$

$$\sigma_{2,zz} U_p = U_s \left(\frac{1}{2} \rho_1 U_p^2 + e_2 - e_1 \right) \tag{5.3}$$

where subscripts 1 and 2 denote values in the initial and final states, respectively.

More information is needed to determine the final state and U_s for a given impact

velocity. It is common to assume that the system rapidly approaches a local equilibrium state behind the shock front. Then the equation of state (EOS) of the material can be used to relate ρ, e and the stress. Pastine's curves in Fig. 5.1 assume that the stress tensor is isotropic so $\sigma_{2,zz}$ equals the hydrostatic pressure P. This condition is valid for fluids, and becomes valid for solids when σ_{zz} is much larger than the yield stress. For weaker shocks the full constitutive law must be used and the response may become anisotropic.

For shock studies of solids, the stress state is often characterized by the longitudinal shock stress amplitude $\sigma \equiv \sigma_{2,zz}$ and characteristic shear stress: $\tau \equiv \sigma_{2,zz} - \frac{1}{2}\left(\sigma_{2,xx} + \sigma_{2,yy}\right)$ [145, 147]. A state with shear stress $\tau = 0$ corresponds to the case of purely hydrostatic loading considered by Pastine. In the limit of linear elasticity, shocks are acoustic pulses traveling at the adiabatic sound speed c_s and τ/σ is determined by the Poisson ratio. In anisotropic elastic solids, both c_s and τ depend on the direction of impact, producing coupling between longitudinal and transverse waves that can permit complex, mixed-mode elastic fronts [148].

Sufficiently strong impacts activate plasticity and yield in solids. The smallest shock stress that activates plastic yield, σ_{HEL}, is called the Hugoniot elastic limit (HEL) — a critical parameter for applications [16, 17]. Yield causes a qualitative change in material response, which can result in a two wave elastic-plastic front structure, with each wave traveling at a different velocity [16, 17]. The elastic front elevates σ to σ_{HEL}. The plastic front follows, mediated by activation of plastic mech-

anisms [16, 17]. Increasing U_p increases the speed of the plastic front which may eventually overtake the elastic front [16, 17]. Shocks with only a plastic front are called "over-driven" [16, 17]. Multi-front structures can also form when shocks drive solid–solid phase transitions. In such cases, elastic, phase transition, and plastic fronts can all propagate simultaneously [17, 149].

In many cases, shock-induced plasticity above σ_{HEL} leads to a fairly constant shear stress, while σ continues to rise with U_p. As the shock strength increases, τ/σ becomes much less than unity, implying that the material flows like a fluid to reach a hydrostatic stress state as assumed by Pastine. In this regime one often finds a linear relationship between U_s and U_p. More relevant to many applications are weak shocks near the HEL where $\tau/\sigma \sim 1$. In this limit, shock propagation is non-trivially coupled to the kinematics of specific plastic mechanisms [136, 137].

The combined nonlinearities of shock and plasticity make weak shocks difficult to study analytically. Materials like crystalline PE are especially challenging, since the large mechanical anisotropy produces anisotropic plasticity as well as elastic instabilities at long length-scales [150]. Consequently, analytic models have focused on the hydrostatic limit of strong shock. The most successful hydrostatic theory is the semi-empirical derivation of Pastine. Pastine derived quasistatic and shock Hugoniot equations of state for crystalline and amorphous phases of PE [21, 22]. Carter and Marsh later showed that mixing Pastine's models for different phases quantitatively reproduces experimental shock Hugoniot data for semicrystalline PE [18]. Semicrys-

talline PE is well described by hydrostatic theory since the soft amorphous phase yields isotropically for $\tau > 100$ MPa [151], leading to effective hydrostatic loading for shocks with $U_p \geq 0.75$ km/s.

With the expanding applications of drawn PE, there is renewed interest in extending models to weak shocks. Progress requires anisotropic characterization of the crystalline and amorphous phases, but this is very difficult to accomplish experimentally. Instead, many have turned to molecular simulation, which has proven an effective method for studying weak shock and plasticity in many materials [8,136–146]. Several MD studies have investigated shock propagation in semicrystalline and amorphous PE [23, 146], and amorphous composites [145] of PE using coarse-grained or united-atom potentials. Such studies give useful insight into molecular mechanisms of shock deformation, but do not provide quantitatively accurate equations of state and specific heats. For example, existing coarse-grained potentials give the wrong equilibrium crystal structure of PE and thus would not reproduce the plastic deformation mechanisms discussed below. The need for accurate atomistic potentials is well illustrated by the recent work of Mattsson *et al.* [9]. They measured the hydrostatic ($\tau = 0$) shock Hugoniot of crystalline PE with quasistatic methods that do not explicitly model dynamic impact. Comparing Hugoniots for a variety of atomistic potentials, they found most over-predict the material stiffness at pressures above 1 GPa. While some coarse-grained models may capture the material stiffness, they typically underestimate e and the specific heat because they do not include energy

flow into internal vibrations, although some advanced constant-energy variants can capture these effects [152].

The need for quantitatively accurate potentials motivated our development of the AIREBO-M reactive potential for hydrocarbons [10]. AIREBO-M's intermolecular interactions are fit to post-Hartree-Fock quantum calculations for the interactions of small alkane dimers. With only this training set, AIREBO-M reproduces the anisotropic deformation of crystalline PE seen in diamond anvil experiments, as well as Pastine's hydrostatic theory up to 40 GPa [10]. This means AIREBO-M accurately models the strong shock regime seen in experiments. In this paper we use AIREBO-M to explore weak shocks in purely crystalline and amorphous phases of PE.

5.3 Methods

5.3.1 Atomic Potential and Integration

We model polyethylene with the AIREBO-M potential using the LAMMPS software package [10, 35]. In the standard LAMMPS distribution, covalent interactions are modeled by the second generation REBO (REBO2) of Brenner *et al.* [51], which is known to over-predict the tensile forces for covalent bond-breaking [5]. This can be seen in Figure 5.2, which compares various MD model predictions for the dissociation energy and force for breaking the C-C bond in ethane to quantum chemistry calculations. Classical force fields like AIREBO, REBO2, and REAXFF [50] all show

anomalously large dissociation forces relative to quantum calculations. Their binding energy is correct but the interaction range is too short by about 2 Å, so the C-C dissociation forces are too large. Pastewka *et al.* have created a bond-screening modified REBO2 (REBO2scr), which removes these anomalous forces during C-C dissociation [5]. The REBO2scr covalent energies were used during calibration of AIREOB-M [10] and to model tensile failure of PE [13].

We use AIREBO-M with the REBO2scr covalent terms for all tensile loading simulations because bond-breaking occurs. For compressive shock, no bond-breaking was observed, so we use the faster unscreened potential. We verified that for the highest impact velocity studied, 5 km/s, screened and unscreened potentials gave consistent results and that backbone C-C bonds remained in the range of separations where the two potentials are the same. The maximum temperature rises rapidly with impact velocity and was as high as 2000K for 5 km/s. However, this is only 10% of the binding energy and not enough to rupture bonds during our simulations. PE normally becomes unstable at much lower temperatures and longer time scales when exposed to oxygen and other reactive molecules.

Initial equilibrations integrate the equations of motion using velocity-Verlet with a 1 fs time step. They are performed in an NPT ensemble using a Nose-Hoover thermostat and barostat with time constants of 0.25 and 2.0 ps, respectively. Dynamic shock simulations use a much lower 0.1 fs time step and are performed within an NVE ensemble, modeling adiabatic shock conditions. We monitored the energy throughout

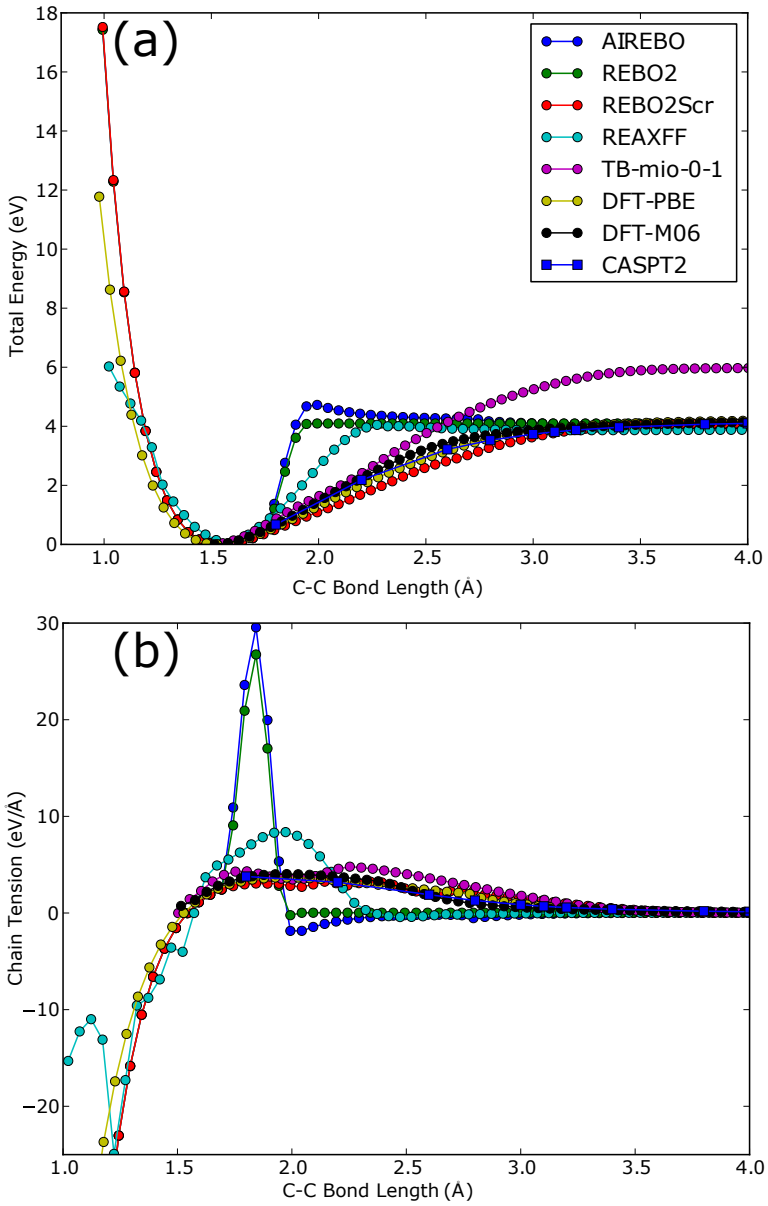

Figure 5.2: Dissociation energy (a) and force (b) for the C-C bond of ethane for various models. Classical AIREBO [11], REBO2 [51], REBO2scr [5], and REAXFF [50] potentials are compared to quantum chemistry calculations using tight-binding with the mio-0-1 basis set [153], DFT with the PBE [154] and M06 [155] basis sets, and CASPT2 [156, 157], which is a pertubative post-Hartree-Fock method and the most accurate. The MD potentials have correct binding energies but AIREBO, REBO2, and REAXFF all show anomalously large dissocation forces due to interaction cut-offs near 2Å. REBO2scr's neighbor screening removes these artifacts and best matches the quantum calculations.

simulations to ensure that energy was conserved.

5.3.2 Initial Configurations and Equilibration

One amorphous and four crystalline samples were generated for dynamic impact simulations. All configurations have periodic boundary conditions in all three directions. The two box dimensions transverse to shock propagation are of approximately equal length, ranging between 5 and 17 nm. To test for finite size effects, we performed several additional simulations for crystalline configurations with double the transverse box lengths. These simulations showed no observable difference in shock speed and mechanism of plastic deformation. The box dimension along the direction of shock must vary with the system in order to allow sufficient propagation time for accurate measurement of shock speeds. Shocks in amorphous PE and along the transverse [100] and [010] directions of the crystal require a propagation length of about 150 nm. Shock along the much stiffer crystal chain axis [001] required a substantially longer propagation length $\sim$ 300 nm, due to the fast-moving elastic precursor front (Sec. 5.4.4). In order to measure the steady-state amplitude of the [001] elastic precursor, we had to generate an additional system about 1μm long. In all cases, we align the shock axis with the z axis of the simulation box.

Amorphous configurations are prepared with the recently published method of Sliozberg *et al.* [158]. This melt equilibration method is a variant of the "fast push-off method" of Auhl *et al.* [159], and is fully described in Ref. [158]. M = 1500

chains of length N = 1000 are modeled by the united-atom potential of Paul *et al.* [160] and equilibrated at T = 300 K. After the united atom system is equilibrated, we reintroduce hydrogens along the chain backbones and perform a short energy minimization with AIREBO-M interactions to relax their positions. This is done with the FIRE minimizer and a timestep of 15 fs. We then allow the system box to relax over 2 ns of NPT equilibration with a target P=1 atm. This was sufficient time for the system density to equilibrate to a value of ~ 825 kg/m^3.

Orthorhombic crystal configurations are made by copying the orthorhombic PE unit cell, which contains an ethylene from each of two chains, to make a supercell of the desired geometry. At 300 K and ambient pressure, AIREBO-M gives an orthorhombic unit cell with lattice vectors (a,b,c) $\approx$ (7.35,4.94,2.54) Å, which we align with the Cartesian axes of the simulation box. All chains are periodic, each connecting to itself across the periodic boundaries. This arrangement models chains with lengths much longer than our simulation box dimensions, which would be typical for experimental molecular weights. Before shocking, we equilibrate crystals to T=300 K and P = 1 atm for 100 ps in an NPT ensemble.

5.3.3 Shock Generation

Following the approach in recent studies [23, 145–147], we generate shocks by rigidly constraining a slab of molecules to impact the material as an effective rigid piston, see Fig. 5.3. After equilibration, the periodic boundary conditions along the

shock direction are removed and atoms within 2.5 nm of the resulting boundaries are constrained to act as rigid slabs (dark gray in Fig. 5.3). For compressive shocks, the right slab is held fixed, while the left is constrained to move at a constant impact velocity $U_p = 100 - 5000$ m/s along the z-axis (Fig. 5.3a). The mobile slab acts as a rigid piston, compressing quiescent material (green) and imposing a jump in particle velocity to U_p (red material). This generates a shock front (red/green boundary) that propagates into the sample at a speed U_s. Data is collected until the shock front reaches the fixed rigid slab and is reflected.

While impacts initially compress material, coincident tensile deformation is often an important failure mechanism for oriented PE materials. To model tensile loading, the left slab is displaced leftward along z (Fig. 5.3b). The systems were large enough for us to determine that neither amorphous nor crystalline PE produce steady shocks in tension (see sec. 5.4).

Another common technique for generating shocks is to impact a finite sample with free boundaries upon a rigid wall that interacts with the material via power-law or idealized hard-wall interactions. He *et al.* recently showed that, except in regions very close to the piston, all these techniques generate essentially the same shock behavior [143]. A great advantage of the material piston technique we use is that it can generate shocks within systems prepared with periodic boundary conditions. There is no need to create and equilibrate free surfaces, which can be challenging for both crystalline and amorphous polymers. Free surfaces also introduce finite-

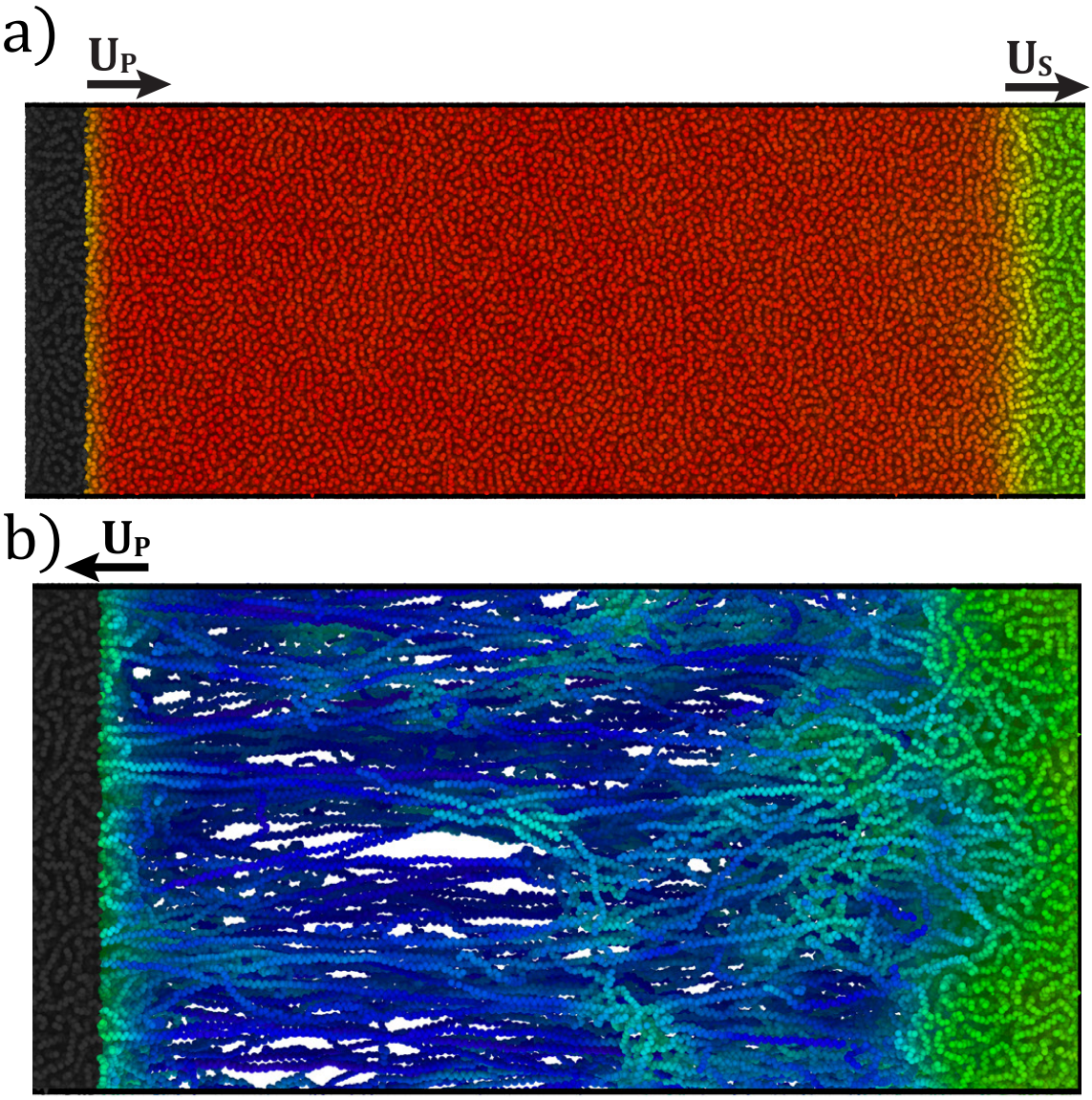

Figure 5.3: Snapshots of amorphous PE configurations illustrating shock generation. After equilibration, atoms within 2.5 nm of the ends of the sample are constrained to move as rigid slabs along the horizontal z-axis. (a) Compressive loading obtained by moving the left slab to the right at $U_p = 1.5$ km/s produces a shock propagating to the right at $U_s \approx 4.6$ km/s. (b) Tensile loading obtained by moving the left slab to the left at speed $U_p = 1.5$ km/s does not produce a stable shock. The system forms a craze and then fails. Configurations are colored qualitatively by the local density of atoms—low (blue) to high (red). Amorphous system dimensions are $16.6 \times 16.6 \times 155$ nm. Only the leftmost 47 nm and 35 nm are shown for a and b respectively.

size and edge effects which can complicate equilibration and measurement of bulk properties [161].

5.3.4 Analysis Techniques

Shock waves drive systems into a nonequilibrium state, with sharp jumps in thermodynamic and hydrodynamic variables across the propagating front. In order to track this dynamic process, we must compute local measures of state variables. The system is divided into bins $\sim$ 1 nm wide along the shock direction. The average velocity u_i is obtained by a simple average over atoms in each bin. More care should be taken with the virial contributions to the local stress tensor, since they depend on multiple atoms that may be in different bins [162–164]. For the relatively coarse bins used here, partitioning the virial contributions evenly among the participating atoms was sufficient to capture the magnitude of discontinuities in the stress tensor at shock fronts. The element of the local stress tensor along Cartesian directions i and j was computed as

$$\begin{aligned}\sigma_{ij} = -\frac{1}{V_s}\sum_{\alpha}^{Nbin}\Bigg[mu_iu_j + \frac{1}{2}\sum^{pairs}(r_{i,1}f_{j,1} + r_{i,2}f_{j,2}) + \\ \frac{1}{3}\sum^{triples}(r_{i,1}f_{j,1} + r_{i,2}f_{j,2} + r_{i,3}f_{j,3}) + \\ \frac{1}{4}\sum^{quads}(r_{i,1}f_{j,1} + r_{i,2}f_{j,2} + r_{i,3}f_{j,3} + r_{i,4}f_{j,4})\Bigg]_{\alpha},\end{aligned} \tag{5.4}$$

where V_s is the volume of a bin, α indexes the atoms within a bin, u is an atom's velocity, and f_j is the force along j on atom α resulting from pair-wise interactions or covalent bonds (pairs) or torsion interactions (triples and quads). The first term on the right of Eq. 5.4 represents the kinetic contribution to σ_{ij} and the remaining terms give the virial contributions to the stress.

The stresses of greatest interest are the shock stress $\sigma = \sigma_{zz}$ and characteristic shear stress $\tau = \sigma_{zz} - \frac{1}{2}(\sigma_{xx} + \sigma_{yy})$. The former is a measure of shock strength, while the latter is useful in determining the nature of any plasticity behind the shock front. For each system we present profiles of σ and τ along the shock direction in Sec. 5.4. Pastine's hydrostatic approximation requires that τ/σ_{zz} be small and deviations from his predictions for U_s in Fig. 5.1 are associated with large values of this ratio.

Stress and velocity profiles are calculated at 0.2 ps intervals for each shock simulation. Fig. 5.4 visualizes one such time-series for the particle velocities in the amorphous configuration of Fig. 5.3a. The boundary of the white and yellow region is the piston traveling in the +z direction at $U_P = 1.5$ km/s. The shock front accelerates material from $u_z = 0$ (black) to $u_z = U_p$ (yellow) and travels into the material at a speed $U_s > U_p$. To measure U_s we track the midpoint of the front, where $u_z = \frac{1}{2}U_p$ (white dashed line). U_s is obtained from a least-squares fit to the front position versus time. The standard error of a typical fit is less than 0.01 km/s. When the shock front reaches the far side of the sample, it reflects off the rigid material and back into the sample (small black triangle in upper right of Fig. 5.4). We do not analyze data after

reflection occurs. The range of impact velocities studied, 0.1 to 5 km/s, overlaps with the experimental data shown in Fig. 5.1. We did not extend the simulations to higher U_p because shock produced conditions outside the range where AIREBO-M has been tested. As shown below, even for $U_p = 4$ km/s the pressure behind shock fronts is near 40 GPa. The corresponding temperature is about 1000 K. For $U_p = 5$ km/s the temperature nearly doubles and at higher velocities bond breaking and other effects may become important.

An advantage of studying shock with MD simulations is that they provide the explicit trajectories for all atoms as the shock transits the system. By analyzing these trajectories in tandem with dynamic profiles of σ and τ, we can identify specific plastic mechanisms that relax τ and "fluidize" the material. In Sec. 5.4 we color atomic configurations either by particle velocity, the orientation of the zig-zag carbon bonds along chain backbones or by a local measure of deviatoric strain developed by Falk and Langer [163,165]. In the last case, which we use to visualize [001] shocks, we use the relative motion within a radius of 15 Å to determine the strain. We choose this radius so that the strain measure captures the buckling of chain backbones which occurs at the scale of ~ 100 Å.

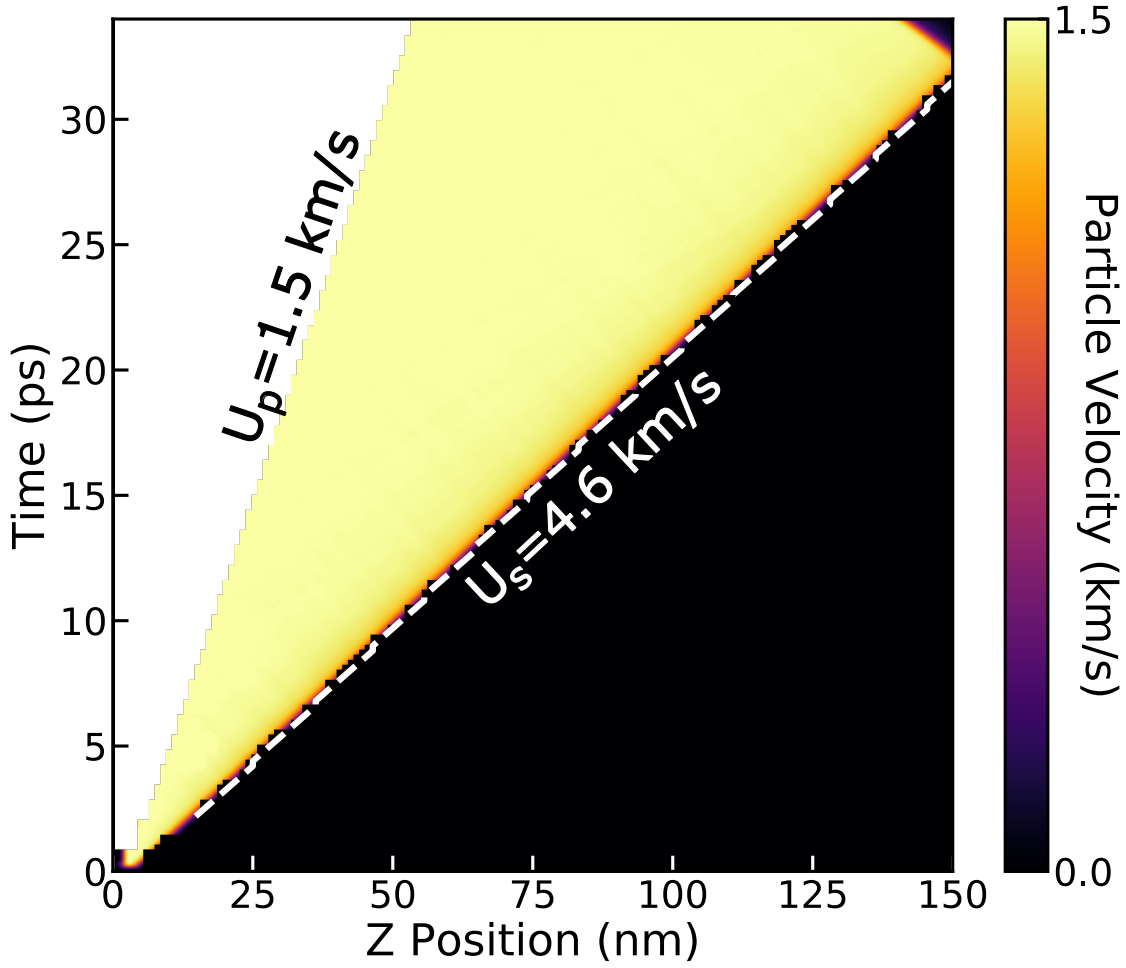

Figure 5.4: Time evolution of particle velocity (u_z) profiles for the amorphous system in Fig. 5.3a. The piston moves along z at $U_p = 1.5$ km/s, and is indicated by the white/yellow border. A shock traveling at U_s accelerates material from $u_z = 0$ (black) to $u_z = U_p$ (yellow). The white dashed line tracks the front where $u_z = 0.5U_p$. Least-squares fits to this line give $U_s \approx 4.6$ km/s

5.4 Results and Discussion

5.4.1 Amorphous phase

Unaligned PE forms a semicrystalline structure at room temperature, with 40–55% of the system in the amorphous phase [1]. Aligning PE by drawing reduces the amorphous content but does not eliminate it. About $5-10\%$ remains amorphous for highly drawn fibers [3]. Amorphous regions and their boundaries are typically much weaker than the crystal and can act as strength limiting defects. Thus, characterizing the mechanical properties of purely amorphous PE is an essential step toward understanding the mechanics of the more complex and heterogeneous semicrystalline structures [21].

Compressive shocks with $U_p = 0.1$–3.5 km/s were generated in amorphous PE. A single plastic front formed for all cases — as illustrated in Fig. 5.3a. Shock velocities obtained by tracking the shock front are plotted as purple pentagons in Fig. 5.1. For $U_p \geq 0.5$ km/s, U_s is a nearly linear function of U_p and agrees with Pastine's hydrostatic model. For lower impact velocities, the MD results lie above the hydrostatic predictions.

Stress profiles of the shocked configurations show that breakdown of hydrostatic behavior coincides with the weak shock regime (large τ/σ). Fig. 5.5 plots profiles of σ and τ at 13 ps after impact for several U_p from 0.3–3.5 km/s. Profiles are plotted as a function of distance from the moving piston ($z = 0$). Fronts propagate rightward,

elevating σ and τ from 0 in the quiescent state at large z. When $U_p = 0.3$ km/s (blue), $\tau = 0.14$ GPa and $\sigma = 0.51$ GPa are similar in magnitude, explaining why U_s lies above the hydrostatic Hugoniot. As U_p increases, σ grows rapidly with increasing rate, while the rate of increase of τ is limited by plastic deformation. This plastic relaxation leads to a rapid drop in τ/σ to ~ 0.075 at $U_p = 3.5$ km/s (black), and recovery of hydrostatic shock behavior. Even for the lowest rates studied, plastic deformation is observed behind the shock front. A HEL may exist below $\sigma = 0.1$ GPa, but there may not be a sharp onset of plasticity since simulations have found that some plasticity always occurs when amorphous systems are strained [166].

We do not observe an elastic precursor wave for amorphous shock, indicating material is over-driven for even our lowest $U_p = 0.1$ km/s. This is reasonable given the low stiffness and strength of amorphous PE. Uniaxial compression simulations on the amorphous sample using an engineering strain rate of 10^8 s^{-1} give a Young's modulus $E \approx 1$ GPa and yield stress $\sigma_y \approx 50MPa$. The former corresponds to a sound speed $c_s = (E/\rho)^{1/2} \approx 1.2$ km/s, which is about half of the slowest shock speed. Assuming $\sigma_{HEL} \sim \sigma_y$, we can estimate a maximum impact velocity $U_p \sim c_s\sigma_y/E \approx 60$ m/s before yield occurs. At this low U_p we face limitations similar to experiments; shocks are too weak for us to reliably track them above the thermal noise in our dynamic simulations.

We have also simulated amorphous PE in tensile shock loading. In this case, steady shock fronts do not form. Instead, strain localizes rapidly and nucleates a

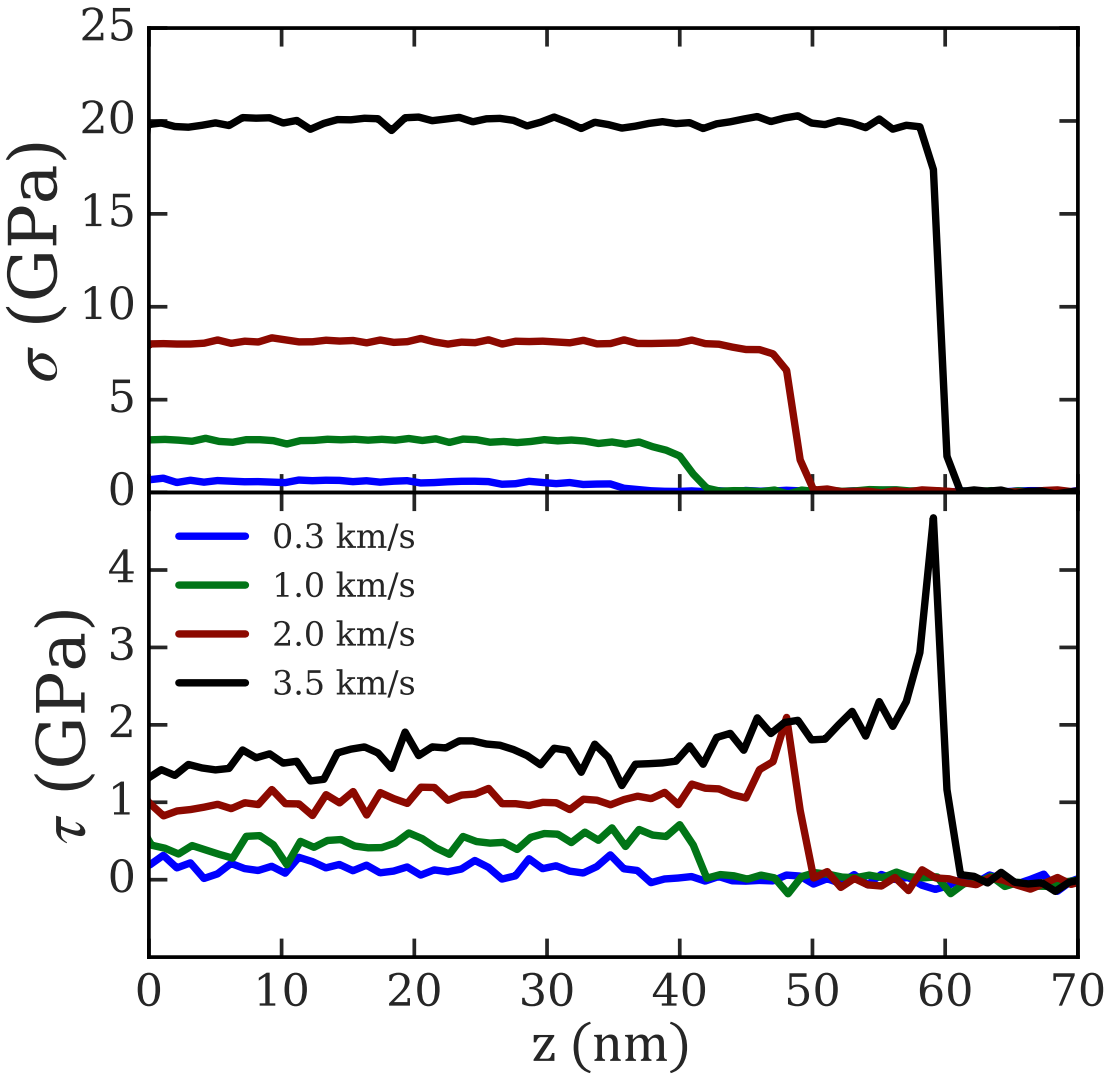

Figure 5.5: Shock (σ) and shear (τ) stress profiles in amorphous PE for several U_p. All profiles are at $t = 13$ ps after impact and are plotted as a function of distance from the impacting piston. Shocks propagate to the right, elevating the stress from the quiescent state $\sigma = \tau = 0$. The rise in the steady value of σ with impact velocity becomes more rapid as U_p increases, while the rate of increase in τ is limited by plastic deformation. Hydrodynamic shock is recovered as τ/σ becomes small.

craze near the piston (Fig. 5.3b). Once nucleated, further work by the piston goes towards growing the craze. Eventually the craze fractures, releasing the tensile load. The study of craze growth under high-rate loading and how it differs from quasistatic loading is relevant to failure in many unaligned polymer materials. We defer analysis of this case to future work.

5.4.2 Shock Along Crystal a-axis [100]

In the plane perpendicular to the chain backbone, chains pack in a "herring-bone" structure with alternating orientations of the chain backbone to form an orthorhombic crystal (Fig. 5.6(a)). This structure is determined by van der Waals interactions that have cohesive energies $\sim$ 100 times weaker than backbone bonds [10]. The stiffness along the [100] direction is just 8 GPa compared to 260 GPa along the [001] direction. Because van der Waals interactions are both weak and nondirectional, chains can translate and rotate into new structures in response to applied loads, leading to complex crystal plasticity and crystal-crystal phase transitions. For example, experiments show pressure can convert some of a semicrystalline sample into a metastable monoclinic crystal [167, 168]. Analytic and quantum chemistry studies have explored thermodynamic stability of the monoclinic phase, but identifying specific transition mechanisms has remained an open question. As we now discuss, tracking atomic displacements allows us to identify how the monoclinic phase forms during shock when chains slip along the (110) plane and rotate collectively to locally reduce shear

stresses.

Results for the shock velocity along the [100] direction are plotted as red circles in Fig. 5.1. The shock velocity shows a sharp break at $U_p = 0.7$ km/s. For $U_p \geq 0.7$ km/s, simulation results are in excellent agreement with Pastine's hydrostatic model. For $U_p < 0.7$ km/s, the shock velocity is systematically higher than hydrostatic predictions. We can identify the break in the U_p–U_s curve with the onset of crystal plasticity, i.e. the HEL. Shocks on the low-speed branch generate fully recoverable deformation. There is a small increase in density accompanied by small changes in backbone orientation as seen for 0.4 km/s in Fig. 5.7(a).

Shocks with $U_p \geq 0.7$ km/s cause plastic deformation. Fig. 5.7(b) shows that at 0.7 km/s most chains are packed more tightly and retain the alternating orientations associated with the herringbone structure of the orthorhombic crystal. Plastic deformation occurs through shear by a nearest-neighbor chain spacing along some (110) planes of the orthorhombic crystal. This plane orientation has the largest resolved shear stress under uniaxial loading and shear along these planes leads to a local increase in density.

As U_p increases, shock produces a transition to the denser monoclinic phase. Fig. 5.6(b) shows how molecules transform from orthorhombic to monoclinic order by shearing slightly along alternate diagonal (110) planes and rotating to have a uniform alignment. The two choices of shear plane lead to different orientations of the monoclinic structure with angle $\pm 12^o$ to the z-axis (Fig. 5.6(a)). Fig. 5.7(c) illustrates

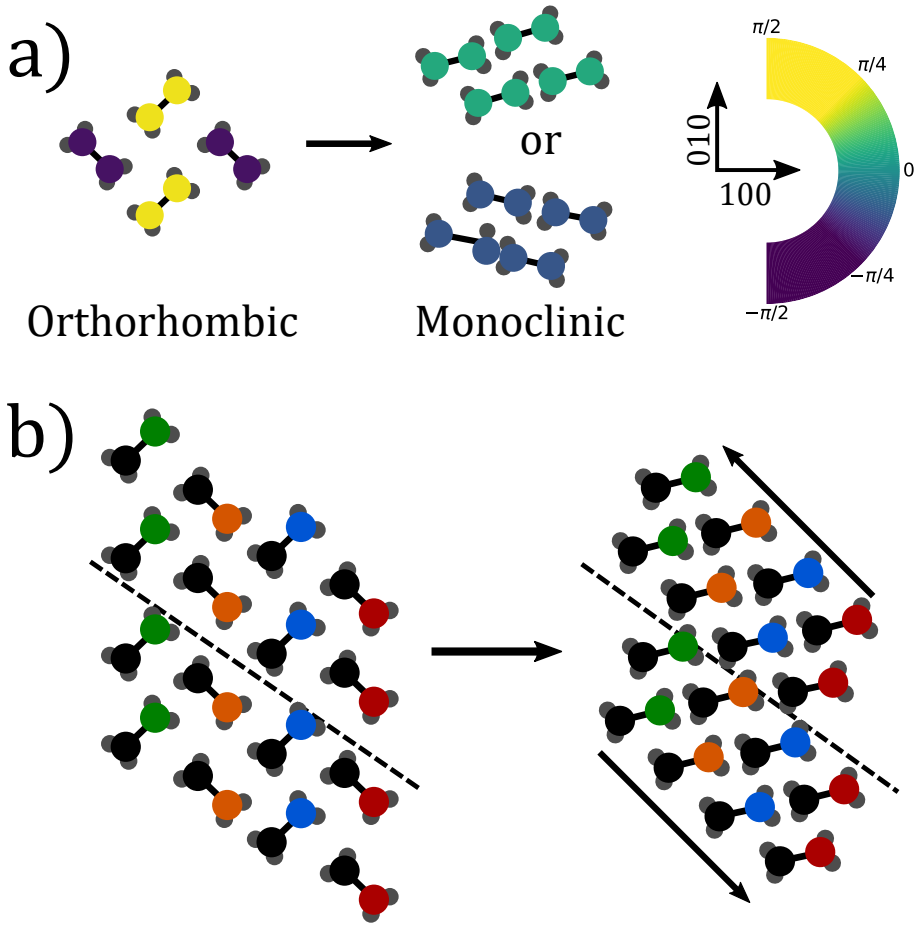

Figure 5.6: Projections of atoms along chain backbones showing changes for impact along the horizontal [100] axis. (a) In the orthorhombic crystal (left), chains form a herringbone structure with alternating angles of $\pm 43^o$ to the [100] axis. Shock transforms regions into the monoclinic crystal structure (right) with all molecules aligned at an angle of $\pm 20^o$ to the [100] axis. Colors indicate orientation of the backbone relative to the [100] axis with the color map shown on the right. The same color map is used in Fig. 5.7. (b) A diagram showing how molecules rearrange into a monoclinic phase during [010] shock. One atom on each chain is colored to indicate successive (100) planes in order to show how molecules rotate and planes shear to form the monoclinic phase. All colored atoms are at the same height out of the page along [001] and the dashed line indicates a plane where shear occurs. Diagonal lines of molecules parallel to the dashed line rotate clockwise to move closer together. At the same time, chains reorient coherently to point in the same direction. The system shears by one chain spacing along the dotted line. This pattern repeats with shear along every second diagonal parallel to the dotted line.

how this transition evolves for $U_p = 2.0$ km/s. Moving from the shock front to the left one sees a region where chains are beginning to lose the alternating herringbone orientation and adopt one of the two monoclinic orientations, corresponding to uniform regions of medium blue or aquamarine. There are twin boundaries between the two orientations. Fig. 5.7(d) shows that increasing U_p to 4.0 km/s produces more complete conversion to the monoclinic state and an even greater increase in density.

Figure 5.8 shows profiles of σ and τ for the systems shown in Fig. 5.7. For $U_p = 0.4$ km/s, $\tau \sim \sigma \approx 1$ GPa. Between $U_p = 0.4$ km/s and $U_p = 4.0$ km/s, σ rises nonlinearly from about 1 GPa to 35 GPa. The value of τ remains near 1 GPa up to $U_p = 0.7$ km/s where plastic deformation first occurs. It then rises slowly with U_p and saturates near 3 GPa between 2-4 km/s. The strong saturation in τ implies a nearly hydrostatic pressure state behind the shock, and explains the agreement with the hydrostatic predictions at larger U_p.

From the above results, the HEL corresponds to a stress of $\sigma_{HEL} \sim 1$ GPa. Above this limit, we see no evidence of an elastic precursor, indicating shock above the HEL is always over-driven. We also do not observe separate plastic and phase transition fronts at high velocities, which we will show do occur for [010] shock. The region where plasticity develops remains narrow, rather than growing as the product of time and the difference between two front velocities.

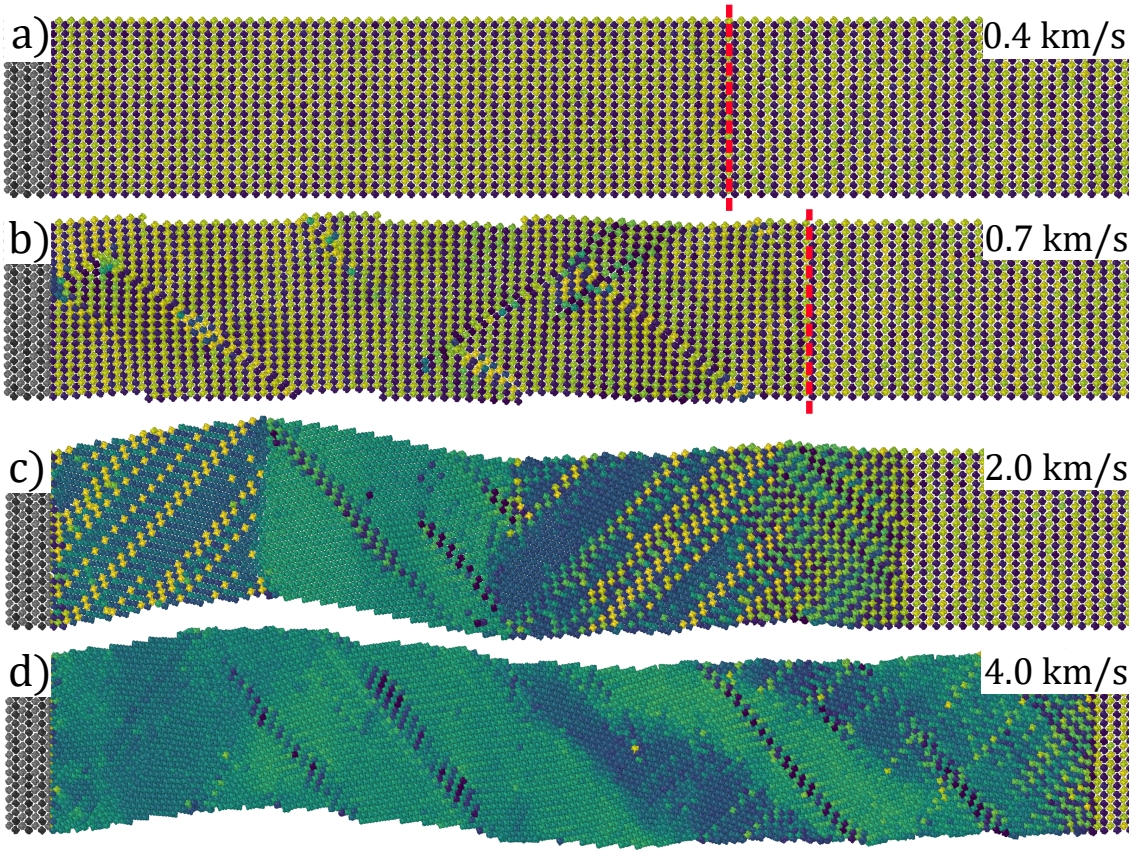

Figure 5.7: Atomic configurations from a-axis [100] shock simulations at $t = 14.4$ ps after impact for $U_p = 0.4$, 0.7, 2.0, and 4.0 km/s (**a-d**). System dimensions are $9.84 \times 10.18 \times 157$ nm. The first ~ 63 nm along the z-axis are shown in the rest-frame of the piston (gray atoms) located at the far left. Chains are colored by the angle of the zig-zag carbon backbone relative to the z-axis [100]. As in Fig. 5.6, the herringbone structure of the orthorhombic crystal leads to alternating yellow and purple molecules. Monoclinic regions have uniform orientations corresponding to an aquamarine or medium blue (See color map in Fig. 5.6). (a) For $U_p = 0.4$ km/s there is a small increase in density behind the shock front (dashed line) but no plasticity. (b) For $U_p = 0.7$ km/s there is plastic deformation through slip along diagonal (110) planes. (c-d) At higher velocities regions are deformed into monoclinic crystals with one of two orientations through the mechanism illustrated in Fig. 5.6(b).

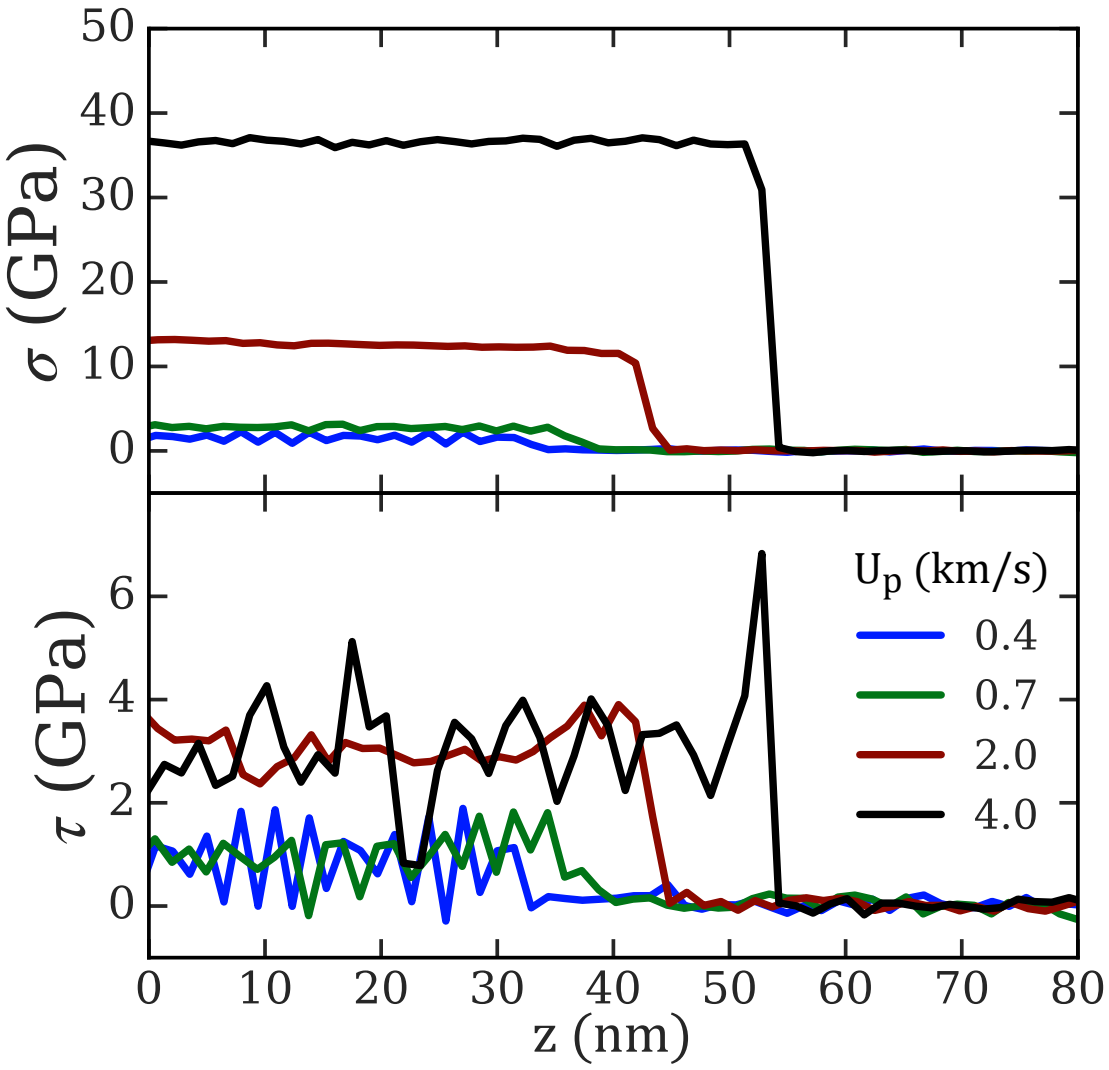

Figure 5.8: Profiles of σ and τ as a function of distance from the piston z for the [100] shock configurations of Fig. 5.7, where $t = 14.4$ps. (a) The shock stress rises rapidly with U_p. (b) The increase in shear stress is limited by plastic deformation and saturates for large U_p. The hydrostatic approximation becomes valid for $\sigma \gg \tau$.

5.4.3 Shock Along Crystal b-axis [010]

Given the weak, non-directional nature of van der Waals interactions, one might expect transverse shocks in PE to be relatively insensitive to the specific plane of impact. Indeed, many theories, textbooks, and experimental analyses approximate aligned PE crystals with transversely isotropic elasticity and plasticity, and thus predict direction-independent shock properties. While our simulations show the transverse Young's modulus is nearly isotropic, we find that the intimate coupling of chain translations and rotations during plastic flow leads to strong anistropy in shock propagation.

Simulation results for U_s under impact along [010] are summarized by the green points in Fig. 5.1. One difference from the [100] results is that the jump indicating the onset of unrecoverable plastic deformation is much earlier, between 0.3 and 0.4 km/s instead of 0.6 and 0.7 km/s. A second difference is that the shock velocity for [010] rises above all other results between about 1.8 and 4.0 km/s. This implies a substantial rise in τ that is not relaxed by plastic deformation. In addition, for U_p between 2.8 and 4 km/s there is a second, slower shock front at which plasticity releases shear stress (open squares in Fig. 5.1).

We can understand the origin of the differences between [100] and [010] by contrasting the transverse deformation of the orthorhombic PE unit cell under strain. As illustrated in Fig. 5.6, the four chains in the initial unit cell are arranged in a herring bone pattern, forming a rhombus that is longer along [100] than [010]. When com-

pressed along [100], the cell becomes more square. This arrangement is susceptible to slip along [110] with chain rotations producing the monoclinic transition discussed in the previous section and illustrated in Fig. 5.6. In contrast, compression along [010] makes the rhombus more asymmetric. As shown in Fig. 5.9, the unit cell collapses into a densely packed orthorhombic phase with chains rotating so their backbones are closer to the [100] direction. Although this phase has the same symmetry as the equilibrium structure, it appears to be a distinct phase separated by a free energy barrier due to steric constraints from the packing of hydrogens on different chains. A similar phase was observed in quasistatic MD simulations of crystalline PE at high pressures [10]. Chains in this phase are tightly interlocked and strong steric interactions hinder chain rotation and translation, suppressing (110) slip and monoclinic reorientations. The result is enhancement of the yield stress in the densely packed phase that produces deviations from the hydrostatic model.

For $U_p < 0.4$ km/s deformation is fully recoverable. For $0.4 \leq U_p \leq 1.6$ km/s, U_s is close to the hydrostatic model. In this regime, the region behind the shock front contains coexisting regions of the two orthorhombic phases. As shown in Fig. 5.10 (a-c), the fraction of dense orthorhombic phase (alternating green/blue) grows with U_p and the entire region is in this phase for $U_p = 1.6$ km/s.

This transformation between phases should not be confused with the formation of multiple crystal grains through plastic deformation that is commonly observed in crystalline materials. Many materials exhibit coexisting crystal domains separated

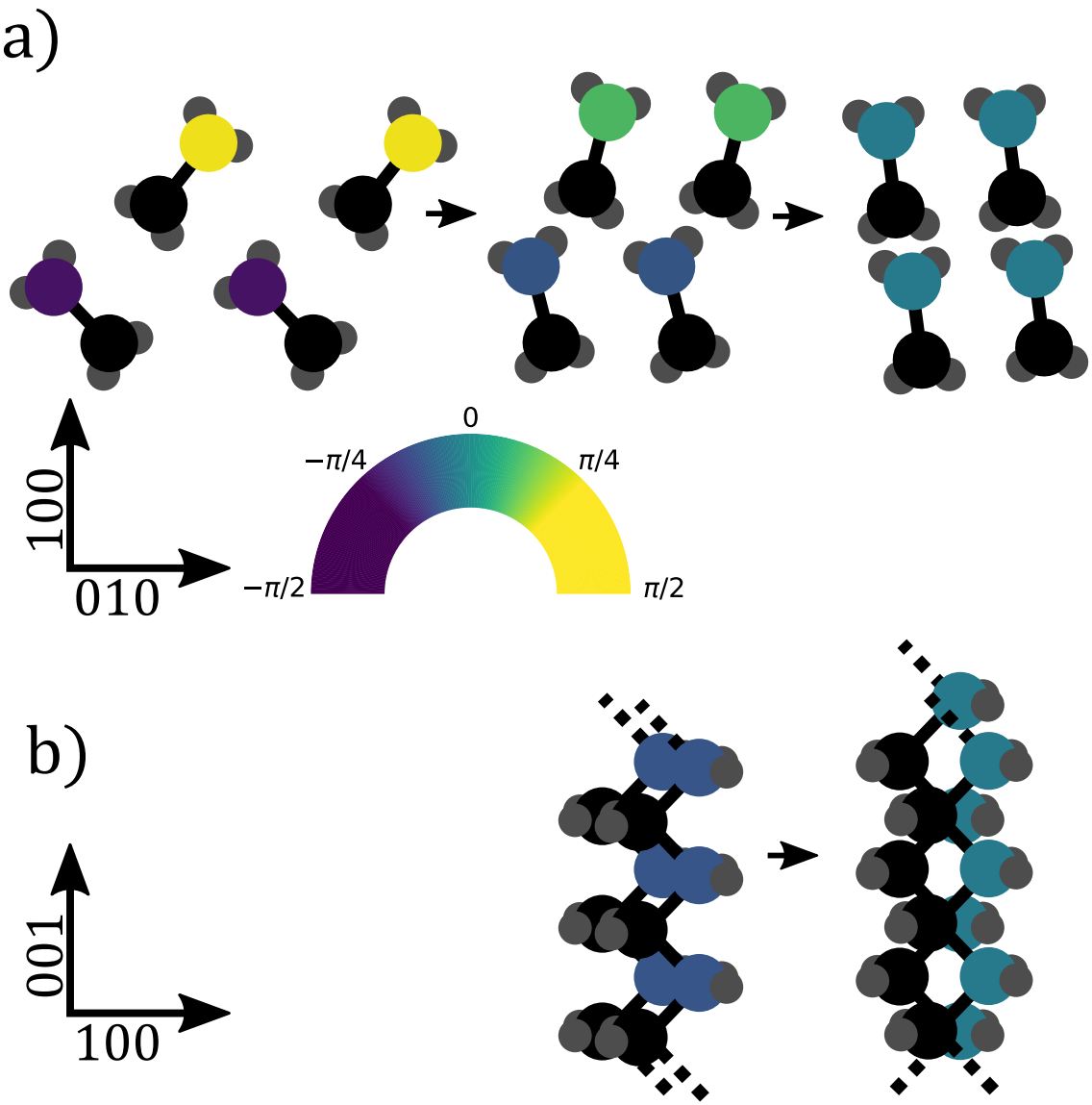

Figure 5.9: Schematic showing crystals and transition paths for shock along [010]. (a) Projections along the chain axis. A pair of unit cells of the equilibrium orthorhombic crystal is shown on the left. Shock first compresses the crystal into a denser orthorhombic phase shown in the center. At very high pressures there is a further transition to a new structure. Colored atoms are at the same height into the page along [001] in the initial state and the color indicates the angle of the molecule relative to the [100] axis with the color map shown in the center. (b) Projections in the plane perpendicular to the [010] direction showing shear along alternate chains so that hydrogen atoms are at different heights to minimize steric repulsion.

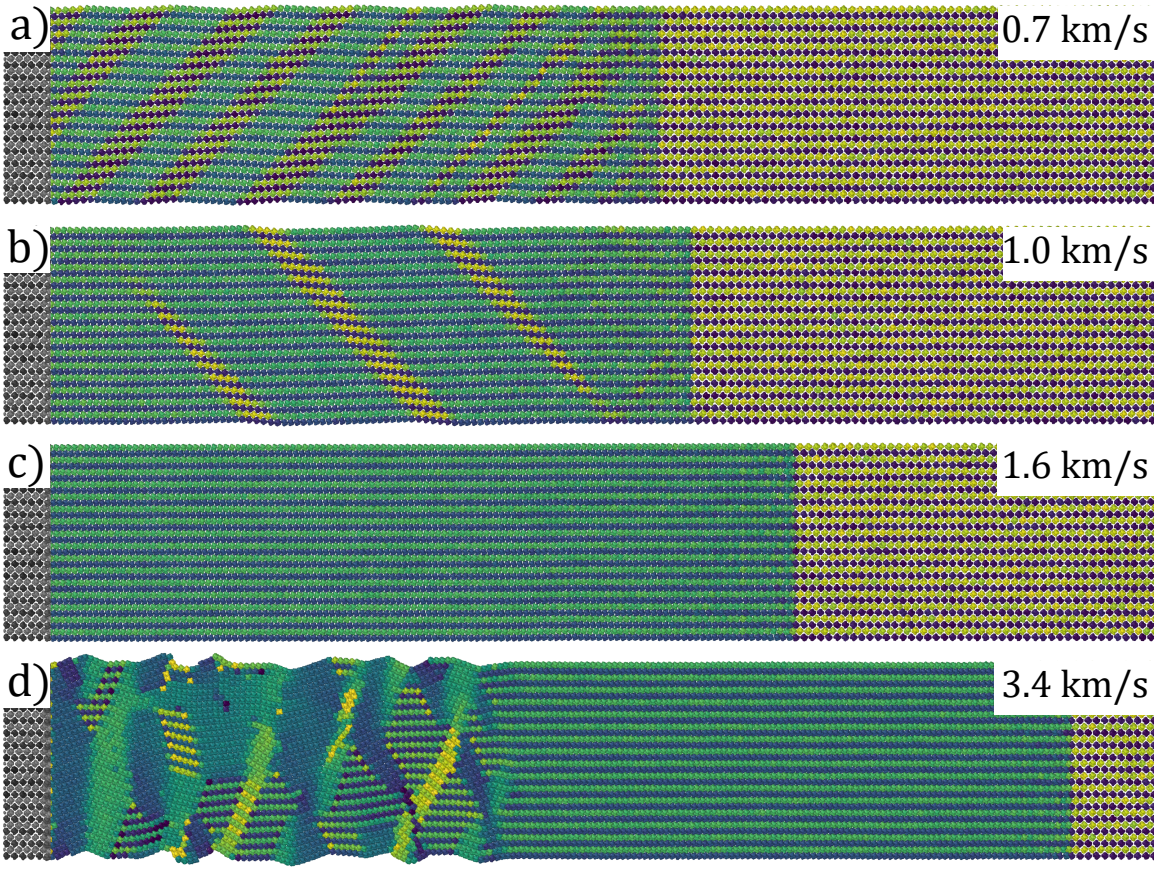

Figure 5.10: Atomic configurations of b-axis [010] shock simulations at $t = 10.0$ ps after impact for $U_p = 0.7, 1.0, 1.6$, and 3.4 km/s (**a-d**). System dimensions are $10.2 \times 11.7 \times 153$ nm with only the first 70 nm along the z-axis shown. Piston atoms are gray and other molecules are colored by their orientation relative to the vertical [100] axis (see colormap in Figure 5.9). (a-b) For $U_p < 1.6$ km/s, shock generates a banded structure with two coexisting orthorhombic crystal structures, the initial phase (yellow/purple) and a compressed phase (blue/green). Material slips at the boundary of these phases, relaxing shear. (c) At $U_p = 1.6$ km/s the entire system is converted into the compressed phase, which hinders chain slip and yield. (d) For U_p between 2.8 and 4.0 km/s there are two shock fronts. The first converts the system to the dense phase. At the second, the dense phase deforms plastically into domains of a new crystal structure. For $U_p \geq 4.0$ km/s the two fronts merge.

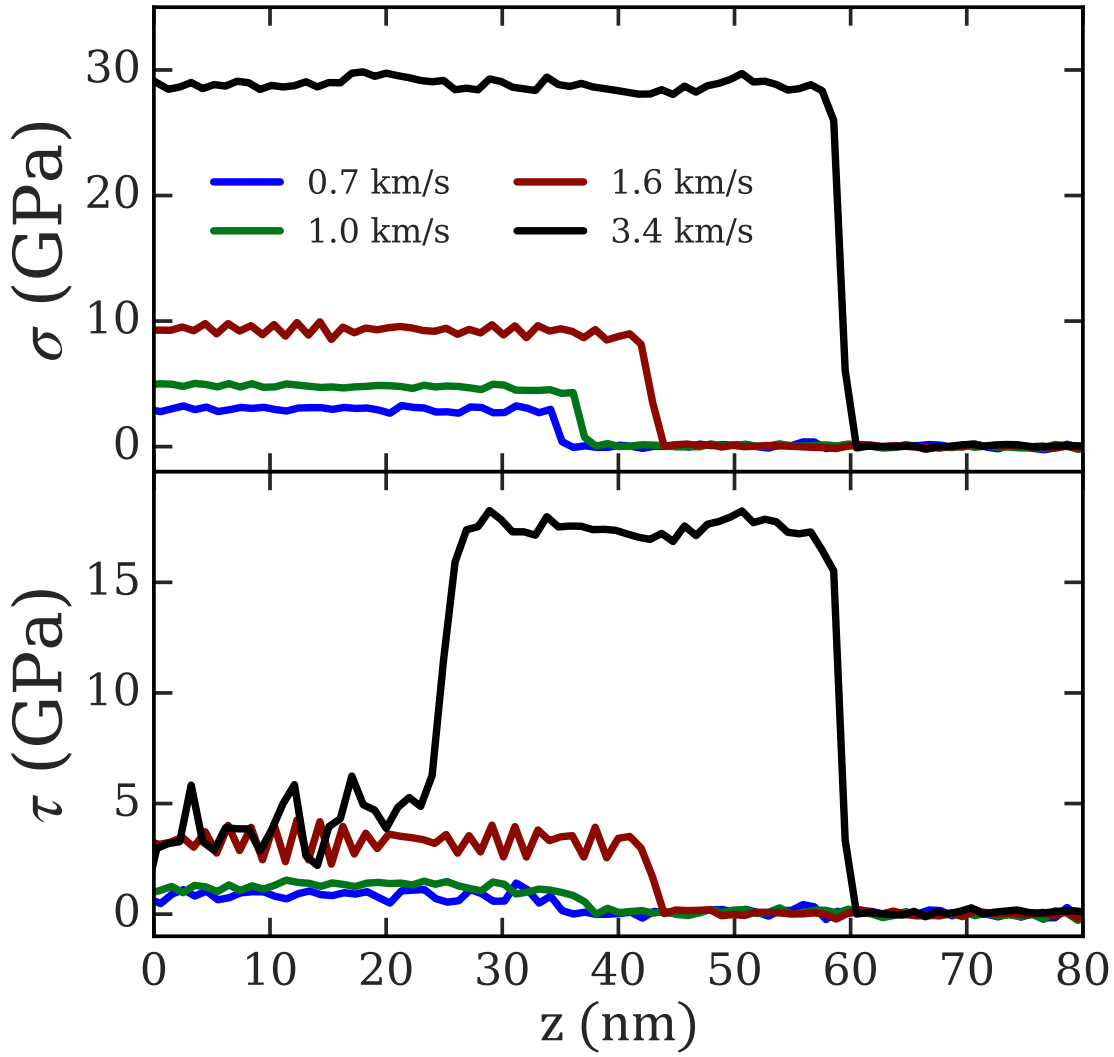

Figure 5.11: Profiles of σ and τ as a function of distance from the piston for the [010] shock configurations of Fig. 5.10a-d at $t = 10$ ps after impact.The shock stress behind the front σ rises rapidly and non-linearly with U_p. At velocities where the initial and dense orthorhombic phases coexist, material slips at phase boundaries and τ saturates at ~ 2 GPa (blue and green curves). Once shocks fully compress chains into the dense phase, chain mobility is hindered and τ rises substantially. Sufficiently strong shocks nucleate plasticity in the compressed phase, producing a second plastic wave which unloads the shear stress (black curve).

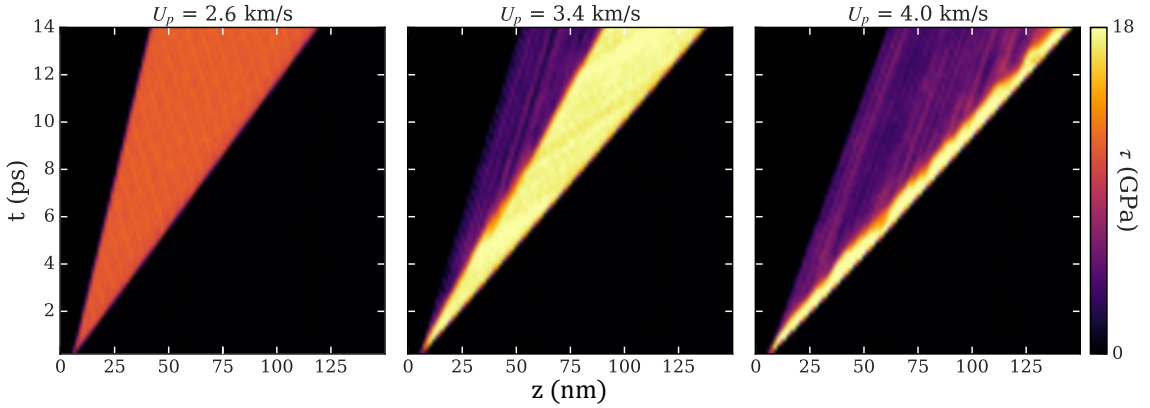

Figure 5.12: Plots of the shear stress vs. time and position for [010] shocks. (a) For $U_p = 2.6$ km/s there is a single shock that raises τ to 6.4 GPa. (b) For $U_p = 3.4$ km/s the first shock advances at $U_s = 9.5$ km/s and raises τ to 18 GPa. The second shock lowers τ to 4 GPa and moves at $U_s = 6.2$ km/s. (c) For $U_p = 4.0$ km/s the two shock fronts have merged into a region of fixed width that advances at $U_s = 10.0$ km/s.

by grain boundaries. These grains are usually misoriented regions of the same crystal phase. The two distinct regions seen behind [010] shocks in Fig. 9 a-c are not reoriented domains of the same phase, but separate crystal structures. They both share orthorhombic symmetry, but have distinct lattice constants and unit-cell structure. In this system, the plastic process is the transformation of the initial unit-cell into the second orthorhombic structure.

Fig. 5.11 shows stress profiles for different U_p. When the two orthorhombic phases coexist, material shears easily along the diagonal phase boundaries, relaxing τ to ~ 1 GPa. The shear stress can not easily relax when the entire region is in the dense phase. Strong steric interactions hinder chain rearrangement and suppress plasticity behind the front. This produces a substantial increase in τ with U_p, up to ~ 18 GPa for $U_p = 3.4$ km/s (Fig. 5.11), and elevates U_s above the hydrostatic shock speed.

Eventually shear stresses become large enough to initiate plasticity within the collapsed phase. This produces a two front shock structure for U_p between 2.8 and 4.0 km/s. An example of the deformation behind each front is shown for $U_p = 3.4$ km/s in Fig. 5.10(d). At the first shock front, material is converted into the collapsed phase and τ rises dramatically to ~ 18 GPa (Fig. 5.11). This is followed by a plastic front where shear produces a transition to a new crystal structure and τ drops to ~ 4 GPa. The two front structure is clear in the plot of τ in Fig. 5.11 but the plastic front produces very little change in σ.

The new phase behind the plastic front has a constant molecular orientation but is not the same as the monoclinic phase produced by [100] shocks. As shown in Fig. 5.9, chain reorientation is accompanied by translation of alternating chains by one carbon spacing along the chain backbone. This moves hydrogens on neighboring chains to different heights, allowing them to form an interdigitated structure that minimizes steric repulsion. As for the monoclinic phase in [100] shocks, there are two twins with molecular orientations corresponding to aquamarine and medium blue colors. Regions with these dense structures coexist with orthorhombic regions behind the plastic shock in Fig. 5.10(d).

Figure 5.12 shows the spatiotemporal variation in τ for three representative velocities. At $U_p = 2.6$ km/s there is a single jump in τ associated with the phase transformation to the dense orthorhombic phase (Fig. 5.12(a)). For $U_p = 3.4$ km/s there are two clear shock fronts propagating at different velocities (Fig. 5.12(b)). As

U_p increases, the velocity of the plastic front rises towards that of the phase transformation front. For $U_p \geq 4.0$ km/s the plastic front propagates at the same velocity. This is evident in Fig. 5.12(c), where the region of dense orthorhombic crystal has a small constant width ahead of the plastically deformed state. In this high velocity regime, the stress is nearly hydrostatic ($\tau/\sigma < 0.1$) and the [010] shock velocities coincide with the hydrostatic model.

5.4.4 Shocking Along Crystal c-axis [001]

5.4.4.1 Axial Compression

The stiff backbone bonds aligned along the **c**-axis of the PE crystal support a sound speed of $c_s \approx 16$ km/s that is greater than any U_s we measure. This leads to a two wave "elastic-plastic" shock structure for compression along [001] [16]. As illustrated in the snapshots of σ for $U_p = 3.0$ km/s in Fig. 5.13, an elastic precursor propagates at the speed of sound (c_s) in the shock direction. This elevates the stress to the Hugoniot Elastic Limit (HEL). A plastic shock follows at a speed U_s (Fig. 5.1), relaxing the shear stress by activating plastic deformation mechanisms. We did not reach the over-driven limit for axial shock since the maximum $U_s \approx 11$ km/s for $U_p = 5.0$ km/s is well below $c_s = 16$ km/s. This is in sharp contrast to transverse and amorphous shock where no elastic precursor was observed and systems were over-driven even for our lowest $U_p = 0.1$ km/s.

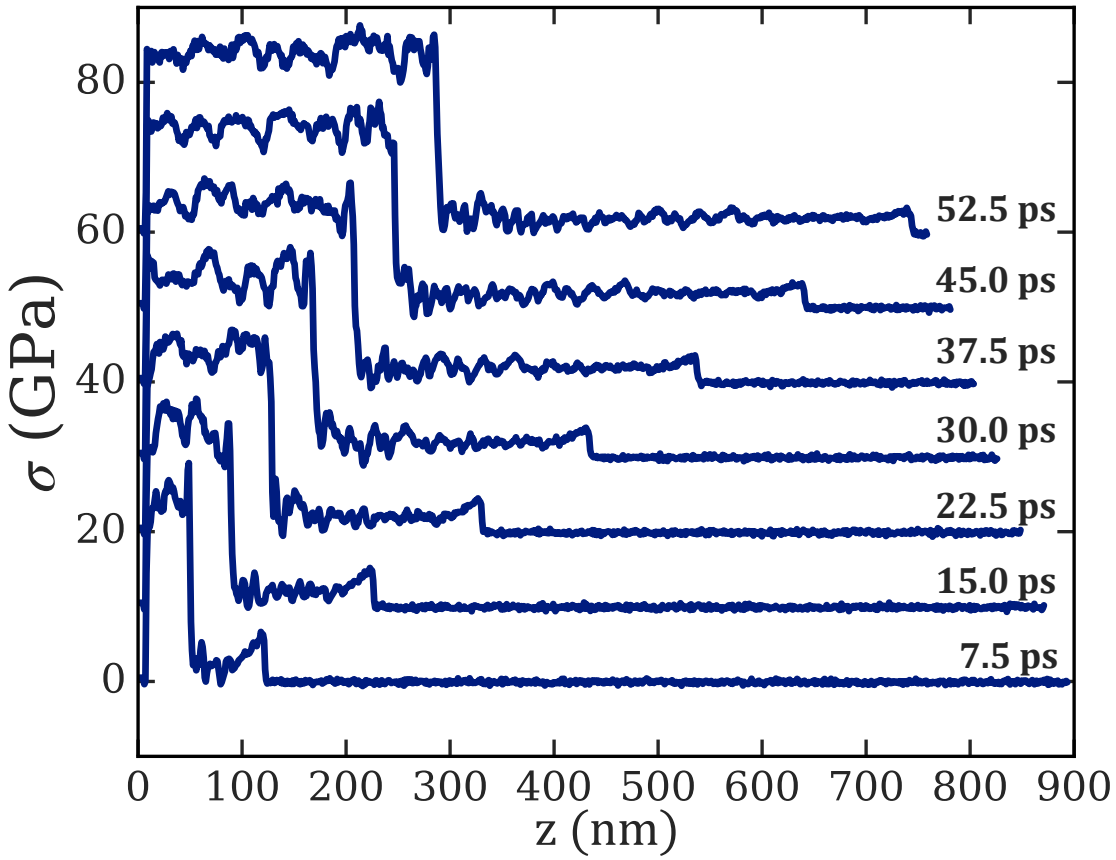

Figure 5.13: Profiles of the shock stress (σ) at equal time intervals for a shock propagating 1 micron along [001] with U_p = 3.0 km/s. Successive profiles are offset vertically by 10 GPa to prevent overlap. The shock has a two wave elastic-plastic structure, with the elastic precursor traveling at the adiabatic sound speed $\sim$ 16 km/s. The precursor raises the stress to the HEL, $\sigma_{HEL} \approx 1.9$ GPa. Buckling occurs at the slower plastic front and raises σ above 20 GPa.

As noted in Section 5.2, the steady state amplitude of the elastic precursor stress should be independent of U_p and corresponds to σ_{HEL}, the shock analog of a quasistatic yield stress [16]. Shocks with amplitudes $\sigma > \sigma_{HEL}$ activate irreversible plastic mechanisms as they transit the system. For quasistatic compression, plasticity is known to occur through a chain buckling instability analogous to Euler buckling [150, 169, 170]. Understanding the dynamic buckling mechanism in shock is important for the design of fiber and fiber reinforced composite materials which often fail by buckling and kinking of fibers within the matrix material [171].

The curves in Fig. 5.13 show stress profiles of a $U_p = 3.0$ km/s shock at 7.5 ps intervals. Accurate resolution of the elastic precursor requires large propagation distances, so that the stress can be averaged over a large enough distance to remove thermal noise. This required about ~ 50 ps and a system length of 1 μm, compared to 300 nm for determining U_s for plastic shocks. Taking the average stress at $t = 52.5$ ps for the full elastic region, we obtain an elastic limit $\sigma_{HEL} = 1.87$ GPa, corresponding to a piston velocity $U_p = 0.116$ km/s. This value is consistent with the critical buckling stress σ_c of PE under quasistatic loading. For a crystal with chains of length L and unit-cell area A

$$\sigma_c = \frac{\pi^2 EI}{AL^2} + G \tag{5.5}$$

where EI is the flexural rigidity and G is the shear modulus [150]. For long chains, $\sigma_c \approx G$. Calculating values of G along different crystallographic directions gives σ_c between 1.7 to 3.1 GPa, depending on the buckling direction. The lowest values are

close to σ_{HEL} and correspond to buckling in the (010) plane.

Fig. 5.14 shows molecular configurations at $t = 12$ ps after impact for U_p between 0.2 and 4.0 km/s. For $U_p < 0.116$ km/s the system is below the HEL and there is no buckling or other plastic deformation. Above the elastic limit (Fig. 5.14), all systems show transverse fluctuations that develop into buckles. As expected from Eq. 5.5, buckles develop in the [010] plane where G is lowest. These buckles locally rotate the crystal structure, reducing the modulus along the propagation axis and facilitating the collapse of buckled material into a denser configuration behind the plastic shock front. The rotation angle tends to saturate at the value where successive chains can lock into registry by sliding by a lattice constant relative to their neighbors. This condition is met at $U_p = 1$ km/s. As U_p increases further, the frequency of the buckles increases.

The stress profiles for the above systems are shown in Fig. 5.15. The shock stress rises rapidly from about 2 GPa to almost 40 GPa while buckling allows the shear stress to relax below 2 GPa a short distance behind the shock front. Note that this is comparable to the shear stress produced by the elastic shock that propagates ahead of the plastic shock. Although τ saturates for $U_p > 0.116$ km/s, Fig. 5.1 shows shock velocities lie below the hydrostatic predictions until $U_p \geq 2.0$ km/s. The hydrostatic prediction is based on conservation laws across a single interface. The elastic front carries part of the input energy ahead of the plastic shock front, reducing the drive at the plastic front and thus lowering its velocity. Since the pressure behind the elastic

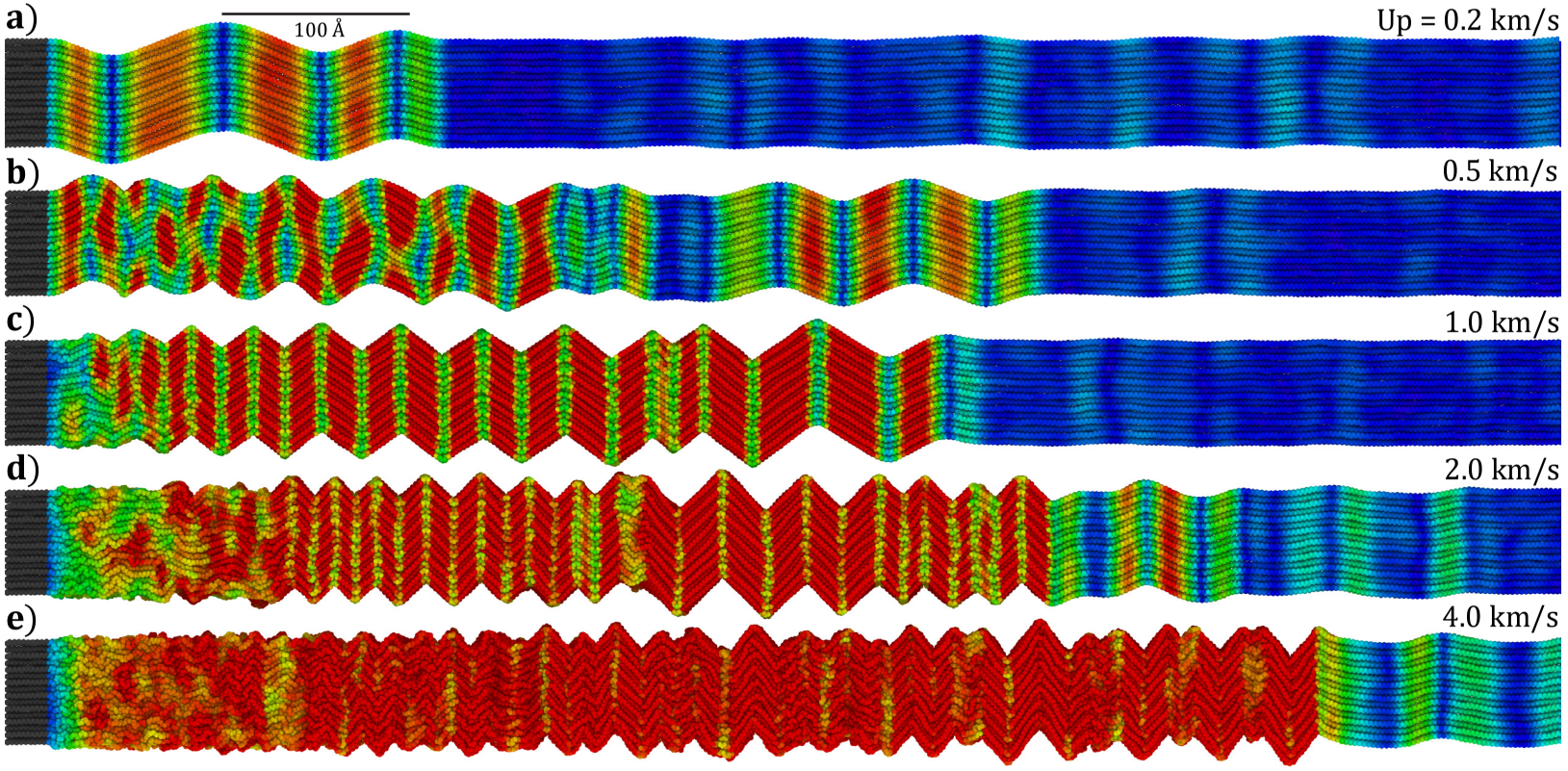

Figure 5.14: Atomic configurations showing plasticity for c-axis [001] shock simulations at $t = 12$ ps after impact for $U_p = 0.2$–4.0 km/s (**a-e**). System dimensions are $5.85 \times 5.41 \times 305$ nm. Plots are in the frame of reference of the left slab and only the leftmost 83 nm along the z-axis are shown. The elastic shock has passed out of the field of view in all cases. Gray atoms belong to the piston and other atoms are colored according to the local strain (Sec. IIID) [163], with blue undeformed and green, orange and red indicating progressively higher strain. Shock activates a buckling instability that sharpens into kinks mediated by a sequence of gauche dihedrals as U_p increases to 1.0 km/s. The characteristic length scale of buckles starts at $L \approx 100$ Å and decreases with increasing U_p.

front is independent of U_p while the pressure behind the plastic front grows rapidly, U_s approaches the hydrostatic curve as U_p increases.

Extending our analysis to quantitatively predict how the two wave structure influences U_s is not straightforward. While jump conditions for dual elastic-plastic wave-forms can be derived, they usually assume that the material is both isotropic and linear elastic. Even then, the complexity of the constituitive equations usually requires numerical techniques to predict the structure and evolution of the shock waves [16]. Such approximations can work well for ductile metals, but are inappropriate for PE with its highly anisotropic and nonlinear elasticity. Continuum frameworks can be extended to anisotropic nonlinear elasticity and plasticity [172], but solutions require extensive numerical simulations that are beyond the scope of our study.

Analytic treatment of buckling kinematics is similarly challenging, but Fig. 5.14 illustrates several qualitative features worth noting. The plastic front shows a qualitative change in structure with increasing U_p. Plastic shocks with $U_p < 0.5$ km/s form smooth bending undulations of the chain backbone, as in Fig. 5.14a. Such bends are mediated by small deflections of dihedral angles around the trans conformation, and can be described by an elastic theory with an effective bending stiffness [150]. Buckles first form with a characteristic length-scale of ~ 100 Å, which decreases with increasing U_p. We can understand this scale by revisiting the elastic arguments of Eq. 5.5. Previously, we considered buckling in the $L \to \infty$ limit where $\sigma_c \approx G$, and is independent of length. If instead we fix σ at some value above G and ask

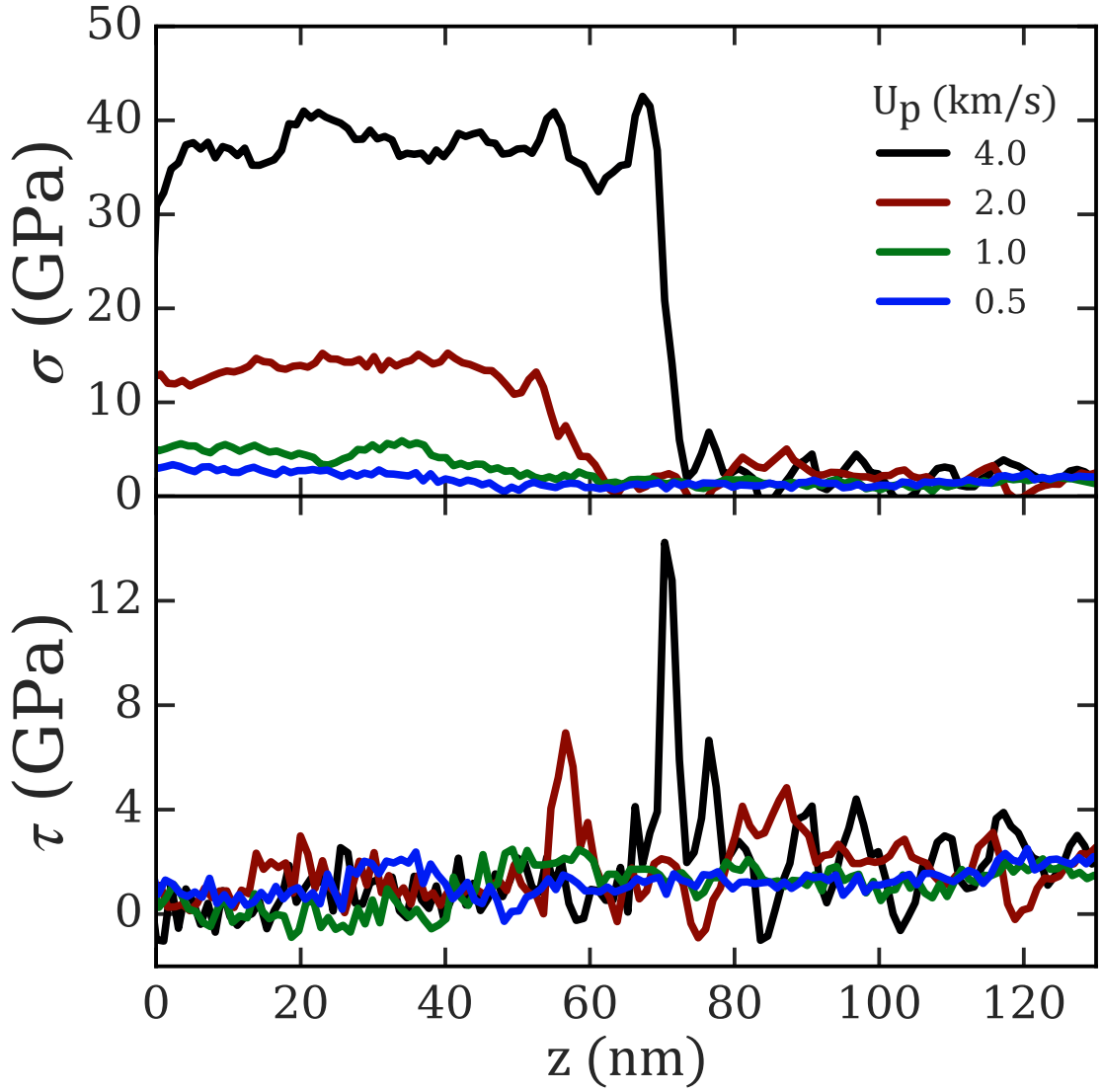

Figure 5.15: Profiles of the shock stress (σ) and shear stress (τ) at t=12 ps after impact for the [001] shock configurations in Fig. 5.14a-e. The value of σ rises rapidly with U_p. For $U_p > 0.116$ km/s ($\sigma > 1.87$ GPa) chains become unstable to buckling and collapse, keeping the value of τ behind the front below 2 GPa.

at what L buckling becomes favorable, we can extract a length-scale. Consider the elastic precursor propagating in the axial direction at speed c_s. After a time δt, it has traveled a distance $L = c_s \delta t$, while the piston has compressed this material an amount $\delta L = U_p \delta t$, resulting in a stress $\sigma \approx E(\delta L/L) = E(U_p/c_s)$. Substituting this stress in Eq. 5.5 and solving for L^2 gives:

$$L^2 = \frac{c_s}{U_p}\left(\pi^2 \frac{I}{A} + \frac{G}{E}\right) \approx \pi^2 \frac{c_s}{U_p}\frac{I}{A} \tag{5.6}$$

where the approximation on the right is valid for $G \ll E$. In this limit, $L \sim (U_p/c_s)^{-1/2}$, with a proportionality constant set by the geometry of the crystal unit-cell. We can estimate the area-moment I of the unit-cell as that of a uniform rectangle, giving $I/A = \frac{1}{12}(a^2 + b^2) \approx 6.54$ Å^2. This gives $L \approx 94$ Å $= 37c$ for $U_p = 0.116$ km/s, consistent with our observations (Fig. 5.14a).

For $U_p \geq 0.5$ km/s, we observe a condensation of smoothly bending chains into sharp kinks, analogous to fold–crease transitions observed in thin sheets (Fig. 5.14c) [173–175]. Kinks form behind the shock front and are mediated by a series of consecutive gauche-rotated dihedrals (green), which can be considered a form of "bending plasticity". Buckles condense into kinks when the elastic bending energy overcomes the trans–gauche energy barrier. This transition can be associated with a critical curvature of chain bending that depends on the specific form of the dihedral energy. Increasing U_p drives kink generation more rapidly, until kinks form almost immediately at the shock front (Fig. 5.14d-e).

5.4.4.2 Axial Tension

Stable tensile (rarefaction) shocks are uncommon in most solids but can occur provided the material's stress–strain relationship possesses a region of positive curvature. A good example is Kolsky's generation of tensile shocks in vulcanized rubber, which are stabilized by the strain hardening portion of the nonlinear stress–strain curve [176]. Unlike rubber, polyethylene crystals (and fibers) do not exhibit strain hardening [13, 82, 83]. Tensile shocks stretch the covalent back-bone bonds of the chains. Covalent bond energies are anharmonic, showing decreasing stiffness as they dissociate. This produces a tensile stress–strain relation with negative curvature—i.e., large amplitude tensile distortions travel slower than small amplitude distortions [16, 17]. Because of this property, crystalline PE does not form steady shock fronts in axial tension. Instead, tensile fronts disperse as they propagate—as illustrated in Fig. 5.16.

Fig. 5.16 plots particle velocity profiles for $U_p = 1.4$ km/s tensile fronts at several consecutive times (solid lines). The profiles are shifted so that all are centered at the origin with the leading edge on the right. The front profile is not steady, but broadens linearly in time. This linear broadening implies that all profiles collapse onto a universal curve when the horizontal axis is divided by the corresponding time. Dashed lines show this collapse for $U_p = 1.4$ km/s and similar collapses were found for other $U_p \leq 1.6$ km/s. Bond anharmonicity also influences the overall speed of the tensile front, measured by tracking the midpoint of the jump in particle velocity. For

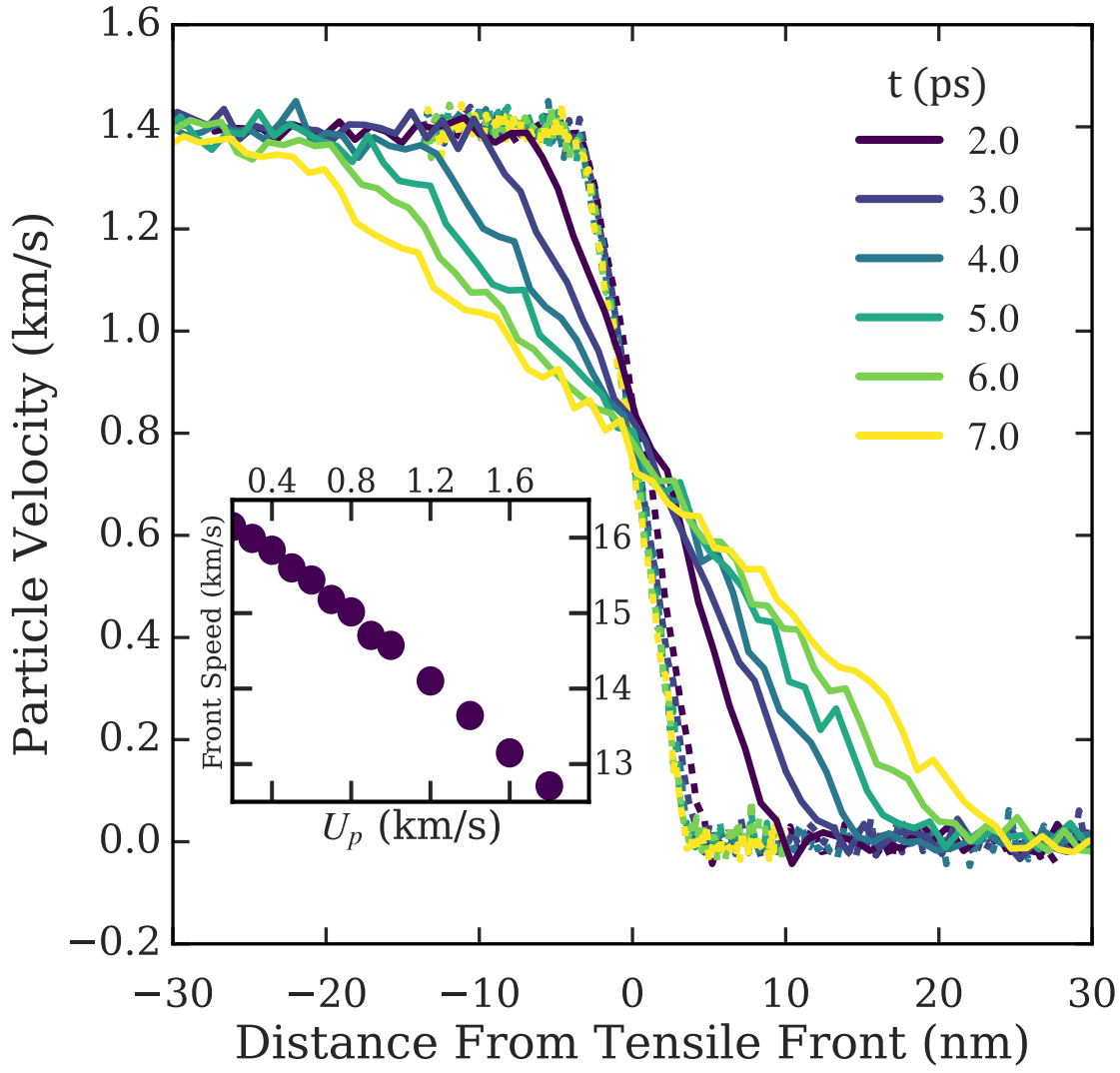

Figure 5.16: Particle velocity profiles of a $U_p = 1.4$ km/s tensile front at uniform time intervals from $t = 2$ to 7 ps after tensile loading along [001] (solid lines). Fronts are shifted so the center is at the origin and the leading edge is to the right. Anharmonic softening of backbone bonds in tension causes the tensile front to broaden linearly in time. Dividing the horizontal axis by t collapses all profiles on a single curve (dashed lines). The group velocity of the front decreases with increasing U_p (inset).

low U_p, tensile fronts propagate at about the speed of sound $c_s = 16$ km/s. Increasing U_p leads to a linear drop in front speed, as shown in the inset of Fig. 5.16.

For simulations with $U_p \geq 1.8$ km/s, the crystal fails catastrophically by chain fracture. Fig. 5.17 illustrates this behavior for $U_p = 2$ km/s. Atoms are colored by particle velocity for three consecutive times during the fracture process. Red atoms are traveling leftward with the piston at $u = U_p$, while blue atoms are at rest. Chain fracture unloads the tensile front, producing a finite-width tensile pulse that moves away from the piston (green atoms in Fig. 5.17). Other then their finite width, pulses show similar properties to the tensile fronts. They broaden over time and their group velocity decreases with increasing amplitude. The amplitude of pulses tends to decrease with increasing U_p, since fracture occurs more rapidly and unloads the crystal more effectively. At very large U_p, fracture is nearly instantaneous and generates very weak tensile pulses traveling with speed c_s.

We can compare the observed onset of chain fracture to quasi-static results. Uniaxial tension simulations with affine extension of the periodic box were done at $T = 300$K and an engineering strain rate of 10^8 s^{-1} that is low enough for stress to equilibrate across the sample. Chains fractured at an engineering strain of about 0.11. For a tensile front traveling at the speed of sound, the effective engineering strain behind the front should be $\sim U_p/c_s$. This suggests we should observe fracture when $U_p \approx 0.11 c_s \approx 1.76$ km/s, which agrees well with our dynamic measurements.

In this analysis we have studied an idealized PE crystal with effectively infinite

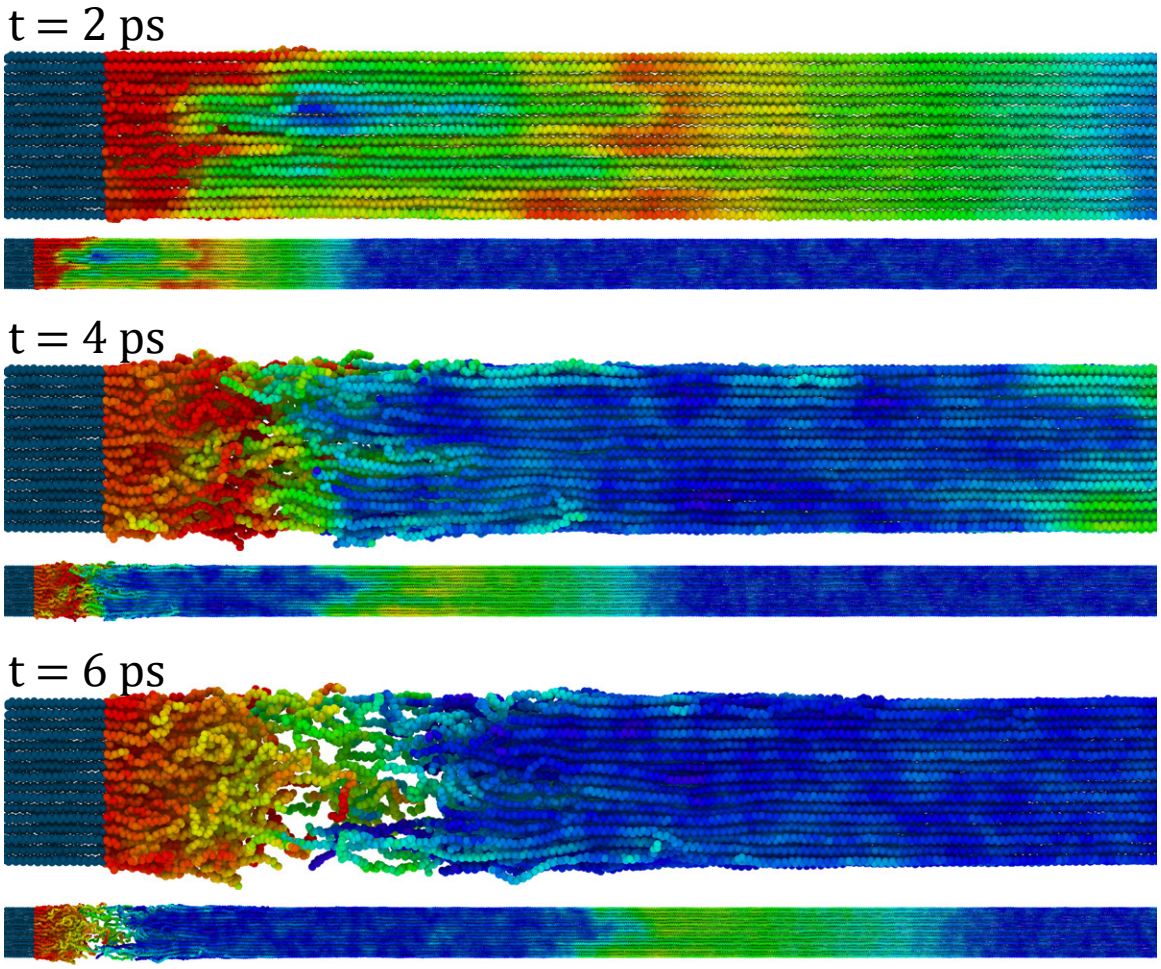

Figure 5.17: Atomic configurations for a $U_p = 2$ km/s tensile loading along [001] at $t = 2$, 4, and 6 ps. Two magnifications are shown for each time with a closeup (40 nm) above a larger view (136 nm). The piston (gray) moves leftward at 2 km/s and configurations are plotted relative to its position. Atoms are colored qualitatively by particle velocity, with red atoms moving leftward at U_p and blue atoms at rest. Chains fracture quickly after shock, forming a tensile pulse (green atoms) that propagates into the material at $\sim c_s$.

chains (no chain ends). The only mode of tensile failure is fracture by chain scission. Chapter 3 showed that PE crystals with chain ends do not yield by chain scission during quasistatic loading. Instead, chains slip by nucleating 1D dislocations at chain ends [13]. The presence of chain ends could modify the dynamic fracture process by introducing dislocations and slip as additional yield mechanisms. Whether chain slip would prevent scission during shock is not obvious. Both mechanisms could compete to relax shock induced stresses, but if the rate of slip is slow relative to the rate of shock loading, then chain scission would still occur. We defer studying this competition of plastic relaxation mechanisms during high rate loading to future work.

5.5 Summary and Conclusions

In this chapter we studied shock loading of amorphous and crystalline polyethylene under both compressive and tensile loading with impact velocities from 100 m/s to 5 km/s. Tensile loading is common in applications of fibers in weaves and composites. Stable shock fronts are only expected when a material hardens under strain. Polyethylene does not strain harden under tension and no stable shock front was observed. Amorphous samples fail through craze formation, growth and fracture near the loading region. Crystals in fibers are typically aligned with chain backbones along the fiber. Tensile loading in this direction at $U_p < 2$ km/s produces a front that broadens linearly with time rather than a true shock front. The tension behind the

front grows with U_p, and for $U_p \geq 2$ km/s the system fails through chain fracture. We expect that this may be an upper bound for fracture in semicrystalline fibers since amorphous regions, chain ends and other defects not included in our simulations will facilitate fracture.

Compressive loading of amorphous PE produces simple shock fronts. Because the yield stress is low, the shock velocity agrees with Pastine's hydrostatic model for $U_p \geq 0.5$ km/s. For $U_p = 0.3$ km/s the shear stress behind the shock front is about a quarter of the compressive stress and U_s is about 10% above Pastine's prediction. The discrepancy grows with decreasing U_p. No elastic precursor was observed and we estimate that the system will remain overdriven until U_p is lower than about 60 m/s.

Compressive loading of crystals produces strongly anisotropic behavior with a wide range of shock structures related to different modes of plastic deformation and crystal phase transformations. This variety of behavior is sensitive to both the crystal packing and chemical structure of the chain backbones. Thus, MD simulations require a fully atomistic treatment of interactions in order to accurately resolve and predict mechanisms of crystal plasticity. Hugoniot elastic limits were identified for shock along the three principal crystal directions and associated with direction-specific plastic deformation mechanisms.

Elastic precursor fronts were only observed for loading along the chain axis where the sound velocity (16 km/s) is much higher than in other directions (~ 3 km/s) and also larger than the highest impact velocities studied (5 km/s). The stress behind the

elastic precursor gave $\sigma_{HEL} = 1.87$ GPa, corresponding to $U_p = 0.116$ km/s at the elastic limit. As expected from this result, simulations at $U_p = 0.1$ km/s showed no plastic deformation. At $U_p \geq 0.2$ km/s, loading along the chain backbone produced transverse fluctuations that developed into buckles in the [010] plane where the shear stress $G = 1.7$ GPa is lowest. The buckles increase the density by compressing the weaker intermolecular bonds instead of the strong covalent backbone bonds. In the long wavelength limit the critical buckling stress approaches G and the observed σ_{HEL} is close to the value of G in the [010] plane. Including the wavelength dependence (Eq. 5.5) we find that the driving stress at $U_p = 0.2$ km/s should produce a wavelength of 94 Å, which is close to the observed wavelength in Fig. 5.14a. The wavelength of buckles decreases as U_p increases and the buckles sharpen into kinks for $U_p \geq 1$ km/s. Between kinks, chains rotate to an angle where neighboring chains have slipped laterally by about a lattice constant so that hydrogens on neighboring chains pack efficiently at high density. As U_p increases, this angle remains nearly constant but the spacing between kinks decreases. By $U_p = 4$ km/s the kink spacing is only a few monomers and the structure becomes more disordered.

The linear response in the plane perpendicular to chain backbones is nearly isotropic, but shock leads to highly anisotropic deformation mechanisms. Shock along the [100] axis produces a single shock front. At impact velocities $U_p < 0.7$ km/s, shock produces recoverable deformation and U_s lies above Pastine's hydrostatic prediction. Plasticity occurs above the HEL, corresponding to $U_p \approx 0.7$ km/s.

Initially plasticity involves slip along (110) planes. As U_p increases, more and more of the material is converted into a monoclinic phase with two twin orientations. Shear along twin boundaries helps to relieve shear stress, leading to fairly hydrostatic conditions. Experiments have also found evidence for formation of a monoclinic phase under compression [168, 177].

For shock along the [010] direction, plasticity sets in at a lower velocity of $U_p \sim 0.5$ km/s. For $U_p < 1.6$ km/s, plasticity produces a banded structure where a dense orthorhombic phase coexists with the equilibrium orthorhombic phase. For $U_p \geq 1.6$ km/s the entire system converts to the dense phase, which has a very high yield stress. For U_p between 2.8 and 4.0 km/s there is a two front structure. The first is a transformation front, that produces the dense orthorhombic phase and has a shock velocity above Pastine's theory because of the large yield stress. The second is a plastic front where the deformation relaxes the shear stress. The dense orthorhombic phase is deformed into a new monoclinic structure through chain rotation and translation of alternating chains along the chain backbone. Shear along the boundary between two twins of the monoclinic structure relieves the shear stress. For $U_p > 4.0$ km/s one can still identify a region of dense orthorhombic phase ahead of the monoclinic structures. However, this dense region has a constant width and is thus part of a single shock front with a velocity near Pastine's prediction.

Real crystalline PE contains crystal defects like chain-ends and amorphous inclusions, which can substantially alter the crystal's mechanics and plasticity [13, 23].

Additionally, amorphous phases in processed PE can be substantially aligned and denser than in unprocessed samples. In a companion paper, Elder et al. applied similar MD techniques to show crystal–amorphous phase boundaries in oriented PE reflect shocks and significantly attenuate shock energy [23]. It was also shown that shock propagation through amorphous PE is sensitive to density and alignment. Continued study is needed to understand how additives, defects, and nanoscale heterogeneity scatter shocks and compete with the plastic mechanisms we identify here.

PE is never purely amorphous or crystalline in applications. Further studies are needed to better understand how phase heterogeneity modifies shock behavior. While a mean-field mixing of pure phase Hugoniot's is sufficient to capture shocks in isotropic semicrystalline PE [18], this approach is unlikely to succeed for processed PE in fibers and composites. These anisotropic systems exhibit complex hierarchies of crystal and amorphous phases which span from nanometer to millimeter scales [81]. Capturing such structures is beyond the scope of molecular simulations, but our pure phase data should be valuable input for micromechanics models which can capture PE's mesocale structure. Continued multi-scale investigation could identify strategies for tuning shock absorption in high performance PE.

Chapter 6

Nonlinear Extensional Rheology of Entangled Polymers

The development of an accurate molecular model for polymer dynamics in complex flows has been the focus of intense research for more than 50 years. The tube model [4] has been incredibly successful in describing the dynamics of polymers in terms of entanglements with other chains that form a temporary confining tube that hinders diffusion. It captures the linear response of chemically distinct melts in terms of a universal function of the number of entanglements per chain Z and a material specific entanglement time τ_e and stress scale G_e. However a growing number of experiments show new physics must be incorporated to understand strongly nonlinear flows that are relevant to industrial applications. A striking example is that melts with identical Z and linear response can show opposite trends in strong elongational flows, with

viscosity rising or falling with increasing rate [25, 26, 32, 178, 179].

A number of attempts have been made to generalize the tube model based on different hypotheses about molecular mechanisms, including convective constraint release under shear [180], segmental stretch [181, 182], interchain pressure [183], formation and destruction of "slip-links" [36, 184–186], and friction reduction in elongational flows [28, 32, 187, 188]. To date, no generalization of the tube model has been able to predict behavior in strong elongational flows [25, 26, 32, 178] and experiments have not provided direct measures of changes in chain conformation during flow. Recent neutron scattering experiments have measured the residual anisotropy of chains in deformed melts after they have been quenched to a glass, but data are currently limited to strains well below steady-state ($\epsilon < 0.6$) [189, 190]. It remains unclear how the confining tube changes in nonlinear flows, how chain conformations affect dissipation and what role chemistry [191], Z, chain length, and the equilibrium entanglement length N_e play in determining the molecular mechanisms underlying nonlinear behavior.

Molecular dynamics (MD) simulations are an ideal platform for relating macroscopic response to molecular structure [192, 193], but it has been difficult to simulate strong elongational flows at sufficiently large strains to reach steady state [190, 194, 195]. In this chapter we use a recently developed technique [33, 34] to overcome this barrier. The simulations capture experimental trends in both the transient and steady state nonlinear viscosity of melts with different Z and entanglement length

N_e [32, 191]. Trends in viscosity with rate, Z and N_e are explained as a cross-over from the Newtonian limit to a high rate limit for aligned chains. A simple scaling law for the high rate behavior is derived and verified. The observed macroscopic response is shown to arise from changes in chain statistics that can be described as alignment and contraction of a confining tube with increasing strain rate. Surprisingly, changes in segment orientation only depend on the degree of entanglement Z, while chain stretching at high rates only depends upon the equilibrium entanglement length N_e. For all rates and melts, the steady-state stress is quantitatively related to changes in chain entropy over segments of length N_e.

Polymers are modeled with the well-studied Kremer-Grest bead-spring model [196] using LAMMPS [35]. All beads interact with a truncated Lennard-Jones (LJ) potential and results are presented in reduced LJ units. Linear chains of N beads are bound together with a FENE potential with mean bond length $b \approx 0.96$. To vary tube model parameters, the chain stiffness is controlled by a bond bending potential $k_{bend}(1 - \cos\alpha)$, where α is the angle between successive bonds. For the melt labeled M1, $k_{bend} = 1.5$ and there are $N_e \approx 28$ beads per rheological entanglement length [197]. For melt M2, $k_{bend} = 0.75$ and $N_e \approx 51$ [197].

Experiments typically plot dynamic viscosity data in reduced units based on tube theory to facilitate comparison between different melts [27, 32, 191]. Times are scaled by the entanglement time τ_e and the viscosity by $G_e\tau_R$, where the Rouse time $\tau_R = \tau_e Z^2$ is the characteristic time for a stretched chain to relax to its equilibrium contour

length and $G_e = \rho k_B T/N_e$ is the entanglement modulus. A dimensionless measure of flow rate is the Rouse-Weissenberg number $Wi_R = \dot{\epsilon}\tau_R$. Previous studies have measured $\tau_e \approx 1.98 \times 10^3$ and 6×10^3 for M1 and M2 melts, respectively [198,199].

Melts with M chains are equilibrated at temperature $T = 1$ and density $\rho = 0.85$ with standard methods [159]. M1 melts have $M = 1640$, $N = 112$; $M = 1094$, $N = 168$; $M = 734$, $N = 250$; or $M = 368$, $N = 500$, corresponding to $Z \approx 4$, 6, 9 or 18, respectively. M2 melts have M=918, N=200; M=354, N=300 or M=405, N=450, corresponding to $Z \approx 4$, 6 or 9, respectively. Melts are deformed at constant Hencky strain rate $\dot{\epsilon} = \partial \ln \Lambda/\partial t$ with Λ the stretch along the z-axis. Since polymers are nearly incompressible, the two perpendicular directions contract by $1/\sqrt{\Lambda}$. Flow is maintained by integrating the SLLOD equations of motion, and Generalized Kraynik-Reinelt boundary conditions are used to prevent the simulation box from becoming too small in the perpendicular directions [33,34]. Flows rates range from $Wi_R = 0.06$ to 52. We stop at Wi_R of 52 to avoid heating, which occurs as the relative flow velocities of neighboring monomers ($\sim \dot{\epsilon}b$) approaches the thermal velocity. This is particularly important for with low N since $\dot{\epsilon}$ increases with decreasing N at any fixed Wi_R.

Figure 6.1 shows how the extensional viscosity $\eta_{ex} \equiv \sigma_{ex}/\dot{\epsilon}$ evolves with time as polymers are elongated from equilibrium random coils into their steady state conformations at $Wi_R = 0.06$ to 52. Results are presented for two melts with the same $Z \approx 9$, but different lengths and entanglement lengths, $N_e \approx 28$ for M1 and 51 for M2.

In all cases, the viscosity increases over several decades in time before approaching an asymptotic steady-state value $\bar{\eta}_{ex}$. As predicted by tube theory, the two melts have nearly the same scaled response at the lowest rates, $Wi_R = 0.06$ and 0.16. Moreover, the simulations approach the analytic prediction for linear response from the tube model with $Z = 9$ (thick black line) [29].

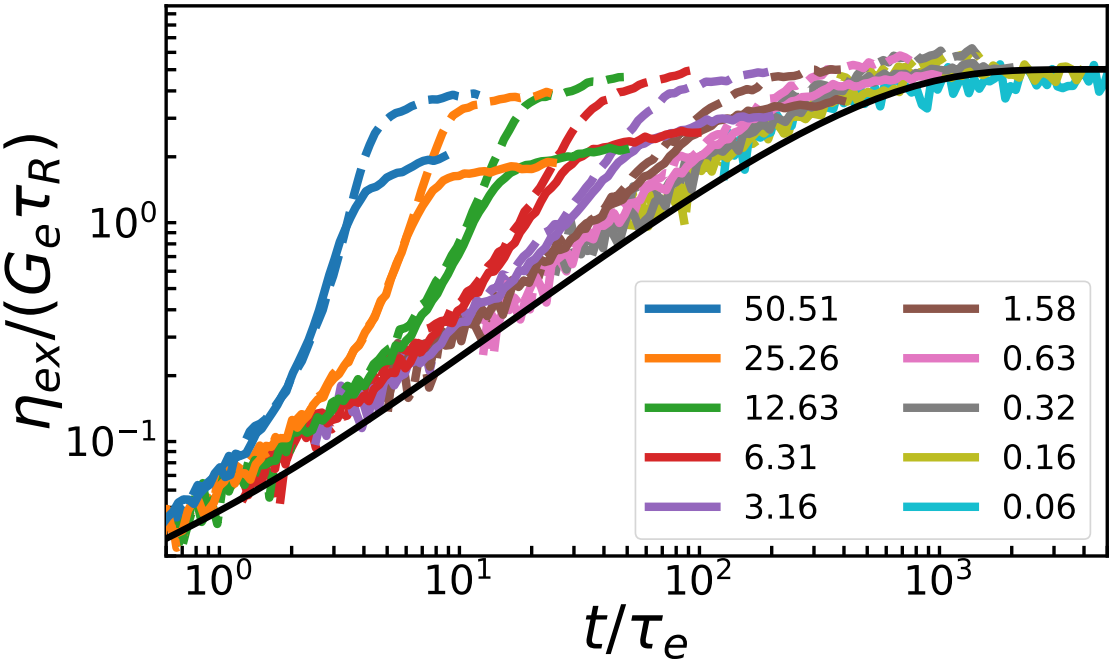

Figure 6.1: Reduced extensional viscosity η_{ex} as a function of time for two melts with $Z \approx 9$ at Wi_R from 0.06 to 52 (colors in legend). The M1 melt has $N = 250$, $N_e \approx 28$ (solid lines) and the M2 melt has $N = 450$, $N_e \approx 51$ (dashed lines). At low Wi_R both melts approach the analytic prediction from the tube model for linear response at $Z = 9$ (black line). As Wi_R increases, the two melts show increasing deviations from each other and from linear response. The steady-state viscosity at large times, $\bar{\eta}_{ex}$, shows little change with Wi_R for the M2 melt but drops rapidly with increasing Wi_R for the M1 melt.

As Wi_R increases, the viscosity grows more rapidly with time than the linear response curve and approaches a new steady-state viscosity at progressively earlier

times. The two melts show identical initial deviations from linear response at each Wi_R, but approach different steady state viscosities. They also exhibit one puzzling aspect of experimental data, the variation of $\bar{\eta}_{ex}$ with Wi_R is qualitatively different for different polymers [32, 191]. Here M1 shows a substantial decrease of $\bar{\eta}_{ex}$ with increasing Wi_R, while this shear thinning is nearly absent for $M2$ at this Z.

The linear viscoelastic envelope (LVE) shown in Fig. 6.1 is derived with the field theory of Likthman and McLeish for monodisperse, linear polymers [29]. The theory has three parameters: the entanglement time τ_e, the entanglement modulus $G_e = \rho k_b T/N_e$, and the number of entanglements per chain $Z = N/N_e$. We do not fit these parameters to match the analytic theory to our simualtions. Instead, we use the values for τ_e and N_e measured in previous MD simulation studies [197–199]. The agreement between simulations and the analytic model supports our use of coarse-grained MD to study entangled polymer rheology.

The simulations in Fig. 6.1 reproduce the time-dependent evolution of viscosity that is observed in experiments, while achieving strains that are not currently experimentally accessible. In the remainder of the chapter we focus on the steady-state behavior at long times. The steady-state extensional stress $\sigma_{ex} = \sigma_{zz} - \frac{1}{2}(\sigma_{xx} + \sigma_{yy})$ and chain statistics are obtained by averaging simulation data over the strain interval $\epsilon \in [5.5, 6.0]$.

Figure 6.2(a) shows the rate dependence of the steady state viscosity $\eta_{ex} \equiv \sigma_{ex}/\dot{\epsilon}$ normalized by the value in the Newtonian limit η_{ex}^N. Data for M1 and M2 melts

are shown alongside experimental results for polystyrene (PS) at similar Z. The significant difference between results for M1 and M2 melts at any common value of Z is consistent with the deviations from tube theory found in past experiments [32]. Although Z is not enough to determine the nonlinear response, all melts show common trends with increasing Z. For both simulations and experiments, the longest chains begin to shear-thin at the lowest Wi_R and show the largest drop in viscosity. The decrease is almost an order of magnitude for M1 and PS at $Z = 18$ and 21, respectively. As Z decreases, the onset of shear thinning moves to larger Wi_R and the decrease in η_{ex} decreases. Indeed shorter chains show some initial shear thickening for all systems [28, 32, 179].

Simulations allow us to directly correlate these changes in macroscopic response with changes in molecular structure. Snapshots in Fig. 6.3 show chains evolve from nearly equilibrium random coils at $Wi_R << 1$ to nearly straight configurations by $Wi_R = 51.5$. This evolving orientational order can be described by the nematic order parameter $P_2(n) = \frac{1}{2}\langle 3\langle \cos^2\theta_n\rangle - 1\rangle$, where $\langle\rangle$ indicates an ensemble average and θ_n is the angle between the extension axis and the vector $\vec{R}(n)$ between beads separated by n bonds. As shown in Fig. 6.4(a) and (b), $P_2(n) = 0$ when chains are randomly oriented at low Wi_R and approaches unity at high Wi_R, corresponding to complete alignment. Alignment occurs first at the full chain length ($N-1$ bonds) and affects smaller n as Wi_R increases. The rate where $P_2(N-1)$ approaches unity coincides with the onset of a decrease in η_{ex}/η_N. Both changes imply that deformation is faster

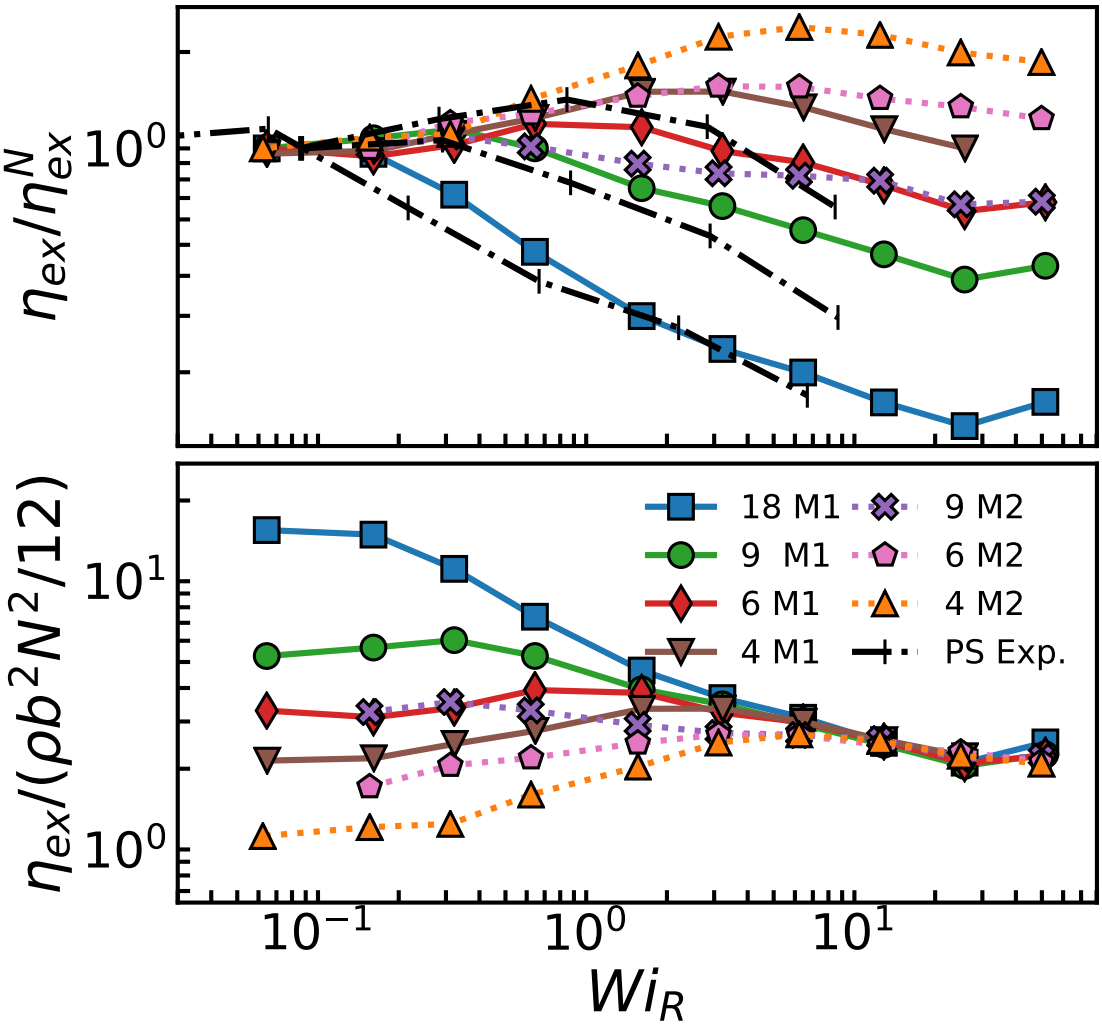

Figure 6.2: (a) Ratio of steady state viscosity η_{ex} to Newtonian viscosity vs. Wi_R from simulations of M1 and M2 melts at the indicated Z and experiments on PS at $Z = 7.5$ [179], 10 [28], and 21 [32] (top to bottom). (b) Simulation data from panel (a) renormalized by the formula for the asymptotic drag on straight chains (Eq. 6.4). Results for all chains collapse at large Wi_R.

than the longest relaxation time, the disentanglement time τ_d for chains to escape their tubes.

An expression for τ_d that includes fluctuations in contour length was derived by Doi and later refined by Likhtman et al. [29, 200]:

$$\tau_d(Z) = 3Z^3\tau_e\left(1 - \frac{3.38}{\sqrt{Z}} + \frac{4.17}{Z} - \frac{1.55}{Z^{3/2}} + \mathcal{O}(Z^{-2})\right) \tag{6.1}$$

Fig. 6.5 plots $P_2(N-1)$ versus $Wi_d = \epsilon\dot{\tau}_d(Z)$ for all melts and $\dot{\epsilon}$. All data collapse onto a universal curve which shows a rapid increase in orientation at $Wi_d \approx 1$. $P_2(N-1) \approx 0.3$ for $\dot{\epsilon}\tau_d = 1$ and saturates near unity for $\dot{\epsilon}\tau_d \gtrsim 5$. Note, this expression neglects the diffusion of the neighboring chains forming the confining tube. A recent MD study of similar systems found accounting for these effects with the "double reptation" approximation accurately described melt viscoelasticity [201]. This approximation would decrease τ_d in Eq. 6.1 by about a factor of 2 for all melts.

Alignment at the entanglement scale saturates at larger Wi_R (Fig. 6.4(b)). In the low rate regime ($Wi_R \leq 1$), $P_2(N_e)$ is the same for different melts at the same Z. By $Wi_R = 1$, $P_2(N_e)$ exceeds 0.5 for all melts, and the results collapse on to a common curve for $Wi_R >> 1$. For $\dot{\epsilon}\tau_d > 1$ chains are deformed faster than they can escape their tubes. For $Wi_R > 1$ the tube is being deformed and aligned along the extension direction faster than chains can relax to their equilibrium length along the tube. As a result, segments are stretched and aligned at shorter and shorter scales as Wi_R increases.

A measure of straightening is provided by $R(n)$ the root mean squared (rms)

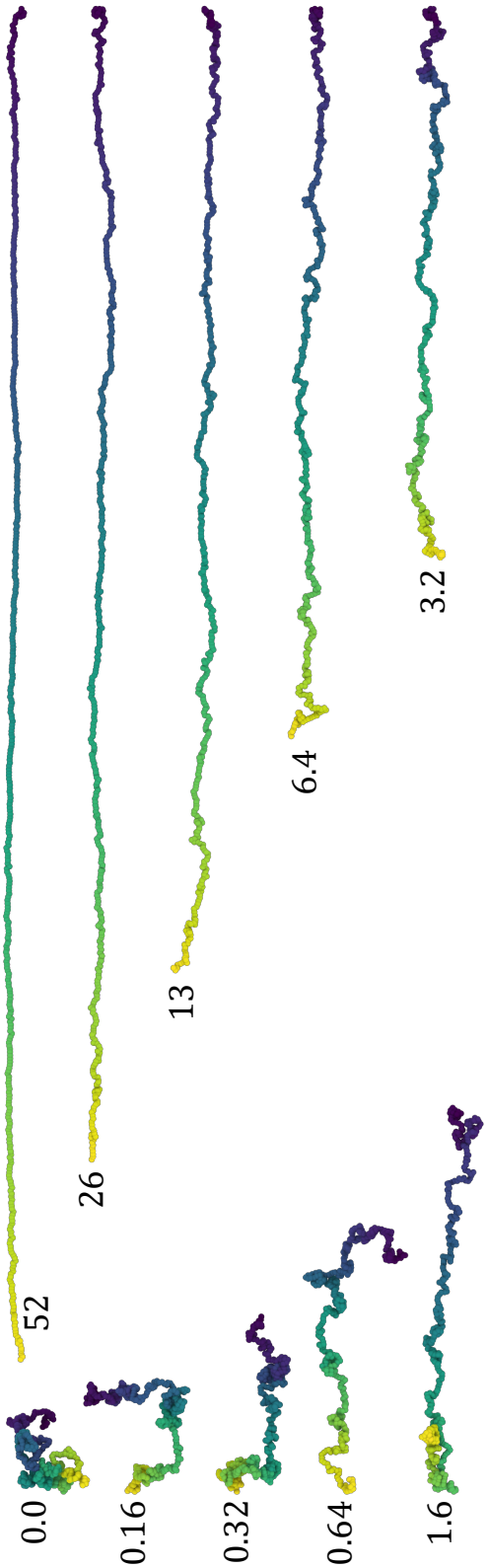

Figure 6.3: Snapshots of a chain in an M2 melt with $Z = 9$ at the indicated Wi_R. Note that as Wi_R increases the chains become more aligned along the extension direction and are more confined in the perpendicular plane. The chosen chains have end-end lengths equal to the average rms length for the system.

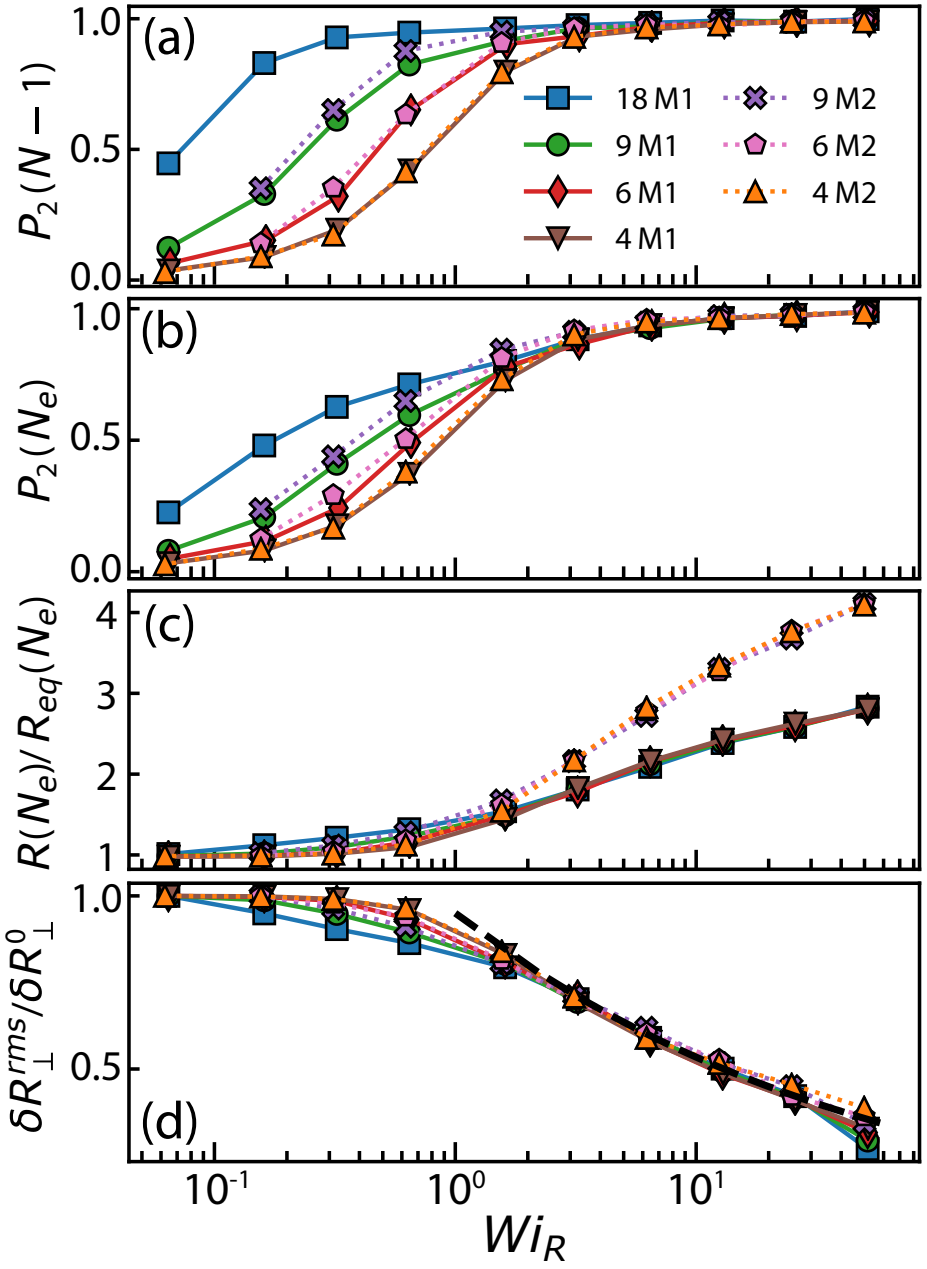

Figure 6.4: (a) Orientational order at the end-end scale $P_2(N-1)$ vs. Wi_R for M1 and M2 melts at the values of Z indicated in the legend. (b) Orientational order at the scale of equilibrium entanglements. (c) Measure of tube elongation given by stretch of tube segments of length N_e. (d) Measure of decrease in tube radius given by change in rms deviation of monomers from the line between endpoints of segments of length N_e. A black dashed line indicates $\sim Wi_R^{1/4}$ scaling.

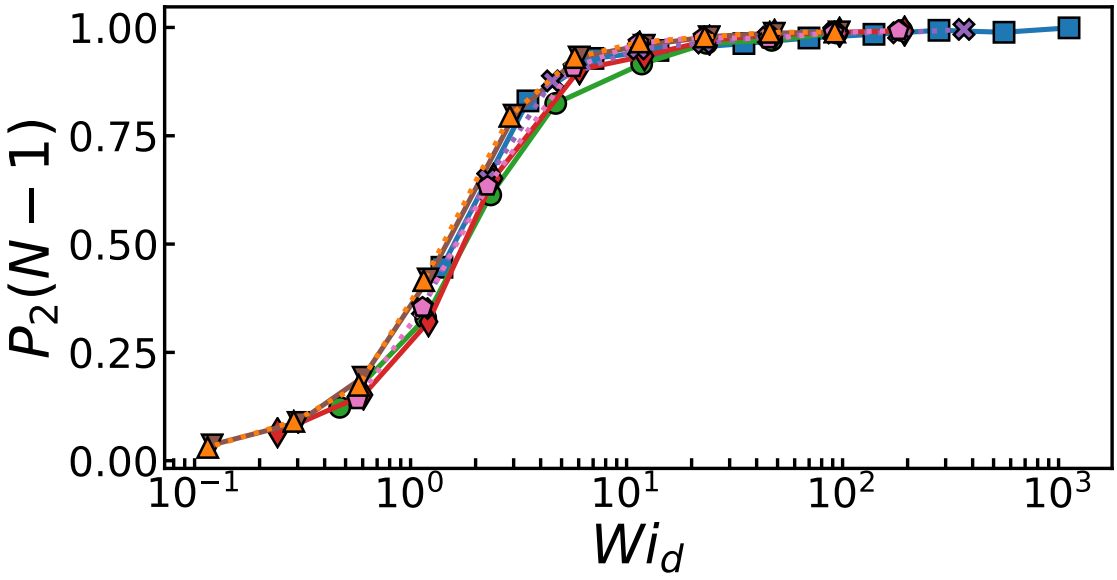

Figure 6.5: Steady-state end-end vector orientation $P_2(N-1)$ of all melts plotted versus $Wi_d = \dot{\epsilon}\tau_d$ with τ_d defined by Eq. 6.1.

length of $\vec{R}(n)$. This must be less than the contour length between beads nb, where the bond length b remains essentially unchanged at the highest Wi_R considered here. The fraction of the fully extended length $R(n)/nb$ is shown in Fig. 6.6. At $Wi_R = 0.06$ chains have a near equilibrium conformation. The ratio $R_{eq}(n)/nb$ decreases slowly with increasing n at small n because k_{bend} makes the chain fairly straight. The behavior changes above the Kuhn length $\ell_K \equiv bC_\infty$, where the chain stiffness constant C_∞ is 2.8 and 2.2 for M1 and M2, respectively [198]. At larger n, chains are random coils and $R_{eq}(n)/nb = \sqrt{C_\infty/n}$ (black solid line in Fig. 6.6). For $Wi_R = 0.06$, short chains follow the equilibrium behavior at all n. For the longer chains shown, there is a slight straightening and reduced rate of decrease in $R(n)/nb$ at large n because $\dot{\epsilon}\tau_d \sim 1$.

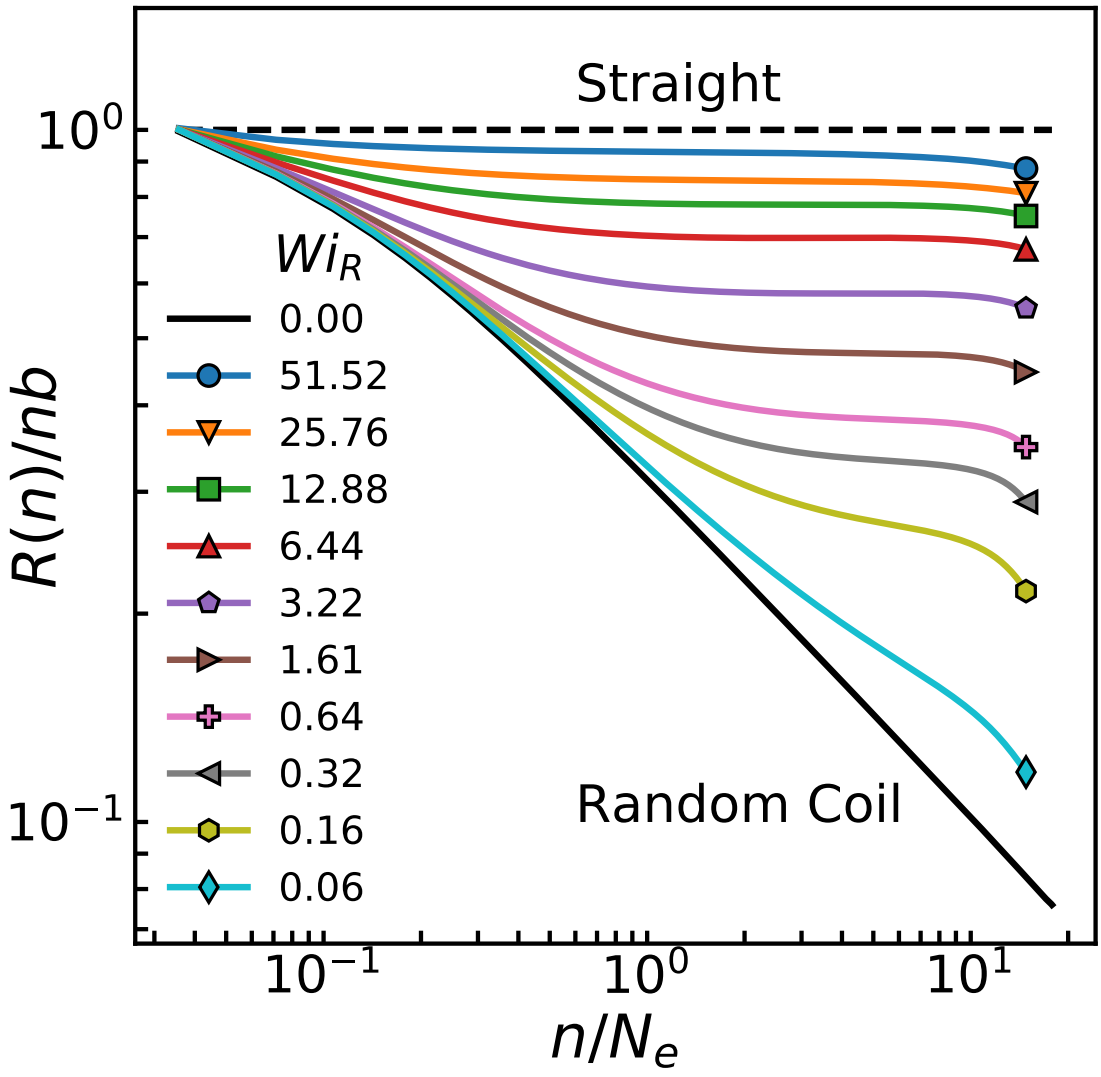

Figure 6.6: Ratio of rms length to contour length $R(n)/nb$ as a function of n for a $Z = 18$ M1 melt at the indicated Wi_R. The solid black line corresponds to the equilibrium coil structure with $R(n)/n \sim (C_\infty/n)^{1/2}$ for n larger than C_∞. Flow straightens chains at scales larger than N_e for $Wi_R < 1$. For $Wi_R > 1$, the chain becomes straight on progressively smaller scales. The small drop at large n indicates that chains are less aligned within an entanglement or two from their ends.

The scale at which there is significant straightening decreases from N to N_e as Wi_R increases towards unity. For $Wi_R > 1$ the behavior is qualitatively different, with $R(n)/nb$ saturating at large n. Saturation starts near N_e for $Wi_R = 1.61$ and moves to smaller n as Wi_R increases. These results are exactly as expected from the snapshots in Fig. 6.3. Flow increases the length of chains and reduces fluctuations around their end-end vector.

The changes in $R(n)$ imply changes in the conformation of the tube confining each chain. In equilibrium the tube has a radius of order $R_{eq}(N_e)$ and is a random walk at larger scales with a Kuhn length of order $R_{eq}(N_e)$. Under elongation, Fig. 6.4 shows that the tube stretches and narrows. The increase in tube length per N_e can be measured by calculating the ratio $R(N_e)/R_{eq}(N_e)$. As shown in Fig. 6.4c, the tube length remains nearly constant as Wi_R increases to unity and then rises rapidly. Results for each melt collapse on to a common curve and at large Wi_R approach the maximum possible stretch $\lambda_{max} = N_e b/R_{eq}(N_e) = 3.16$ and 4.8 for M1 and M2, respectively.

To characterize the change in tube diameter we consider segments of length N_e and evaluate the maximum rms fluctuation $\delta R_\perp$ in the plane perpendicular to the end-end vector. Only the central 20% of each segment is included because the fluctuation goes to zero at the ends of each segment. As for the tube length, the tube radius begins to change rapidly for $Wi_R > 1$ (although there is a small change for the longest chains when $\dot{\epsilon}\tau_d > 1$). The fractional change in tube radius at $Wi_R > 1$ is nearly the same for

all Z and both melts. In all cases $\delta R_\perp$ is of order b at the largest Wi_R, corresponding to a nearly straight chain.

Short segments are able to retain a nearly equilibrium conformation up to higher Wi_R. Since the relaxation time scales as n^2, one may expect that the relaxed length $n_{rel}(Wi_R)$ scales as $Wi_R^{-1/2}$. The length of the corresponding random walk should set the tube radius, leading to a prediction that $\delta R_\perp \propto Wi_R^{-1/4}$ until the radius approaches the bond length. The tube length should grow as the number of segments of length n_{rel} times the rms length of each, implying $R(N_e)/R_{eq}(N) \propto (N_e/n_{rel})(n_{rel}/N_e)^{1/2} \propto N_e^{1/2} Wi_R^{1/4}$ until it saturates at λ_{max}. The scaling range is not large enough to accurately test these scaling exponents, but the thick dashed line in Fig. 6.4(d) shows that the decrease in $\delta R_\perp$ is consistent with a $-1/4$ power law.[1]

The alignment of chains by flow implies a reduction in their entropy that contributes to the steady-state stress σ_{ex}. While there is also an energetic contribution, it is much smaller until the tension in the chain $\sim k_b T$ per Kuhn length. These large stresses are difficult to realize in experiments and typically similar to the yield stress of the *solid* polymer [30]. One can calculate the stress due to the entropic force $\vec{F}(n)$ of segments of length n stretched to $\vec{R}(n)$. The density of such segments is ρ/n, where ρ is the monomer density. The stress tensor $\sigma_{ij} = (\rho/n)\langle F_i(n) R_j(n)\rangle$ where i and j are cartesian coordinates [30]. Since the force is directed parallel to R, the

[1] Marrucci and Ianniruberto proposed a theory predicting $\delta R_\perp \propto Wi_R^{-1/4}$ based on an inter-chain tube pressure. However, the dynamics of their theory predicts a cross-over to this scaling controlled by τ_d [183]. This cannot describe our data which shows $\delta R_\perp$ only depends on τ_R for $Wi_R > 1$.

extensional stress is $\sigma_{ex} = (\rho/n)\langle R(n)F(n)P_2(n)\rangle$ Inserting the standard result for the force on a random chain yields

$$\sigma_{ex}^{ent}(n) = \frac{\rho k_B T}{C_\infty}\left\langle \frac{R(n)}{nb} L^{-1}\left(\frac{R(n)}{nb}\right) P_2(n)\right\rangle \tag{6.2}$$

where the inverse Langevin function L^{-1} accounts for the nonlinear reduction in entropy as segments approach full extension [4, 30].

In the Newtonian limit, the tube model relates the stress to the change in entropy of segments with length $n \sim N_e$. A network of entanglements is assumed to carry the stress at larger scales [4]. It is not clear whether the same n should be used in Eq. 6.2 for the highly aligned states at large Wi_R. However, $\sigma_{ex}^{ent}(n)$ is insensitive to n at large Wi_R because of the plateau in $R(n)/nb$ (Fig. 6.6). Figure 4 plots the total measured steady-state stress versus $\sigma_{ex}^{ent}(N_e)$ for all simulated liquids in steady state. The two quantities are in excellent agreement for all melts and over three orders of magnitude in reduced stress. Deviations only become significant at the largest Wi_R where the chains are nearing complete alignment and Eq. 6.2 becomes singular. In this regime, the tension in the chain is large enough to stretch segments shorter than a Kuhn segment, leading to an increase in the bond-bending energy and deviation from Eq. 6.2. While there is no analytic extension of Eq. 6.2 to full extension, corrections can be calculated numerically as discussed in Ref. [202, 203].

To obtain the viscosity in the large Wi_R limit we equate the macroscopic rate of dissipation per unit volume $\eta_{ex}\dot{\epsilon}^2$ to the microscopic dissipation. Since chains are nearly fully extended, we consider a single straight chain in an extensional uniaxial

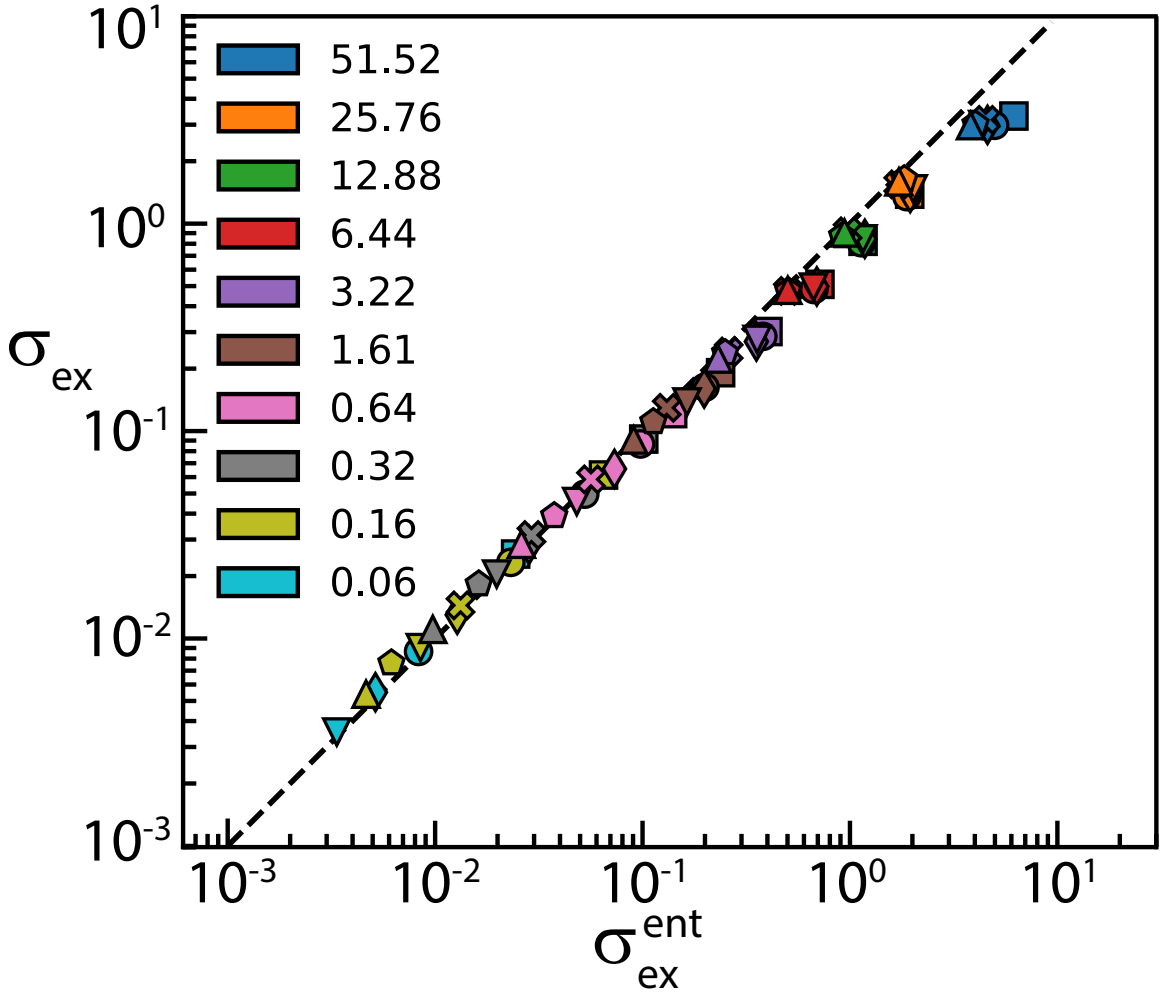

Figure 6.7: Comparison of steady-state stress from simulations σ_{ex} to the entropic stress from Eq. 6.2. Colors correspond to the values of Wi_R in the legend and symbols indicate the melt. M1 at $Z = 18$ (squares), 9 (circles), 6 (diamonds), and 4 (down triangles). M2 at $Z = 9$ (X), 6 (pentagons), 4 (up triangles).

flow. The entire chain must have the same average velocity, so the mean velocity Δv of its monomers relative to their neighbors grows linearly with distance x from the chain center as $\Delta v = \dot{\epsilon} x$. If there is a linear drag force with drag coefficient ζ, each monomer dissipates energy at a rate $\zeta \Delta v^2$. Averaging the dissipation over x gives a dissipation per monomer of

$$\left\langle \zeta \Delta v^2 \right\rangle = \zeta b^2 N^2 \dot{\epsilon}^2 / 12 \tag{6.3}$$

and thus

$$\eta_{ex} = \rho \zeta b^2 N^2 / 12 \tag{6.4}$$

In general, ζ will depend upon the chemical structure and interactions of the chain backbone.

Figure 6.2(b) shows η_{ex} normalized by $\rho b^2 N^2/12$. Results for both models and all chain lengths collapse onto a universal curve at large Wi_R whose limiting value corresponds to ζ. Note that M1 and M2 are expected to have nearly the same ζ because they have identical monomer masses, bond lengths and interchain interactions. The main difference is that M2 is more rigid and this becomes irrelevant for aligned chains. The derived value of $\zeta \approx 2$ is consistent with the viscosity of short chains.

The above results explain many experimental observations on the nonlinear response of polymers under strong elongational flow and relate them to changes in chain conformation. At all Wi_R the steady-state stress is quantitatively described by the entropic forces associated with chain straightening on segments of length N_e. This

entropic stress is balanced by drag forces that also depend on chain conformation and scale with different powers of Z at low and high Wi_R.

For small Wi_R, chains remain close to Gaussian random walks. As predicted by the tube model and shown in Fig. 6.8, $\eta_{ex} \sim \eta_N$ and scales as $G_e \tau_e Z^x \propto \zeta_N N_e Z^x$ where $x \approx 3.4$ for well entangled chains and ζ_N is the monomer drag in the Newtonian limit. At high rates, chains are straight and η_{ex} rises as ζN^2. The ratio between the Newtonian and high-rate viscosity scales as $\sim Z^{1.4} \frac{\zeta_N}{N_e \zeta}$. The Z dependence explains why the amount of extension-rate thinning increases with chain length in both experiments [32, 178, 179] and simulations (Fig. 6.2). The thinning of long chains can be fit to a power law with a Z dependent exponent over about one decade in rate.

Chemistry enters through N_e and the drag coefficients. Rate thickening may be observed at small Z for melts like M2 with small $\frac{\zeta_N}{N_e \zeta}$. The increased stiffness of M1 chains decreases N_e and increases the amount of thinning. Diluting with short chains increases N_e, which may be part of the reason solutions show less shear thinning [28, 32, 187, 188]. There is also evidence that solutions suppress changes in drag because solvent molecules are less aligned by flow [28, 32, 187, 188]. Changes in monomer drag with alignment as Wi_R increases are small in our systems because the monomers are spherical. Large effects may be expected for polymers with large and rigid side groups.

Many recent methods identify entanglements with contacts between the primitive paths of polymers [204–206]. These methods suggest that there are no entanglements

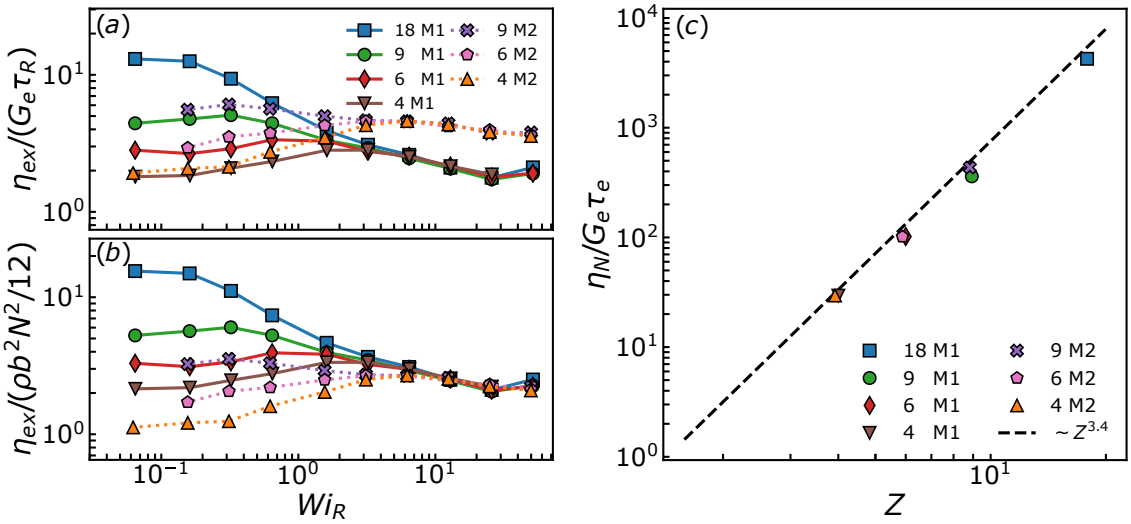

Figure 6.8: Comparison of η_{ex} data normalized by their high and low Wi_R scalings. (a) The viscosity normalized by tube theory parameters. Different models with the same Z coincide at low Wi_R. At high Wi_R the ratio is independent of Z but different for different models. (b) η_{ex} normalized as in Fig. 6.2 with Eq. 6.4 to give the asymptotic, high-rate drag on straight chains. Results for all melts collapse at large Wi_R. (c) Scaled Newtonian viscosity $\eta_N/G_e\tau_e$ as a function of Z. Simulated melts exhibit the approximate $\eta_N \sim Z^{3.4}$ scaling expected for well entangled melts (dashed line).

between the highly aligned chains at large Wi_R [36,184–186]. However, our measured chain statistics show that chains are highly confined at large Wi_R and the volume of the tube associated with the length and radius in Fig. 6.4 decreases as Wi_R rises. Studies of chain relaxation will play an important role in unraveling the relationship between entanglements and the confining tube at high rate and are the subject of the next chapter.

Chapter 7

Stress Relaxations From Steady Extensional Flows

7.1 Introduction

Entangled polymer liquids exhibit highly correlated many-body dynamics and a rich hierarchy of viscoelastic relaxation modes that emerge from the topological entanglement of chains at long length scales. As discussed in the previous chapter, the canonical tube theory for entangled polymer dynamics excels in equilibrium and linear response, but breaks down when nonlinear elongational flows are applied. We have seen that some equilibrium ideas, like the entropic stress, can be extended to steady-state extensional flows. However, a much harder problem is characterizing the *dynamic* behavior of flowing polymers when they are far from equilibrium. This

requires understanding the nonequilibrium evolution of chain statistics while chains are adapting to flow, which is very difficult to measure experimentally. Instead, experiments usually measure the evolution of rheological properties like the extensional stress $\sigma_{ex}(t)$ or viscosity $\eta_{ex}(t)$ [27]. Microscopic details of the fluid structure must then be inferred by fitting experimental data to hydrodynamic models for entangled polymer flow [4, 27]. Modelers postulate analytic expressions to describe molecular processes that may occur during relaxation, and these mechanisms are validated based on how well they improve agreement between models and experiments. This indirect approach has been quite effective at developing accurate models for nonlinear shear flow [27,193]. However, nonlinear extension remains challenging, with many competing and contradictory model frameworks that remain unvalidated.

Stress relaxations are a particularly convenient experimental protocol for comparing models to experiments. During a stress relaxation experiment, a controlled flow history $\dot{\epsilon}(t)$ is imposed for $t < 0$ and the decay of $\sigma_{ex}(t)$ is monitored for $t > 0$. Experimentalists try to generate idealized flow histories that are easily compared to hydrodynamic models. Common choices are relaxation from a rapid step-strain ($\dot{\epsilon}(t) \propto \delta(t)$), or relaxation from a steady-state flow where $\dot{\epsilon}(t)$ can be assumed constant prior to relaxation. For extensional flows, step-strains are much more common than steady-state relaxtions. This is because generating steady-state flows requires large Hencky strains and samples become thin filaments. Stress relaxations can be interrupted by capillary instabilities and other issues related to the fragile sample

geometry [27].

In this chapter, we use molecular dynamics to perform stress relaxations from the steady-state extensional flows generated in the previous chapter [112]. The periodic boundary conditions of our simulations (described in [33, 34]) suppress the flow instabilities that plague experiments and allow us to observe complete relaxation of the extensional stress $\sigma_{ex}(t)$ from steady state. In addition, MD simulations provide the molecular details of the evolving chain conformations during flow, which we characterize and relate to trends in $\sigma_{ex}(t)$.

7.2 Model and Methods

7.2.1 Kremer-Grest Bead Spring Model

Polymers are modeled with a Kremer-Grest bead-spring model [196]. All beads have a mass m and interact with a purely repulsive Lennard-Jones potential $U_{LJ}(r) = 4u\left[(a/r)^{12} - (a/r)^{6})\right]$ that is cutoff at $r_c = 2^{1/6}a$. The short cutoff is computationally efficient but makes the interactions between beads purely repulsive. An experimental polymer with no attractive interactions would fly apart. However, simulations allow us to fix the polymer density, and Grest recently showed that adding monomer attraction to bead-spring melts does not change their rheological behavior for our chosen density $\rho = 0.85/a^3$ [207]. Covalent bonds between adjacent monomers on a chain are modeled with the finitely extensible nonlinear elastic (FENE) potential

$U(r) = -0.5(KR^2)\ln(1-(r/R)^2)$, with K=30 u/a^2 and R=1.5 a. Chain stiffness is set by an angle potential between neighboring bonds ($U_{bend} = k_{bend}(1-\cos\alpha)$) where α is the angle between two adjacent bonds on a chain and $k_{bend} = 1.5\ u$. All physical quantities in the text are reported in reduced LJ units. The units of length, energy, and time are reduced by a, u and $\tau = \sqrt{ma^2/u}$, respectively.

For linear chains with N monomers, the tube model of entangled polymer dynamics characterizes the equilibrium properties of the melt in terms of the degree of entanglement $Z = N/N_e$, and a chemically specific entanglement time $\tau_e \sim N_e^2$ and plateau modulus $G_e = \rho k_b T/N_e$ [4]. τ_e characterizes how long it takes for a chain to feel the effect of entanglements from neighboring chains, and G_e is the free energy density of the entanglement network. The tube theory parameters of the bead-spring model we use have been thoroughly characterized in prior studies [197, 198]. They have found that $\tau_e \approx 1.98 \times 10^3\tau$ and $N_e \approx 28$ beads. We will use $N = 500$ beads so $Z = N/N_e \approx 18$ rheological entanglements per chain. The Rouse time $\tau_R = \tau_e Z^2$ is the longest dissipative relaxation time for chains to relax stretch within their confining tubes, and is $\approx 324\tau_e$ for the bead-spring model. Finally, the disentanglement time τ_d characterizes the time required for the chain to escape its confining tube. The analytic form for τ_d is more complex, since it is renormalized by fluctuations of the chain stretch. Grest et al. [201] found τ_d for the bead-spring model is best modeled by the expression of Likhtman et al. [29] with the double reptation approximation: $\tau_d = \frac{3}{2}(1 - \frac{3.38}{Z^{1/2}} + \frac{4.17}{Z} - \frac{1.55}{Z^{3/2}})\tau_e Z^3$. This gives $\tau_d \approx 11\tau_R$ for our chains, which agrees

well with our data.

7.2.2 Simulating Extension and Relaxation

The LAMMPS software package is used to integrate the equations of motion with a time step $\Delta t = 0.007\tau$ [35]. All simulations are run at a temperature of $T = 1\ u/k_b$ and constant monomer density $\rho = 0.85/a^3$. A Nose-Hoover thermostat with a damping time of 10τ regulates the temperature. We varied the thermostat damping time and and found 10τ is sufficient to control the temperature while also slow enough to not introduce numerical artifacts for our fastest flow rates. If the damping time is too short, then the thermostat can artificially increase the viscosity.

Startup uniaxial extensional flow simulations stretch the fluid along the z-axis at a constant Hencky strain rate $\dot{\epsilon} = \frac{\partial \log \Lambda}{\partial t}$, where Λ is the stretch along the flow axis, z. As in the last chapter, we will use the Rouse Weissenberg number $Wi_R \equiv \dot{\epsilon}\tau_R$ as a dimensionless measure of strain rate. Polymer liquids are nearly incompressible, so the perpendicular directions are both contracted by $1/\sqrt{\Lambda(t)}$ to preserve volume. During flow, the SLLOD algorithm is used so that the thermostat only couples to the peculiar velocities of the particles [208, 209]. Generalized Kraynik-Reinelt (GKR) boundary conditions systematically remap the simulation box during flow, ensuring that the box never becomes too narrow in the contracting dimensions. GKR boundaries are a generalization of the Kraynik-Reinelt boundary conditions for planar flows. We use the method derived by Dobson [33] and implemented in LAMMPS by Nicholson and

Rutledge [34]. The total momentum of a simulation can drift during extensional flow due to numerical integration errors. To correct for this, we reset the center of mass momentum of the system to 0 every 100 time steps.

We begin stress relaxations once systems reach a maximum Hencky strain between $\epsilon = 6 - 6.4$. Relaxations for all but the lowest two Wi_R start at $\epsilon = 6$, while lowest begin at the slightly larger values indicated in Figure 7.1(a). This larger strain does not influence the behavior of these low Wi_R systems, where the steady-state is well developed and has become insensitive to ϵ. The maximum strains are larger than what experiments typically associate with steady-state and larger than the limit of $\epsilon \approx 5.5$ that has been reliably achieved in a filament stretching rheometer [27,178,179]. Simulations can reach these strains because the periodic boundary conditions enforce a homogeneous flow and suppress instabilities that disrupt experimental flows.

7.2.3 Chain Statistics

Systems are sheared to a Hencky strain $\epsilon > 6$ where the stress and chain statistics appear to be nearing steady-state values. Then extension is stopped and complete snapshots of all monomer positions are recorded at intervals of $\tau_e/4$. Chain statistics are calculated for each snapshot and averaged over all chains. End-end statistics are calculated from the displacement vectors connecting each chain's ends. When computing internal statistics for segments with $n < N - 1$ bonds, each chain is partitioned into multiple segments of length n and statistics are calculated for each

segment. Unless stated, averages are carried out over all segments of all chains. Statistics for the initial steady-states are computed by averaging over all snapshots in the strain interval $\epsilon \in [5.5, 6.0]$. Since the stress relaxation is a dynamic process, quantities computed are averaged over all chains at a given time, and are not averaged over time unless otherwise noted. We use a subscript 'eq' to denote the value of statistics in the equilibrium state.

7.3 Results and Discussion

7.3.1 The Extensional Stress

Figure 7.1(a) shows the extensional stress $\sigma_{ex} = \sigma_{zz} - \frac{1}{2}(\sigma_{xx} + \sigma_{yy})$ during startup uniaxial elongational flow with constant Wi_R ranging from 0.16 to 25. The stress increases before plateauing to a steady-state stress once ϵ is larger than about 2. The steady stress increases with increasing Wi_R and the shape of the rise changes as Wi_R increases above 1. At low Wi_R, the σ_{ex} curves have negative curvature and plateau to a well defined steady-state. When $Wi_R > 1$, σ_{ex} rises rapidly with a positive curvature that is reminiscent of strain hardening in solid polymers. The plateaus at large Wi_R are not flat and continue to show a slow rise with increasing ϵ out to the largest strains we have considered (up to $\epsilon > 6.5$).

We can relate this slow growth to the continuing evolution of the conformational statistics of the chains. Deformation rapidly changes the average stretch and orienta-

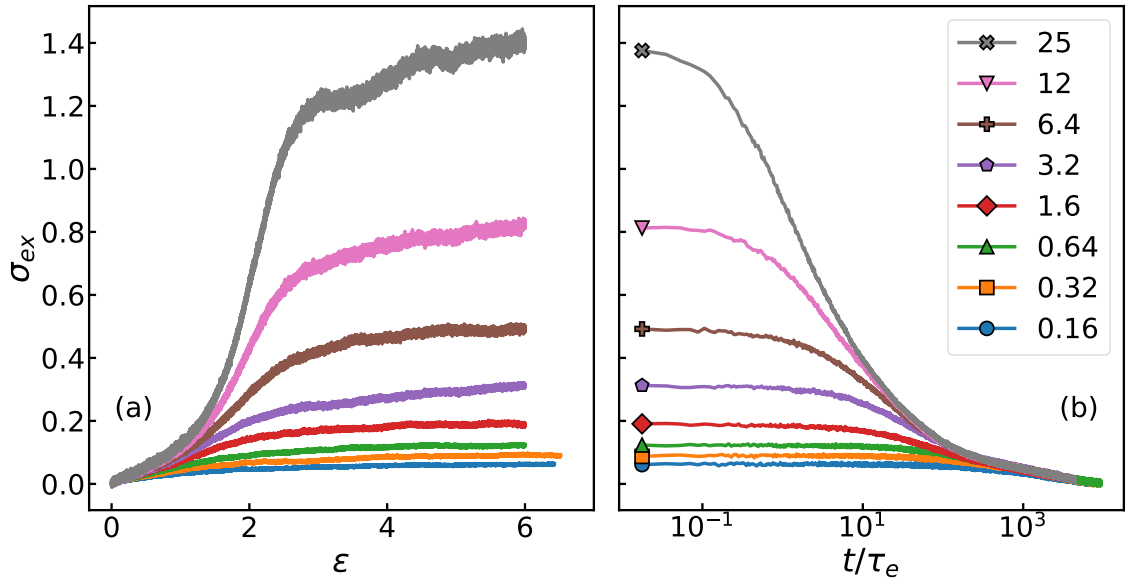

Figure 7.1: (a) The extensional stress σ_{ex} versus strain during startup uniaxial extensional flows for all Wi_R. The terminal point of (a) is the starting state for each stress relaxation shown in (b). Relaxations plot $\sigma_{ex}(t)$ versus t/τ_e, with t the time since flow ceased.

tion of polymer conformations, but the full probability distribution functions of these quantities take time to equilibrate to a steady-state distribution. This can affect quantities like the stress, which are sensitive to the tails of conformation distributions—i.e., the most extreme chain conformations present. Experiments are typically limited to $\epsilon \sim 3$ to 6 and report values at the largest strain as steady-state [26, 26, 178, 179]. Our results suggest that true steady state is not reached until much larger values. The problem is particularly acute for high rates, since the total stretch time scales inversely with Wi_R. For example, simulations at $Wi_R = 25$ reach $\epsilon = 6$ after only $< \tau_R/5$ and one may expect that times larger than τ_R are needed to fully adapt to the flow.

Although it is not the focus of this chapter, we note that it will be interesting to study the kinetic processes that control how chain conformations adapt to flow and approach steady state. Experiments by Schroeder et al. [210, 211] have explored the distinct kinetic pathways entangled chains take to stretch during flow and relaxation. They find that chains extended by flow approach their steady conformations by a variety of kinetic pathways, some taking much longer than others. This "molecular individualism" emerges from the competition of convection and diffusion and is a potential explanation of the slow growth we observe at large Wi_R. Detailed analysis of our chain statistics should reveal whether this is the case and provide useful data to compare to these experiments.

Figure 7.1(b) shows the relaxation of $\sigma_{ex}(t)$ with reduced time t/τ_e, where t is the time since flow ceased. Figure 7.2 plots the same data on a log-log scale. For all Wi_R, σ_{ex} relaxes over many decades in time and does not completely decay until $t > 2\tau_d$. All systems exhibit an initial plateau before σ_{ex} begins to decrease. The delay time decreases with increasing Wi_R and should be associated with the fastest relaxation mode that is driven out of equilibrium by the flow.

As for start-up, σ_{ex} exhibits different behavior as Wi_R increases. For $Wi_R < 1$, the delay time is long and σ_{ex} begins relaxing only after a time $\sim \tau_d$. For $Wi_R > 1$, the delay time decreases and σ_{ex} relaxes rapidly. Separate curves with $Wi_R > 1$ converge toward each other, with all superposing after a few τ_R ($\sim 350\tau_e$). These high Wi_R curves then converge onto the low Wi_R curves after about $\tau_d \approx 3500\tau_e$.

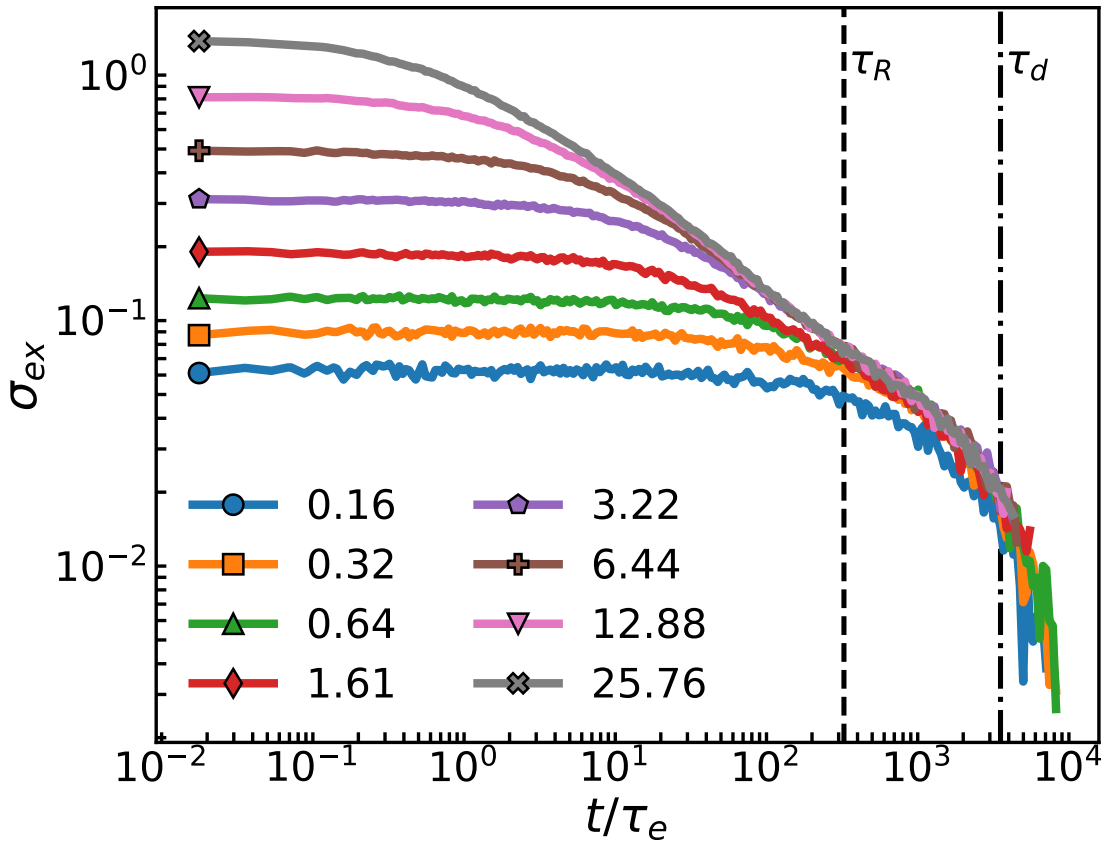

Figure 7.2: Extensional stress relaxations $\sigma_{ex}(t)$ versus t/τ_e with t the time since flow ceased. Relaxations start from steady-state flows at Wi_R indicated by the symbol at the first recorded time. τ_R/τ_e and τ_d/τ_e are indicated by a dashed and a dash-dotted line, respectively.

The qualitative behavior of σ_{ex} is consistent with the spectrum of relaxation modes predicted by rheological models. Many theories model relaxation in entangled melts with two spectrums of exponential relaxation modes [4, 27]. One spectrum is due to reptation relaxing chain orientation and is governed by τ_d. The other is due to stretch relaxation and governed by τ_R. It is common to assume individual modes are decoupled, however, recent simulation studies have shown this is generally not true [212]. Nonetheless, the Rouse and reptation mode spectrums are a useful framework for discussing and interpreting our data.

For $Wi_R < 1$, flow is strong enough to orient chain primitive paths but not stretch them much. Rouse-like modes should remain near equilibrium, and σ_{ex} for different Wi_R converge for times $\sim \tau_d$. For $Wi_R > 1$, models predict that flow both orients and stretches chain primitive paths. Larger Wi_R should stretch chains more, leading to a more rapid onset of retraction as higher Rouse modes are populated. The highest Wi_R curves "catch-up" with each-other as they retract and relax their higher order Rouse modes. The retraction process ends after a few τ_R, when the $Wi_R > 1$ curves superpose. After retraction, these systems must still undergo reptation to relax their orientation. This leads to their convergence with the low Wi_R curves at long times.

7.3.2 Chain Stretch and Orientation

Simulations allow us to test model predictions by directly observing the evolution of chain conformations during relaxation. Figure 7.3 shows typical chain conforma-

tions at four times during relaxation for all Wi_R. The flow axis is along the vertical direction, and each chain shown has an end-end vector $R(N)$ equal to the rms value for chains at the corresponding time. A chain in the equilibrium coil conformation is shown in the upper right for reference. At $t = 0$, chains are in their steady-state conformations. For all Wi_R, the extensional flow has extended the primitive paths of the chains along the flow axis. The stretch rises rapidly for $Wi_R > 1$ and chains are nearly fully extended by $Wi_R = 25$. Detailed analysis of these steady-state flows is provided in the previous chapter.

Figure 7.3 shows chain conformations at $t = 0$, τ_R, and τ_d after flow ceases. Low Wi_R systems show little visual change in their conformations until times $\sim \tau_d$, consistent with the relaxation of σ_{ex} in Figure 7.1 and 7.2. In contrast, chains at large $Wi_R > 1$ undergo rapid retractions such that average conformations at different Wi_R become nearly indistinguishable after $\sim \tau_R$. For times $\geq \tau_d$, chains begin losing orientational order as they escape their confining tubes. In this regime, relaxation from all Wi_R is dominated by reptation and the longest relaxation time τ_d.

We can quantify the degree of chain straightening shown in Figure 7.3 with the internal distance function $R(n)$, which is the RMS magnitude of the vector $\vec{R}(n)$ between beads connected by n bonds, averaged over the ensemble of segments. $R(n)$ must be less than the contour length nb and it is convenient to work with the extension ratio $R(n)/nb$. Here we use the mean bond length b for the given state, but even at the highest Wi_R in steady state this is $< 1\%$ greater than the equilibrium value. In

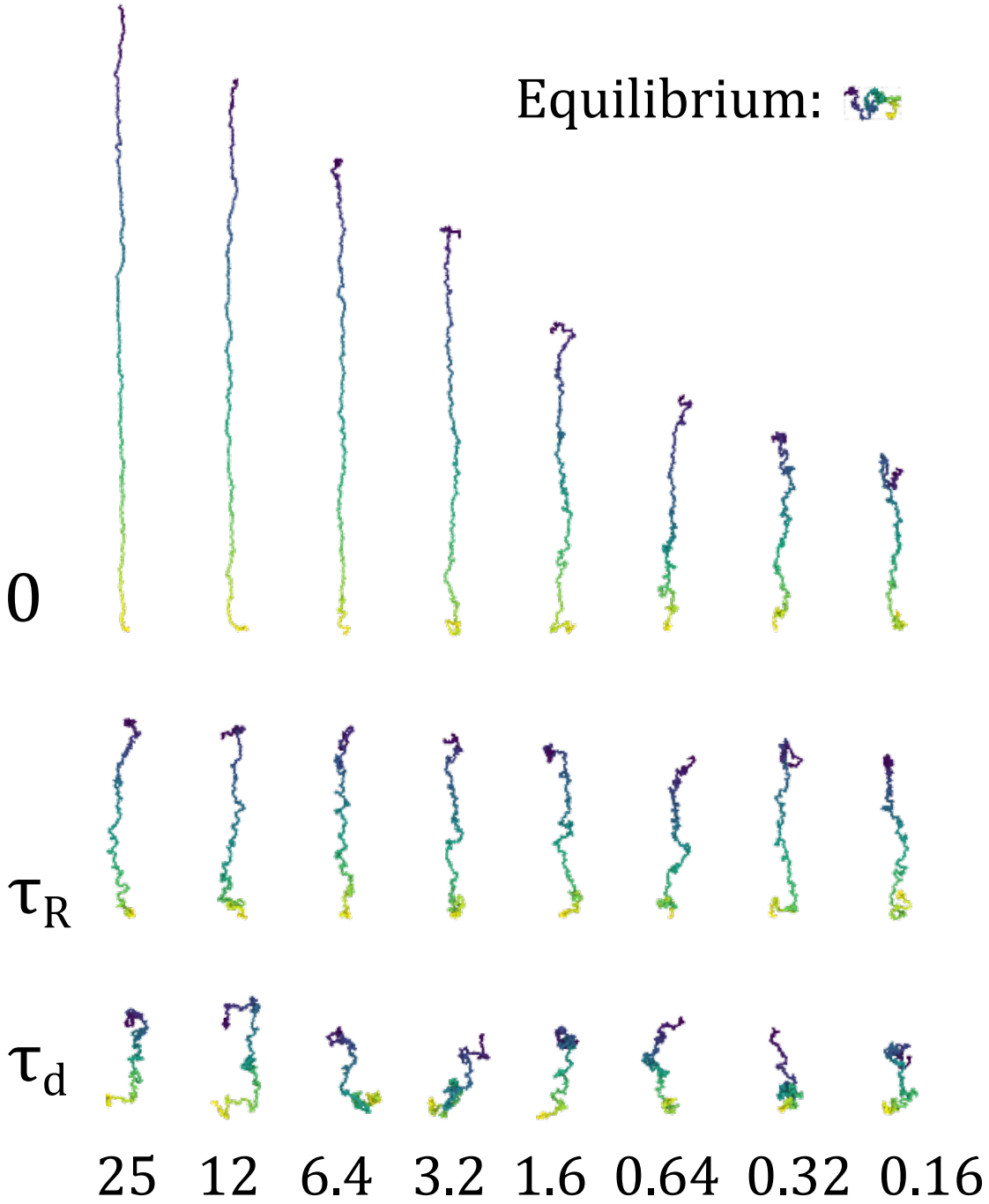

Figure 7.3: Typical chain conformations for $t = 0$, τ_R, and τ_d after relaxation for all Wi_R. The conformations correspond to chains with the average end-end vector at the indicated time. For $Wi_R > 1$, chains retract rapidly over τ_R and converge to the equilibrium primitive path length and diameter. Once $t > \tau_d$, all conformations begin to lose their orientational order as their ends explore regions outside of the initial aligned tube.

equilibrium, $R(n) = R_{eq}(n)$ and $R(n)/nb \sim n^{-1/2}$ when n is larger than the Kuhn length. For a fully extended chain $R(n)/nb = 1$, and if a chain is partially extended above some scale n_* then $R(n)/nb$ will approach a constant ≤ 1 for $n > n_*$.

Figure 7.4(a)-(c) plots $R(n)/nb$ at different times. The equilibrium conformation $R_{eq}(n)/nb$ is indicated with a black line and scales as $n^{-1/2}$ at large n. It shows some straightening at short scales due to the backbone stiffness, before transition to a random walk with $R(n)/nb \sim n^{-1/2}$ above the Kuhn length. The steady-state configurations in Figure 7.4(a) all show straightening for n larger than the entanglement length N_e. This is indicated by the plateau in $R(n)/nb$ at large n and corresponds to the alignment of the "tubes" formed by entanglements. As Wi_R increases above 1, the scale of straightening moves to progressively smaller n, corresponding to the stretch of the chains' primitive paths.

Figure 7.4(b) plots $R(n)/nb$ at $t = \tau_R$ and shows the effect of chain retraction. As is also seen visually in Figure 7.3, chains for all $Wi_R > 0.16$ have rapidly relaxed to similar conformations, with their $R(n)/nb$ curves superposing. The common curve deviates from equilibrium at about N_e and then saturates. This is consistent with the primitive path relaxing to its equilibrium length, but being completely oriented along the flow direction. This can be verified by observing that the common plateau value ~ 0.3 corresponds to $R(N-1) \approx 145$, which is equal to the equilibrium primitive path length $ZR_{eq}(N_e)$ of the chains. Thus, all systems relax back to their *equilibrium* primitive path length after retraction, even after being fully aligned by flow.

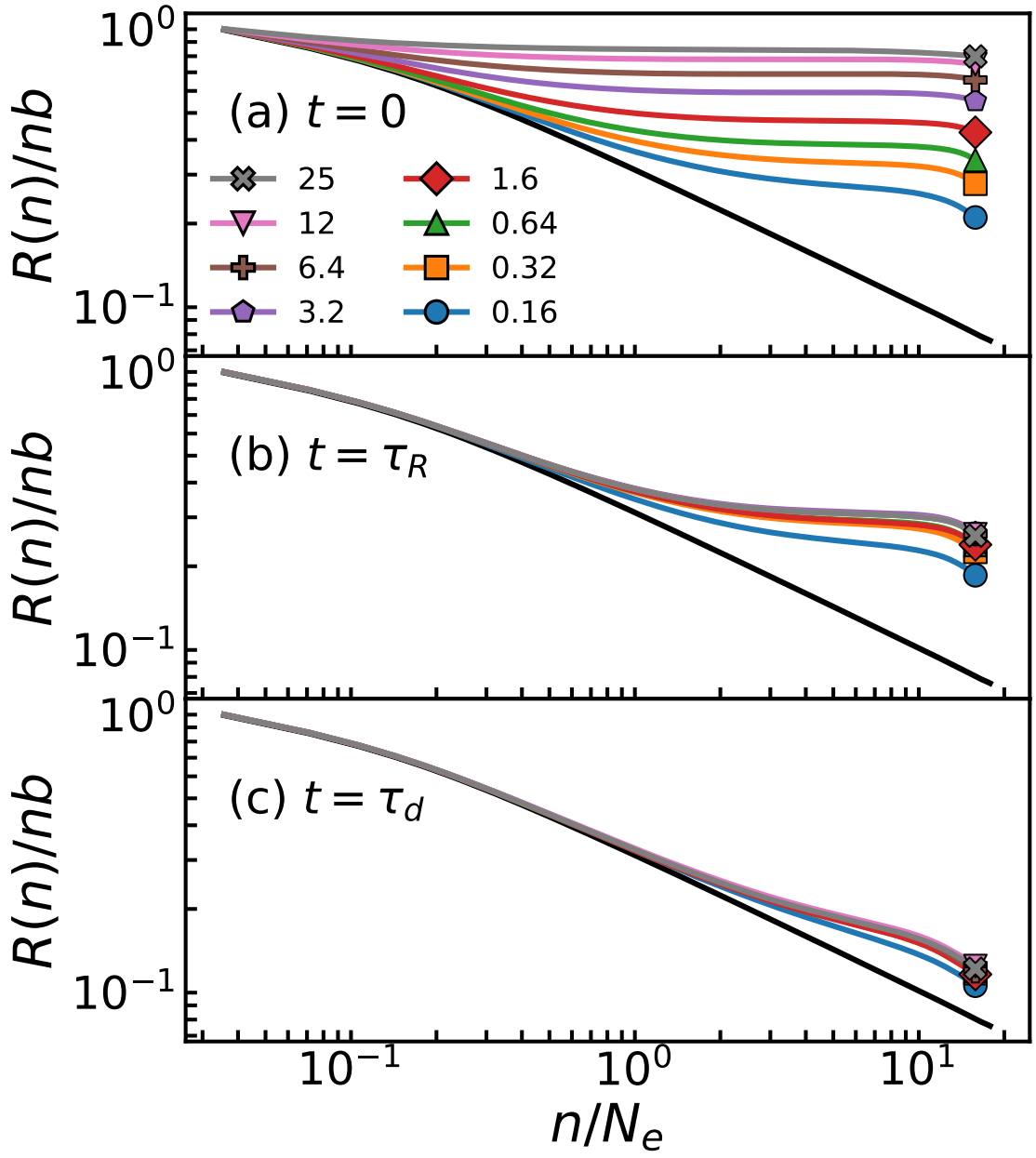

Figure 7.4: $R(n)/nb$ versus n/N_e for all Wi_R at (a) $t = 0$, (b) $t = \tau_R$, and (c) $t = \tau_d$. The solid black lines correspond to an equilibrium coil. Rapid retraction causes systems with initially fully aligned conformations to converge to a common conformation at $t = \tau_R$ (b). They then relax in the same way. The $Wi_R = 0.16$ curve remains distinct from the others at τ_R because its chains were not fully aligned by the flow (see Figure 7.3).

$R(n)/nb$ for the lowest $Wi_R = 0.16$ does not superpose with the other Wi_R and shows almost no change between Figure 7.4(a) and (b) because the flow rate was insufficent to fully orient the confining tube down to N_e. This is evident by its lower plateau value in Figure 7.4(b). The only way for this system to continue relaxing is via reptation which does not occur until $t \sim \tau_d$. Figure 7.4(c) shows $R(n)/nb$ after τ_d and, as anticipated, we see that $R(n)/nb$ curves for all Wi_R have converged as all systems undergo terminal relaxation through reptation.

A beautiful quality of Figure 7.4 is that the equilibrium entanglement length-scale N_e naturally emerges during relaxation. Even though N_e is an emergent confinement produced through the interaction of *many chains* [4, 31], we can directly extract it by monitoring the evolution of *single chain* statistics. Perhaps equally compelling is that the value of N_e that emerges after retraction is the same as in equilibrium. This challenges several recent models of nonlinear polymer rheology [36,186,213,214], which assume or predict N_e changes as chains become highly oriented.

Rheological theories usually model chain extension with a stretch $\lambda(n)$ equal to $R(n)/R_{eq}(n)$ evaluated at specific scales like the end-end $n = N - 1$ or entanglement $n = N_e$ scale [4, 30]. $\lambda(N-1)$ gives a measure of the overall extension of the chain, while $\lambda(N_e)$ gives the stretch per N_e of the primitive path. Figure 7.5 (a) and (b) show the evolution of $\lambda(N-1)$ and $\lambda(N_e)$ for all Wi_R. The large initial value of the end-end stretch reflects both the alignment of the confining tube and the stretch of the chain within the tube. Thus, $\lambda(N-1)$ does not completely relax until both

retraction and reptation have occured. The superposition of these two relaxations can be seen in Figure 7.5(a) for large Wi_R. Considering the $Wi_R = 25$ system, $\lambda(N-1)$ starts decreasing almost immediately ($t > \tau_e$) due to retraction, before superposing with the other curves once $t > 2\tau_R$ and reptation takes over. The terminal region is governed by reptation and is the only process present for the lowest $Wi_R = 0.16$ system.

Meanwhile, the entanglement stretch $\lambda(N_e)$ is much less sensitive to reptation, since the confining tube only constrains the chain at scales larger than N_e. Thus, relaxation of $\lambda(N_e)$ is dominated by chain retraction and rapidly decays over a few τ_R. Interestingly, $\lambda(N_e)$ does not fully relax over the Rouse time scale. Instead, relaxation slows and does not finish until reptation has occured. This suggests chains cannot completely relax their stretch through Rouse-like motion, as is assumed by many rheological models. Instead, we observe a finite, residual stretch of the primitive path for stretches less than ~ 1.2. This value is likely non universal and specific to this bead spring model. The existence of such a residual stress has been proposed by Wang et al. [215]. They hypothesize retraction is arrested by a "cohesive barrier" that resists the entropic tension in the stretched chain. Others have shown that the confinement imposed by entanglements can couple Rouse modes, producing "non-Rouse" relaxation behavior [212]. Determining the origin of this residual stretch is an important topic but beyond the scope of this chapter. We defer further investigation to our future work.

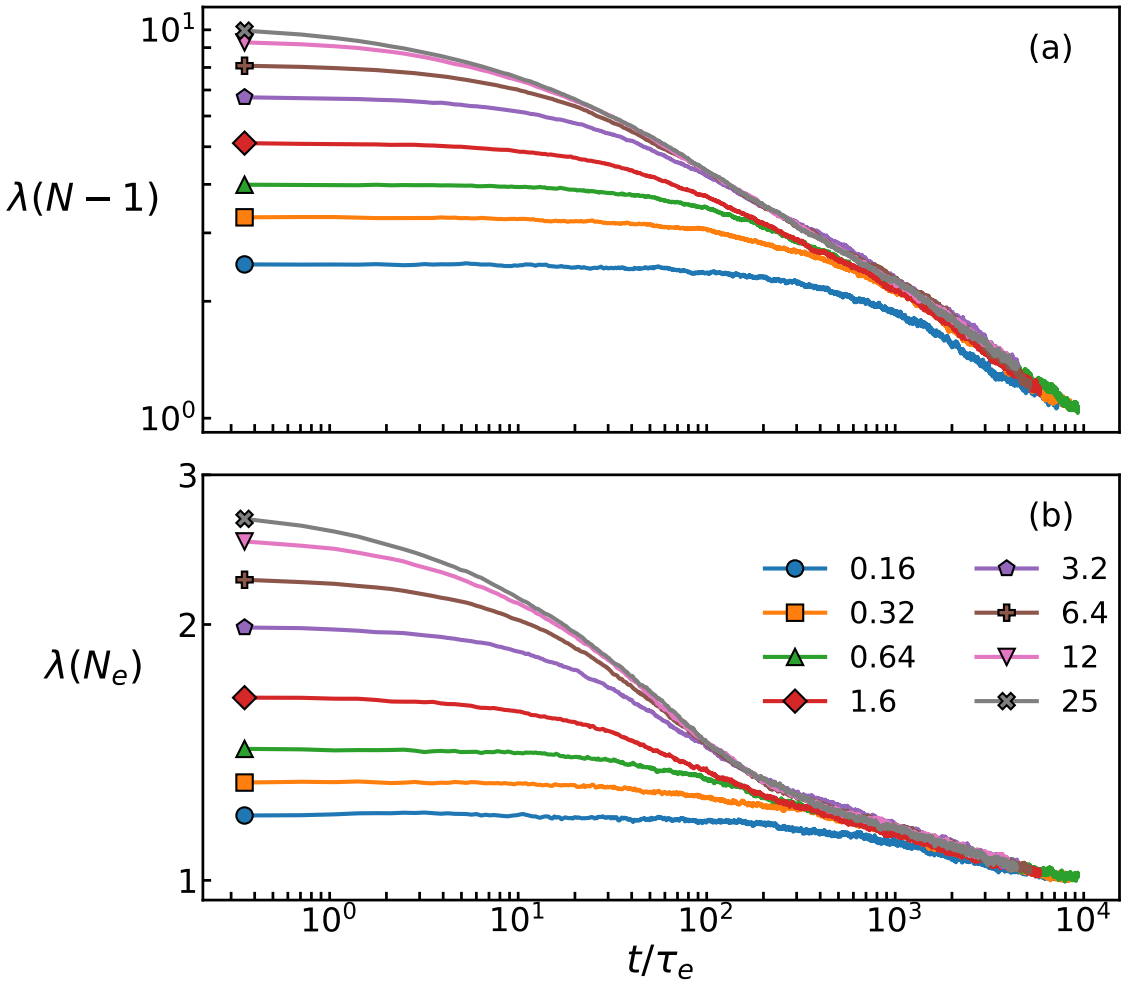

Figure 7.5: Relaxation for segment stretch $\lambda(n)$ at (a) the end-end scale $n = N-1$ and (b) the entanglement scale $n = N_e$. $\lambda(N-1)$ relaxes by a combination of retraction and reptation, while relaxation of $\lambda(N_e)$ is dominated by retraction. However, residual stretches less than about 1.2 persist at N_e until they are relaxed by reptation.

At high Wi_R, the lateral fluctuations of chains relative to the primitive path are suppressed as chains are stretched by the tension induced by the flow. After flow ceases, the retraction of the chain reduces the free energy cost for monomers moving laterally within their confining tubes. As the primitive path length decreases during retraction, the lateral fluctuations of the chains increase and provide a measure for the diameter of the confining tube. Quantifying a tube diameter is challenging because the confinement of chains by entanglements is a dynamic many-body effect, so a tube radius cannot be uniquely determined from single chain statistics. Past work on the Kremer-Grest model has used a variety of techniques to analyze the confining tube using primitive path analysis or geometric annealing [204–206]. This work provides values of N_e, C_∞ and the equilibrium tube diameter $a_{eq} = R_{eq}(N_e) = C_\infty N_e b^2$, where $R_{eq}(N_e)$ is the rms length of segments of N_e monomers. The value of $R(N_e)$ stops being a useful measure of confinement once chains are extended by flow. Changes in $R(N_e)$ are dominated by the increase in the length along extension, while the tube radius is associated with fluctuations about the primitive path in the perpendicular directions. There is still debate about how to extend primitive path methods to highly aligned chains, but the lateral fluctuations of segments of length N_e should scale with the shrinking diameter of chain confinement.

In Figure 7.6 we plot the evolution of two measures of the lateral fluctuations of the chains for all Wi_R. Figure 7.6(a) plots the perpendicular fluctuation of monomers within a segment of length N_e relative to the segment's end-end vector. The fluc-

tuation $\delta r_\perp$ depends on the chemical distance n from the start of the segment and must go to zero at both ends. For Gaussian chains, the maximum fluctuation occurs at $n = N_e/2$ and this is the value we measure. Figure 7.6(b) plots $G_\perp$, which is the square-root of the sum of the two smallest eigenvalues of an N_e segment's radius of gyration tensor. Both measures are averaged over all segments on all chains. The ratio of the tube diameters from these measures to the equilibrium tube diameter is readily computed for equilibrium Gaussian chains. One finds: $2\delta r_\perp/a_{eq} = (2/3)^{1/2}$ and $2G_\perp/a_{eq} = (246/1549)^{1/2}$ [216].

Both measures show qualitatively similar behavior. At high Wi_R, chain stretch suppresses lateral fluctuations. For low Wi_R, where little stretch occurs, the diameter is nearly unchanged from its equilibrium value. During relaxation, large Wi_R chains show a rapid increase in diameter over the Rouse time scale. Similar to the stretch, the large Wi_R systems converge to a common curve after a few τ_R, by which time they have almost completely recovered their equilibirum tube diameter. The rapid recovery of the *equilibrium* tube diameter is signficant and suggests, quite suprisingly, that the emergent confinement of interacting chains is insensitive to their orientation. That is to say, chains whose primitive paths are uniformly aligned, confine each other in the same manner as chains whose primitive paths randomly cross each other.

Once retraction is complete, reptation dominates the final stage of relaxation as t approaches τ_d. The chain loses its orientational order as it slowly escapes its oriented tube and replaces it with a random walk. We can describe the orientation with the

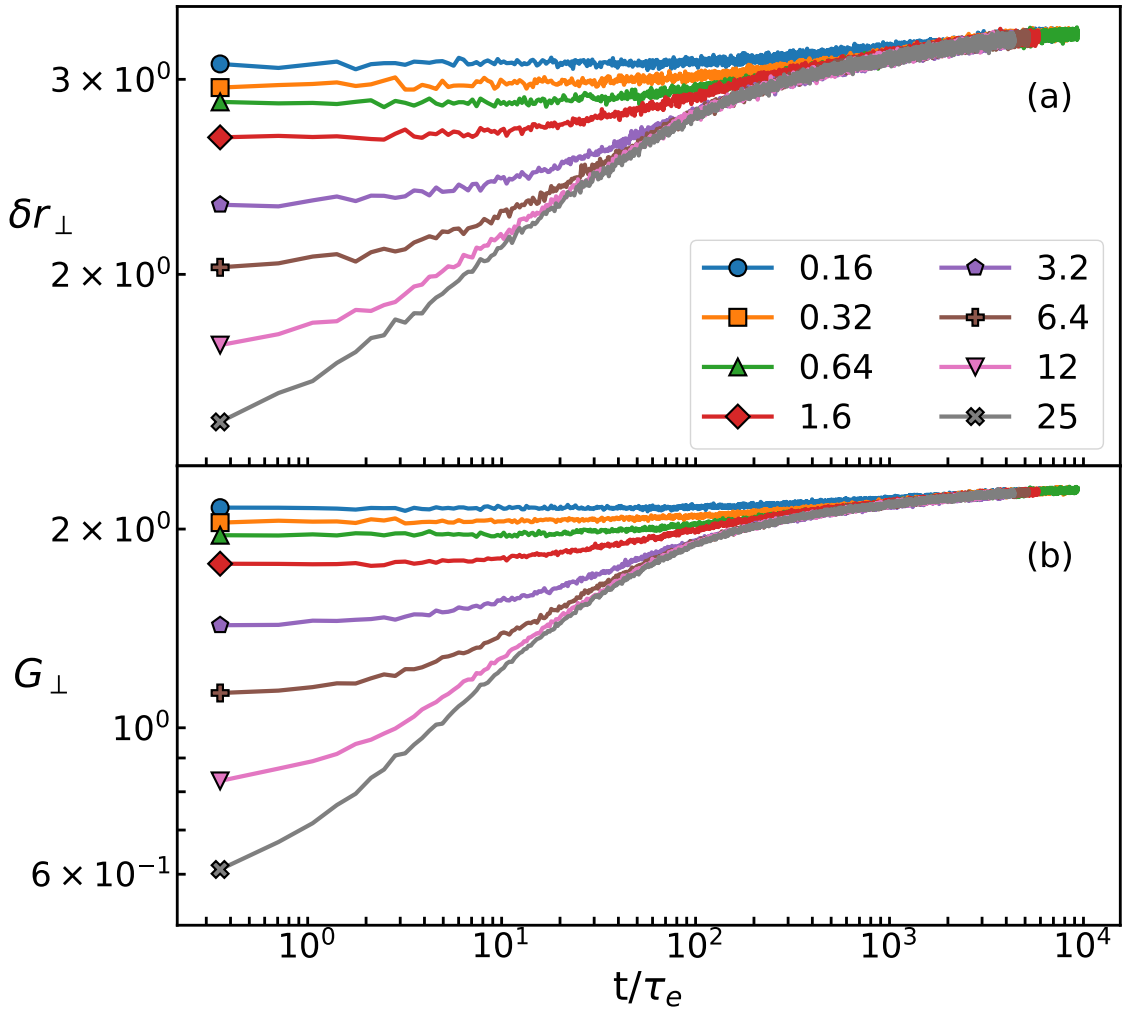

Figure 7.6: Two measures of tube diameter are shown as a function of time for each Wi_R. (a) The tube diameter calculated by the fluctuations of monomers perpendicular to the end-end vector of segments of length N_e, averaged over the inner 20% of monomers of each segment. (b) The tube diameter calculated from the sum of the two smallest eigenvalues of the radius of gyration tensor for chain segments of length N_e.

nematic order parameter $P_2(n) = \frac{1}{2}\langle 3\langle \cos^2\theta_n\rangle - 1\rangle$, where θ_n is the angle between the extension axis and the vector $\vec{R}(n)$ between beads separated by n bonds. $P_2 = 0$ when segments are randomly oriented and $P_2 = 1$ when segments are fully aligned by flow. Simple reptation theory predicts $P_2(n) \propto e^{-t/\tau_d}$ for all $n > N_e$ [4, 30]. That is, orientation at the scale of the chain ends will decay at the same rate as for shorter segments within the chain.

We verify this behavior in Figure 7.7 by plotting the evolution of P_2 versus t/τ_R for $n = N - 1$ (a) and $n = N_e$ (b). We have normalized curves for all Wi_R by their value at $t = 3\tau_R$ to remove any early time behavior due to retraction. P_2 at both scales decays exponentially and in good agreement with a relaxation $\propto e^{-t/\tau_d}$, which is shown by black dashed lines. The decay of $P_2(N-1)$ is noisier than for $P_2(N_e)$ because their are many more N_e-scale segments to average over in a given configuration. The similar relaxation rate at both scales is consistent with reptation theory. However, it is again surprising that τ_d shows no change with Wi_R. Like the recovery of the equilibrium primitive path length and tube diameter after retraction, the *equilibrium* reptation time τ_d appears to be a robust quantity that survives for highly oriented melt configurations.

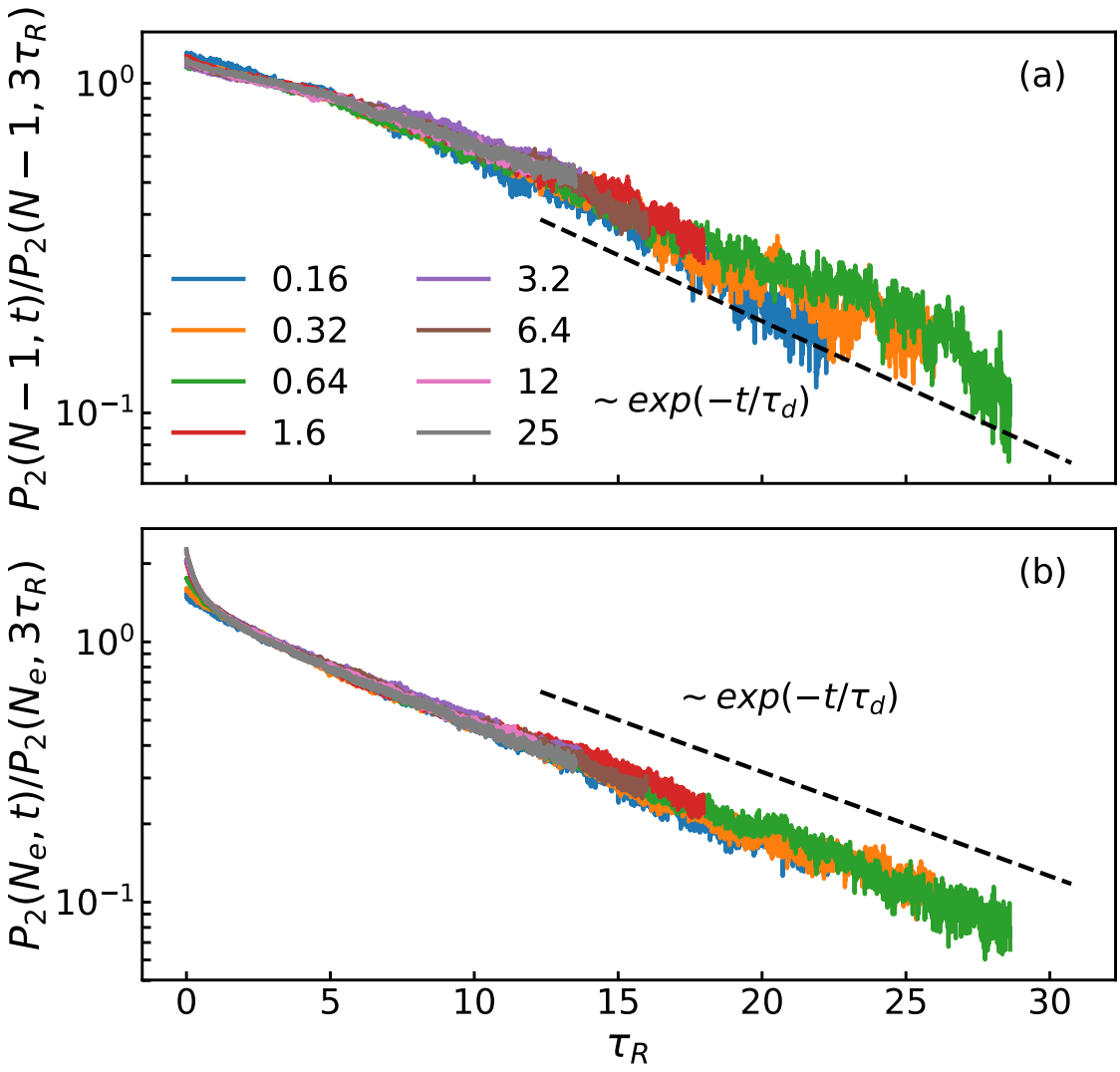

Figure 7.7: Relaxation of the nematic orientational order parameter for all Wi_R at (a) the end-end scale $P_2(N)$ and (b) the entanglement scale $P_2(N_e)$. Curves are normalized by the value of P_2 at $t = 3\tau_R$ to remove any effect of retraction. Orientation at both scales decays exponentially with t/τ_d as illustrated by the black dashed lines.

7.4 Discussion and Conclusions

Molecular simulations of stress relaxations from steady-state extensional flows reveal unexpected connections between the dynamics of polymer melts near and far from equilibrium. Extensional flows uniformly align chains along the extension axis, allowing the primitive path to be unambiguously identified and its evolution to be tracked. As Wi_R increases above ~ 1, the chain primitive paths stretch and the lateral fluctuations of chains decrease in steady state. After flow ceases, chains retract over times $\sim \tau_R$, rapidly approaching the equilibrium primitive path length. The perpendicular fluctuations of segments of length N_e also rapidly increase over $\sim \tau_R$ toward a value corresponding to their equilibrium statistics. We observe residual stretches ~ 1.2 after initial retraction that do not completely relax until the terminal relaxation time. This residual stretch may be evidence of thermal or kinetic confinement barriers hindering simple Rouse retraction, as suggested by Wang et al. [215] or Jagannathan et al. [212].

The rapid recovery of the equilibrium primitive path length and width suggests that the equilibrium entanglement scale N_e is also rapidly recovered. This is supported by the relaxation of the orientational order of chains, which decays exponentially with a chracateristic time equal to the equilibrium reptation time τ_d. The reptation time depends strongly upon $Z = N/N_e$, implying that the equilibrium N_e is also recovered after retraction.

It is surprising that chains in fully oriented melts reptate similarly to those in equi-

librium. The qualitative picture usually used to visualize entanglement is illustrated in Figure 7.8(a). In this picture, the tube diameter a and the entanglement length N_e are controlled by the characteristic separation between interchain crossings that form topological constraints (TC). It is these TCs that are measured by primitive path analysis (PPA) [204] or geometric annealing codes like Z1 [205] or CReTA [206]. These metrics find that the number of TCs decreases as chains become highly aligned by nonlinear flows [185]. In this view of entanglement, a reduction in TCs would suggest there is an overall decrease in chain confinement due to entanglement, with N_e and a increasing and the primitive path length decreasing [4, 30]. Several recent rheological theories also predict that chain confinement should decrease with increasing orientation of the primitive path [213, 214, 217].

Our results reveal a very different picture of confinement in highly oriented melts, illustrated in Figure 7.8(b). We observe that the complete alignment of the primitive paths produces almost no change in the primitive path length or diameter after retraction. The equilibrium tube diameter is preserved in spite of the fact that the oriented chains inter-digitate less than they do in equilibrium. This suggests that the confinement associated with "entanglement" is subtler than the picture in Figure 7.8(a) would suggest, and it likely cannot be captured by methods like PPA when chains are highly oriented. Our data also disagrees with the predictions of several rheological models that predict a reduction in chain confinement with increasing orientation of the primitive path [213, 214, 217]. Rather, it may be the case that simpler

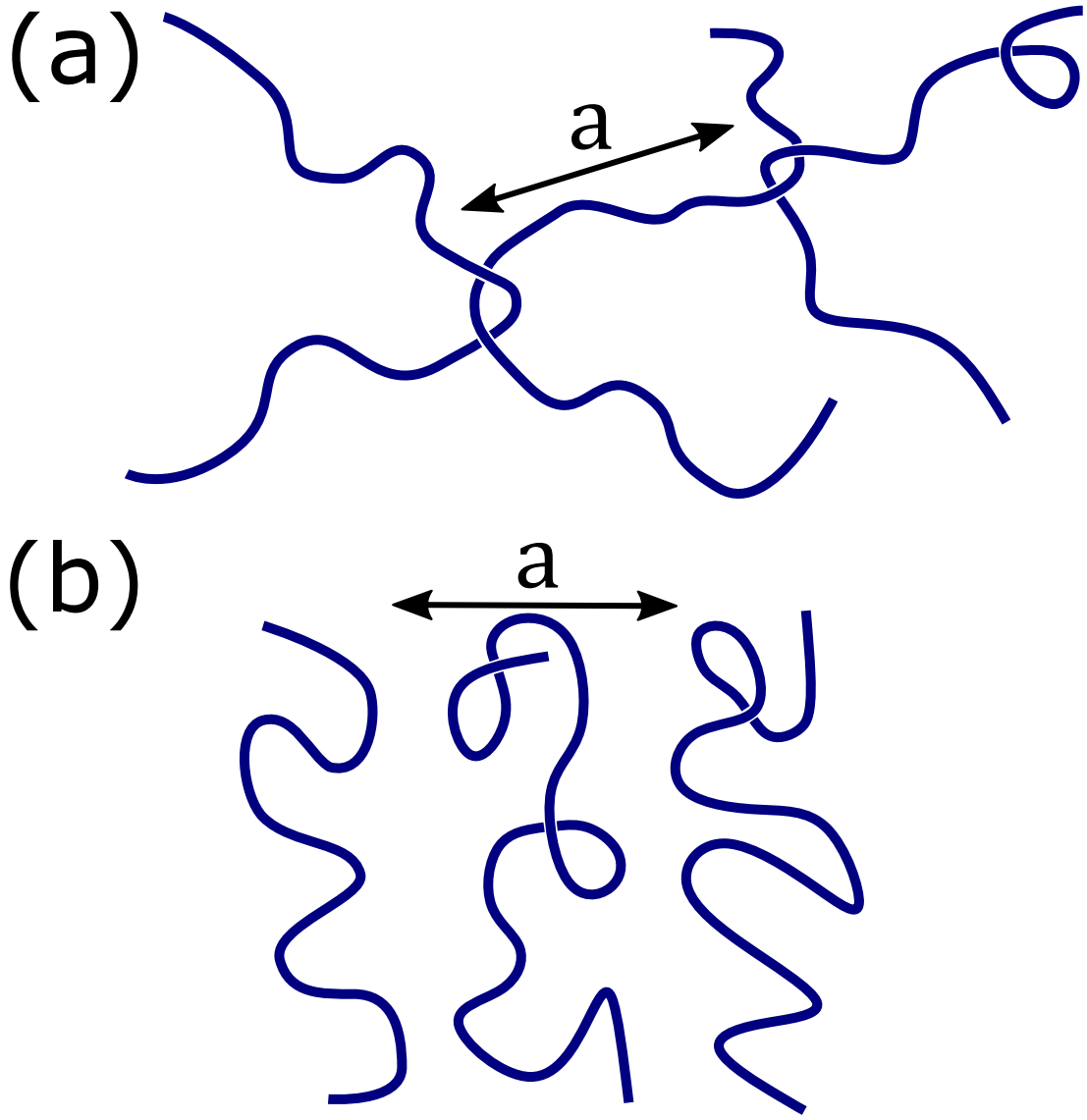

Figure 7.8: (a) Schematic of the conventional picture of chain entanglement and confinement. The characteristic distance between chain crossings in equilibrium determines the entanglement length N_e and the diameter a of the confining tube. (b) Schematic illustrating the chain confinement we observe for highly oriented melts after times $\sim \tau_R$. The uniformly oriented primitive paths intermingle less then in the equilibrium melt. However, both the primitive path length and the diameter of the confining tube a remain the same as in equilibrium.

chain-packing arguments, like those discussed by Qin and Milner [218], are more appropriate.

It is remarkable that the equilibrium values of N_e, a, and τ_d remain relevant quantities even for the most extreme nonlinear extensional flows. Their persistence holds significant implications for the nature of entanglement in oriented fluids, and the necessary structure for future models of nonlinear flow. Our data suggests that the current trend to use quantities like N_e as dynamic variables to capture nonlinear flow behavior may be inappropriate, and new physical mechanisms must be identified to explain nonlinear trends. What those strategies should be is not yet clear, but we believe the simulation methods described here will provide invaluable guidance in the coming years.

Bibliography

[1] I. M. Ward and J. Sweeney, *Mechanical Properties of Solid Polymers.* John Wiley & Sons, 2012.

[2] I. M. Ward, *Structure and properties of oriented polymers.* Springer Science & Business Media, 2012.

[3] B. Crist, "The ultimate strength and stiffness of polymers," *Annu. Rev. Mater. Sci.*, vol. 25, no. 1, pp. 295–323, 1995.

[4] M. Doi and S. F. Edwards, *The Theory of Polymer Dynamics.* Oxford University Press, 1988, vol. 73.

[5] L. Pastewka, P. Pou, R. Pérez, P. Gumbsch, and M. Moseler, "Describing bond-breaking processes by reactive potentials: Importance of an environment-dependent interaction range," *Phys. Rev. B*, vol. 78, p. 161402, Oct 2008. [Online]. Available: http://link.aps.org/doi/10.1103/PhysRevB.78.161402

[6] V. V. Gobre and A. Tkatchenko, "Scaling laws for van der Waals interactions in nanostructured materials." *Nature communications*, vol. 4, p. 2341, jan 2013.

[7] P. M. Chaikin and T. C. Lubensky, *Principles of condensed matter physics*. Cambridge university press Cambridge, 1995, vol. 1.

[8] T. L. Chantawansri, T. W. Sirk, E. F. C. Byrd, J. W. Andzelm, and B. M. Rice, "Shock hugoniot calculations of polymers using quantum mechanics and molecular dynamics," *J. Chem. Phys.*, vol. 137, no. 20, p. 204901, 2012. [Online]. Available: http://scitation.aip.org/content/aip/journal/jcp/137/20/10.1063/1.4767394

[9] T. R. Mattsson, J. M. D. Lane, K. R. Cochrane, M. P. Desjarlais, A. P. Thompson, F. Pierce, and G. S. Grest, "First-principles and classical molecular dynamics simulation of shocked polymers," *Phys. Rev. B*, vol. 81, no. 5, p. 054103, Feb. 2010. [Online]. Available: http://link.aps.org/doi/10.1103/PhysRevB.81.054103

[10] T. C. O'Connor, J. Andzelm, and M. O. Robbins, "Airebo-m: A reactive model for hydrocarbons at extreme pressures," *J. Chem. Phys.*, vol. 142, no. 2, p. 024903, 2015.

[11] S. J. Stuart, A. B. Tutein, and J. a. Harrison, "A reactive potential for hydrocarbons with intermolecular interactions," *J. Chem. Phys.*, vol. 112,

no. 14, p. 6472, 2000. [Online]. Available: http://link.aip.org/link/JCPSA6/v112/i14/p6472/s1&Agg=doi

[12] H. H. Kausch, "Origin, Extent, and Effect of Molecular Stress Concentration in Fibrillar Structures," *Polymer Engineering and Science*, vol. 19, no. 2, 1979.

[13] T. C. O'Connor and M. O. Robbins, "Chain ends and the ultimate strength of polyethylene fibers," *ACS Macro Lett.*, vol. 5, no. 3, pp. 263–267, 2016.

[14] F. C. Frank and J. H. van der Merwe, "One-dimensional dislocations ." *Proceedings of the Royal Society of London. Series A, Mathematical and Physical Sciences*, vol. 198, no. 1053, pp. 205–216, 1949.

[15] O. M. Braun and Y. S. Kivshar, *The Frenkel-Kontorova Model: Concepts, Methods, and Applications*. Springer Science & Business Media, 2004.

[16] L. Davison, *Fundamentals of Shock Wave Propagation in Solids*. Springer Science & Business Media, 2008.

[17] J. Forbes, *Shock Wave Compression of Condensed Matter: A Primer*. Springer Berlin Heidelberg, 2013.

[18] W. Carter and S. Marsh, "Hugoniot equation of state of polymers," Los Alamos National Lab., NM (United States), Tech. Rep. LA–13006-MS, 1995.

[19] J. Colvin and J. Larsen, *Extreme Physics: Properties and Behavior of Matter at Extreme Conditions*. Cambridge University Press, 2013.

[20] T. C. O'Connor, R. M. Elder, Y. R. Sliozberg, T. W. Sirk, J. W. Andzelm, and M. O. Robbins, "Molecular origins of anisotropic shock propagation in crystalline and amorphous polyethylene," *Physical Review Materials*, vol. 2, no. 3, p. 035601, 2018. [Online]. Available: https://link.aps.org/doi/10.1103/PhysRevMaterials.2.035601

[21] D. J. Pastine, "P, v, t equation of state for polyethylene," *J. Chem. Phys.*, vol. 49, no. 7, pp. 3012–3022, 1968. [Online]. Available: http://scitation.aip.org/content/aip/journal/jcp/49/7/10.1063/1.1670544

[22] ——, "Theoretical shock properties of polymers with applications to polyethylene," in *Colloque Internationale du C.N.R.S. sur Les Proprits Physiques des Solides Sous Pression*. Paris, France: CNRS, 1970, Conference Proceedings.

[23] R. M. Elder, T. C. O'Connor, T. L. Chantawansri, Y. R. Sliozberg, T. W. Sirk, I.-C. Yeh, M. O. Robbins, and J. W. Andzelm, "Shock-wave propagation and reflection in semicrystalline polyethylene: A molecular-level investigation," *Phys. Rev. Materials*, vol. 1, p. 043606, Sep 2017. [Online]. Available: https://link.aps.org/doi/10.1103/PhysRevMaterials.1.043606

[24] H. Dong, Z. Wang, T. C. O'Connor, A. Azoug, M. O. Robbins, and T. D. Nguyen, "Micromechanical models for the stiffness and strength of UHMWPE macrofibrils," *Journal of the Mechanics and*

Physics of Solids, vol. 116, pp. 70–98, 2018. [Online]. Available: http://linkinghub.elsevier.com/retrieve/pii/S0022509617309791

[25] Q. Huang, N. J. Alvarez, Y. Matsumiya, H. K. Rasmussen, H. Watanabe, and O. Hassager, "Extensional rheology of entangled polystyrene solutions suggests importance of nematic interactions," *ACS Macro Letters*, vol. 2, no. 8, pp. 741–744, 2013.

[26] Q. Huang, O. Mednova, H. K. Rasmussen, N. J. Alvarez, A. L. Skov, K. Almdal, and O. Hassager, "Concentrated polymer solutions are different from melts: Role of entanglement molecular weight," *Macromolecules*, vol. 46, no. 12, pp. 5026–5035, 2013.

[27] J. Dealy and R. Larson, *Structure and Rheology of Molten Polymers: From Structure to Flow Bahavior and Back Again*. Hanser Publishers, Munich, 2006.

[28] S. Costanzo, Q. Huang, G. Ianniruberto, G. Marrucci, O. Hassager, and D. Vlassopoulos, "Shear and Extensional Rheology of Polystyrene Melts and Solutions with the Same Number of Entanglements," *Macromolecules*, vol. 49, no. 10, pp. 3925–3935, 2016.

[29] A. E. Likhtman and T. C. B. McLeish, "Quantitative theory for linear dynamics of linear entangled polymers," *Macromolecules*, vol. 35, no. 16, pp. 6332–6343, 2002.

[30] M. Rubinstein and R. H. Colby, *Polymer Physics*. Oxford university press New York, 2003, vol. 23.

[31] P. G. De Gennes, "Reptation of a polymer chain in the presence of fixed obstacles," *The Journal of Chemical Physics*, vol. 55, no. 2, pp. 572–579, 1971.

[32] S. L. Wingstrand, N. J. Alvarez, Q. Huang, and O. Hassager, "Linear and Nonlinear Universality in the Rheology of Polymer Melts and Solutions," *Physical Review Letters*, vol. 115, no. 7, pp. 1–5, 2015.

[33] M. Dobson, "Periodic boundary conditions for long-time nonequilibrium molecular dynamics simulations of incompressible flows," *The Journal of Chemical Physics*, vol. 141, no. 18, p. 184103, 2014.

[34] D. A. Nicholson and G. C. Rutledge, "Molecular simulation of flow-enhanced nucleation in n-eicosane melts under steady shear and uniaxial extension," *Journal of Chemical Physics*, vol. 145, no. 24, 2016.

[35] S. Plimpton, "Fast Parallel Algorithms for Short Range Molecular Dynamics," *Journal of Computational Physics*, vol. 117, pp. 1–19, 1995.

[36] G. Ianniruberto and G. Marrucci, "Convective constraint release (CCR) revisited," *Journal of Rheology*, vol. 58, no. 1, p. 89, 2014. [Online]. Available: http://scitation.aip.org/content/sor/journal/jor2/58/1/10.1122/1.4843957

[37] K. S. Schweizer and D. M. Sussman, "A force-level theory of the

rheology of entangled rod and chain polymer liquids. i. tube deformation, microscopic yielding, and the nonlinear elastic limit," *The Journal of Chemical Physics*, vol. 145, no. 21, p. 214903, 2016. [Online]. Available: https://doi.org/10.1063/1.4968516

[38] M. Iyer, V. Gavini, and T. M. Pollock, "Energetics and nucleation of point defects in aluminum under extreme tensile hydrostatic stresses," *Phys. Rev. B*, vol. 89, no. 1, p. 014108, Jan. 2014. [Online]. Available: http://link.aps.org/doi/10.1103/PhysRevB.89.014108

[39] D. C. Bassett, "A high-pressure phase of polyethylene and chain-extended growth," *J. Appl. Phys.*, vol. 45, no. 10, p. 4146, 1974. [Online]. Available: http://scitation.aip.org/content/aip/journal/jap/45/10/10.1063/1.1663028

[40] G. Gao, R. J. Cannara, R. W. Carpick, and J. A. Harrison, "Atomic-Scale Friction on Diamond : A Comparison of Different Sliding Directions on (001) and (111) Surfaces Using MD and AFM," *Langmuir*, vol. 23, pp. 5394–5405, 2007.

[41] C. Pickard and R. Needs, "High-Pressure Phases of Silane," *Phys. Rev. Lett.*, vol. 97, no. 4, p. 045504, Jul. 2006. [Online]. Available: http://link.aps.org/doi/10.1103/PhysRevLett.97.045504

[42] J. E. Jaffe, J. A. Snyder, Z. Lin, and A. C. Hess, "LDA and GGA calculations

for high-pressure phase transitions in ZnO and MgO," *Phys. Rev. B*, vol. 62, no. 3, pp. 1660–1665, 2000.

[43] M. Dion, H. Rydberg, E. Schröder, D. C. Langreth, and B. I. Lundqvist, "Van der Waals Density Functional for General Geometries," *Physical Review Letters*, vol. 92, no. 24, p. 246401, Jun. 2004. [Online]. Available: http://link.aps.org/doi/10.1103/PhysRevLett.92.246401

[44] K. Lee, E. D. Murray, L. Kong, B. I. Lundqvist, and D. C. Langreth, "Higher-accuracy van der Waals density functional," *Physical Review B*, vol. 82, no. 8, p. 081101, Aug. 2010. [Online]. Available: http://link.aps.org/doi/10.1103/PhysRevB.82.081101

[45] G. Román-Pérez and J. Soler, "Efficient Implementation of a van der Waals Density Functional: Application to Double-Wall Carbon Nanotubes," *Physical Review Letters*, vol. 103, no. 9, p. 096102, Aug. 2009. [Online]. Available: http://link.aps.org/doi/10.1103/PhysRevLett.103.096102

[46] S. Grimme, "Semiempirical GGA-Type Density Functional Constructed with a Long-Range Dispersion Correction," *J Comput Chem*, vol. 27, pp. 1787–1799, 2006.

[47] J.-D. Chai and M. Head-Gordon, "Long-range corrected hybrid density functionals with damped atom-atom dispersion corrections." *Physical chemistry chemical physics : PCCP*, vol. 10, no. 44, pp. 6615–20, Nov. 2008.

[Online]. Available: http://pubs.rsc.org/en/Content/ArticleHTML/2008/CP/B810189B

[48] S. Ehrlich, J. Moellmann, and S. Grimme, "Dispersion-corrected density functional theory for aromatic interactions in complex systems." *Accounts of chemical research*, vol. 46, no. 4, pp. 916–26, Apr. 2013. [Online]. Available: http://dx.doi.org/10.1021/ar3000844

[49] S. Grimme, S. Ehrlich, and L. Goerigk, "Effect of the damping function in dispersion corrected density functional theory." *Journal of computational chemistry*, vol. 32, no. 7, pp. 1456–65, May 2011. [Online]. Available: http://www.ncbi.nlm.nih.gov/pubmed/21370243

[50] K. Chenoweth, A. C. T. Van Duin, and W. A. Goddard, "ReaxFF Reactive Force Field for Molecular Dynamics Simulations of Hydrocarbon Oxidation," *J. Phys. Chem. A*, vol. 112, pp. 1040–1053, 2008.

[51] D. W. Brenner, O. A. Shenderova, and J. A. Harrison, "A second-generation reactive empirical bond order (REBO) potential energy expression for," *Mater. Sci.*, vol. 14, pp. 783–802, 2002.

[52] A. Violi and A. Venkatnathan, "Combustion-generated nanoparticles produced in a benzene flame: a multiscale approach." *J. Chem. Phys.*, vol. 125, no. 5, p. 054302, Aug. 2006. [Online]. Available: http://www.ncbi.nlm.nih.gov/pubmed/16942208

[53] Y. Zheng, S. K. Pregler, J. D. Myers, J. Ouyang, S. B. Sinnott, and J. Xue, "Computational and experimental studies of phase separation in pentacene:C[sub 60] mixtures," *J. Vac. Sci. Technol. B Microelectron. Nanom. Struct.*, vol. 27, no. 1, p. 169, 2009. [Online]. Available: http://scitation.aip.org/content/avs/journal/jvstb/27/1/10.1116/1.3072516

[54] T. Hayashi, T. C. O'Connor, K. Higashiyama, K. Nishi, K. Fujisawa, H. Muramatsu, Y. A. Kim, B. G. Sumpter, V. Meunier, M. Terrones, and M. Endo, "A reversible strain-induced electrical conductivity in cup-stacked carbon nanotubes," *Nanoscale*, vol. 5, pp. 10 212–10 218, 2013. [Online]. Available: http://dx.doi.org/10.1039/C3NR01887C

[55] L. Fontana, D. Vinh, M. Santoro, S. Scandolo, F. Gorelli, R. Bini, and M. Hanfland, "High-pressure crystalline polyethylene studied by x-ray diffraction and ab initio simulations," *Phys. Rev. B*, vol. 75, no. 17, p. 174112, May 2007. [Online]. Available: http://link.aps.org/doi/10.1103/PhysRevB.75.174112

[56] E. Bitzek, P. Koskinen, F. Gähler, M. Moseler, and P. Gumbsch, "Structural Relaxation Made Simple," *Phys. Rev. Lett.*, vol. 97, no. 17, p. 170201, Oct. 2006. [Online]. Available: http://link.aps.org/doi/10.1103/PhysRevLett.97.170201

[57] Y. Zhao and D. G. Truhlar, "The M06 suite of density functionals for main group thermochemistry, thermochemical kinetics, noncovalent interactions,

excited states, and transition elements: two new functionals and systematic testing of four M06-class functionals and 12 other functionals," *Theor. Chem. Acc.*, vol. 120, no. 1-3, pp. 215–241, Jul. 2007. [Online]. Available: http://link.springer.com/10.1007/s00214-007-0310-x

[58] W. Shinoda, M. Shiga, and M. Mikami, "Rapid estimation of elastic constants by molecular dynamics simulation under constant stress," *Phys. Rev. B*, vol. 69, no. 13, p. 134103, Apr. 2004. [Online]. Available: http://link.aps.org/doi/10.1103/PhysRevB.69.134103

[59] J. J. Erpenbeck, "Molecular dynamics of detonation. I. Equation of state and Hugoniot curve for a simple reactive fluid," *Phys. Rev. A*, vol. 46, no. 10, 1992.

[60] J. Andzelm, T. Chantawansri, T. Sirk, E. Byrd, and B. Rice, in *Proceedings of the 15th International Conference on Deformation, Yield, and Fracture of Polymers, Book of Abstracts.* Materials Technology Group, 2012, p. 165.

[61] C.-S. Liu, G. Pilania, C. Wang, and R. Ramprasad, "How critical are the van der Waals interactions in polymer crystals?" *J. Phys. Chem. A*, vol. 116, no. 37, pp. 9347–52, Sep. 2012. [Online]. Available: http://www.ncbi.nlm.nih.gov/pubmed/22937808

[62] M. S. Miao, M.-L. Zhang, V. E. Van Doren, C. Van Alsenoy, and J. L. Martins, "Density functional calculations on the structure of crystalline polyethylene under high pressures," *J. Chem. Phys.*, vol. 115, no. 24, p. 11317, 2001.

[Online]. Available: http://scitation.aip.org/content/aip/journal/jcp/115/24/10.1063/1.1420404

[63] S. Tsuzuki, K. Honda, T. Uchimaru, and M. Mikami, "Estimated MP2 and CCSD(T) interaction energies of n-alkane dimers at the basis set limit: comparison of the methods of Helgaker et al. and Feller." *J. Chem. Phys.*, vol. 124, no. 11, p. 114304, Mar. 2006. [Online]. Available: http://www.ncbi.nlm.nih.gov/pubmed/16555885

[64] T. H. Dunning, "Gaussian basis sets for use in correlated molecular calculations. I. The atoms boron through neon and hydrogen," *J. Chem. Phys.*, vol. 90, no. 2, p. 1007, 1989. [Online]. Available: http://scitation.aip.org/content/aip/journal/jcp/90/2/10.1063/1.456153

[65] L. F. Molnar, X. He, B. Wang, and K. M. Merz, "Further analysis and comparative study of intermolecular interactions using dimers from the S22 database." *J. Chem. Phys.*, vol. 131, no. 6, p. 065102, Aug. 2009.

[66] B. J. Ransil, "Studies in Molecular Structure. IV. Potential Curve for the Interaction of Two Helium Atoms in Single-Configuration LCAO MO SCF Approximation," *J. Chem. Phys.*, vol. 34, no. 6, p. 2109, 1961. [Online]. Available: http://scitation.aip.org/content/aip/journal/jcp/34/6/10.1063/1.1731829

[67] F. B. van Duijneveldt, J. G. C. M. van Duijneveldt-van de Rijdt, and J. H. van

Lenthe, "State of the Art in Counterpoise Theory," *Chem. Rev.*, vol. 94, pp. 1873–1885, 1994.

[68] M. Hanfland, H. Beister, and K. Syassen, "Graphite under pressure: Equation of state and first-order Raman modes M." *Phys. Rev. B*, vol. 39, no. 17, pp. 12 598–12 603, 1989.

[69] M. Reguzzoni, a. Fasolino, E. Molinari, and M. C. Righi, "Potential energy surface for graphene on graphene: Ab initio derivation, analytical description, and microscopic interpretation," *Phys. Rev. B*, vol. 86, no. 24, p. 245434, Dec. 2012. [Online]. Available: http://link.aps.org/doi/10.1103/PhysRevB.86.245434

[70] A. Kolmogorov and V. Crespi, "Registry-dependent interlayer potential for graphitic systems," *Phys. Rev. B*, vol. 71, no. 23, p. 235415, Jun. 2005. [Online]. Available: http://link.aps.org/doi/10.1103/PhysRevB.71.235415

[71] N. J. Capiati and R. S. Porter, "Tensile properties of ultradrawn polyethylene," *J. Polym. Sci. Polym. Phys. Ed.*, vol. 13, no. 6, pp. 1177–1186, Jun. 1975. [Online]. Available: http://doi.wiley.com/10.1002/pol.1975.180130610

[72] S. Rastogi, Y. Yao, S. Ronca, J. Bos, and J. van der Eem, "Unprecedented High-Modulus High-Strength Tapes and Films of Ultrahigh Molecular Weight Polyethylene via Solvent-Free Route," *Macromolecules*, vol. 44, no. 14, pp.

5558–5568, Jul. 2011. [Online]. Available: http://pubs.acs.org/doi/abs/10.1021/ma200667m

[73] W. L. Jorgensen, D. S. Maxwell, and J. Tirado-Rives, "Development and testing of the opls all-atom force field on conformational energetics and properties of organic liquids," *Journal of the American Chemical Society*, vol. 118, no. 45, pp. 11 225–11 236, 1996.

[74] O. Borodin and G. D. Smith, "Development of many-body polarizable force fields for Li-battery components: 1. Ether, alkane, and carbonate-based solvents." *The journal of physical chemistry. B*, vol. 110, no. 12, pp. 6279–92, Mar. 2006. [Online]. Available: http://www.ncbi.nlm.nih.gov/pubmed/16553446

[75] R. Perriot, X. Gu, Y. Lin, V. V. Zhakhovsky, and I. I. Oleynik, "Screened environment-dependent reactive empirical bond-order potential for atomistic simulations of carbon materials," *Physical Review B*, vol. 88, no. 6, p. 064101, Aug. 2013. [Online]. Available: http://link.aps.org/doi/10.1103/PhysRevB.88.064101

[76] A. Liu and S. J. Stuart, "Empirical Bond-Order Potential for Hydrocarbons: Adaptive Treatment of van der Waals Interactions," *J Comp Chem*, vol. 29, no. May, pp. 601–611, 2008.

BIBLIOGRAPHY

[77] A. Kelly and N. H. Macmillan, *Strong Solids*. Oxford University Press, Walton Street, Oxford OX 2 6 DP, UK, 1986., 1986.

[78] K. Tashiro, M. Kobayashi, and H. Tadokoro, "Calculation of three-dimensional elastic constants of polymer crystals. 2. application to orthorhombic polyethylene and poly(vinyl alcohol)," *Macromolecules*, vol. 11, no. 5, pp. 914–918, 1978.

[79] H. V. D. Werff and a. J. Pennings, "Leading Contribution Tensile deformation of high strength and high modulus polyethylene fibers," *Polymer*, vol. 763, pp. 747–763, 1991.

[80] R. Marissen *et al.*, "Design with ultra strong polyethylene fibers," *Mater. Sci. Appl.*, vol. 2, no. 05, p. 319, 2011.

[81] P. B. McDaniel, J. M. Deitzel, and J. W. Gillespie, "Structural hierarchy and surface morphology of highly drawn ultra high molecular weight polyethylene fibers studied by atomic force microscopy and wide angle X-ray diffraction," *Polymer*, vol. 69, pp. 148–158, 2015. [Online]. Available: http://linkinghub.elsevier.com/retrieve/pii/S0032386115004437

[82] M. Hudspeth, X. Nie, and W. Chen, "Dynamic failure of Dyneema SK76 single fibers under biaxial shear/tension," *Polymer*, vol. 53, no. 24, pp. 5568–5574, 2012. [Online]. Available: http://linkinghub.elsevier.com/retrieve/pii/S0032386112007884

[83] M. Hudspeth, B. Claus, N. Parab, B. Lim, W. Chen, T. Sun, and K. Fezza, "In Situ Visual Observation of Fracture Processes in Several High-Performance Fibers," *Journal of Dynamic Behavior of Materials*, vol. 1, no. 1, pp. 55–64, 2015. [Online]. Available: http://link.springer.com/10.1007/s40870-015-0009-3

[84] W. Hoogsteen, H. Kormelink, G. Eshuis, G. Brinke, and A. J. Penninfgs, "Gel-spun polyethylene fibres - Part 1," *Journal of Materials Science*, vol. 23, no. 10, pp. 3467–3474, 1988.

[85] W. Hoogsteen, H. Kormelink, G. Eshuis, G. Brinke, and A. J. Pennings, "Gel-spun polyethylene fibres - Part 2," *Journal of Materials Science*, vol. 23, no. 10, pp. 3467–3474, 1988.

[86] I. A. Gorshkova, G. N. Andreeva, A. V. Savitskii, and I. L. Frolova, "Properties of Oriented Fibers of High-Molecular-Weight Polyethylenes," *Mekhanika Kompozitnykh Materialov*, vol. 2, pp. 326–330, 1987.

[87] D. S. Boudreaux, "Calculations of the strength of the polyethylene molecule," *Journal of Polymer Science Part A-2: Polymer Physics*, vol. 11, no. 7, pp. 1285–1292, Jul. 1973. [Online]. Available: http://doi.wiley.com/10.1002/pol.1973.180110704

[88] S. Suhai, "Quantum mechanical calculation of the longitudinal elastic modulus and of deviations from Hookes law in polyethylene," *The Journal*

of Chemical Physics, vol. 84, no. 9, p. 5071, 1986. [Online]. Available: http://link.aip.org/link/JCPSA6/v84/i9/p5071/s1&Agg=doi

[89] Y. Termonia, P. Meakin, and P. Smith, "Theoretical Study of the Influence of the Molecular Weight on the Maximum Tensile Strength of Polymer Fibers," *Macromolecules*, vol. 18, pp. 2246–2252, 1985.

[90] ——, "Theoretical Study of the Influence of Strain Rate and Temperature on the Maximum Strength of Perfectly Ordered and Oriented Polyethylene," *Macromolecules*, vol. 19, no. 1, pp. 154–159, 1986.

[91] J. Smook, W. Hamersma, and A. J. Pennings, "The fracture process of ultra-high strength polyethylene fibres," *Journal of Materials Science*, vol. 19, no. 4, pp. 1359–1373, Apr. 1984. [Online]. Available: http://link.springer.com/10.1007/BF01120049

[92] D. J. Dijkstra, J. C. M. Torfs, and A. J. Pennings, "Temperature-dependent fracture mechanisms in ultra-high strength polyethylene fibers," *Colloid & Polymer Science*, vol. 267, no. 10, pp. 866–875, 1989.

[93] H. L. Stein, "Ultrahigh molecular weight polyethylenes(uhmwpe)," *ASM International, Engineering Plastics. Engineered Materials Handbook,*, vol. 2, pp. 167–171, 1988.

[94] Y. I. Frenkel and T. Kontorova, "The model of dislocation in solid body," *Zh. Eksp. Teor. Fiz*, vol. 8, no. 1340, 1938.

[95] H. H. Kausch and D. Langbein, "Elastic Interaction between Linear Polymeric Chains and Periodic Potentials," *Journal of Polymer Science: Polymer Physics Edition*, vol. 11, pp. 1201–1218, 1973.

[96] L. I. Manevitch and A. V. Savin, "Solitons in crystalline polyethylene: Isolated chains in the transconformation," *Physical Review E*, vol. 55, no. 4, pp. 4713–4719, 1997.

[97] A. Savin and L. Manevitch, "Solitons in crystalline polyethylene: A chain surrounded by immovable neighbors," *Physical Review B*, vol. 58, no. 17, pp. 11 386–11 400, 1998.

[98] N. K. Balabaev, O. V. Gendelman, and L. I. Manevitch, "Supersonic motion of vacancies in a polyethylene crystal." *Physical Review E*, vol. 64, p. 036702, 2001.

[99] E. A. Zubova, "On the applicability of the Frenkel-Kontorova model to describing the dynamics of vacancies in a polymeric crystal chain," *Journal of Experimental and Theoretical Physics*, vol. 93, no. 4, pp. 895–902, 2001.

[100] S. T. Milner and N. Wentzel, "Twist solitons in ordered phases of

n-alkanes," *Soft Matter*, vol. 7, no. 16, p. 7477, 2011. [Online]. Available: http://xlink.rsc.org/?DOI=c1sm05326d

[101] E. A. Zubova, N. K. Balabaev, A. I. Musienko, E. B. Gusarova, M. A. Mazo, L. I. Manevitch, and A. A. Berlin, "Simulation of melting in crystalline polyethylene." *The Journal of Chemical Physics*, vol. 136, no. 22, p. 224906, Jun. 2012. [Online]. Available: http://www.ncbi.nlm.nih.gov/pubmed/22713072

[102] A. Hammad, T. D. Swinburne, H. Hasan, S. D. Rosso, L. Iannucci, A. P. Sutton, H. Hasan, D. R. S, L. Iannucci, and S. A P, "Theory of the deformation of aligned polyethylene," *Proc. R. Soc. A*, vol. 471, 2015.

[103] H. Eyring, "Viscosity, plasticity, and diffusion as examples of absolute reaction rates," *The Journal of chemical physics*, vol. 4, no. 4, pp. 283–291, 1936.

[104] I. M. Ward and M. a. Wilding, "Creep behavior of ultrahigh-modulus polyethylene: Influence of draw ratio and polymer composition," *Journal of Polymer Science: Polymer Physics Edition*, vol. 22, no. 4, pp. 561–575, 1984.

[105] M. A. Wilding and I. M. Ward, "Creep and stress-relaxation in ultra-high modulus linear polyethylene," *Journal of Materials Science*, vol. 19, no. 2, pp. 629–636, 1984.

[106] V. R. Regel', A. I. Slutsker, and É. E. Tomashevskii, "The Kinetic Nature of

the Strength of Solids," *Uspekhi Fizicheskih Nauk*, vol. 106, no. 2, pp. 193–228, 1972.

[107] L. E. Govaert, C. W. M. Bastiaansen, and P. J. R. Leblans, "Stress-strain analysis of oriented polyethylene," *Polymer*, vol. 34, no. 3, pp. 534–540, 1993.

[108] L. E. Govaert and T. Peijs, "Tensile strength and work of fracture of oriented polyethylene fibre," *Polymer*, vol. 36, no. 23, pp. 4425–4431, 1995.

[109] D. R. Jenket, "Failure Mechanisms of Ultra High Molar Mass Polyethylene Single Fibers at Extreme Temperatures and Strain-Rates," Ph.D. dissertation, University of Maryland, 2017.

[110] J. Wang and K. Smith, "The breaking strength of ultra-high molecular weight polyethylene fibers," *Polymer*, vol. 40, no. 26, pp. 7261–7274, 1999.

[111] D. L. Dorset, "Electron-Diffraction Structure Analysis of Polyethylene. A Direct Phase Determination," *Macromolecules*, vol. 24, no. 5, pp. 1175–1178, 1991.

[112] T. C. O'Connor, R. M. Elder, Y. R. Sliozberg, T. W. Sirk, J. W. Andzelm, and M. O. Robbins, "Molecular origins of anisotropic shock propagation in crystalline and amorphous polyethylene," *Physical Review Materials*, vol. 2, no. 3, p. 035601, 2018. [Online]. Available: https://link.aps.org/doi/10.1103/PhysRevMaterials.2.035601

[113] W. Hoogsteen, G. Brinke, and A. J. Pennings, "DSC experiments on gel-spun polyethylene fibers," *Colloid & Polymer Science*, vol. 1013, pp. 1003–1013, 1988.

[114] W. Hoogsteen, G. Ten Brinke, and a. J. Pennings, "SAXS experiments on voids in gel-spun polyethylene fibres," *Journal of Materials Science*, vol. 25, no. 3, pp. 1551–1556, 1990.

[115] I. M. Ward and J. Sweeney, *Mechanical properties of solid polymers*. John Wiley & Sons, 2012.

[116] F. Zhang and M. A. Collins, "Topological solitons in polyethylene crystals," *Phys. Rev. E*, vol. 49, no. 6, 1994.

[117] F. Zhang, "Motion of twist defects in crystalline polyethylene: A molecular-dynamics study," *Physical Review B*, vol. 59, no. 2, pp. 792–796, 1999. [Online]. Available: http://link.aps.org/doi/10.1103/PhysRevB.59.792

[118] S. W. Mowry and G. C. Rutledge, "Atomistic Simulation of the R c -Relaxation in Crystalline Polyethylene," *Macromolecules*, vol. 35, pp. 4539–4549, 2002.

[119] E. A. Zubova, N. K. Balabaev, and L. I. Manevitch, "Molecular mechanisms of the chain diffusion between crystalline and amorphous fractions in polyethylene," *Polymer*, vol. 48, no. 6, pp. 1802–1813, 2007.

[120] K. Schmidt-Rohr and H. W. Spiess, "Chain Diffusion between Crystalline and

Amorphous Regions in Polyethylene Detected by 2D Exchange 13C NMR," *Macromolecules*, vol. 24, no. 19, pp. 5288–5293, 1991.

[121] B. Crist, C. J. Fisher, and P. R. Howard, "Mechanical properties of model polyethylenes: tensile elastic modulus and yield stress Buckley Crist, Christopher J. Fisher, Paul R. Howard," *Macromolecules*, vol. 22, no. 4, pp. 1709–1718, 1989. [Online]. Available: http://pubs.acs.org/doi/abs/10.1021/ma00194a035{%}5Cnhttp://pubs.acs.org/cgi-bin/searchRedirect.cgi/mamobx/1989/22/i04/pdf/ma00194a035.pdf

[122] T. C. O'Connor, J. Andzelm, and M. O. Robbins, "AIREBO-M: A reactive model for hydrocarbons at extreme pressures." *The Journal of chemical physics*, vol. 142, no. 2, p. 024903, jan 2015. [Online]. Available: http://www.ncbi.nlm.nih.gov/pubmed/25591383

[123] S. W. Siu, K. Pluhackova, and R. A. Böckmann, "Optimization of the OPLS-AA force field for long hydrocarbons," *Journal of Chemical Theory and Computation*, vol. 8, no. 4, pp. 1459–1470, 2012.

[124] H. Sun, "COMPASS: An ab Initio Force-Field Optimized for Condensed-Phase ApplicationsOverview with Details on Alkane and Benzene Compounds," *The Journal of Physical Chemistry B*, vol. 102, no. 38, pp. 7338–7364, 1998. [Online]. Available: http://pubs.acs.org/doi/abs/10.1021/jp980939v

[125] O. M. Braun and Y. S. Kivshar, "Nonlinear dynamics of the Frenkel Kontorova model," *Physics Reports*, vol. 306, pp. 1–108, 1998.

[126] I. Sakurada, T. Ito, and K. Nakamae, "Elastic moduli of the crystal lattices of polymers," *Journal of Polymer Science Part C: Polymer Symposia*, vol. 15, no. 1, pp. 75–91, 1966.

[127] J. Clements, R. Jakeways, and I. M. Ward, "Lattice modulus and crystallite thickness measurements in ultra-high modulus linear polyethylene," *Polymer*, vol. 19, no. 6, pp. 639–644, 1978.

[128] K. Tashiro, G. Wu, and M. Kobayashi, "Morphological effect on the Raman frequency shift induced by tensile stress applied to crystalline polyoxymethylene and polyethylene: spectroscopic support for the idea of an inhomogeneous stress distribution in polymer material," *Polymer*, vol. 29, no. 10, pp. 1768–1778, 1988.

[129] A. Odajima and T. Maeda, "Calculation of the Elastic Constants and the Lattice Energy of the Polyethylene Crystal," *Journal of Polymer Science Part C: Polymer Symposia*, vol. 15, no. 1, pp. 55–74, 1967.

[130] J. Klimeš and A. Michaelides, "Perspective: Advances and challenges in treating van der Waals dispersion forces in density functional theory," *Journal of Chemical Physics*, vol. 137, no. 12, 2012.

[131] R. Shrestha, P. Li, B. Chatterjee, T. Zheng, X. Wu, Z. Liu, T. Luo,

S. Choi, K. Hippalgaonkar, M. P. De Boer, and S. Shen, "Crystalline polymer nanofibers with ultra-high strength and thermal conductivity," *Nature Communications*, vol. 9, no. 1, 2018. [Online]. Available: http://dx.doi.org/10.1038/s41467-018-03978-3

[132] B. Sanborn, A. M. Dileonardi, and T. Weerasooriya, "Tensile Properties of Dyneema SK76 Single Fibers at Multiple Loading Rates Using a Direct Gripping Method," US Army Research Laboratory, Tech. Rep. June, 2014.

[133] P. B. McDaniel, K. E. Strawhecker, J. M. Deitzel, and J. W. Gillespie, "Nanoscale interfibrillar adhesion in UHMWPE fibers," *Journal of Polymer Science, Part B: Polymer Physics*, vol. 56, no. 5, pp. 391–401, 2018.

[134] P. B. McDaniel, J. M. Deitzel, D. Gregory, T. Polakovic, and J. W. Gillespie, "Single fiber peel test to assess ultra high molecular weight polyethylene fiber mesostructure interactions," *Journal of Applied Polymer Science*, vol. 135, no. 16, pp. 1–11, 2018.

[135] H. van der Werff and A. J. Pennings, "Tensile deformation of high strength and high modulus polyethylene fibers," *Colloid Polym. Sci.*, vol. 269, no. 8, pp. 747–763, 1991. [Online]. Available: http://dx.doi.org/10.1007/BF00657441

[136] B. L. Holian, "Modeling shock-wave deformation via molecular dynamics," *Phys. Rev. A*, vol. 37, pp. 2562–2568, Apr 1988. [Online]. Available: http://link.aps.org/doi/10.1103/PhysRevA.37.2562

[137] B. L. Holian and P. S. Lomdahl, "Plasticity induced by shock waves in nonequilibrium molecular-dynamics simulations," *Science*, vol. 280, no. 5372, pp. 2085–2088, 1998.

[138] T. C. Germann, B. L. Holian, P. S. Lomdahl, and R. Ravelo, "Orientation dependence in molecular dynamics simulations of shocked single crystals," *Phys. Rev. Lett.*, vol. 84, pp. 5351–5354, Jun 2000. [Online]. Available: http://link.aps.org/doi/10.1103/PhysRevLett.84.5351

[139] M. Grujicic, B. Pandurangan, W. C. Bell, B. A. Cheeseman, C. F. Yen, and C. L. Randow, "Molecular-level simulations of shock generation and propagation in polyurea," *Mater. Sci. Eng.*, vol. 528, no. 1011, pp. 3799–3808, 2011. [Online]. Available: http://www.sciencedirect.com/science/article/pii/S0921509311001031

[140] B. Arman, Q. An, S. N. Luo, T. G. Desai, D. L. Tonks, T. Çağın, and W. A. Goddard, "Dynamic response of phenolic resin and its carbon-nanotube composites to shock wave loading," *J. Appl. Phys.*, vol. 109, no. 1, p. 013503, 2011. [Online]. Available: http://scitation.aip.org/content/aip/journal/jap/109/1/10.1063/1.3524559

[141] S. Root, T. A. Haill, J. M. D. Lane, A. P. Thompson, G. S. Grest, D. G. Schroen, and T. R. Mattsson, "Shock compression of hydrocarbon foam to 200gpa: Experiments, atomistic simulations, and mesoscale hydrodynamic

modeling," *J. Appl. Phys.*, vol. 114, no. 10, p. 103502, 2013. [Online]. Available: http://scitation.aip.org/content/aip/journal/jap/114/10/10.1063/1.4821109

[142] J. M. D. Lane, G. S. Grest, and T. R. Mattsson, "Hot spot and temperature analysis of shocked hydrocarbon polymer foams using molecular dynamics simulation," *Comput. Mater. Sci.*, vol. 79, pp. 873–876, 2013. [Online]. Available: http://www.sciencedirect.com/science/article/pii/S0927025613003777

[143] L. He, T. D. Sewell, and D. L. Thompson, "Molecular dynamics simulations of shock waves in cis-1,4-polybutadiene melts," *J. Appl. Phys.*, vol. 114, no. 16, p. 163517, 2013. [Online]. Available: http://scitation.aip.org/content/aip/journal/jap/114/16/10.1063/1.4824546

[144] M. G. Fröhlich, T. D. Sewell, and D. L. Thompson, "Molecular dynamics simulations of shock waves in hydroxyl-terminated polybutadiene melts: Mechanical and structural responses," *J. Chem. Phys.*, no. 2, p. 024902, 2014. [Online]. Available: http://scitation.aip.org/content/aip/journal/jcp/140/2/10.1063/1.4853695

[145] Y. Fu, J. Michopoulos, and J.-H. Song, "Dynamics response of polyethylene polymer nanocomposites to shock wave loading," *J. Polym. Sci. B Polym. Phys.*, vol. 53, no. 18, pp. 1292–1302, 2015. [Online]. Available: http://dx.doi.org/10.1002/polb.23758

[146] F. Xie, Z. Lu, Z. Yang, W. Hu, and Z. Yuan, "Mechanical behaviors and molecular deformation mechanisms of polymers under high speed shock compression: A molecular dynamics simulation study," *Polymer*, vol. 98, pp. 294 – 304, 2016.

[147] R. Ravelo, T. C. Germann, O. Guerrero, Q. An, and B. L. Holian, "Shock-induced plasticity in tantalum single crystals: Interatomic potentials and large-scale molecular-dynamics simulations," *Phys. Rev. B*, vol. 88, no. 13, p. 134101, 2013. [Online]. Available: http://link.aps.org/doi/10.1103/PhysRevB.88.134101

[148] J. N. Johnson, "Shock propagation produced by planar impact in linearly elastic anisotropic media," *J. Appl. Phys.*, vol. 42, no. 13, pp. 5522–5530, 1971. [Online]. Available: http://scitation.aip.org/content/aip/journal/jap/42/13/10.1063/1.1659974

[149] D. Bancroft, E. L. Peterson, and S. Minshall, "Polymorphism of iron at high pressure," *J. Appl. Phys.*, vol. 27, no. 3, pp. 291–298, 1956.

[150] S. J. DeTeresa, R. S. Porter, and R. J. Farris, "A model for the compressive buckling of extended chain polymers," *J. Mat. Sci.*, vol. 20, no. 5, pp. 1645–1659, 1985. [Online]. Available: http://dx.doi.org/10.1007/BF00555268

[151] D. Hossain, M. A. Tschopp, D. K. Ward, J. L. Bouvard, P. Wang, and M. F. Horstemeyer, "Molecular dynamics simulations of deformation mechanisms of

amorphous polyethylene," *Polymer*, vol. 51, no. 25, pp. 6071–6083, 2010. [Online]. Available: http://dx.doi.org/10.1016/j.polymer.2010.10.009

[152] M. Lísal, J. K. Brennan, and J. B. Avalos, "Dissipative particle dynamics at isothermal, isobaric, isoenergetic, and isoenthalpic conditions using shardlow-like splitting algorithms," *The Journal of Chemical Physics*, vol. 135, no. 20, p. 204105, 2011. [Online]. Available: https://doi.org/10.1063/1.3660209

[153] M. Elstner, D. Porezag, G. Jungnickel, J. Elsner, M. Haugk, T. Frauenheim, S. Suhai, and G. Seifert, "Self-consistent-charge density-functional tight-binding method for simulations of complex materials properties," *Phys. Rev. B*, vol. 58, pp. 7260–7268, Sep 1998. [Online]. Available: https://link.aps.org/doi/10.1103/PhysRevB.58.7260

[154] J. P. Perdew, K. Burke, and M. Ernzerhof, "Generalized gradient approximation made simple," *Phys. Rev. Lett.*, vol. 77, pp. 3865–3868, Oct 1996. [Online]. Available: https://link.aps.org/doi/10.1103/PhysRevLett.77.3865

[155] Y. Zhao and D. G. Truhlar, "The m06 suite of density functionals for main group thermochemistry, thermochemical kinetics, noncovalent interactions, excited states, and transition elements: two new functionals and systematic testing of four m06-class functionals and 12 other functionals," *Theoretical Chemistry Accounts*, vol. 120, no. 1, pp. 215–241, May 2008.

[156] K. Andersson, P. A. Malmqvist, B. O. Roos, A. J. Sadlej, and K. Wolinski,

"Second-order perturbation theory with a casscf reference function," *Journal of Physical Chemistry*, vol. 94, no. 14, pp. 5483–5488, 1990.

[157] K. Andersson, P. Malmqvist, and B. O. Roos, "Secondorder perturbation theory with a complete active space selfconsistent field reference function," *The Journal of Chemical Physics*, vol. 96, no. 2, pp. 1218–1226, 1992.

[158] Y. R. Sliozberg, M. Kröger, and T. L. Chantawansri, "Fast equilibration protocol for million atom systems of highly entangled linear polyethylene chains," *J. Chem. Phys.*, vol. 144, no. 15, p. 154901, 2016.

[159] R. Auhl, R. Everaers, G. S. Grest, K. Kremer, and S. J. Plimpton, "Equilibration of long chain polymer melts in computer simulations," *J. Chem. Phys.*, vol. 119, no. 24, pp. 12 718–12 728, 2003.

[160] W. Paul, D. Y. Yoon, and G. D. Smith, "An optimized united atom model for simulations of polymethylene melts," *J. Chem. Phys.*, vol. 103, no. 4, pp. 1702–1709, 1995.

[161] K. Kadau, T. C. Germann, P. S. Lomdahl, and B. L. Holian, "Atomistic simulations of shock-induced transformations and their orientation dependence in bcc Fe single crystals," *Phys. Rev. B*, vol. 72, no. 6, p. 064120, 2005. [Online]. Available: http://link.aps.org/doi/10.1103/PhysRevB.72.064120

[162] B. D. Todd, D. J. Evans, and P. J. Daivis, "Pressure tensor for inhomogeneous fluids," *Phys. Rev. E*, vol. 52, pp. 1627–1638, 1995.

[163] M. L. Falk and J. S. Langer, "Dynamics of viscoplastic deformation in amorphous solids," *Phys. Rev. E*, vol. 57, pp. 7192–7205, Jun 1998. [Online]. Available: http://link.aps.org/doi/10.1103/PhysRevE.57.7192

[164] F. Varnik, J. Baschnagel, and K. Binder, "Molecular dynamics results on the pressure tensor of polymer films," *J. Chem. Phys.*, vol. 113, pp. 4444–4453, 2000.

[165] F. Shimizu, S. Ogata, and J. Li, "Theory of shear banding in metallic glasses and molecular dynamics calculations," *Mater. Trans.*, vol. 48, no. 11, pp. 2923–2927, 2007.

[166] J. Rottler and M. O. Robbins, "Yield conditions for deformation of amorphous polymer glasses," *Phys. Rev. E*, vol. 64, p. 051801, Oct 2001. [Online]. Available: https://link.aps.org/doi/10.1103/PhysRevE.64.051801

[167] L. Lin and A. S. Argon, "Structure and plastic deformation of polyethylene," *J. of Materials Science*, vol. 29, no. 2, pp. 294–323, 1994.

[168] K. Russell, B. Hunter, and R. Heyding, "Monoclinic polyethylene revisited," *Polymer*, vol. 38, no. 6, pp. 1409–1414, 1997. [Online]. Available: http://www.sciencedirect.com/science/article/pii/S003238619600643X

[169] M. R. McGann and D. J. Lacks, "Molecular simulation of shear instabilities in polyethylene and n-alkane crystals under axial compression," *Macromolecules*, vol. 31, no. 18, pp. 6356–6361, 1998. [Online]. Available: http://dx.doi.org/10.1021/ma9805203

[170] ——, "Entropically induced euler buckling instabilities in polymer crystals," *Phys. Rev. Lett.*, vol. 82, pp. 952–955, Feb 1999. [Online]. Available: http://link.aps.org/doi/10.1103/PhysRevLett.82.952

[171] J. Lankford, "Compressive failure of fibre-reinforced composites: buckling, kinking, and the role of the interphase," *J. Mater. Sci.*, vol. 30, no. 17, pp. 4343–4348, 1995. [Online]. Available: http://dx.doi.org/10.1007/BF00361515

[172] J. M. Winey and Y. M. Gupta, "Nonlinear anisotropic description for shocked single crystals: Thermoelastic response and pure mode wave propagation," *Journal of Applied Physics*, vol. 96, no. 4, pp. 1993–1999, 2004.

[173] D. P. Holmes and A. J. Crosby, "Draping films: A wrinkle to fold transition," *Phys. Rev. Lett.*, vol. 105, p. 038303, Jul 2010. [Online]. Available: http://link.aps.org/doi/10.1103/PhysRevLett.105.038303

[174] H. King, R. D. Schroll, B. Davidovitch, and N. Menon, "Elastic sheet on a liquid drop reveals wrinkling and crumpling as distinct symmetry-breaking instabilities," *Proc. Natl. Acad. Sci. U.S.A.*, vol. 109, no. 25, pp. 9716–9720, 2012.

[175] F. Brau, P. Damman, H. Diamant, and T. A. Witten, "Wrinkle to fold transition: influence of the substrate response," *Soft Matter*, vol. 9, no. 34, pp. 8177–8186, 2013.

[176] H. Kolsky, "Production of Tensile Shock Waves in Stretched Natural Rubber," *Nature*, vol. 224, p. 1301, 1969.

[177] L. Fontana, M. Santoro, R. Bini, D. Q. Vinh, and S. Scandolo, "High-pressure vibrational properties of polyethylene." *The Journal of chemical physics*, vol. 133, no. 20, p. 204502, nov 2010. [Online]. Available: http://www.ncbi.nlm.nih.gov/pubmed/21133441

[178] A. Bach, K. Almdal, H. K. Rasmussen, and O. Hassager, "Elongational Viscosity of Narrow Molar Mass Distribution Polystyrene Elongational Viscosity of Narrow Molar Mass Distribution Polystyrene," *Society*, vol. 36, no. June, pp. 5174–5179, 2003.

[179] J. K. Nielsen, H. K. Rasmussen, O. Hassager, and G. H. McKinley, "Elongational viscosity of monodisperse and bidisperse polystyrene melts," *Journal of Rheology*, vol. 50, no. 4, pp. 453–476, 2006. [Online]. Available: http://sor.scitation.org/doi/10.1122/1.2206711

[180] G. Marrucci, "Dynamics of entanglements: A nonlinear model consistent with the Cox-Merz rule," *Journal of Non-Newtonian Fluid Mechanics*, vol. 62, no.

2-3, pp. 279–289, 1996. [Online]. Available: http://linkinghub.elsevier.com/retrieve/pii/0377025795014071

[181] D. W. Mead, D. Yavich, and L. G. Leal, "The reptation model with segmental stretch - II. Steady flow properties," *Rheologica Acta*, vol. 34, no. 4, pp. 360–383, 1995.

[182] D. W. Mead, R. G. Larson, and M. Doi, "A molecular theory for fast flows of entangled polymers," *Macromolecules*, vol. 31, no. 22, pp. 7895–7914, 1998.

[183] G. Marrucci and G. Ianniruberto, "Interchain pressure effect in extensional flows of entangled polymer melts," *Macromolecules*, vol. 37, no. 10, pp. 3934–3942, 2004.

[184] A. E. Likhtman, "Single-chain slip-link model of entangled polymers: Simultaneous description of neutron spin-echo, rheology, and diffusion," *Macromolecules*, vol. 38, no. 14, pp. 6128–6139, 2005.

[185] C. Baig, V. G. Mavrantzas, and M. Kröger, "Flow effects on melt structure and entanglement network of linear polymers: Results from a nonequilibrium molecular dynamics simulation study of a polyethylene melt in steady shear," *Macromolecules*, vol. 43, no. 16, pp. 6886–6902, 2010.

[186] M. Andreev, R. N. Khaliullin, R. J. A. Steenbakkers, and J. D. Schieber, "Approximations of the discrete slip-link model and their effect on nonlinear

rheology predictions," *Journal of Rheology*, vol. 57, no. 2, pp. 535–557, 2013. [Online]. Available: http://sor.scitation.org/doi/10.1122/1.4788909

[187] G. Ianniruberto, A. Brasiello, and G. Marrucci, "Simulations of fast shear flows of PS oligomers confirm monomeric friction reduction in fast elongational flows of monodisperse PS melts as indicated by rheooptical data," *Macromolecules*, vol. 45, no. 19, pp. 8058–8066, 2012.

[188] T. Yaoita, T. Isaki, Y. Masubuchi, H. Watanabe, G. Ianniruberto, and G. Marrucci, "Primitive Chain Network Simulation of Elongational Flows of Entangled Linear Chains : Stretch / Orientation-induced Reduction of Monomeric Friction Primitive Chain Network Simulation of Elongational Flows of Entangled Linear Chains : Stretch / Orientation," *Macromolecules*, pp. 1–37, 2012.

[189] Z. Wang, C. N. Lam, W.-R. Chen, W. Wang, J. Liu, Y. Liu, L. Porcar, C. B. Stanley, Z. Zhao, K. Hong, and Y. Wang, "Fingerprinting molecular relaxation in deformed polymers," *Phys. Rev. X*, vol. 7, p. 031003, Jul 2017. [Online]. Available: https://link.aps.org/doi/10.1103/PhysRevX.7.031003

[190] W.-S. Xu, J.-M. Y. Carrillo, C. N. Lam, B. G. Sumpter, and Y. Wang, "Molecular Dynamics Investigation of the Relaxation Mechanism of Entangled Polymers after a Large Step Deformation," *ACS Macro Letters*, pp. 190–195, 2018. [Online]. Available: http://pubs.acs.org/doi/10.1021/acsmacrolett.7b00900

[191] T. Sridhar, M. Acharya, D. A. Nguyen, and P. K. Bhattacharjee, "On the extensional rheology of polymer melts and concentrated solutions," *Macromolecules*, vol. 47, no. 1, 2013.

[192] A. E. Likhtman, S. K. Sukumaran, and J. Ramirez, "Linear viscoelasticity from molecular dynamics simulation of entangled polymers," *Macromolecules*, vol. 40, no. 18, pp. 6748–6757, 2007.

[193] J. Cao and A. E. Likhtman, "Simulating Startup Shear of Entangled Polymer Melts," *ACS Macro Letters*, vol. 4, no. 12, pp. 1376–1381, 2015.

[194] M. Kroger, C. Luap, and R. Muller, "Polymer Melts under Uniaxial Elongational Flow: Stress-Optical Behavior from Experiments and Nonequilibrium Molecular Dynamics Computer Simulations," *Macromolecules*, vol. 30, no. 96, pp. 526–539, 1997.

[195] P. J. Daivis, M. L. Matin, and B. D. Todd, "Nonlinear shear and elongational rheology of model polymer melts by non-equilibrium molecular dynamics," *Journal of Non-Newtonian Fluid Mechanics*, vol. 111, no. 1, pp. 1–18, 2003.

[196] K. Kremer and G. S. Grest, "Dynamics of entangled linear polymer melts: A molecular-dynamics simulation," *The Journal of Chemical Physics*, vol. 92, no. 8, p. 5057, 1990. [Online]. Available: http://scitation.aip.org/content/aip/journal/jcp/92/8/10.1063/1.458541

[197] L. A. Moreira, G. Zhang, F. Müller, T. Stuehn, and K. Kremer, "Direct equilibration and characterization of polymer melts for computer simulations," *Macromolecular Theory and Simulations*, vol. 24, no. 5, pp. 419–431, 2015.

[198] H.-P. Hsu and K. Kremer, "Static and dynamic properties of large polymer melts in equilibrium," *The Journal of Chemical Physics*, vol. 144, no. 15, p. 154907, 2016. [Online]. Available: http://scitation.aip.org/content/aip/journal/jcp/144/15/10.1063/1.4946033

[199] T. Ge, M. O. Robbins, D. Perahia, and G. S. Grest, "Healing of polymer interfaces: Interfacial dynamics, entanglements, and strength," *Physical Review E - Statistical, Nonlinear, and Soft Matter Physics*, vol. 90, no. 1, pp. 1–15, 2014.

[200] M. Doi, "Explanation for the 3.4-power law for viscosity of polymeric liquids on the basis of the tube model," *Journal of Polymer Science: Polymer Physics Edition*, vol. 21, no. 5, pp. 667–684, 1983. [Online]. Available: http://doi.wiley.com/10.1002/pol.1983.180210501

[201] J. X. Hou, C. Svaneborg, R. Everaers, and G. S. Grest, "Stress relaxation in entangled polymer melts," *Physical Review Letters*, vol. 105, no. 6, pp. 1–4, 2010.

[202] M. Blume, P. Heller, and N. A. Lurie, "Classical one-dimensional Heisenberg magnet in an applied field," *Physical Review B*, vol. 11, no. 11, pp. 4483–4497, 1975.

[203] T. Ruijgrok and T. Niemeijer, "The classical one-dimensional Heisenberg magnet in an external magnetic field. Transfer matrix formalism as an application of renormalization group theory "avant la lettre"," *Physica*, vol. 84A, pp. 336–349, 1976.

[204] R. Everaers, S. K. Sukumaran, G. S. Grest, C. Svaneborg, A. Sivasubramanian, and K. Kremer, "Rheology and Microscopic Topology of Entangled Polymeric Liquids," *Science*, vol. 303, no. 5659, pp. 823–826, 2004. [Online]. Available: http://www.sciencemag.org/cgi/doi/10.1126/science.1091215

[205] M. Kröger, "Shortest multiple disconnected path for the analysis of entanglements in two- and three-dimensional polymeric systems," *Computer Physics Communications*, vol. 168, no. 3, pp. 209–232, 2005.

[206] C. Tzoumanekas and D. N. Theodorou, "Topological analysis of linear polymer melts: A statistical approach," *Macromolecules*, vol. 39, no. 13, pp. 4592–4604, 2006.

[207] G. S. Grest, "Communication: Polymer entanglement dynamics: Role of attractive interactions," *The Journal of Chemical Physics*, vol. 145, no. 14, p. 141101, 2016.

[208] D. J. Evans and G. P. Morriss, "Nonlinear-response theory for steady planar couette flow," *Phys. Rev. A*, vol. 30, pp. 1528–1530, Sep 1984. [Online]. Available: https://link.aps.org/doi/10.1103/PhysRevA.30.1528

[209] P. J. Daivis and B. D. Todd, "A simple, direct derivation and proof of the validity of the SLLOD equations of motion for generalized homogeneous flows," *Journal of Chemical Physics*, vol. 124, no. 19, 2006.

[210] C. M. Schroeder, H. P. Babcock, E. S. Shaqfeh, and S. Chu, "Observation of polymer conformation hysteresis in extensional flow," *Science*, vol. 301, no. 5639, pp. 1515–1519, 2003.

[211] K.-W. Hsiao, C. Sasmal, J. Ravi Prakash, and C. M. Schroeder, "Direct observation of dna dynamics in semidilute solutions in extensional flow," *Journal of Rheology*, vol. 61, no. 1, pp. 151–167, 2017. [Online]. Available: https://doi.org/10.1122/1.4972236

[212] J. T. Kalathi, S. K. Kumar, M. Rubinstein, and G. S. Grest, "Rouse mode analysis of chain relaxation in homopolymer melts," *Macromolecules*, vol. 47, no. 19, pp. 6925–6931, 2014, pMID: 25328247. [Online]. Available: https://doi.org/10.1021/ma500900b

[213] G. Ianniruberto, "Quantitative appraisal of a new CCR model for entangled linear polymers," *J. Rheol.*, vol. 59, no. 1, pp. 211–235, 2015. [Online]. Available: http://dx.doi.org/10.1122/1.4903495

[214] D. W. Mead, N. Banerjee, and J. Park, "A constitutive model for entangled polymers incorporating binary entanglement pair dynamics and a configuration dependent friction coefficient," *J. Rheol.*, vol. 59, no. 2, pp. 335–363, 2015.

[Online]. Available: http://scitation.aip.org/content/sor/journal/jor2/59/2/10.1122/1.4905921

[215] S.-Q. Wang, *Nonlinear Polymer Rheology: Macroscopic Phenomenology and Molecular Foundation*. John Wiley & Sons, 2018.

[216] J. Rudnick and G. Gaspari, "The shapes of random walks," *Science*, vol. 237, no. 4813, pp. 384–389, 1987.

[217] D. M. Sussman and K. S. Schweizer, "Microscopic theory of entangled polymer melt dynamics: Flexible chains as primitive-path random walks and supercoarse grained needles," *Phys. Rev. Lett.*, vol. 109, p. 168306, Oct 2012. [Online]. Available: https://link.aps.org/doi/10.1103/PhysRevLett.109.168306

[218] J. Qin and S. T. Milner, "Tube diameter of oriented and stretched polymer melts," *Macromolecules*, vol. 46, no. 4, pp. 1659–1672, 2013.

Vita

Thomas Cathal O'Connor was born in Portsmouth Virginia on September 21, 1989. A child of U.S. Navy officers, he moved frequently, attending school in Wisconsin, Georgia, and Florida, before enrolling at Rensselaer Polytechnic Institute in 2008. He graduated *summa cum laude* with a B.S. in Physics in 2012. He began his Ph.D. in Physics in 2012 with Mark O. Robbins at Johns Hopkins University. His first projects investigated the properties of polyethylene fibers in collaboration with the U.S. Army Research Laboratory. Through this program he developed interests in polymer physics, hydrodynamics, and nonlinear mechanics, which shaped the trajectory of his subsequent research. Thomas's graduate research was recognized with the 2016 Ken Hass Outstanding Student Paper Award from the APS Forum on Industrial and Applied Physics and with a finalist nomination for the 2018 Frank J. Padden Award for excellence in polymer physics research. He recently won the Harry S. Truman Fellowship in National Security Science and Engineering which takes him to the Sandia National Laboratories in Albuquerque, NM.